

Experimental Investigation on Mechanical Properties of Indigenous Rubber Products

Md. Ruhul Amin Rana¹, Mohammad Ikthair Hossain Soiket², Jawad Al Ratu^{3,a)}

¹*Department of Mechanical Engineering, The University of British Columbia (Okanagan), Kelowna V1V 1V7, Canada*

²*Department of Mechanical Engineering, University of Alberta, Edmonton AB T6G 2R3, Canada*

³*Department of Mechanical Engineering, Bangladesh University of Engineering & Technology, Dhaka-1000, Bangladesh*

^{a)}Corresponding author: ratunme@yahoo.com

Abstract. A study on the mechanical properties of different indigenous rubber sample of various companies have been conducted to have an idea of the quality of their rubber comparing with the American Society for Testing and Materials (ASTM) standard value. Two types of sample was taken for analysis: rubber sheet and bi-cycle tube. These rubber products have been procured from the local market. Tensile strength, Percentage of elongation, Hardness were obtained for both the rubber products. Then the statistical analysis was done for each of the properties. It has been observed that none of the products follow the standards.

INTRODUCTION

Until recently modern thinkers believed that rubber originated in 19th century Europe. The ancient Mayan people used latex to make rubber balls, hollow human figures, and as bindings used to secure axe heads to their handles and other functions. Latex [1] is the sap of various plants, most notably the rubber tree. When it is exposed to the air it hardens into a springy mass. The Mayans learned to mix the rubber sap with the juice from morning glory vines so that it became more durable and elastic, and didn't get quite as brittle. In 1791, an Englishman named Samuel Peal discovered a means of waterproofing cloth by mixing rubber with turpentine. English inventor and scientist, Joseph Priestly, got his hands on some rubber and realized it could be used to erase pencil marks on sheets of paper. Charles Goodyear, an American whose name graces the tires under millions of automobiles, is credited with the modern form of rubber. Goodyear's recipe, a process known as vulcanization, was discovered when a mixture of rubber, lead and sulfur were accidentally dropped onto a hot stove. The result was a substance that wasn't affected by weather, and which would snap back to its original form if stretched. The process was refined and the uses for rubber materials increased as well. This new rubber was resistant to water and chemical interactions and did not conduct electricity, so it was suited for a variety of products.

Natural rubber [2] is a linear polymer of an unsaturated hydrocarbon called isoprene (2-methyl butadiene). There may be as many as 11,000 to 20,000 isoprene units in a polymer chain of natural rubber.

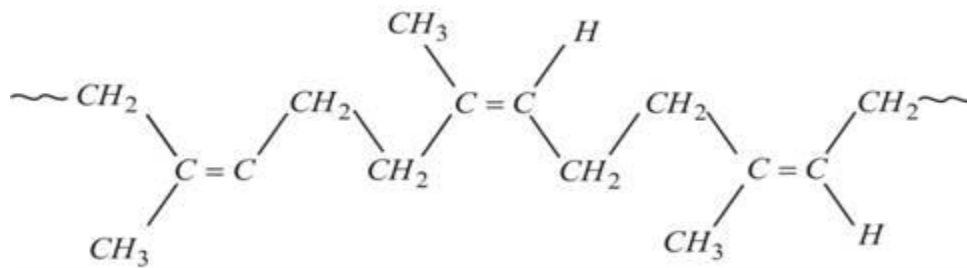


FIGURE. 1. Structure of Natural Rubber.

Because of its elasticity, resilience, and toughness, natural rubber (NR) is the basic constituent of many products used in the transportation, industrial, consumer, hygienic and medical sectors [3]. Of these major end-use markets for rubber, transportation is by far the largest single sector, with tires and tire products accounting alone for over 50% of NR consumption. Truck and bus tires would represent the largest single outlet for NR, followed by automobile tires. Non-tire rubber items include industrial products (for example, transmission and elevator belts, hoses and tubes, industrial lining, and bridge bearings); consumer products (like golf or football balls and other recreational and sports goods, erasers, footwear and other apparel); and articles for use in the medical and health sector (notably, condoms, catheters and surgical gloves) as well as seismic materials (for instance, over 500 and 2,500 buildings are respectively fitted with seismic rubber bearings in China and Japan.

Apart from NR, Today about three quarters of the rubber in production is a synthetic product (synthetic rubber) to obtain certain properties that are absent in natural rubber. In general, Synthetic Rubber [2] (also known as Gutta-Percha) was obtained by the free radical polymerization of Isoprene. The rubber so formed has all trans- Configuration. As a result of this, synthetic rubber has a highly regular zig-zag chain which cannot be stretched .This accounts for non-elasticity of Synthetic Rubber.

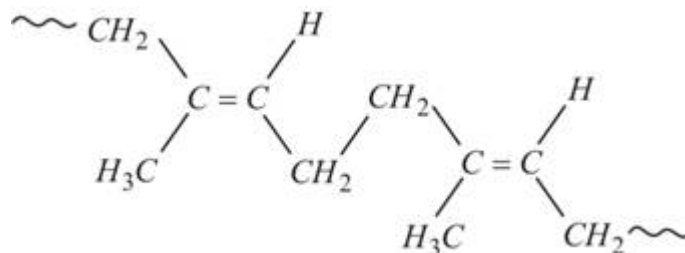


FIGURE. 2. Structure of synthetic Rubber.

There have been developed thousands of rubber manufacturers in Bangladesh which are producing rubber by local technology & technicians without following any standard. Most of them doesn't use any engineers or experts but simple illiterate technicians. So questions arises about the standard of the rubbers with respect to international standard i.e. ASTM, BS etc.

As rubber is an important engineering material, its quality must be assured. It has become important to test its mechanical properties with a view to ascertaining whether it is suitable for the require application. There must be a yearly survey on the rubber for its quality control. But unfortunately there are no such facilities for that. So, being motivated with the facts we decided to work on it to know the present condition of indigenous rubber & to play a role in improvement of its properties.

It could have been a good work if almost all the indigenous rubber products of different industries could be taken into consideration. As a preliminary step only products from two industries were taken and tested to compare their properties with international standard.

THEORY

Following statistical parameters are used in this thesis for statistical analysis :

Mean

If $x_1, x_2, x_3, \dots, x_N$ represent the values of 'N' samples then the sample mean is computed from the relation [4],

$$\mu = (\sum x_i)/N \tag{1}$$

here, $i = 1, 2, 3, \dots, N$

Standard Deviation

The variance can be computed as

$$\sigma_x^2 = \{(x_1 - \mu)^2 + (x_2 - \mu)^2 + \dots + (x_N - \mu)^2\}/(N-1)$$

The sample standard deviation can be written as,

$$\begin{aligned} \sigma_x &= [\{\sum(x_i - \mu)^2\}/(N-1)]^{1/2} \\ &= \{\sum(x_i - \mu)^2\}/(N-1) \end{aligned} \tag{2}$$

Normal Distribution Curve

The most important continuous probability distribution in the entire field of statistics is the normal distribution. If 'x' is the normal random variable with mean μ & variance σ_x^2 , then the expression of the normal distribution curve is,

$$f(x) = \exp[-1/2\{(x-\mu)/\sigma\}^2]/\{\sigma \sqrt{2\pi}\} \tag{3}$$

SPECIMEN PREPARATION & TEST EQUIPMENT

Two types of rubber specimen were used in our analysis. Specimen – A: rubber sheet and Specimen – B: bi-cycle tube. For each specimen 150 samples (totaling 300) were taken. The specimens were prepared by using cutting dies with the help of hydraulic press. The dimensions were maintained according to the ASTM standard [5]. The main equipment used for tensile & elongation test is rubber tensile testing machine. The machine was built in BUET by the previous alumni's. It consists of control panel box, spring balance, gripper, lead screw, 3-Ø motor (1 hp), limit switch, emergency stop switch stopper etc. Apart from that, test data's also measured in a digital machine (JT TOHSI). For hardness, testing Durometer was used.

SAMPLE CALCULATION

Tensile Strength [6] = P/A
 where, P = Applied load , in N
 A = Cross sectional area, in mm^2

For Specimen-A; Sample No. 110

P = 30.41 N
 A = 12.6896 mm^2
 Tensile Strength = $(30.41/12.6896)$ MPa
 = 2.39645 MPa

% of elongation [6] = $[(\text{Final length} - \text{Gauge length}) / \text{Gauge length}] \times 100\%$

For Specimen-B; Sample No. 120

Gauge length = 25 mm
 Final length = 164.9 mm
 % of elongation = $[(164.9 - 25)/25] \times 100\% = 559.6 \%$

TABLE 1. Statistical parameters obtained from experiment

Properties	Statistical Parameters	Sample-A	Sample-B
Tensile Strength	Mean, μ (MPa)	2.37	11.91
	Standard deviation, σ_x (MPa)	0.15	0.92
% of elongation	Mean, μ (%)	80.98	547.78
	Standard deviation, σ_x (%)	14.66	23.03
Hardness	Mean, μ	82.15	50.31
	Standard deviation, σ_x	1.71	0.89

RESULT ANALYSIS

The mean value of tensile strength obtained from test for specimen – A and specimen – B is 2.37 MPa and 11.91 MPa respectively. While according to ASTM standard [5] the minimum value of tensile strength should be 15.5 MPa.

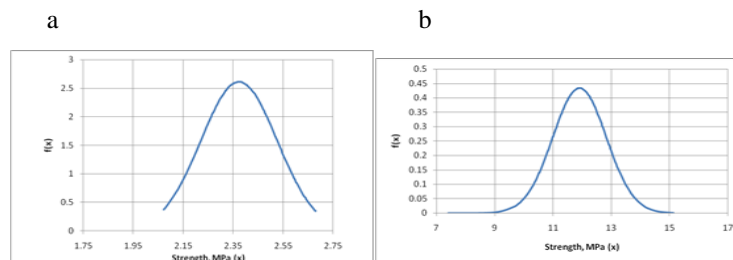


FIGURE. 3. Normal distribution curve for tensile test of (a) sample-A; (b) sample-B

The mean value of percentage of elongation obtained, 80.98% for specimen – A and 547.78% for specimen – B while the ASTM standard is 350%. [7].

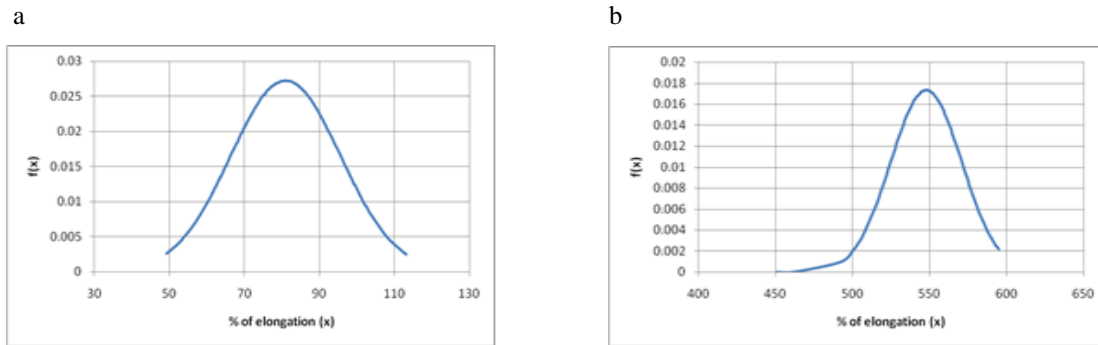


FIGURE. 4. Normal distribution curve for percentage elongation test of (a) sample-A; (b) sample-B

For vulcanized rubber products the acceptable range of hardness (Shore-A) number is 60 ± 5 [8]. But from experiment, it was found that the mean value of hardness of specimen – A is 82.15 & for specimen – B, it is 50.31.

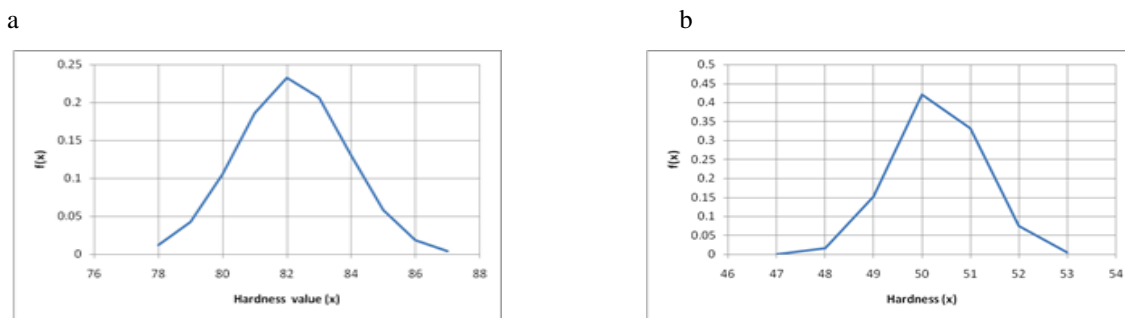


FIGURE. 5. Normal distribution curve for hardness test of (a) sample-A; (b) sample-B

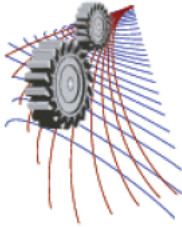
DISCUSSION

The rubber products were produced locally & sold in the market without test. The manufacturers are not following any standard; as a matter of fact the people of this country are purchasing rubber products of non-standard mechanical properties. More integrated prediction can be made if the effect of temperature on the various properties of natural rubber can be studied along with other mechanical properties of rubber e.g. ash content, compression set, shear modulus can be determined.

REFERENCES

- [1] Antoon Versteegde: transient structures of bamboo. Available from: URL: http://www.versteegde.nl/History_of_Elastic_and_Rubber_Bands.html
- [2] Xamplified Free Online Education Resource. Rubber. Available from: URL: <http://www.chemistrylearning.com/rubber/>
- [3] Indolatex. Main Uses of Natural Rubber. Available from: URL: <http://indolatex.com/main-uses-of-natural-rubber/>
- [4] J. E. Shigley, Mechanical Engineering Design, first metric ed., McGraw-Hill, Columbus, 1986, pp. 162-169.
- [5] ASTM D412-98a, Standard Test Methods for Vulcanized Rubber and Thermoplastic Rubbers and Thermoplastic Elastomers-Tension, ASTM International, West Conshohocken, PA, 1998.

- [6] A.C. Mandal and M.Q. Islam, Mechanics of Materials- Laboratory Practice, BUET Press, Dhaka, 1999, pp. 5-6.
- [7] ASTM D1456-86(2001), Standard Test Method for Rubber Property—Elongation at Specific Stress, ASTM International, West Conshohocken, PA, 1986.
- [8] ASTM D2240-05, Standard Test Method for Rubber Property—Durometer Hardness, ASTM International, West Conshohocken, PA, 2005,



Comparison Between 2D and 3D Modeling of Heat Transfer for a Solar Collector

R. Nasrin^{a), 1}, M.A. Alim¹, Mohammad Ali² and Md. S. Alam³

¹*Department of Mathematics, Bangladesh University of Engineering & Technology, Dhaka-1000, Bangladesh*

²*Department of Mathematics, Chittagong University of Engineering and Technology, Chittagong-4349, Bangladesh*

³*Department of Mathematics, Jagannath University, Dhaka-1100, Bangladesh*

^{a)}Corresponding author: rehena@math.buet.ac.bd

Abstract. Solar energy is one of the best sources of renewable energy with minimal environmental impact. The forced convection in solar collector continues to be a very active area of research during the past few decades. Commercial applications of solar collectors include swimming pool, space heating, car washes, military laundry facilities and eating establishments. Solar water heating systems are useful most likely to be cost effective for facilities with water heating systems that are expensive to operate or with operations such as laundries or kitchens that require large quantities of hot water. In this analysis 2D as well as 3D heat transfer models are developed of a flat plate solar collector (FPSC). The heat transfer medium is considered as water based copper nanofluid. The governing partial differential equations are solved using finite element method with Galerkin's weighted residual technique. In order to evaluate the temperature and velocity within the collector, the energy balance equation and Navier Stoke's equation are solved numerically. Average Nusselt number (Nu), average temperature (T_{av}), collector efficiency (η) for both nanofluid and base fluid through the collector are presented as function of the solid volume fraction of Cu nanoparticles. It is observed that upto a certain range of the concentration variation increases the rate of heat transfer and collector efficiency for nanofluid more than that of pure water. The output results of 2D and 3D numerical analyses are compared. It is concluded that in order to get higher outlet temperature and thermal efficiency of solar collector 3D numerical analysis is needed. Code validation is also shown with the literature available.

INTRODUCTION

Solar flat plate collectors are commonly used for domestic and industrial purposes and have the largest commercial application amongst the various solar collectors. This is mainly due to simple design as well as low maintenance cost. Solar radiation is radiant energy emitted by the sun. It is particularly electromagnetic energy. Solar irradiance (I) is the combination of bright light and radiant heat. Heat transfer due to emission of electromagnetic waves is known as thermal radiation. The heat transfer rate per unit area as thermal radiation is called radiative heat flux. Forced convection is a mechanism in which fluid motion is generated by an external source. Significant amounts of heat energy can be transported very efficiently by this system and it is found very commonly in everyday life, including central heating, air conditioning, steam turbines and in

many other machines. The fluids with solid-sized nanoparticles suspended in them are called “nanofluids”. Applications of nanoparticles in thermal field are to augment warmth transport from solar collectors to luggage compartment tanks, to pick up proficiency of coolants in transformers. Karanth et al. [1] numerically simulated a solar flat plate collector using Discrete Transfer Radiation Model. A 3D model of the collector involving the water pipe, absorber plate, the glass top and the air gap in-between the absorber plate and the glass top was modeled to provide for conduction, convection and radiation in their analysis. Bégin et al. [2] performed non-similar mixed convection heat and species transfer along an inclined solar energy collector surface with cross diffusion effects, where the resulting governing equations were transformed and then solved numerically using the local nonsimilarity method and Runge-Kutta shooting quadrature. Manjunath et al. [3-4] analyzed three dimensional conjugate heat transfers through unglazed solar flat plate collector. They used finned tubes and the heat transfer simulation due to solar irradiation to the fluid medium, increased with an increase in the mass flow rate. Vestlund [5] studied gas-filled flat plate solar collector. The gases examined were argon, krypton and xenon in his thesis paper. CFD analysis of solar flat plate collector was conducted by Ingle et al. [6]. His work attempted to present numerical simulation of solar collector developed exclusively for grape drying. CFD analysis of triangular absorber tube of a solar flat plate collector was performed by Basavanna and Shashishekar [7] where the numerical results obtained using the experimentally measured temperatures are compared to the temperatures determined by the CFD model. Tagliafico et al. [8] reviewed dynamic thermal models and CFD analysis for flat-plate thermal solar collectors. They presented an updated review of models for flat-plate thermal solar collectors, including a proper classification and a description of their main characteristics and performance. Struckmann [9] and Kalogirou [10] conducted project and survey reports on solar thermal collectors respectively. Very recently, Nasrin and Alim [11-12] developed a semi-empirical relation for forced convective analysis through a solar collector. A new correlation was derived from their obtained results and it was easy to use heat transfer purposes.

From the above literature review it is mentioned that some 2D numerical analyses have been done using nanofluids, some experimental works also have been conducted but a very few 3D numerical studies have been completed using traditional fluid that is water, gas, air etc. The overall goal of this study is to numerically simulate 2D as well as 3D models of heat transfer by nanofluids through a flat plate solar collector. The investigation is to be carried out at different values of solid volume fraction (ϕ) of Cu nanoparticles. The results obtained in 2D and 3D analyses are compared. The importance of 3D numerical study for FPSC is shown.

Nomenclature

A	Surface area of the collector (m^2)	U_{in}	Input velocity of fluid (ms^{-1})
C_p	Specific heat at constant pressure (J kg^{-1} K^{-1})	X, Y	Dimensionless coordinates
h	Local heat transfer coefficient (W m^{-2} K^{-1})	x, y	Dimensional coordinates (m)
I	Intensity of solar radiation (W m^{-2}),	Greek Symbols	
k	Thermal conductivity ($\text{W m}^{-1} \text{K}^{-1}$)	α	Fluid thermal diffusivity ($\text{m}^2 \text{s}^{-1}$)
L	Length of the riser pipe (m)	β	Thermal expansion coefficient (K^{-1})
m	mass flow rate (Kg s^{-1})	ϕ	Nanoparticles volume fraction
Nu	Nusselt number	ν	Kinematic viscosity ($\text{m}^2 \text{s}^{-1}$)
Pr	Prandtl number	η	collector efficiency
Re	Reynolds number,	θ	Dimensionless temperature
T	Dimensional temperature (K)	ρ	Density (kg m^{-3})
T_{in}	Input temperature of fluid (K)	μ	Dynamic viscosity (N s m^{-2})
T_{out}	Output temperature of fluid (K)	V	Dimensionless velocity field
u, v	Dimensional velocity components (m s^{-1})	Subscripts	
U, V	Dimensionless velocities	col	collector
		f	fluid
		nf	nanofluid
		s	solid particle

PROBLEM FORMULATION

The temperature distribution of absorber plate has a symmetry form on each riser pipe. Thus one riser pipe is considered for numerical simulation.

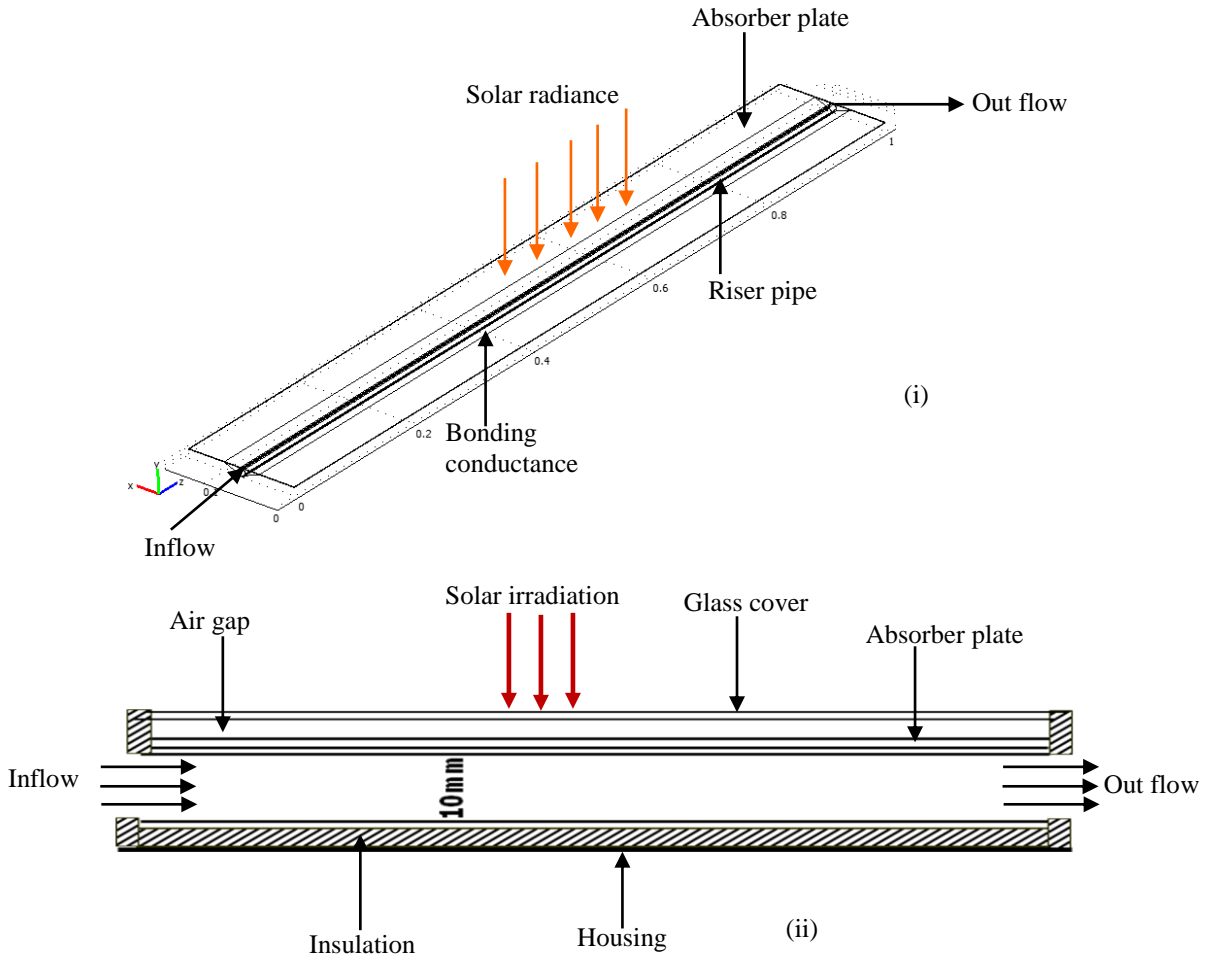


FIGURE 1. Computational domain of FPSC (i) 3D and (ii) 2D view

The nanoparticles are generally spherical shaped and diameter is taken as 10 nm. The nanofluid is considered as single phase laminar flow and surfactant analysis is neglected. The glass top surface is exposed to solar irradiation. It is made up of borosilicate which has thermal conductivity of 1.14 W/mK and refractive index of 1.47, specific heat of 750 J/kgK and coefficient of sunlight transmission of 95%. The wavelength of visible light is roughly 0.7 μm . Thickness of glass cover is 0.005m. There is an air gap of 0.005m between glass cover and absorber plate. Length, width and thickness of the absorber plate are 1m, 0.15m and 0.0005m respectively. The riser pipe has inner diameter 0.01 m and thickness 0.0005m. Coefficients of heat absorption and emission of copper absorber are 95% and 5% respectively. A trapezium shaped bonding conductance of copper metal is located from middle one-third part of width of the absorber plate. It covers the three-fourth part of the riser pipe. It is as long as the absorber plate and tube. The computation domain is the copper

absorber plate containing a fluid passing copper riser pipe with bonding conductance. The riser pipe is generally ultrasonically welded to the absorber plate. The absorber plate is modeled to provide for conduction, convection and radiation in the analysis. Figure 1 shows the computational domain in 3D as well as 2D views.

Let I be the intensity of solar radiation and A be any surface area, then the amount of energy received by any surface is: $Q_i = I.A$ (1)

This equation is modified for solar collector surface as it is the product of the rate of transmission of the cover (τ) and the absorption rate of the absorber (α). Thus, $Q_{recv} = I(\tau\alpha)A$ (2)

Some heat is lost to the atmosphere by convection and radiation process. The rate of heat loss (Q_{loss}) depends on the collector overall heat transfer coefficient (U_l) and the collector temperature.

$$Q_{loss} = U_l A (T_{col} - T_{amb}) \quad (3)$$

The rate of useful energy extracted by the collector (Q_{usfl}) is:

$$Q_{usfl} = Q_{recv} - Q_{loss} = I(\tau\alpha)A - U_l A (T_{col} - T_{amb}) \quad (4)$$

Another form of rate of heat extraction from the collector can be measured as

$$Q_{usfl} = mC_p (T_{out} - T_{in}) \quad (5)$$

where m , C_p , T_{in} and T_{out} are the mass flow rate per unit area, the specific heat at constant pressure, inlet and outlet fluid temperatures respectively.

To calculate the collector average temperature is difficult. The equation (4) may not be convenient. It is convenient to define a quantity that relates the actual useful energy gain of a collector to the useful gain if the whole collector surface is at the fluid inlet temperature. This quantity is known as

“the collector heat removal factor (F_R)” and is expressed as: $F_R = \frac{mC_p (T_{out} - T_{in})}{A [I(\tau\alpha) - U_L (T_{in} - T_{amb})]}$ (6)

The maximum possible useful energy gain in a solar collector occurs when the whole collector is at the inlet fluid temperature. The actual useful energy gain (Q_{usfl}), is found by multiplying the collector heat removal factor (F_R) by the maximum possible useful energy gain. Thus equation (4)

can be modified as follows: $Q_{usfl} = F_R A [I(\tau\alpha) - U_L (T_{in} - T_{amb})]$ (7)

Equation (7) is known as the “**Hottel-Whillier-Bliss equation**”. The heat flux per unit area of

absorber surface (q) is now denoted as $\frac{Q_{usfl}}{A} = q = I\tau\alpha - U_L (T_{in} - T_{amb})$.

The 3D governing equations are as follows

$$\frac{\partial u}{\partial x} + \frac{\partial v}{\partial y} + \frac{\partial w}{\partial z} = 0 \quad (8)$$

$$\rho_{nf} \left(u \frac{\partial u}{\partial x} + v \frac{\partial u}{\partial y} + w \frac{\partial u}{\partial z} \right) = -\frac{\partial p}{\partial x} + \mu_{nf} \left(\frac{\partial^2 u}{\partial x^2} + \frac{\partial^2 u}{\partial y^2} + \frac{\partial^2 u}{\partial z^2} \right) \quad (9)$$

$$\rho_{nf} \left(u \frac{\partial v}{\partial x} + v \frac{\partial v}{\partial y} + w \frac{\partial v}{\partial z} \right) = -\frac{\partial p}{\partial y} + \mu_{nf} \left(\frac{\partial^2 v}{\partial x^2} + \frac{\partial^2 v}{\partial y^2} + \frac{\partial^2 v}{\partial z^2} \right) \quad (10)$$

$$\rho_{nf} \left(u \frac{\partial w}{\partial x} + v \frac{\partial w}{\partial y} + w \frac{\partial w}{\partial z} \right) = -\frac{\partial p}{\partial z} + \mu_{nf} \left(\frac{\partial^2 w}{\partial x^2} + \frac{\partial^2 w}{\partial y^2} + \frac{\partial^2 w}{\partial z^2} \right) \quad (11)$$

$$u \frac{\partial T}{\partial x} + v \frac{\partial T}{\partial y} + w \frac{\partial T}{\partial z} = \frac{\alpha_{nf}}{\alpha_f} \frac{1}{Pr} \left(\frac{\partial^2 T}{\partial x^2} + \frac{\partial^2 T}{\partial y^2} + \frac{\partial^2 T}{\partial z^2} \right) (12) \left(\frac{\partial^2 T_a}{\partial x^2} + \frac{\partial^2 T_a}{\partial y^2} + \frac{\partial^2 T_a}{\partial z^2} \right) = 0 \quad (13)$$

Here, $\alpha_{nf} = k_{nf} / (\rho C_p)_{nf}$ is the thermal diffusivity, $\rho_{nf} = (1-\phi)\rho_f + \phi\rho_s$ is the density, $(\rho C_p)_{nf} = (1-\phi)(\rho C_p)_f + \phi(\rho C_p)_s$ is the heat capacitance, $\mu_{nf} = \frac{\mu_f}{(1-\phi)^{2.5}}$ is the viscosity of

Brinkman model [13], $k_{nf} = k_f \frac{k_s + 2k_f - 2\phi(k_f - k_s)}{k_s + 2k_f + \phi(k_f - k_s)}$ is the thermal conductivity of Maxwell

Garnett (MG) model [14] and $Pr = \frac{\nu_f}{\alpha_f}$ is the Prandtl number. The boundary conditions of the computation domain are:

1. at all solid boundaries of the riser pipe: $u = v = w = 0$
2. at the solid-fluid interface: $k_f \left(\frac{\partial T}{\partial N} \right)_{fluid} = k_a \left(\frac{\partial T}{\partial N} \right)_{solid}$
3. at the inlet boundary of the riser pipe: $T = T_{in}$, $w = w_{in}$
4. at the outlet boundary: convective boundary condition $p = 0$
5. at the top surface of the absorber: heat flux $-k_a \frac{\partial T_a}{\partial z} = q = I\tau\alpha - U_L(T_{in} - T_{amb})$
6. at the other surfaces of absorber plate: $\frac{\partial T_a}{\partial N} = 0$
7. at the outer boundary of riser pipe: $\frac{\partial T_a}{\partial N} = 0$
8. at the outer boundary of bonding conductance: $\frac{\partial T_a}{\partial N} = 0$, where N is the distances either along x or y or z directions acting normal to the surface respectively.

The average Nusselt number at the top heated surface of riser pipe (2D simulation) is

$$Nu = -\int_0^1 \frac{k_{nf}}{k_f} \frac{\partial \theta}{\partial Y} dX \quad \text{and} \quad \text{at the inner surface of riser pipe (3D simulation) is}$$

$$Nu = \frac{\iint_s \overline{Nu} ds}{\iint_s ds} = -\frac{1}{\pi DL} \frac{k_{nf}}{k_f} \iint_s \sqrt{\frac{\partial^2 \theta}{\partial X^2} + \frac{\partial^2 \theta}{\partial Y^2} + \frac{\partial^2 \theta}{\partial Z^2}} ds \quad \text{where } L \text{ is the height of absorber tube. The}$$

above equations are non-dimensionalized by using the following dimensionless quantities $X = \frac{x}{D}$, $Y = \frac{y}{D}$, $Z = \frac{z}{D}$, $\theta = \frac{(T - T_{in})k_f}{qD}$. A measure of a flat plate collector

performance is the collector efficiency (η) defined as the ratio of the useful energy gain (Q_{usfl}) to the incident solar energy. The instantaneous thermal efficiency of the collector is:

$$\eta = \frac{\text{useful gain}}{\text{available energy}} = \frac{Q_{usfl}}{AI} = \frac{F_R A [I(\tau\kappa) - U_L(T_{in} - T_{amb})]}{AI} = F_R(\tau\kappa) - F_R U_L \frac{(T_{in} - T_{amb})}{I}$$

NUMERICAL IMPLEMENTATION

The Galerkin finite element method [15-17] is used to solve the non-dimensional governing equations along with boundary conditions for the considered problem. Conservation equations are

solved for the finite element method to yield the velocity and temperature fields for the water flow in the absorber tube and the temperature field for the absorber plate. The equation of continuity has been used as a constraint due to mass conservation and this restriction may be used to find the pressure distribution. Then the velocity components (u, v, w) and temperatures (T, T_a) of governing equations (8-13) are expanded using a basis set. The Galerkin finite element technique yields the subsequent nonlinear residual equations. Gaussian quadrature technique is used to evaluate the integrals in these equations. The non-linear residual equations are solved using Newton–Raphson method to determine the coefficients of the expansions. The convergence of solutions is assumed when the relative error for each variable between consecutive iterations is recorded below the convergence criterion such that $|\psi^{n+1} - \psi^n| \leq 1.0e^{-6}$, where n is the number of iteration and Ψ is a function of any one of u, v, w, T and T_a .

Mesh Generation

The computational domains with irregular geometries by a collection of finite elements make the method a valuable practical tool for the solution of boundary value problems arising in various fields of engineering. Figure 2 displays the 3D and 2D finite element meshes of the present physical domain.

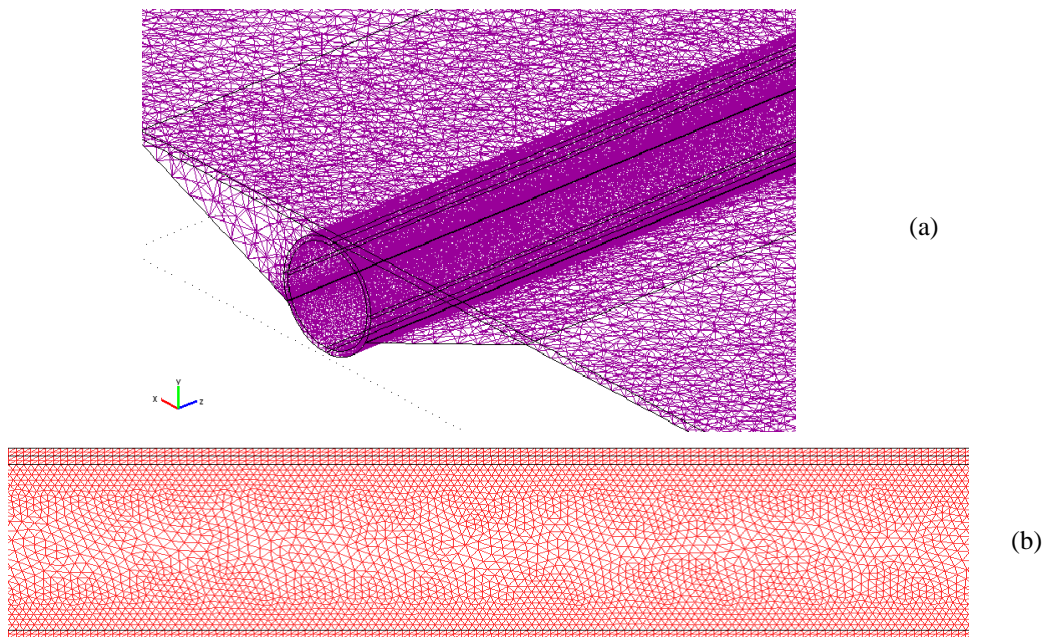


FIGURE 2: Finite element meshing of FPSC (a) 3D and (b) 2D

Grid Independent Test

The arrangement of discrete points throughout the domain is simply called a grid. Finite element method can be applied to unstructured grids. This is because the governing equations in this method are written in integral form and numerical integration can be carried out directly on the unstructured grid domain in which no coordinate transformation is required. The mesh is composed of tetrahedral element type with ten nodes in subdomain and triangular element size with

six nodes in boundaries. The grid independence test is performed to check validity of the quality of mesh on the solution. There is no significant change in Nu taking element size 27,04,288 but it is time consuming. This is shown in Table 1. The computation procedure runs taking 14,20,465 elements in 3D simulation. Thermo-physical properties for water and Cu nanoparticle is shown in Table 2.

Table 1: Grid Sensitivity Test at $Pr = 5.8, I = 215 \text{ W/m}^2, \phi = 2\%$

Elements	4,51,098	7,26,222	14,20,465	27,04,288
Physical Properties	Fluid phase (Water)		Cu	
$C_p(\text{J/kgK})$	4179		385	
$\rho(\text{kg/m}^3)$	997.1		8933	
$k(\text{W/mK})$	0.613		400	
$\alpha \times 10^7(\text{m}^2/\text{s})$	1.47		1163.1	
Nu (Nanofluid)	2.12154	2.28451	2.433717	2.433807
Nu (Base fluid)	1.89124	2.00312	2.10124	2.10168
Time (s)	1469.587	3846.507	78381.181	99579.254

Table 2: Thermo physical properties of fluid and nanoparticles

Code Validation

The result obtained from present numerical code is verified against the existing result available in the literature. A comparison of temperature contour plot of absorber plate is shown in figure 3 between the result using present code and Kranath et al. [1]. The numerical study is performed at $I = 800 \text{ w/m}^2$, inlet velocity = 0.005 m/s, density (copper) = 8900 Kg/m^3 , specific heat (copper) = 385 J/kgK , viscosity (water) = 0.000959 Kg/ms , specific heat (water) = 4179 J/kgK , thermal conductivity (copper) = 387 W/mK and thermal conductivity (water) = 0.6 W/mK . A good agreement is observed from figure 3.

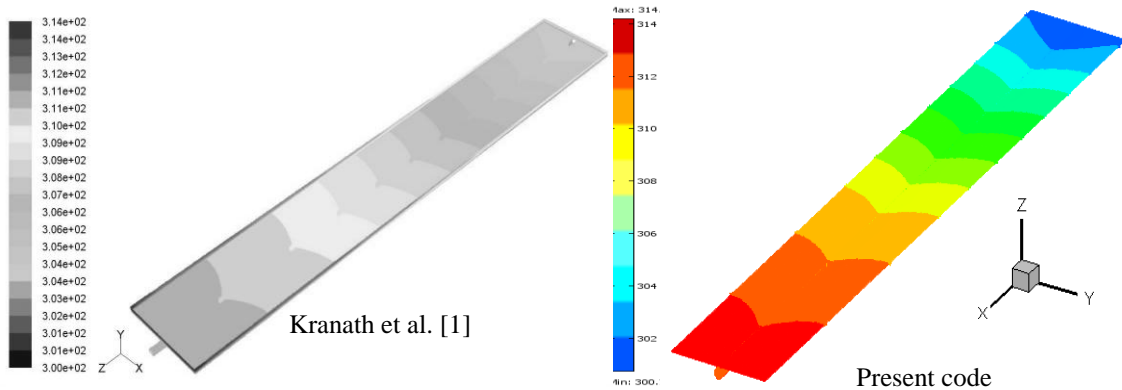


FIGURE 3: Code validation of temperature contour of absorber plate

RESULTS AND DISCUSSION

Figure 4 represents the surface temperature for different values of solid volume fraction ($\phi = 0\%, 1\%, 2\%, 3\%$) of Cu nanoparticles at $Pr = 5.8$ and $I = 215 \text{ W/m}^2$ in 2D simulation. Initially at $\phi =$

0% ie. water is heat transfer medium then the absorber temperature is low. Adding nanoparticle with base fluid from 0% to 3% the temperature of absorber plate as well as output nanofluid become high gradually. The temperature of contour plot for different values of solid volume fraction ($\phi = 0\%$, 1%, 2%, 3%) of Cu nanoparticles at $I = 215 \text{ W/m}^2$ in 3D simulation is expressed in figure 5. Initially at $\phi = 0\%$ ie. water is working fluid then the temperature contour of absorber plate is not high. Mixing nanoparticle with base fluid from 0% to 3% the temperature of absorber plate as well as output nanofluid temperature increase.

Four comparisons are made between 2D and 3D analyses for a flat plate solar collector and are shown in figure 6 (i)-(iv). Figure 6(i-iii) displays values of heat transfer rate, mean output

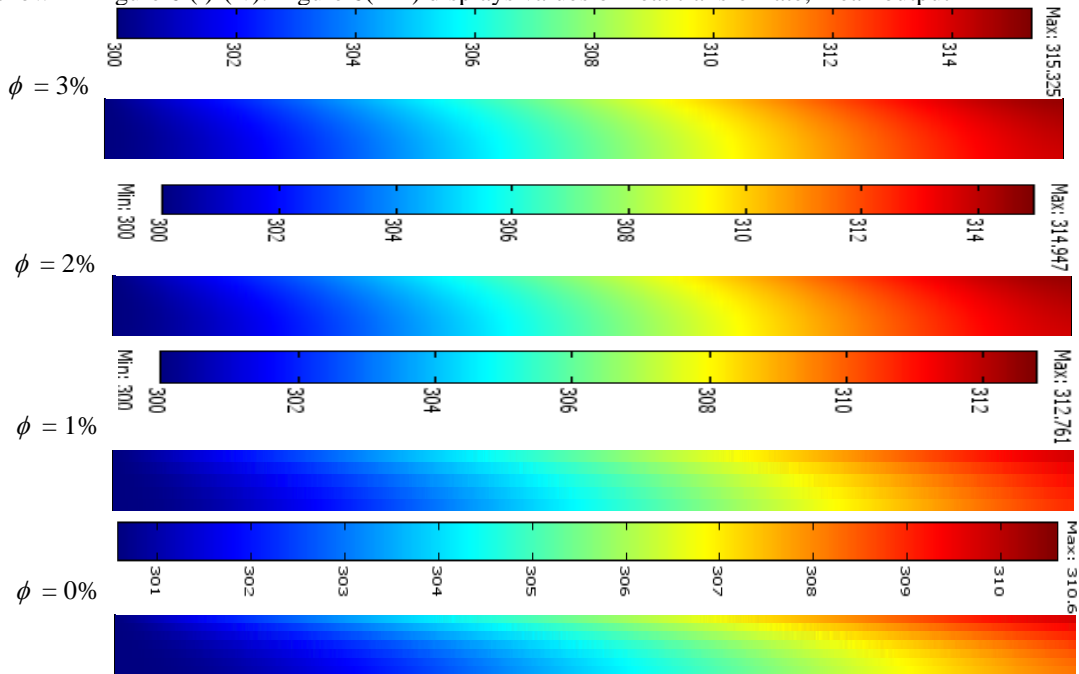


FIGURE 4: Effect of ϕ on surface temperature in 2D simulation

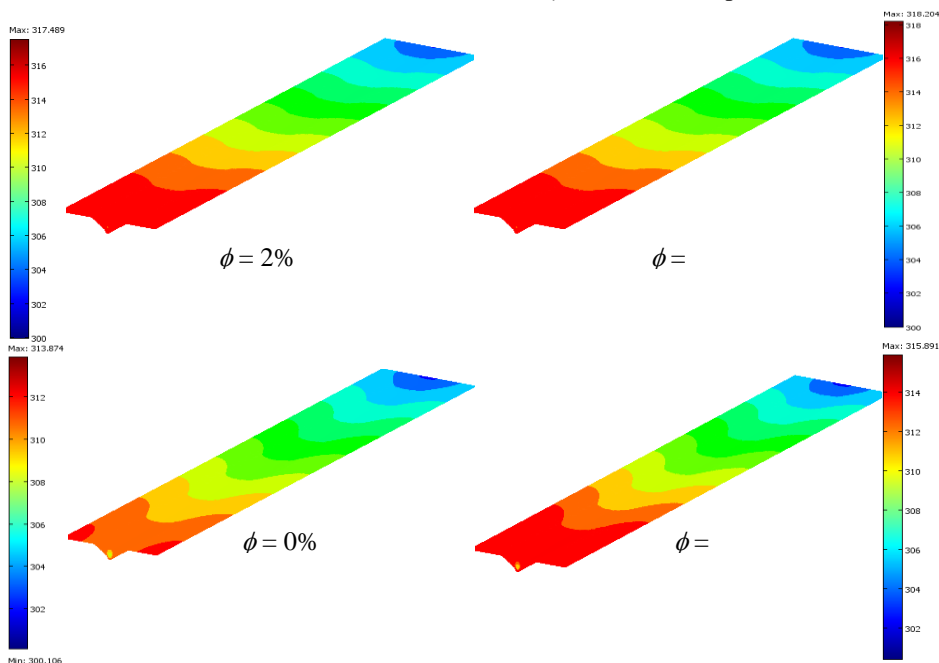


FIGURE 5. Temperature of contour plot at different ϕ in 3D simulation

temperature and thermal efficiency versus different values of solid volume fraction of water-Cu nanofluid with $Pr = 5.8$ and $I = 215 \text{ W/m}^2$. Temperature distribution for 2% concentrated water-Cu nanofluid from top of the absorber plate to the bottom of the riser pipe at the position 0.67m of FPSC is shown in 6(iv). In the region from top of absorber plate upto centre of fluid, a little bit higher temperature is found for 3D analysis than that of 2D analysis. Again in the region from centre of fluid to outer surface of riser pipe, the temperature distribution of 2D analysis doesn't reflect actual concept of FPSC at all. That's why 3D numerical analysis represents accurate heat transfer phenomena of FPSC.

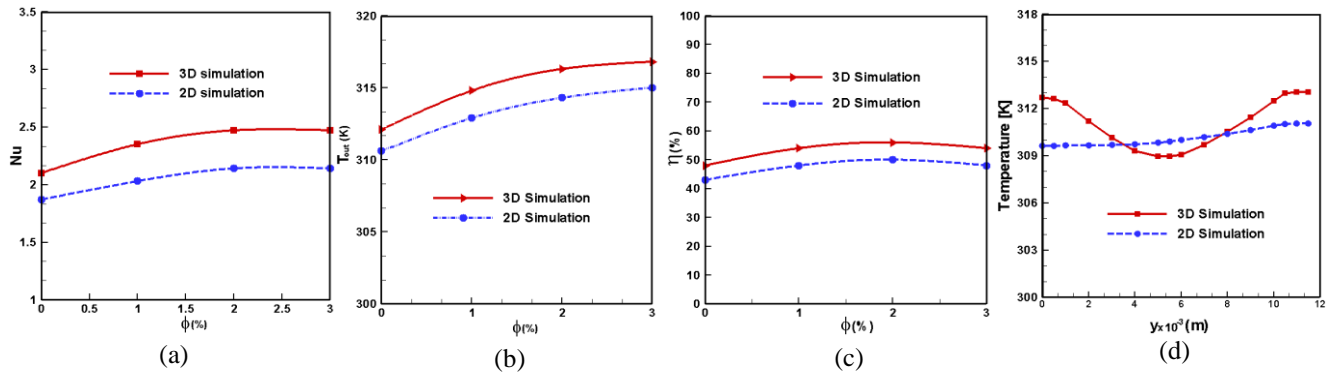


FIGURE 6: Comparison (a) heat transfer rate, (b) mean output temperature, (c) collector efficiency (d) temperature

In 3D computation (figure 1(i)) the whole riser pipe becomes hot by conductive heat transfer process with absorber. Then cold fluids enter the riser pipe, collect heat from whole solid pipe surface, become hot and finally more heated output fluids are obtained. But in 2D computation (longitudinal cross-section of 3D view that is figure 1(ii)) only the top boundary of riser pipe becomes hot by conductive heat transfer process with absorber. There is no way to transfer heat by conduction from absorber to bottom boundary of riser pipe. Thus bottom boundary of pipe doesn't become hot. Then cold fluids enter the riser pipe, collect heat from top solid boundary of pipe and become hot. But at the same time cold bottom boundary of riser pipe tries to collect heat from hot fluids. Thus finally less heated output fluids are obtained than 3D computation.

CONCLUSION

Thermal behavior of fluids on forced convective boundary layer flow is accounted through a solar flat plate collector both in 2D and 3D simulations. Importance of 3D numerical simulation is explained showing differences interms of various comparisons. Following conclusions have been drawn from the results of the numerical analysis:

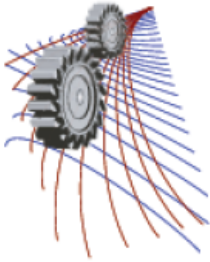
- Water/Cu nanofluid enhances thermal efficiency about 8% in 3D simulation.
- 17% heat transfer rate is obtained for increasing ϕ from 0% to 2% in 3D simulation.
- More heat transfer rate of about 3% is obtained in 3D simulation than 2D.
- In 3D simulation mean outlet temperature of water increases about 1.4K than 2D.
- Collector efficiency increases about 5% in 3D simulation than 2D.

ACKNOWLEDGEMENT

The present numerical work is done in the Department of Mathematics, Bangladesh University of Engineering & Technology, Dhaka-1000, Bangladesh.

REFERENCES

- [1] K.V. Karanth, M.S. Manjunath, N.Y. Sharma, Numerical simulation of a solar flat plate collector using discrete transfer radiation model (DTRM) – a CFD approach, Proc. of the World Cong. on Engg., London, U.K., III, 2011.
- [2] OA. Bég, A. Bakier, R. Prasad, SK. Ghosh, Numerical modelling of non-similar mixed convection heat and species transfer along an inclined solar energy collector surface with cross diffusion effects, World J. of Mech., Vol. 1, pp. 185-196, 2011.
- [3] M.S. Manjunath, K.V. Karanth, N.Y. Sharma, Three dimensional numerical analysis of conjugate heat transfer for enhancement of thermal performance using finned tubes in an economical unglazed solar flat plate collector, Proc. of the World Cong. on Engg., London, U.K., III, 2011.
- [4] M.S. Manjunath, K.V. Karanth, N.Y. Sharma, A comparative CFD study on solar dimple plate collector with flat plate collector to augment the thermal performance, World Academy of Sci., Engg. and Tech., Vol. 6, pp. 10-21, 2012.
- [5] J. Vestlund, Gas-filled flat plate solar collector, Ph. D. Thesis, Building Services Engg., Dept. of Energy and Environ., Chalmers University of Technology, Gothenburg, Sweden, 2012.
- [6] P.W. Ingle, A.A. Pawar, B.D. Deshmukh, K.C. Bhosale, CFD analysis of solar flat plate collector, Int. J. of Emerg. Techn. and Adv. Engg., Vol. 3, No. 4, pp. 337-342, 2013.
- [7] S. Basavanna and K.S. Shashishekar, CFD analysis of triangular absorber tube of a solar flat plate collector, Int. J. Mech. Eng. & Rob. Res., Vol. 2, No. 1, pp. 19-24, 2013.
- [8] I.A. Tagliafico, F. Scarpa, M.D. Rosa, Dynamic thermal models and CFD analysis for flat-plate thermal solar collectors – a review, Renew. and Sust. Energy Rev., Vol. 2, No. 30, pp. 526-537, 2014.
- [9] F. Struckmann, Analysis of a flat-plate solar collector, Project Report 2008 MVK160 Heat and Mass Transport, 2008, Lund, Sweden.
- [10] Soteris A. Kalogirou, Solar thermal collectors and applications, Progress in Energy and Combustion Science, 30, 2004, 231–295.
- [11] R. Nasrin and M.A. Alim, Semi-empirical relation for forced convective analysis through a solar collector, Solar Energy, Vol. 105, pp. 455-467, 2014.
- [12] R. Nasrin, S. Parvin and M.A. Alim, Heat transfer and collector efficiency through direct absorption solar collector with radiative heat flux effect, Num. Heat Transf. Part A- Appl., Vol. 68, No. 8, pp. 887-905, 2015
- [13] HC. Brinkman, The viscosity of concentrated suspensions and solution, J. Chem. Phys., 20, 571-581, 1952.
- [14] J.C. Maxwell-Garnett, Colours in metal glasses and in metallic films. Philos. Trans. Roy. Soc. A 203, 1904, 385–420.
- [15] C. Taylor, P. Hood, A numerical solution of the Navier-Stokes equations using finite element technique. Computer and Fluids, 1, 1973, 73–89.
- [16] P. Dechaumphai, Finite element method in engineering. 2nd ed., Chulalongkorn University Press, Bangkok, 1999.
- [17] E.B. Ogut, Natural convection of water-based nanofluids in an inclined enclosure with a heat source, Int. J. of Thermal Sciences, 48, 11, 2009, 2063-2073.



Production of Hydrogen from Brine Electrolysis Using Solar Energy & Possibilities of Energy Saving

H. Nasim Bin Jasim^{a)}, Rajon Bhuiyan, Rezaul Karim, Chandan Sarkar

^{a)}*Department of Mechanical Engineering, Rajshahi University of Engineering & Technology, Rajshahi, 6204*

^{a)}Corresponding author: nasim@nasimbinjasim.com

Abstract. As the demand for energy is growing faster due to society up gradation and rapid industrialization, the renewable energy sources hold promise for the future energy resources. In this paper, a new concept for hydrogen production from brine solution by an electrochemical method was investigated. Experiments are done in two electrolyzers for various voltages, currents, TDS, temperature and electrolytes. For H shaped electrolyzer the highest efficiency is 6.71% in 13.5V and 0.58A. For rectangular electrolyzer highest efficiency is 15% at 12V and 5.25A. Influence of temperature is also investigated. Cost estimation and evaluation of the process are also made.

INTRODUCTION

Hydrogen fuel as an alternative low cost energy source of conventional petroleum based fuels like petrol, diesel and kerosene etc. It is almost a complete substitute of fuel with better weight-to-power ratio, when used as automotive fuel. It reduces fuel cost of vehicle and reduces the pollution load and vehicle emission to improve air quality increasing pollution free environment. So, the study about the generation of hydrogen gas is very important. In a Developing method, water levels in the electrolysis cell and water tank are maintained between pre-defined intervals by a water level control unit. Hydrogen is not stored in the system and is produced only when the engine is running and the gas is immediately introduced into the intake manifold. Amongst all the processes of producing hydrogen, electrolysis is the easiest and efficient process. The project is comprehensively based on chemical change due to electric current. In this project, brine solution and (KOH+water) act as the electrolyte from which decent amount of hydrogen is produced.

Nomenclature

HPR	hydrogen production rate
TDS	total dissolved solute
V	voltage
I	current
t	time

CAUSES OF USING SEA WATER/BRINE SOLUTION

Sea-water accounts for approximately 97% of the Earth's water reserves, and so sea-water electrolysis offers significant advantages against other hydrogen producing technologies. So, a highly attractive procedure for electrolytic

hydrogen production is to produce hydrogen directly from sea-water, the electrical conductivity of which is due to soluble salts. Sea-water electrolysis is basically determined by near-electrode processes, which are intrinsic for the electrolysis of sodium chloride solutions, as sea water has a peculiar chemical composition with a prevalence of NaCl. Thermodynamic and kinetic analysis along side of other preliminary experiments have shown that electrolysis of sea-water is now a perspective method for H₂ production. Also, depending on the reaction conditions, it is possible to recover the following target products: hydrogen, oxygen, chlorine, alkali and sodium hypochlorite, drinking water. Sea-water direct electrolysis creates useful by-products, such as alkalis from catholyte and acids from anolyte.

USED ELECTROLYZERS

H shaped electrolyzer

At first the flux will be filled up with brine solution. Then make the hole in the cork with the help of cork borer and enter the electrodes through it and fit to the bottom end of the H-beaker. And then confirm its insulation by using insulating material m-seal. Then the whole set up will be placed in the wooden base. After solidification of m-seal, the brine solution will be poured just close to the top end of the H-beaker. One electrode will be connected to the positive end of the solar panel will be turned into anode and here oxygen will be produced. And the other electrode which will be connected to the negative end of the solar panel will be turned into cathode and here hydrogen will be produced. Maximum of 20volts in power supply apparatus (solar panel) will be selected. About 3-6 hours later, it needs to check the produced hydrogen and oxygen gases.

Rectangular electrolyzer

At first, brine solution of particular concentration was made. Then it was poured into the rectangular beaker. In beaker, electrodes were attached at their particular position. Gas collectors were set to collect gases. At the cathode plastic bottle and at the anode measuring cylinder were set. To provide power to the electrolyzer/beaker a chargeable battery was charged by inverter from solar panels. Then the beaker electrodes were connected to the battery. One electrode was connected to the positive end of the battery was turned into anode and here oxygen/chlorine gas was produced. And the other electrode which was connected to the negative end of the battery was turned into cathode and here hydrogen was produced. Maximum of 16volts in power supply apparatus (solar panel) will be selected. Chemical reactions were started. Hydrogen gas was produced at the negative electrode (cathode) and chlorine/oxygen gas was produced at the positive electrode (anode). With the help of a multimeter voltages, currents were measured. Production rates were taken for various parameters. Several experiments were done by changing concentration of the solution and for various voltages and currents. Temperatures at various times were taken by thermometer. pH of different concentrated solution were measured.

EXPERIMENTAL EQUIPMENT & PROCEDURE

Selection of Electrodes

At the cathode

The more reactive a metal is the more it prefers being ions. Therefore, if a reactive metal such as zinc or magnesium is present it will remain as the ions. The H⁺ ions will accept the electrons and hydrogen gas will be given off at the cathode. If a less reactive metal, such as copper or silver is present it would rather accept the electrons than H⁺. Hence, the metal forms at the cathode.

At the anode

If halide ions are present, Cl⁻, Br⁻, I⁻, they will give up their electrons to become molecules of Cl₂, Br₂ and I₂ respectively. If no halogen is present, OH⁻ will give up electrons more readily than other non-metal ions, and oxygen forms. Finally, graphite is selected as electrodes. Care must be taken in choosing an electrolyte, since an anion from the electrolyte is in competition with the hydroxide ions to give up an electron.

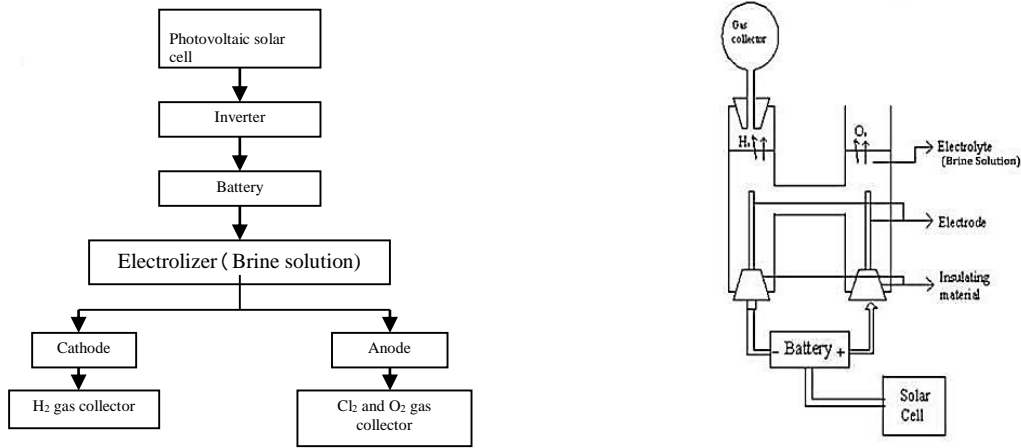


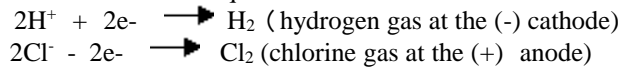
FIGURE. 1. (a) Block diagram for hydrogen production; (b) Schematic diagram for hydrogen production (H shaped)

Electrolyte selection

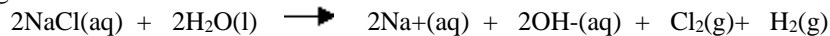
The following cations have lower electrode potential than H⁺ and are therefore suitable for use as electrolyte cations : Li⁺, Rb⁺, K⁺, Cs⁺, Ba²⁺, Sr²⁺, Ca²⁺, Na⁺ and Mg²⁺. Sodium and lithium are frequently used, as they form inexpensive, soluble salts (Brine solution). Strong acids such as sulfuric acid (H₂SO₄) and strong bases such as potassium hydroxide (KOH) and sodium hydroxide (NaOH) are frequently used as electrolytes. Finally, brine solution and KOH are selected as electrolytes.

Electrolysis of brine

Brine is merely sodium chloride (NaCl) dissolved in water. By performing electrolysis on brine, three substances will be found. They are chlorine, hydrogen and sodium hydroxide. Electrolysis of brine gives hydrogen at the cathode and chlorine at the anode. The reactions at each electrode are called half equations. The half equations are written so that the same number of electrons occur in each equation.



Hydrogen ions gain electrons (reduction) to form hydrogen atoms. The hydrogen atoms combine to form molecules of hydrogen gas. Chloride ions lose electrons (oxidation) to form chlorine atoms. The chlorine atoms combine to form molecules of chlorine gas. The overall reaction is



EFFICIENCY CALCULATION

Input energy, $E_i = VIt$(1)
 Output energy, $E_{\text{output}} = mC_v$ (2)

Here, m = Mass of hydrogen gas, C_v = Calorific value of hydrogen gas.
 Efficiency, $\eta = \text{Output energy} / \text{Input energy}$ (3) When, $V = 13.5\text{V}$, $I = 0.58\text{A}$, $t = 3600\text{sec}$
 Then from equation (1), input energy $E_i = 13.5 * 0.58 * 3600 = 28.188\text{KJ}$
 Mass of hydrogen gas, $m = \rho v$(4)
 Density of hydrogen gas, $\rho = 0.084\text{Kg m}^{-3}$, Volume of hydrogen gas $v = 150.12 * 10^{-6}\text{m}^3$
 From equation (4) mass of hydrogen gas,
 $m = 0.084 * 150.12 * 10^{-6}$
 $= 12.6 * 10^{-3}\text{gram}$
 Calorific value of hydrogen gas, $C_v = 150 \text{Kj/gm}$. [11]
 Then from equation (2) output energy $E_{\text{output}} = 12.6 * 10^{-3} * 150$
 $= 1.89\text{KJ}$
 From equation (3) Efficiency, $\eta = E_{\text{output}} / E_{\text{input}} = 1.89 / 28.188 = 6.71\%$

RESULTS AND DISCUSSION

FOR H SHAPED ELECTROLYZER

Fig 2.(a) shows that the hydrogen production is increased with increase in TDS at different voltages. But after 70 g/L the hydrogen production rate is decreased with increase in TDS. Fig 2.(b) shows that the hydrogen production is increased with increase in TDS at different currents. But after 70 g/L the hydrogen production rate is decreased.

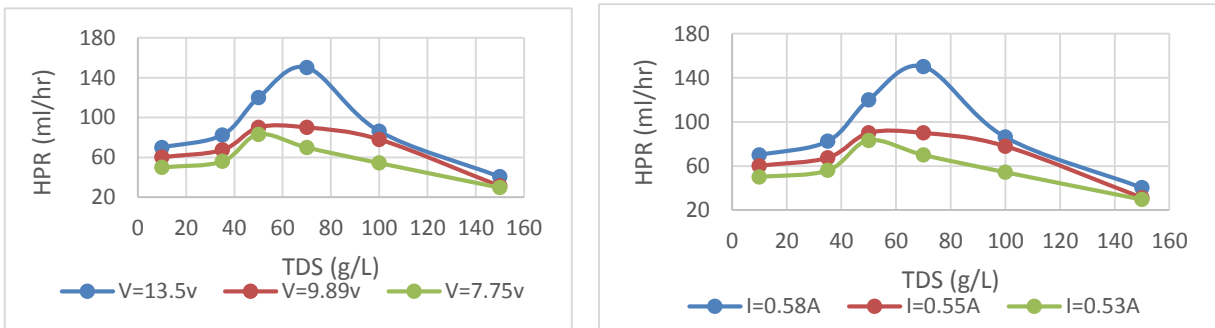


FIGURE. 2. (a) HPR VS TDS at different voltages ; (b)HPR vs TDS at different currents

Result for Potassium hydroxide (KOH) with water

Fig. 3. (a) shows that the hydrogen production is increased with increase of current at different TDS. Fig. 3. (b) shows that the efficiency is increased with increase in hydrogen production rate at different TDS. The efficiency is maximum for 100g/L TDS.

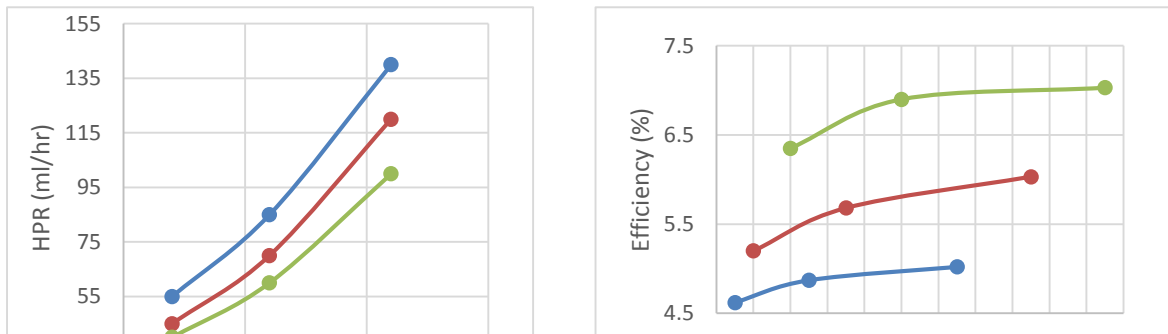


FIGURE. 3. (a) HPR VS current; (b)Efficiency vs HPR at different voltages

Fig. 4. (a) shows that the efficiency is increased with increase in temperature fastly. But after certain time the efficiency is increase very slowly wiht increasein temperature.

Fig. 4. (b) shows that the efficiency is increased fastly with increase in current. But after certain time the efficiency is increase very slowly with increase in current.

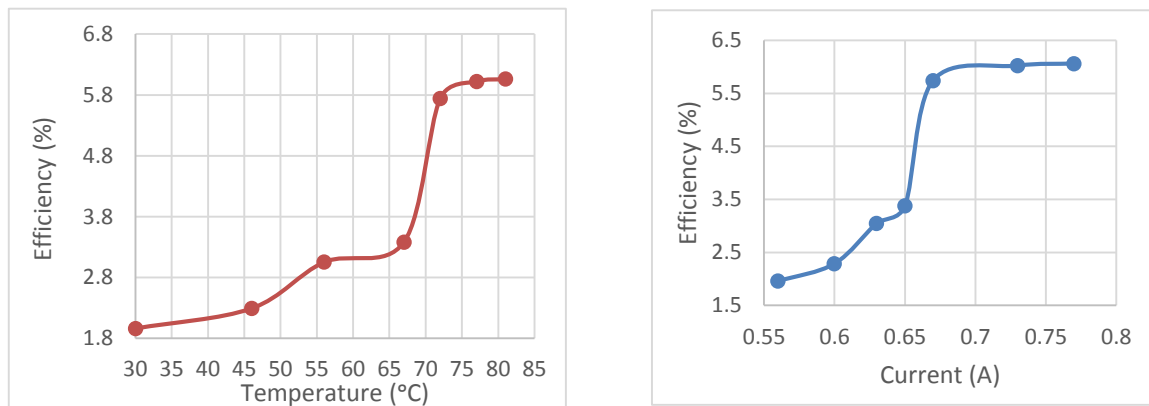


FIGURE. 4. (a) Efficiency VS temperature; (b) efficiency vs current

By applying the electrolysis process the output of the project was hydrogen gas, but the production rate was very slow. Water alone not a good conductor, so there added some Nacl and KOH in the experiment. The production of hydrogen can be increased by supplying high temperature and current which we saw in the graph. The generated amount of hydrogen gas is proportional to the total electrical charge that was sent through the solution. The efficiency of electrolysis was increased by using a rectangular electrolyzer instead of the H shaped electrolyzer. The necessary data were taken from the experiment to measure production rates of hydrogen to calculate efficiencies at constant voltage with various currents and concentrations.

Result for Rectangular Electrolyzer.

For brine solution, Fig. Fig. 5. (a) shows that the efficiency is increased fastly with increase in current. But after 3.90A the efficiency is increased very slowly. Fig. 5. (b) shows that the efficiency is increased with increase in TDS fastly. But after certain time the efficiency is increase very slowly with increase in TDS.

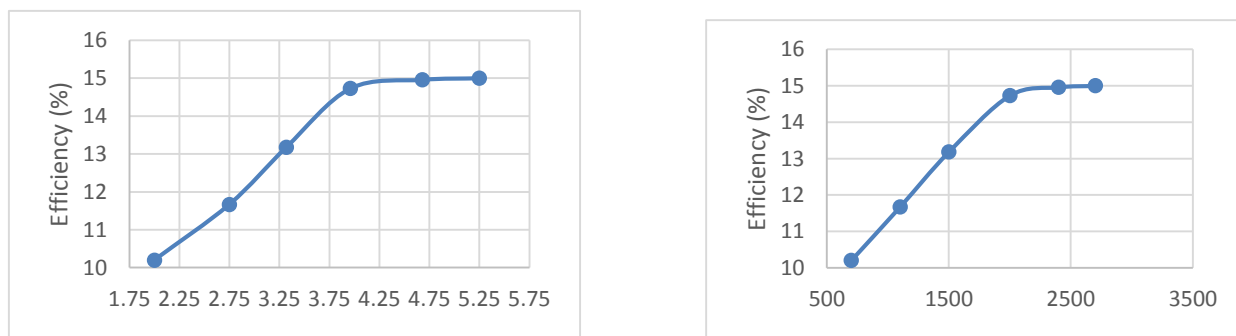


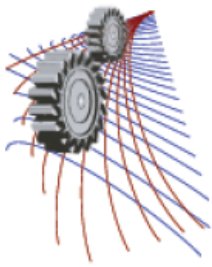
Fig. 5. (a) Efficiency VS Current at constant voltage ; (b) efficiency vs HPR

CONCLUSION

Amongst all the processes of producing hydrogen, electrolysis is the easiest and efficient process. The project is comprehensively based on chemical change due to electric current. In this project, brine solution and (KOH+water) act as the electrolyte from which decent amount of hydrogen is produced. For brine solution (H shaped beaker), the highest efficiency was 7.09% at 7.75V, 0.53A and 50g/L TDS. For KOH solution, the highest efficiency was 7.03% obtained at 12.2V, 0.56A, 100TDS g/L. But for rectangular beaker, the highest efficiency was 15% ,obtained at 5.25a, 12V, and 150 g/L TDS

REFERENCES

- [1] Bangladesh Power Development Board. September 2012. "Installed capacity of power plants (fuel wise) in September 2012" 6 September 2012, <http://www.bpdb.gov.bd>
- [2] Energy Information Administration. 19 September 2012. "INTERNATIONAL ENERGY OUTLOOK 2011: World total energy consumption by region and fuel, Reference case, 2006-2035 Table." 14 August 2012,
- [3] http://www.eia.gov/forecasts/ieo_table.cfm.
- [4] Bangladesh Power Development Board. September 2012. "Planning for Solar and Wind Projects." 6 September 2012, <<http://www.bpdb.gov.bd>>.
- [5] Gupta C.L. and Garg H.P. (1967), "Performance studies on solar air heater", solar Energy, 11(5) pp. 25-31.
- [6] A Student's Guide to Alternative Fuel Vehicles, article, retrieved 8th January 2012, from <http://www.energyquest.ca.gov/transportation/index.html>.
- [7] Properties of hydrogen, received 25th March 2012 [Online], Available: <http://en.wikipedia.org/wiki/Hydrogen>.
- [8] Z. Dülger and K.R. Özçelik "Fuel economy improvement by on board electrolyti hydrogen production" International Journal of Hydrogen Energy 25 (2000) 895-897.
- [9] Module 1: Hydrogen Properties, College of Desert, December 2001. <http://www.popularmechanics.com/cars/alternative-fuel/news/2690341>.
- [10] Ammar A. Al-Rousan "Reduction of fuel consumption in gasoline engines by introducing HHO gas into intake manifold" International Journal of Hydrogen Energy 35 (2010) 12930-12935.
- [11] "A review on water electrolysis" published by Emmanuel Zoulias, Elli Varkaraki, Nicolaos Lymberopoulos, (Centre for Renewable Energy Sources (CRES), Pikermi, Greece) Christodoulos N. Christodoulou and George N. Karagiorgis (Frederick Research Center (FRC), Nicosia, Cyprus).



Determination of Various Physiochemical Properties of Different Non-Edible Oils Available in Bangladesh

Rajon Bhuiyan^a, H. Nasim Bin Jasim^a, M. S. Babu^a and Chandan Sarkar^a

¹ *Department of Mechanical Engineering, Rajshahi University of Engineering & Technology, Rajshahi, 6204*

^aCorresponding author: nasim@nasimbinjashem.com

Abstract. This paper investigates the various physiochemical properties of different non-edible oils e.g. Neem oil (*Azadirachta indica*), Pitraj oil (*Aphanamixis polystachaya*), Karanja oil (*Pongamia pinnata*) and Castor oil (*Ricinus communis*) available in Bangladesh to compare with those of conventional fuel (diesel) properties. The properties include FT-IR analysis, flash point, fire point, density, viscosity and cetane number. The Fourier transform infrared (FT-IR) showed that the diesel fuel contained mainly alkanes and alkenes where the non-edible oils contain esters, halide and also alkanes and alkenes. Cetane number analysis showed that the non-edible oils contain lower cetane number than the diesel fuel. But the density, viscosity, flash point and fire point of the non-edible oils higher than the diesel fuel. In the latter part of this investigation, a well known Arrhenius equation was used to make a relationship between viscosity and temperature. A reciprocal relationship was proved between temperature and viscosity by evaluating the viscosities of the non-edible oils at different temperature between 323K to 373K. From this correlation the activation energy and the infinite and zero temperature viscosities were determined and this correlation was proved its accuracy with the R2 value of 0.990. It was also recommended that this correlation was assumed not for lower temperature.

INTRODUCTION

Hydrogen fuel as an alternative low cost energy source of conventional petroleum based fuels like petrol, diesel and kerosene etc. It is almost a complete substitute of fuel with better weight-to-power ratio, when used as automotive fuel. It reduces fuel cost of vehicle and reduces the pollution load and vehicle emission to improve air quality increasing pollution free environment. So, the study about the generation of hydrogen gas is very important. In a Developing method, water levels in the electrolysis cell and water tank are maintained between pre-defined intervals by a water level control unit. Hydrogen is not stored in the system and is produced only when the engine is running and the gas is immediately introduced into the intake manifold. Amongst all the processes of producing hydrogen, electrolysis is the easiest and efficient process. The project is comprehensively based on chemical change due to electric current. In this project, brine solution and (KOH+water) act as the electrolyte from which decent amount of hydrogen is produced.

CAUSES OF USING SEA WATER/BRINE SOLUTION

Sea-water accounts for approximately 97% of the Earth's water reserves, and so sea-water electrolysis offers significant advantages against other hydrogen producing technologies. So, a highly attractive procedure for electrolytic hydrogen production is to produce hydrogen directly from sea-water, the electrical conductivity of which is due to soluble salts. Sea-water electrolysis is basically determined by near-electrode processes, which are intrinsic for the

electrolysis of sodium chloride solutions, as sea water has a peculiar chemical composition with a prevalence of NaCl. Thermodynamic and kinetic analysis along side of other preliminary experiments have shown that electrolysis of sea-water is now a perspective method for H₂ production. Also, depending on the reaction conditions, it is possible to recover the following target products: hydrogen, oxygen, chlorine, alkali and sodium hypochlorite, drinking water. Sea-water direct electrolysis creates useful by-products, such as alkalis from catholyte and acids from anolyte.

USED ELECTROLYZERS

H Shaped Electrolyzer

At first the flux will be filled up with brine solution. Then make the hole in the cork with the help of cork borer and enter the electrodes through it and fit to the bottom end of the H-beaker. And then confirm it's insulation by using insulating material m-seal. Then the whole set up will be placed in the wooden base. After solidification of m-seal, the brine solution will be poured just close to the top end of the H-beaker. One electrode will be connected to the positive end of the solar panel will be turned into anode and here oxygen will be produced. And the other electrode which will be connected to the negative end of the solar panel will be turned into cathode and here hydrogen will be produced. Maximum of 20volts in power supply apparatus (solar panel) will be selected. About 3-6 hours later, it needs to check the produced hydrogen and oxygen gases.

Rectangular Electrolyzer

At first, brine solution of particular concentration was made. Then it was poured into the rectangular beaker. In beaker, electrodes were attached at their particular position. Gas collectors were set to collect gases. At the cathode plastic bottle and at the anode measuring cylinder were set. To provide power to the electrolyzer/beaker a chargeable battery was charged by inverter from solar panels. Then the beaker electrodes were connected to the battery. One electrode was connected to the positive end of the battery was turned into anode and here oxygen/chlorine gas was produced. And the other electrode which was connected to the negative end of the battery was turned into cathode and here hydrogen was produced. Maximum of 16volts in power supply apparatus (solar panel) will be selected. Chemical reactions were started. Hydrogen gas was produced at the negative electrode (cathode) and chlorine/oxygen gas was produced at the positive electrode (anode). With the help of an multimeter voltages, currents were measured. Production rates were taken for various parameters. Several experiments were done by changing concentration of the solution and for various voltages and currents. Temperatures at various times were taken by thermometer. pH of different concentrated solution were measured.

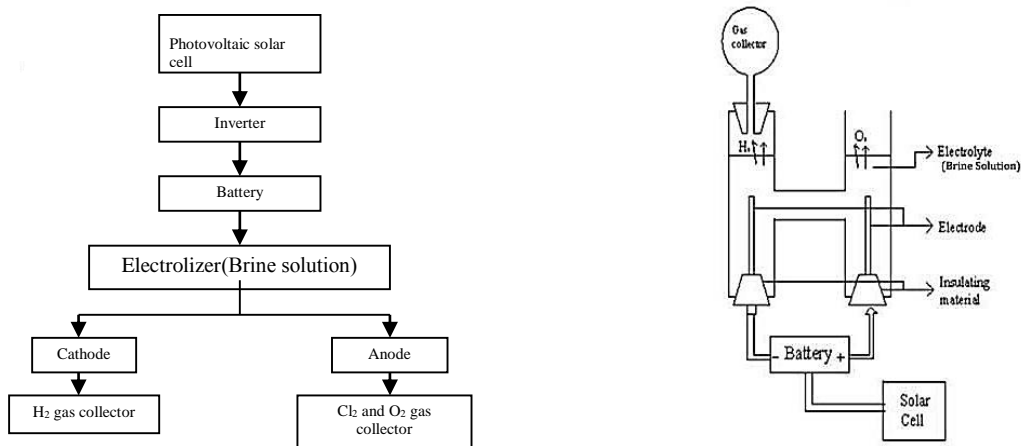


FIGURE. 1. (a) Block diagram for hydrogen production; (b) Schematic diagram for hydrogen production (H shaped)

EXPERIMENTAL EQUIPMENT & PROCEDURE

Selection Of Electrodes

At The Cathode

The more reactive a metal is the more it prefers being ions. Therefore, if a reactive metal such as zinc or magnesium is present it will remain as the ions. The H⁺ ions will accept the electrons and hydrogen gas will be given off at the cathode. If a less reactive metal, such as copper or silver is present it would rather accept the electrons than H⁺. Hence, the metal forms at the cathode.

At The Anode

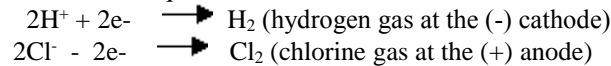
If halide ions are present, Cl⁻, Br⁻, I⁻, they will give up their electrons to become molecules of Cl₂, Br₂ and I₂ respectively. If no halogen is present, OH⁻ will give up electrons more readily than other non-metal ions, and oxygen forms. Finally, graphite is selected as electrodes. Care must be taken in choosing an electrolyte, since an anion from the electrolyte is in competition with the hydroxide ions to give up an electron.

Electrolyte Selection

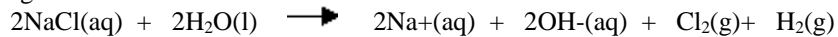
The following cations have lower electrode potential than H⁺ and are therefore suitable for use as electrolyte cations: Li⁺, Rb⁺, K⁺, Cs⁺, Ba²⁺, Sr²⁺, Ca²⁺, Na⁺ and Mg²⁺. Sodium and lithium are frequently used, as they form inexpensive, soluble salts (Brine solution). Strong acids such as sulfuric acid (H₂SO₄) and strong bases such as potassium hydroxide (KOH) and sodium hydroxide (NaOH) are frequently used as electrolytes. Finally, brine solution and KOH are selected as electrolytes.

Electrolysis Of Brine

Brine is merely sodium chloride (NaCl) dissolved in water. By performing electrolysis on brine, three substances will be found. They are chlorine, hydrogen and sodium hydroxide. Electrolysis of brine gives hydrogen at the cathode and chlorine at the anode. The reactions at each electrode are called half equations. The half equations are written so that the same number of electrons occur in each equation.



Hydrogen ions gain electrons (reduction) to form hydrogen atoms. The hydrogen atoms combine to form molecules of hydrogen gas. Chloride ions lose electrons (oxidation) to form chlorine atoms. The chlorine atoms combine to form molecules of chlorine gas. The overall reaction is



EFFICIENCY CALCULATION

Input energy, $E_i = VIt$(1)

Output energy, $E_{\text{output}} = mC_v$(2)

Here, m = Mass of hydrogen gas, C_v = Calorific value of hydrogen gas.

Efficiency, $\eta = \text{Output energy} / \text{Input energy}$ (3) When, $V = 13.5\text{V}$, $I = 0.58\text{A}$, $t = 3600\text{sec}$

Then from equation (1), input energy $E_i = 13.5 * 0.58 * 3600 = 28.188\text{KJ}$

Mass of hydrogen gas, $m = \rho v$(4)

Density of hydrogen gas, $\rho = 0.084\text{Kg m}^{-3}$, Volume of hydrogen gas $v = 150.12 * 10^{-6}\text{m}^3$

From equation (4) mass of hydrogen gas,

$$m = 0.084 * 150.12 * 10^{-6}$$

$$= 12.6 * 10^{-3}\text{gram}$$

Calorific value of hydrogen gas, $C_v = 150 \text{ KJ/gm}$. [11]
 Then from equation (2) output energy $E_{\text{output}} = 12.6 \cdot 10^{-3} \cdot 150$
 $= 1.89 \text{ KJ}$
 From equation (3) Efficiency, $\eta = E_{\text{output}} / E_{\text{input}} = 1.89 / 28.188 = 6.71\%$

RESULTS AND DISCUSSION

For H Shaped Electrolyzer

Fig 2.(a) shows that the hydrogen production is increased with increase in TDS at different voltages. But after 70 g/L the hydrogen production rate is decreased with increase in TDS. Fig 2. (b) shows that the hydrogen production is increased with increase in TDS at different currents. But after 70 g/L the hydrogen production rate is decreased.

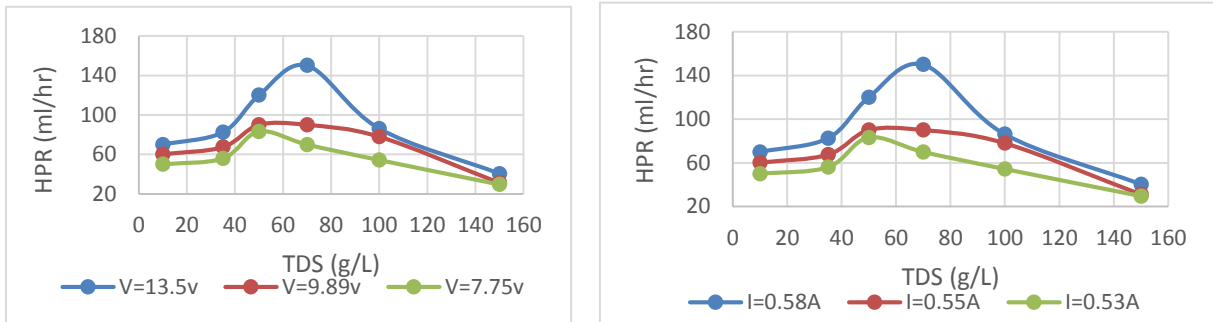


FIGURE. 2. (a) HPR VS TDS at different voltages ; (b)HPR vs TDS at different currents

Result for Potassium Hydroxide (KOH) with Water

Fig. 3. (a) shows that the hydrogen production is increased with increase of current at different TDS. Fig. 3. (b) shows that the efficiency is increased with increase in hydrogen production rate at different TDS. The efficiency is maximum for 100g/L TDS.

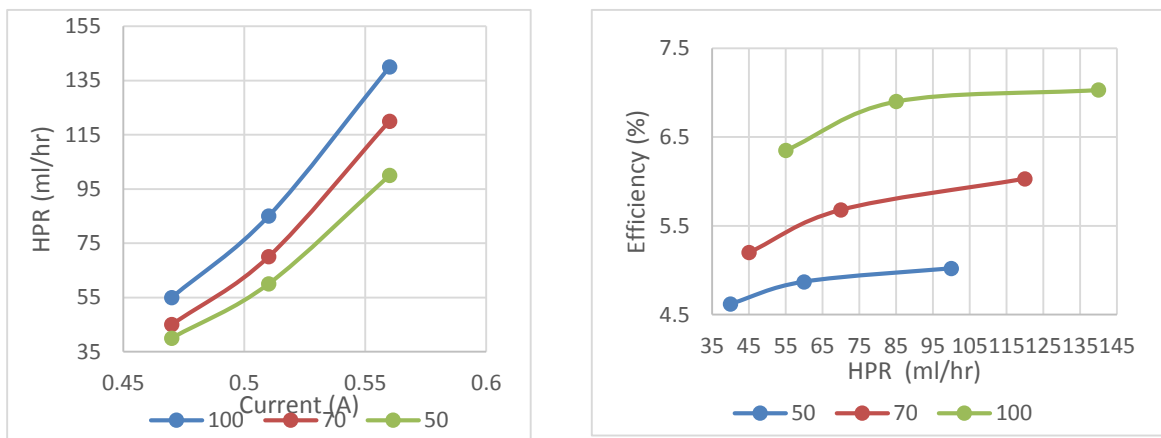


FIGURE. 3. (a) HPR VS current; (b)Efficiency vs HPR at different voltages

Fig. 4. (a) shows that the efficiency is increased with increase in temperature fastly. But after certain time the efficiency is increase very slowly with increase in temperature.

Fig. 4. (b) shows that the efficiency is increased fastly with increase in current. But after certain time the efficiency is increase very slowly with increase in current.

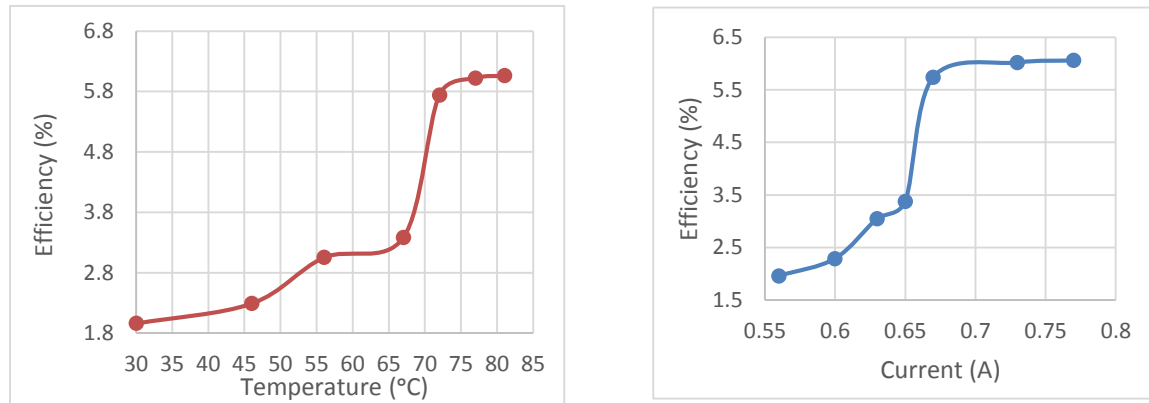


FIGURE. 4. (a) Efficiency VS temperature; (b) efficiency vs current

By applying the electrolysis process the output of the project was hydrogen gas, but the production rate was very slow. Water alone not a good conductor, so there added some NaCl and KOH in the experiment. The production of hydrogen can be increased by supplying high temperature and current which we saw in the graph. The generated amount of hydrogen gas is proportional to the total electrical charge that was sent through the solution. The efficiency of electrolysis was increased by using a rectangular electrolyzer instead of the H shaped electrolyzer. The necessary data were taken from the experiment to measure production rates of hydrogen to calculate efficiencies at constant voltage with various currents and concentrations.

RESULT FOR RECTANGULAR ELECTROLYZER.

For brine solution, Fig. Fig. 5. (a) shows that the efficiency is increased fastly with increase in current. But after 3.90A the efficiency is increased very slowly. Fig. 5. (b) shows that the efficiency is increased with increase in TDS fastly. But after certain time the efficiency is increase very slowly with increase in TDS.

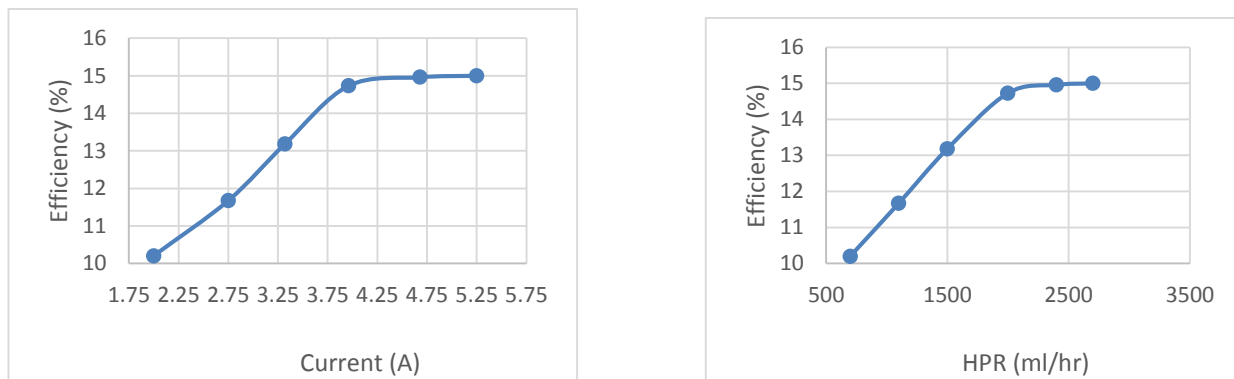


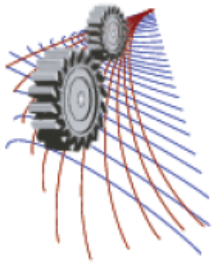
FIGURE. 5. (a) Efficiency VS Current at constant voltage ; (b) efficiency vs HPR

CONCLUSION

Amongst all the processes of producing hydrogen, electrolysis is the easiest and efficient process. The project is comprehensively based on chemical change due to electric current. In this project, brine solution and (KOH+water) act as the electrolyte from which decent amount of hydrogen is produced. For brine solution (H shaped beaker), the highest efficiency was 7.09% at 7.75V, 0.53A and 50g/L TDS. For KOH solution, the highest efficiency was 7.03% obtained at 12.2V, 0.56A, 100TDS g/L. But for rectangular beaker, the highest efficiency was 15% ,obtained at 5.25a, 12V, and 150 g/L TDS

REFERENCES

- [1] Bangladesh Power Development Board. September 2012. "Installed capacity of power plants (fuel wise) in September 2012" 6 September 2012, <http://www.bpdb.gov.bd>
- [2] Energy Information Administration. 19 September 2012. "INTERNATIONAL ENERGY OUTLOOK 2011: World total energy consumption by region and fuel, Reference case, 2006-2035 Table." 14 August 2012,
- [3] http://www.eia.gov/forecasts/ieo_table.cfm.
- [4] Bangladesh Power Development Board. September 2012. "Planning for Solar and Wind Projects." 6 September 2012, <<http://www.bpdb.gov.bd>>.
- [5] Gupta C.L. and Garg H.P. (1967), "Performance studies on solar air heater", solar Energy, 11(5) pp. 25-31.
- [6] A Student's Guide to Alternative Fuel Vehicles, article, retrieved 8th January 2012, from <http://www.energyquest.ca.gov/transportation/index.html>.
- [7] Properties of hydrogen, received 25th March 2012 [Online], Available: <http://en.wikipedia.org/wiki/Hydrogen>.
- [8] Z. Dülger and K.R. Özçelik "Fuel economy improvement by on board electrolyti hydrogen production" International Journal of Hydrogen Energy 25 (2000) 895-897.
- [9] Module 1: Hydrogen Properties, College of Desert, December 2001. <http://www.popularmechanics.com/cars/alternative-fuel/news/2690341>.
- [10] Ammar A. Al-Rousan "Reduction of fuel consumption in gasoline engines by introducing HHO gas into intake manifold" International Journal of Hydrogen Energy 35 (2010) 12930-12935.
- [11] "A review on water electrolysis" published by Emmanuel Zoulias, Elli Varkaraki, Nicolaos Lymberopoulos, (Centre for Renewable Energy Sources (CRES), Pikermi, Greece) Christodoulos N. Christodoulou and George N. Karagiorgis (Frederick Research Center (FRC), Nicosia, Cyprus).



A Finite Volume Discretization Technique to Simulate & Visualize an Inviscid Supersonic Flow over a Blunt Body

Al Shahriar^{1, a)} and Md. Mahbubul Alam^{2, b)}

^{1,2} Department of Mechanical Engineering, Chittagong University of Engineering & Technology (CUET),
Chittagong-4349, Bangladesh

^{a)}Corresponding author: al.shahriar.bd@ieee.org

^{b)}malam@cuet.ac.bd

Abstract. A finite volume discretization technique is researched to visualize a two dimensional inviscid supersonic flow over a blunt body. The geometry is drawn by MATLAB PDE toolbox where a circle is, cross section of a cylinder which is represented as a blunt body, set in the center of a relatively large rectangular domain. By using the same toolbox, triangular unstructured meshes are generated in the area bounded by cylinder circumference and the edges of the rectangle. The finite volume numerical approach is exploited to approximate state vector of conservative variable by a time marching forward Euler integration and simultaneously an upwind difference scheme, HLLC Scheme, is used to approximate the flux of governing equations. Time steps are calculated locally for each computational cell where CFL condition is considered to provide stability during simulation & to converge towards the piecewise approximate solution at every local region (cell). A freestream state vector implements far field boundary conditions. Flow regimes is visualized by varying the upstream Mach number, pressure distribution & density distribution where shock wave & subsonic regions can be identified. Drag and lift co-efficient are also computed from pressure distribution along the surface of the body.

INTRODUCTION

Computational fluid dynamics (CFD) is a method based on numerical techniques to solve and analyze problems involving fluid flows. Supersonic flow problem is the most studied topic in the areas of interest in CFD. Supersonic flow behaves very differently from subsonic flow. Fluid builds up a stagnation pressure while flowing over a body at supersonic speed. As the impact with the object brings the moving fluid to rest, the pressure disturbance cannot propagate upstream, thus, when the fluid finally does strike the object, it is forced to change its properties in an extremely violent and irreversible fashion. As a result, shock wave forms in the flow field. This paper deals with a same type of problem where a blunt body is subjected to supersonic flow. It is one of the most studied problems in fluid dynamics that has caught the interest of hundreds of aerodynamicists from the 1940s to this day [1].

Problem Definition

This work is associated with the flow field investigation over a blunt body i.e. a cylinder where the time dependent Euler's equations are numerically solved by the using a finite volume method to approximate the inviscid supersonic flow around a cylinder at $M_\infty = 2$. The solution will march in time till the steady state is reached. The shock will be captured as a part of the solution. The computer code is developed to visualize the velocities e.g. Mach number of every grids inside the computational domain. The outer computational boundary is a square and length of its each side is set to 10 times the cylinder diameter. This paper concentrates on in developing the finite volume algorithm and a shock capturing method.

MATHEMATICAL MODELING & NUMERICAL APPROACH

The finite volume method (FVM) represents and evaluates a partial differential equation (PDE) in the form of an algebraic equation. FVM is a conservative method because of the flux entering a given volume is identical to that leaving the adjacent volume. Another advantage of the FVM is that it is easily formulated to allow for unstructured meshes. For developing a FVM to solve a fluid flow problem the most basic process is to discretize the computational domain into simple geometric shapes. In this work, triangular cells are generated by MATLAB PDE Toolbox. In Fig. 1 (c) a portion of discretized domain is shown where the cells are denoted by Arabic numerals.

Governing Equations

In most engineering applications, the physical system is governed by a set of conservation laws. The conservation laws of a fluid system are described in integral form for a fixed physical domain as FVM requires the integral form of governing equations. Consider a fixed control volume, a two-dimensional physical domain (C) with a boundary of the domain (δC), shown in Fig.1 (a), through which a compressible inviscid fluid flows. As it is a derivation of Euler equation, no viscous effect is considered. According to the conservation of mass, Mass can be neither created nor destroyed. Conservation of momentum states that the time rate of change of momentum of a body equals the net force exerted on it. Another fundamental principle is contained in the first law of thermodynamics which states that energy can be neither created nor destroyed; it can only change in form. By applying these laws to the 2D fluid flowing through the fixed control volume equation (1) to (4) can be obtained. These equations represent Cauchy equations of conservation of mass, balance of momentum and energy, and can be seen as particular Navier–Stokes equations with no viscosity and no thermal conductivity [2].

$$\text{Conservation of mass:} \quad \frac{d}{dt} \iint_C \rho dA + \oint_{\delta C} \rho \vec{V} \cdot \vec{n} dS = 0 \quad (1)$$

$$\text{Conservation of x-momentum:} \quad \frac{d}{dt} \iint_C \rho u dA + \oint_{\delta C} \rho u \vec{V} \cdot \vec{n} dS = - \oint_{\delta C} P \vec{n} \cdot \vec{i} dS \quad (2)$$

$$\text{Conservation of y-momentum:} \quad \frac{d}{dt} \iint_C \rho v dA + \oint_{\delta C} \rho v \vec{V} \cdot \vec{n} dS = - \oint_{\delta C} P \vec{n} \cdot \vec{j} dS \quad (3)$$

$$\text{Conservation of Energy:} \quad \frac{d}{dt} \iint_C \rho E dA + \oint_{\delta C} \rho E \vec{V} \cdot \vec{n} dS = - \oint_{\delta C} P \vec{n} \cdot \vec{V} dS \quad (4)$$

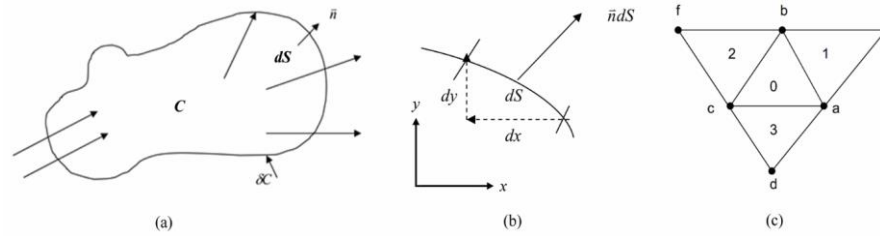


FIGURE 1. (a) Fixed Control Volume (b) Boundary of Control Volume (c) A portion of Discretized Control Volumes

These governing equations can be written very compactly and two new terms has been introduced: Conservative State Vector (U) & Flux Vector (F)

$$\frac{d}{dt} \iint_C U dA + \oint_{\delta C} F dS = 0 \quad (5)$$

Where,

$$U = \begin{bmatrix} \rho \\ \rho u \\ \rho v \\ \rho E \end{bmatrix} \quad F = \begin{bmatrix} \rho \vec{q} \\ \rho u \vec{q} + P n_x \\ \rho v \vec{q} + P n_y \\ \rho \vec{q} H \end{bmatrix}$$

$$\vec{q} = \vec{V} \cdot \vec{n} = V n \cos \theta = u n_x + v n_y$$

Time Marching Approximation of State vector

The time-derivative term of Eq. (5) can be simplified a little for the approximation of cell 0, shown in Fig.1 (c).

$$A_0 \frac{dU_0}{dt} - \oint_{\partial C_0} F dS = 0 \quad (6)$$

The simplest way is to apply forward Euler in the first term of Eq. (6). Hence the difference equation of \mathbf{U} for 2D Euler equation for the cell 0 and for $(t+\Delta t)$ th step by a forward Euler is,

$$A_0 \frac{U_0^{t+\Delta t} - U_0^t}{\Delta t} - \oint_{\partial C_0} F dS = 0 \quad (7)$$

Rearranging Eq. (7) results in

$$U_0^{t+\Delta t} = U_0^t + \frac{\Delta t}{A_0} \left(\oint_{\partial C_0} F dS \right) \quad (8)$$

Here, the dependent flow field variable is solved progressively in steps of time which means \mathbf{U}_0 at time level $(t+\Delta t)$ is calculated from the known value time level t . This method of obtaining steady state solution by marching towards time is known as time marching solution [3] [4].

Approximation of Flux by HLLC Flux Function

The flux in cell 0 is manipulated by the cells around it. So surface flux integral in Eq. (8) can also be simplified:

$$\oint_{\partial C_0} F dS = \int_a^b F_0 dS + \int_b^c F_0 dS + \int_c^a F_0 dS \quad (9)$$

Since this problem is related with supersonic flow which may result in a shock wave. As the shock wave is some sort of discontinuity in the flow, flux vector (\mathbf{F}) needs to be approximated in a very sensitive & sophisticated manner. In computational physics, upwind schemes denote a class of numerical discretization methods for solving hyperbolic PDEs. This scheme attempts to discretize hyperbolic PDEs by using differencing biased in the direction determined by the sign of the characteristic speeds. Historically, the origin of upwind methods can be traced back to the work of Courant, Isaacson, and Rees who proposed the CIR method [5]. Total variation diminishing scheme, flux splitting, flux limiters, Godunov schemes, approximate Riemann solvers, HLLC, HLLC etc. methods are broadly classified as upwind schemes since those techniques attempt to properly account for the propagation of information throughout the flow. Numerical approximation that is used for the largest and smallest signal velocity in the Riemann problem, the same technique is also used here. Harten, Lax and van Leer introduced a method to approximate flux at discontinuity which was then later developed by Einfeldt is known as HLLC flux function. Numerical approximation of the largest and smallest signal velocity in the Riemann problem also used to develop the theoretical results of Harten, Lax and van Leer [6]. According to this method the first term of right hand side in Eq.(9) i.e. flux at the interface between the cell 0 & cell 1 (edge ab) can be obtained as follows,

$$\int_a^b F_0 dS = \frac{S_{\max(ab)} F_1 - S_{\min(ab)} F_0 + S_{\max(ab)} S_{\min(ab)} (U_0 - U_1)}{S_{\max(ab)} - S_{\min(ab)}} \quad (10)$$

Stability Criteria & CFL Definition

The Courant–Friedrichs–Lewy (CFL) condition is a necessary condition for convergence while solving certain PDEs (usually hyperbolic PDEs) by a numerical method [7]. It arises in the numerical analysis of explicit time integration schemes. The physical significance of the CFL criterion is that Δt must be less than or at most equal to the time required for a sound wave to propagate between two adjacent grid points. The condition is named after Richard Courant, Kurt Friedrichs, and Hans Lewy who described it in their paper in 1928 [8]. Specifically, the CFL number for cell 0 & edge ab is to be defined as,

$$CFL = \frac{\Delta t}{2A} s_{\max(0)} l_{ab} \quad (11)$$

For stability, the algorithm requires that $CFL < 1$ in general. It is recommended to use, $CFL = 0.9$. Since Eq. (8) requires the value of $\Delta t/A$, the CFL number is used to calculate $\Delta t/A$ by rearranging Eq. (11).

Far field Boundary Conditions & Local Time Stepping

The method to implement boundary conditions at the outer (i.e. far field) boundary is through a function using the state vector from the interior triangle as one of the inputted state vectors and the free stream state vector as the other inputted state vector.

Local time stepping is the idea of using a different time step in each control volume to accelerate the convergence of the solution to the steady state. This means that the iterations are not accurate in time, but since the unsteady evolution of the flow is not of interest the lack of time accuracy is not a problem. If a single value of Δt were used in each cell, then the value of Δt would need to be set so that the calculation is stable for all cells. When the grid contains very small and large cells, the time step will generally be constrained by the smaller cells, As a result, the larger cells are being evolved at a potentially much smaller Δt than the stability limit would require for them.

PROGRAMMING & FRAMEWORK

An intelligent programming procedure is used to calculate the variables in the program sequentially. The program is designed in such a way that it can be restarted using the current value stored in memory for further iteration. The programming algorithm is shown in a flow chart which is given in Fig. 3. A total of 26112 cells are generated in the computational domain for calculation. To define geometry of the domain MATLAB® PDE Toolbox is used. Some of its functions are also used to generate and refine the meshes into smaller sizes which is shown in Fig.2 (b).

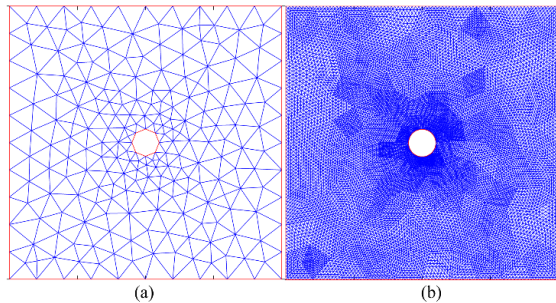


FIGURE 2. (a) Geometry of computational domain & unstructured meshes; (b) refined meshes

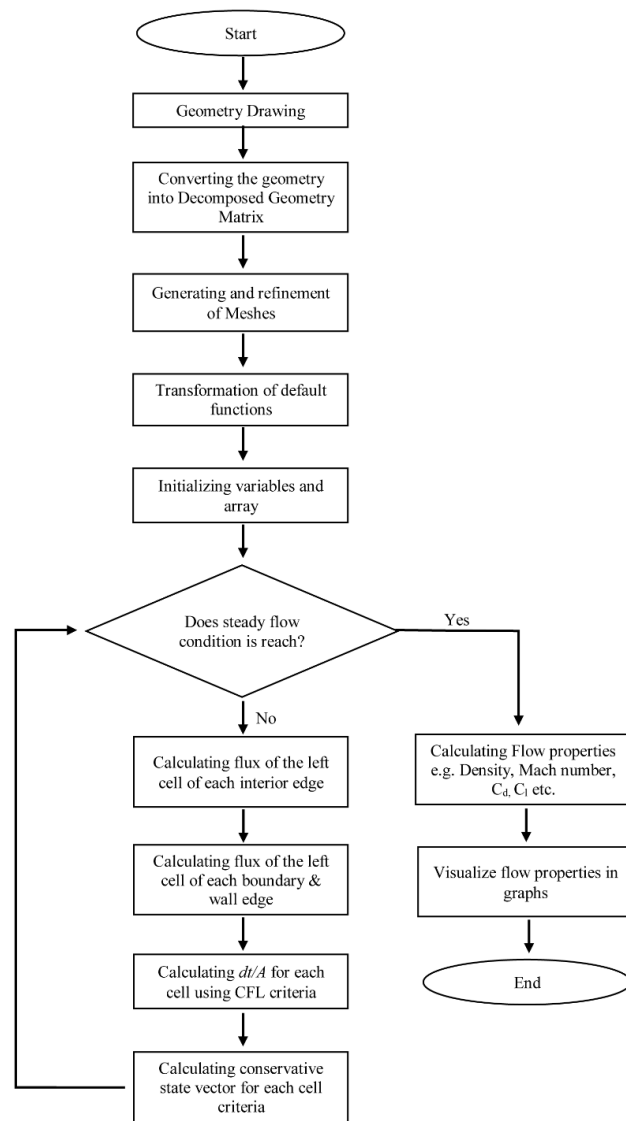


FIGURE 3. Flow chart

RESULT AND DISCUSSION

The time derivative is approximated by a forward Euler and the spatial derivatives by an upwind schemes to obtain the solution by marching in time till the convergence is reached. Various studies have been made to accelerate the convergence by controlling the time step as the CFL stability criteria. In certain cases, did not yield a convergent solution. Various upwind methods have been tried to apply for better solution and visualization of the shock, but failed because of programing difficulty. But finally this result shows a good agreement with other theoretical & experimental data. Table 1 shows some extreme values of various flow field properties that are obtained at the end of the simulation. The simulation is done with considering dimensionless parameters in overall experiment and observation.

TABLE 1. Various properties (dimensionless) of the stable flow after 2500th iteration

Properties	Values	Properties	Values
Drag Co-efficient, C_d	0.2963	Maximum density	3.0955
Lift Co-efficient, C_l	-0.0019	Minimum density	0.0186
Maximum Mach Number	5.7342	Maximum Pressure	4.1070
Minimum Mach Number	0.0160	Minimum Pressure	0.0030

The shock is captured as a part of the solution which can be identified clearly. The blue region generated on the Fig.4 (a) is subsonic region. The direction of the flow is from left to right. A curved bow shock wave is formed just in front of the cylinder. A narrow conical shaped subsonic region also generated behind the cylinder due to the back pressure drop. This low pressure results in a high Mach flow around this conical subsonic region.

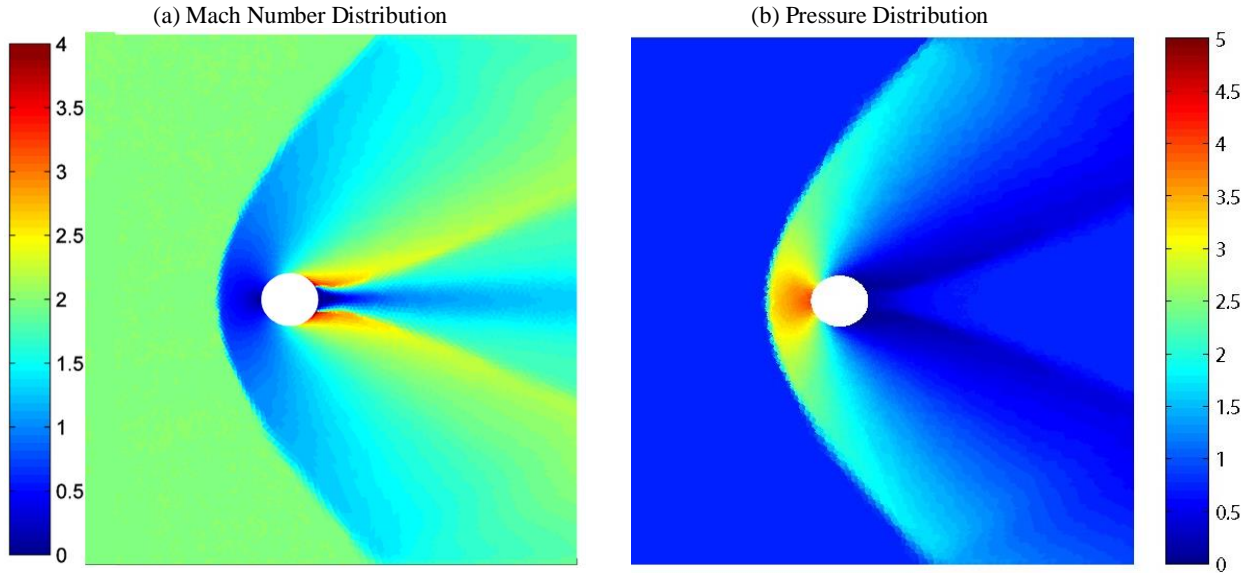


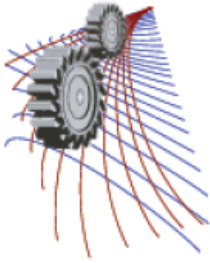
FIGURE 4. Distribution of (a) Mach number and (b) Pressure distribution after 2500th iteration

CONCLUSION

The fundamental theory of this work is that the numerical solution of the overall flow field is constructed by integrating piecewise approximate solution at every local region (cell). The basic numerical techniques in CFD have been developed as a series of worked examples, which can be easily programmable. But, it is very difficult to deal with the art of CFD. It requires practice of writing excellent codes and clear concept on fluid & mathematics related with numerical techniques to explore the issues raised in modern CFD. This study with its aim to acquire knowledge about the interactions between fluid dynamics & mathematics.

REFERENCES

1. John D. Anderson, *Computational Fluid Dynamics: The Basics with Applications*, McGraw-Hill, New York, 1995, pp. 30.
2. G. K. Batchelor, *An Introduction to Fluid Dynamics*. Cambridge University Press, 1967, ISBN 0-521-66396-2.
3. G. Moretti, M. Abbett, A Time independent Computational Method for Blunt Body Flows, *AIAA J.*, vlo 4, no. 12, 1966, pp. 2136-2141
4. W. Y. Soh, Time-marching solution of incompressible Navier-Stokes equations for internal flow, Volume 70, Issue 1, May 1987, pp. 232–252
5. R. Courant, E. Isaacson, M. Rees, On the Solution of Nonlinear Hyperbolic Differential Equations by Finite Differences, *Comm. Pure Appl. Math.* 5, 1952, pp. 243-255.
6. A. Harten, P. D. Lax, B. Van Leer, On upstream differencing and Godunov-type schemes for hyperbolic conservation laws, *SIAM Rev.*, 25, 1983, pp. 35-61.
7. R. Courant, K. Friedrichs, H. Lewy, Über die partiellen Differenzgleichungen der mathematischen Physik, *Mathematische Annalen* (in German) 100 (1): 32–74, 1928, doi:10.1007/BF01448839.
8. R. Courant, K. Friedrichs, H. Lewy, On the partial difference equations of mathematical physics, AEC Research and Development Report, NYO-7689, New York, 1956, pp. V + 76.



Structural and Impedance Spectroscopy Analysis of Sr Doped $\text{Ba}(\text{Fe}_{0.5}\text{Ta}_{0.5})\text{O}_3$ Ceramics

M.K.H Bhuiyan^{1,a)}, M. N. I Khan² and A. K. M. Akther Hossain¹

¹Department of Physics, Bangladesh University of Engineering and Technology, Dhaka 1000, Bangladesh

²Materials Science Division, Atomic Energy Centre, Dhaka-1000, Bangladesh

^{a)}Corresponding author: kamrul04122@gmail.com

Abstract. Polycrystalline $\text{Ba}_{1-x}\text{Sr}_x(\text{Fe}_{0.5}\text{Ta}_{0.5})\text{O}_3$ ceramics ($x=0.0,0.2$) were prepared by standard solid state reaction technique. XRD analysis of the compound indicated the formation of single phase simple cubic structure. Scanning electron micrographs show the formation of grains with average grain size of $23\ \mu\text{m}$ and $21\ \mu\text{m}$ for $x=0.0$ and $x=0.2$ respectively. The impedance spectroscopy is applied to investigate the ac electrical properties of the compositions at room temperature and in the frequency range of 100 Hz to 10 MHz. From the analysis of impedance spectra it is found that the real and imaginary part of the impedance decrease with increasing frequency and both are found to increase with Sr substitution. Cole-Cole plots show that the diameter of both the semicircles due to grain and grain boundary increases due to Sr substitution. The frequency depended electrical data are analyzed in the frame work of modulus formalisms. The electrical modulus spectra also reflect the contributions from capacitive grain and grain boundary effects; the large resolved semicircle arc caused by the grain effect and the small poorly resolved semicircle arc was attributed to the grain boundary. The role of Sr in modifying structural and impedance spectroscopy properties of this ceramics has been explained.

INTRODUCTION

Polycrystalline $\text{Ba}_{1-x}\text{Sr}_x(\text{Fe}_{0.5}\text{Ta}_{0.5})\text{O}_3$ ceramic with the perovskite structure having a general formula ABO_3 have of various physical properties which are suitable for device applications. The physical properties of this ceramic are strongly affected by the structure and morphology [1-3]. Recently, much attention has extensively been studied also drawn substantial interest for their promising electrical characteristics and some potential technological applications such as multilayer capacitors, non-volatile memory devices, optoelectronic devices etc.[4,5]. Substitution of proper cations at A and/or B sites have led to the enhancement paid to BSFT due to its high Curie temperature, barrier type property, and anisotropic physical properties [6–8]. Because of its properties and performances, BSFT, prepared by various methods was investigated by several other researchers [9]. Most of these materials were lead based and were suitable for their use due to their high dielectric permittivity, relatively low sintering temperature and temperature dependent diffuse dielectric maxima. But the presence of lead makes these materials toxic and thus has ecological restriction. Hence there is a great demand for new environmental friendly materials. Several studies have been made to obtain lead free ceramics [10–16]. Electric modulus spectroscopy is an important tool for simultaneous electrical and dielectric characterization of the materials. This technique has been widely used to characterize the dielectric behavior single crystal, polycrystalline, and amorphous ceramic materials [17]. In the present study Sr and Ta have been substituted in BaFeO_3 to obtain better piezoelectric properties and expected to be appropriate for the ceramic applications.

EXPERIMENTAL PROCEDURES

A standard solid state reaction method has been used for the preparation of BSFT samples. Initially, the precursor materials in an appropriate stoichiometric ratio (BaCO_3 , SrCO_3 , Fe_2O_3 and Ta_2O_5) have been mixed in an agate mortar for 24 h. The physical mixture so obtained was then calcined in an alumina crucible at 1050°C for 5 h. The process of grinding and calcination was repeated till the formation of the material $\text{Ba}_{1-x}\text{Sr}_x(\text{Fe}_{0.5}\text{Ta}_{0.5})\text{O}_3$ was confirmed. Subsequently, the calcined powder was pressed into cylindrical pellets of diameter 12 mm and thickness 1 mm with polyvinyl alcohol (PVA) as the binder. The pellet was then sintered in an air atmosphere at a temperature of 1450°C for 5h with a heating rate of $10^\circ\text{C}/\text{min}$ and cooling rate of $5^\circ\text{C}/\text{min}$ in a furnace to establish the course of nucleation for the grain growth and to facilitate the decomposition of the substituent oxides/carbonates. The sintered pellets were finally polished with fine emery paper to make their faces flat and parallel followed by coating with a conducting silver paint for electrical measurements. X-ray diffraction (XRD) studies have been carried out to confirm compound formation and phase identification using an X-ray powder diffractometer. The XRD pattern of the sample pellet was recorded at room temperature using $\text{Cu-K}\alpha$ radiation ($\lambda=1.5418\text{\AA}$) The microstructure of the material has been studied using a field emission scanning electron microscope FESEM, (JOEL-JSM, 7600 F Japan).The frequency dependent impedance measurements were carried out using a Wayne Kerr impedance analyzer (B 6500 series) in the frequency range of 100 Hz to 100 MHz.

RESULTS AND DISCUSSION

Structural and micro structural analysis

Rietveld refinements on the XRD data of BSFT were done by selecting the space group $\text{Pm } 3\text{m} (123)$. Fig. 1 illustrates the observed XRD patterns for BSFT. The XRD analyses indicated that BSFT has a simple cubic unit cell. The peaks in the pattern were perfectly assigned to the elements present in $\text{Ba}_{1-x}\text{Sr}_x(\text{Fe}_{0.5}\text{Ta}_{0.5})\text{O}_3$. This clearly indicated the purity of chemical composition of BSFT. The XRD patterns are virtually the same and show only single phase perovskite structure without the evidence of the second phase. It implies that Sr^{2+} ions have entered the unit cell maintaining the perovskite structure of solid solution. The grain size has an important role to control the properties of the ceramic materials. Figure 2(a) and 2(b) shows the micro graph of the surface of the $\text{Ba}_{1-x}\text{Sr}_x(\text{Fe}_{0.5}\text{Ta}_{0.5})\text{O}_3$ samples sintered at 1450°C for $x=0$ and $x=0.2$ respectively. From the figure it was shown that there is coexistence of small and large grain. The average grain size has been calculated using the relation $\bar{D} = 1.56\bar{L}$. Where \bar{D} is the average grain size and \bar{L} is the average intercept length over a large number of grains as measured on the plane of the sample.

The average grain size obtained $23\mu\text{m}$ and $21\mu\text{m}$ for $x=0$ and $x=0.2$ respectively. Grain size is influenced by the rate of nucleation, grain growth rate and temperature. The grain size decreases because the nucleation rate is greater than the growth rate for $x=0.2$ composition and also for the high mobility of the Sr ions in the BSFT ceramics.

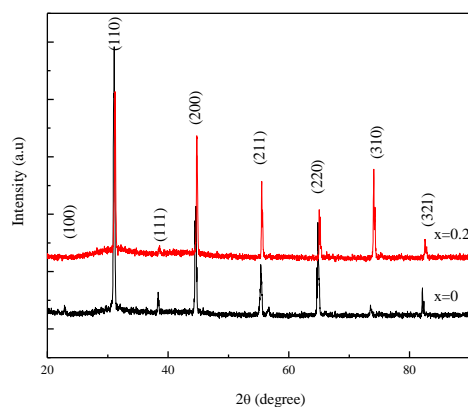


FIGURE 1. XRD patterns of $\text{Ba}_{1-x}\text{Sr}_x(\text{Fe}_{0.5}\text{Ta}_{0.5})\text{O}_3$ for $x=0$ and 0.2 sintered at 1450°C .

Impedance analysis

Figure 3 (a) shows the variation of real part of impedance (Z') of BSFT for $x=0$ and $x=0.2$ with frequency at room temperatures. It is observed that the magnitude of Z' decreases for both cases with an increase frequency which indicates an increase in conductivity with rise frequency. Fig.3(b) shows the variation of the imaginary part of impedance (Z'') of BSFT for $x=0$ and $x=0.2$ with frequency at room temperatures. A typical peak broadening which is slightly asymmetric in nature can be observed rise with frequency. The broadening in the peaks indicates frequency dependent electrical relaxation phenomena in the material [18]. There is no significant change in Z' with the Sr doping BFT, whereas there was a change at low frequency obtained

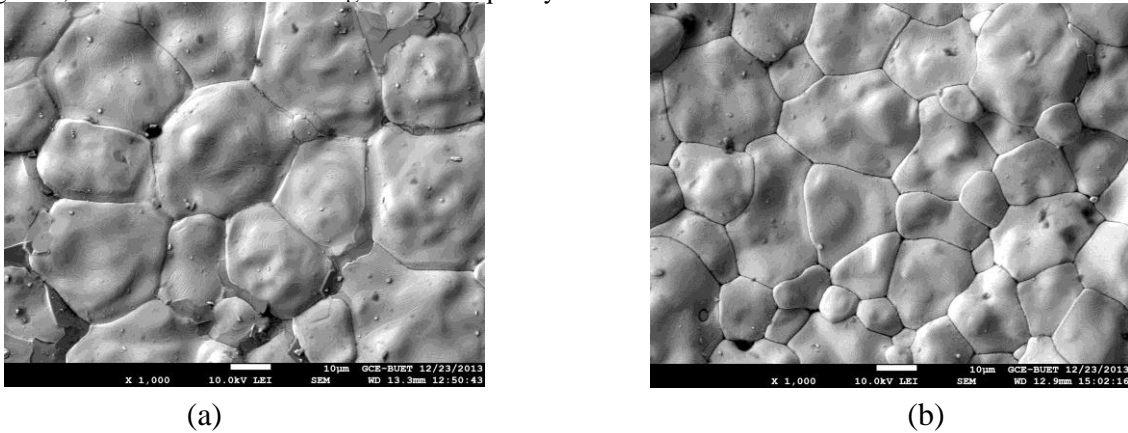


FIGURE 2. Typical SEM micrograph of $Ba_{1-x}Sr_x(Fe_{0.5}Ta_{0.5})O_3$ (a) for $x=0$ and (b) for $x = 0.2$ sintered at $1450^\circ C$.

Electric modulus analysis

From the physical point of view the electrical modulus corresponds to the relaxation of the electric field in the materials when the electric displacement remains constant. The usefulness of the modulus representation in the analysis of the relaxation properties has been demonstrated for polycrystalline ceramic. Typical features of $M^*(\omega)$ include abroad, asymmetric peak in the imaginary part and a sigmoidal step in the real part. The similarity of these shapes of loss and storage of mechanical stress associated with relaxation processes and has naturally led to similar interpretation.

Figure 4(a) shows the variation of M' with frequency at room temperature. The plots clearly show very low value of M' in the low frequency region and a sigmoidal increase in the value of M' with the frequency may be attributed to the conduction phenomena due to short range mobility of charge carriers. Also, the value of M' decreases with the rise in frequency and the curves are well dispersed. This behavior supports the long range mobility of charge carriers and the dispersive nature of the modulus.

Figure 4(b) shows the variation of imaginary part of complex modulus with frequency at room temperature. The M'' vs. fr plots are characterized by clearly resolved peaks in the pattern appearing significant a symmetry and the peak positions have a tendency to shift towards higher frequency and also side broader with the rise in frequency. The low frequency side of the M'' peak represents the range of frequencies in which charge carriers can move over a long distance. The high-frequency side of the M'' peak represents the range of frequency in which the charge carriers are spatially confined to their potential wells and thus could be made to have localized motion within the well. The region where the peak occurs is indicative of the transition from long range to short range mobility with increase in frequency. Further, the appearance of a peak in the modulus spectrum provides a clear indication of conductivity relaxation. Further, $M''(\omega)$ curves become broadened upon increasing frequency suggesting an increase in non-Debye behavior. From the figure it is observed that with Sr doping the value of M' and M'' was observed for the higher mobility of the Sr.

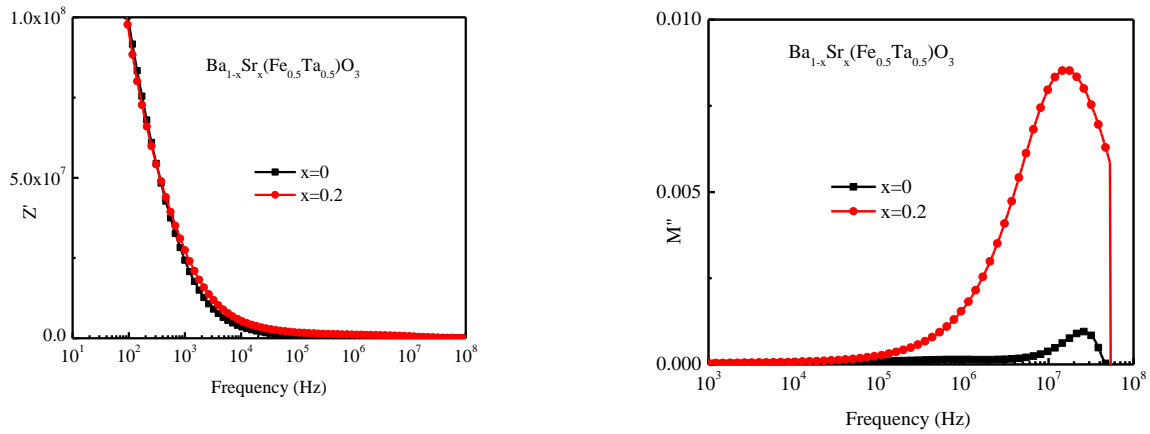


FIGURE 3. Variation of real part of (a) impedance spectra Z' (b) imaginary part of impedance Z'' with log frequency of various $\text{Ba}_{1-x}\text{Sr}_x(\text{Fe}_{0.5}\text{Ta}_{0.5})\text{O}_3$ sintered at 1450°C .

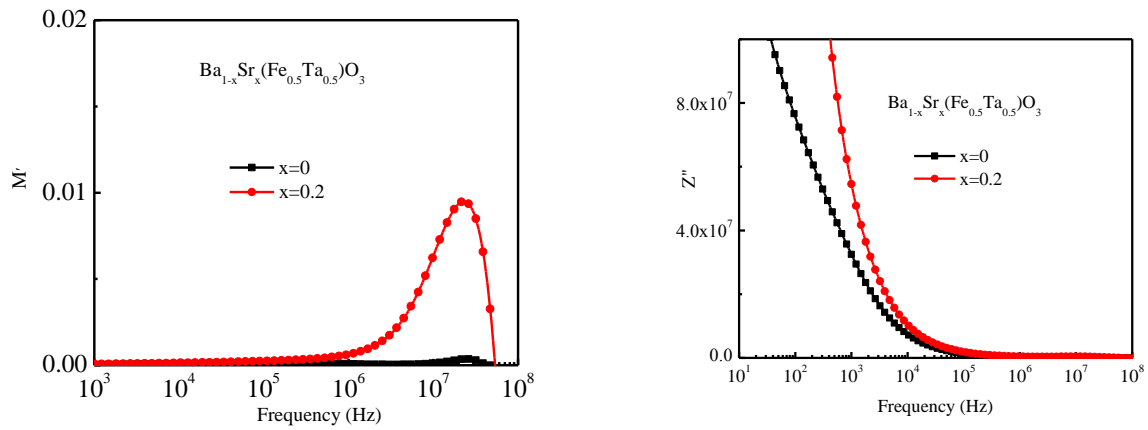


FIGURE 4. Variation of real part of modulus (a) M' and (b) imaginary part of modulus M'' with log frequency of various $\text{Ba}_{1-x}\text{Sr}_x(\text{Fe}_{0.5}\text{Ta}_{0.5})\text{O}_3$ sintered at 1450°C .

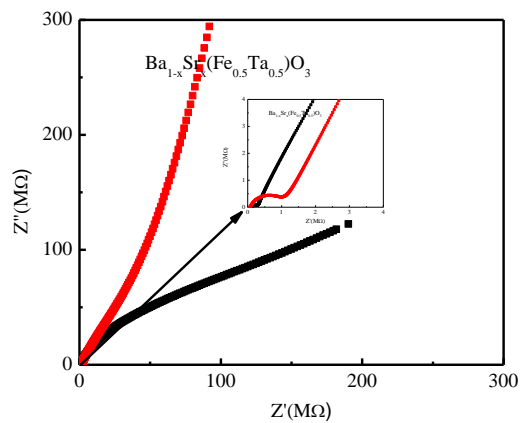


FIGURE 5. Cole Cole plot of complex impedance of various $\text{Ba}_{1-x}\text{Sr}_x(\text{Fe}_{0.5}\text{Ta}_{0.5})\text{O}_3$ sintered at 1450°C .

Figure 5 shows cole cole plot of complex impedance of BSFT taken over a wide frequency range at room temperature. A semicircle could be observed due to grain contribution (fig. inset) and upon increasing the frequency two semicircles could be traced. This clearly indicates the existence of grain boundary coming in to force .Hence, grain and grain boundary effect could be separated at these compositions. This result successfully explains the presence of grain boundaries in BSFT which is consistent with SEM Fig.2(a,b) where grains are well separated by grain boundaries.

CONCLUSION

Polycrystalline $\text{Ba}_{1-x}\text{Sr}_x(\text{Fe}_{0.5}\text{Ta}_{0.5})\text{O}_3$ ($x=0.0,0.2$) (BSFT) ceramics were prepared by standard solid state reaction method. XRD patterns analysis showed that all the BSFT ceramics in a perovskite type simple cubic structure. Morphological study by field emission scanning electron microscopy has indicated the polycrystalline nature of the material. The impedance analysis has indicated the presence of grain and grain boundary contribution in the materials which is found to increase with the Sr content. Electric modulus studies supported the hopping type of conduction in BSFT.

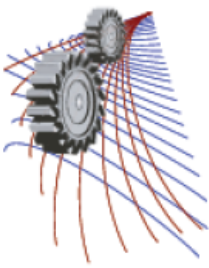
ACKNOWLEDGMENT

This work is supported by the CASR of Bangladesh University of Engineering and Technology (BUET).

REFERENCES

1. S. H. Beyon, K. Park, and M. Itoh, Structure and Ionic Conductivity of NaLnTiO_4 ; Comparison with Those of $\text{Na}_2\text{Ln}_2\text{Ti}_3\text{O}_{10}$ ($\text{Ln} = \text{La}, \text{Nd}, \text{Sm}, \text{and Gd}$), *J. Solid.State. Chem.* **121**, 430-436 (1996).
2. Toda, Y. Kameo, S. Kurita and M. Sato, Crystal structure determination and ionic conductivity of layered perovskite compounds NaLnTiO_4 ($\text{Ln} = \text{rare earth}$) *J. Alloy. Compd.* **234**, 19-25 (1996).
3. S. Y. Kim, JM. Oh, J. Chulpark and S. H. Byeon, Structure of New Layered Oxides $\text{M}^{\text{II}}_{0.5}\text{LaTiO}_4$ ($\text{M} = \text{Co}, \text{Cu}, \text{and Zn}$) Synthesized by the Ion-Exchange Reaction, *Chem. Mater.* **14**, 1643-1648 (2002).
4. V.V. Shvartsman, J. Dec, T. Lukasiewicz, A.L. Khalkin, W.K. Leemann, Evolution of the Polar Structure in Relaxor Ferroelectrics Close to the Curie Temperature Studied by Piezoresponse Force Microscopy, *Ferroelectrics.* **373** 77-85 (2008) .
5. F.J. Walker, A. Mckee, Thin-film perovskites-ferroelectric materials for integrated optics, *Nanostruct. Mater.* **7**, 221-227 (1996).
6. A.Z. Simões, M.A. Ramirez, C.S. Riccardi, E. Longo, J.A. Varela, Growth of $\text{SrBi}_4\text{Ti}_4\text{O}_{15}$ thin films in a microwave oven by the polymeric precursor method, *J. Alloy. Compd.* **455**, 407-412 (2008).
7. S. Luo, Y. Noguchi, M. Miyama, T. Kudo, Rietveld Analysis and Dielectric Properties of $\text{Bi}_2\text{WO}_6 - \text{Bi}_4\text{Ti}_3\text{O}_{12}$ Ferroelectric System, *Mater. Res. Bull.* **36** 531-540 (2001).
8. A.Z. Simões, L.S. Cavalcante, E. Longo, J.A. Varela, C.S. Riccardi, B. Mizaikoff, Nature of defects for bismuth layered thin films grown on Pt electrodes, *Appl. Phys. Lett.* **90**, 082910-(1-3) (2007).
9. R.Q. Chu, Z.J. Xua, Z.G. Zhub, G.R. Li, Q.R. Yin, Synthesis of $\text{SrBi}_4\text{Ti}_4\text{O}_{15}$ powder and ceramic via auto-combustion of citrate–nitrate gel, *Mater. Sci. Eng. B.* **122** 106-109 (2005).
10. M. Kosec, V. Bobnar, M. Hrovat, I. Bernard, B. Malic, J. Holc, Relaxor-like dielectric properties and history dependent effects in a new lead-free $\text{K}_{0.5}\text{Na}_{0.5}\text{NbO}_3\text{-SrTiO}_3$ ceramic system, *J. Mater. Res.* **19**, 1849-1854 (2004).
11. J. Ravez, A. Simon, Some Solid State Chemistry Aspects of Lead-Free Relaxor Ferroelectrics, *J. Solid.State. Chem.* **162**, 260-265 (2001) .
12. I.P. Raveski, S.A. Prosandeev, E.V. Colla, J.L. Dellis, M.E.L. Marssi, L. Jastrabic, Linear Versus Nonlinear Field dependance of Dielectric Stiffness in Relaxors, *Ferroelectrics.* **317**, 53-5 (2005).
13. A.N. Salak, M.P. Seabra, V.M. Ferreira, Structure dependent microwavedielectric properties of $(1-x)\text{La}(\text{Mg}_{1/2}\text{Ti}_{1/2})\text{O}_3\text{-xLa}_{2/3}\text{TiO}_3$ ceramics, *J. Am. Ceram. Soc.* **87**, 21(1-14) (2004).

- 14 A. Dixit, S.B. Majumder, R.S. Katiyar, Relaxor behavior in sol-gel-derived $\text{BaZr}_{(0.40)}\text{Ti}_{(0.60)}\text{O}_3$ thin films, *Appl. Phys. Lett.* **82**, 2679-2681 (2003)
- 15 G. Li, S. Liu, F. Liao, S. Tian, X. Jing, J. Lin, Y. Uesu, K. Kohn, K. Saitoh, M. Terauchi, N. Di, Z. Cheng, The structural and electric properties of the perovskite system $\text{BaTiO}_3\text{-Ba}(\text{Fe}_{1/2}\text{Ta}_{1/2})\text{O}_3$, *J. Solid.State. Chem.* **177**, 1695-1703 (2004).
- 16 K. Prasad, Priyanka, K.P. Chandra, A.R. Kulkarni, Structural and electrical properties of lead-free perovskite ceramic: $\text{Ba}(\text{In}_{1/2}\text{Nb}_{1/2})\text{O}_3$, *J. Non. Cryst.Solids.* **357**, 1209-1217 (2011).
- 17 K. Prabakar, S.P. MallikarjunRao, Complex impedance spectroscopy studies on fatigued soft and hard PZT ceramics, *J. Alloy. Compd.* **437**, 302-310 (2007).
- 18 Lily, K. Kumari, K. Prasad, R.N.P. Choudhary, Impedance spectroscopy of $(\text{Na}_{0.5}\text{Bi}_{0.5})(\text{Zr}_{0.25}\text{Ti}_{0.75})\text{O}_3$ lead-free ceramic, *J. Alloy. Compd.* **53**, 325-331 (2008).



Implementation of Control Chart for Statistical Process Control Considering Temperature and Humidity Effect in Synthetic Staple Fiber Industry

Abu Md. Saifuddoha ^{1,a)} and Md. Saiful Islam ^{2, b)}

¹Student of Department of industrial Engineering and management, Khulna University of Engineering and Technology, Fulbariget, Khulna-9203, Bangladesh

²Student of Department of industrial Engineering and management, Khulna University of Engineering and Technology, Fulbariget, Khulna-9203, Bangladesh

^{a)}Corresponding author: saifsf08@gmail.com

^{b)}saifuliem@gmail.com

Abstract. The purpose of this paper is to identify various fluctuations of temperature and humidity effecting synthetic staple fibers quality such as strength and tenacity as a final finished product and address these fluctuations effect through implementation of control chart for establishing statistical process control over synthetic fiber production process. Critical observations and test results are analyzed to show that temperature and humidity effect over synthetic staple fiber quality such as strength and tenacity. Establishing statistical process control in the synthetic staple fiber-processing sector is one key to improving the quality of synthetic staple fiber sector considering temperature and humidity effect. The resultant variations and fluctuations are addressed through categorizing various kinds of fiber by implementing control chart. The paper addresses the fluctuations and variations of synthetic fiber quality such as strength and tenacity due to temperature and humidity effect in the production processing of synthetic fiber industry, using control chart as an approach to solve these variations which was hardly attempted before. Strength and tenacity individually prioritized to reduce fluctuations into the entire production process system.

INTRODUCTION

The manufacture of synthetic fibers represents a huge industry, both in the Bangladesh and worldwide. In the twenty first century, the dollar value of synthetic fibers was roughly \$100 billion in the worldwide. We sometimes forget how much of these fibers we consume, especially since the appeal of "natural" fibers of cotton and wool has grown in recent years. Despite questions of aesthetics and taste, there should continue to be a significant demand for synthetic fibers, in large part because these fibers can be tailor-made to provide specific properties that natural fibers cannot provide.

Statistical methods play a vital role in the quality improvement process in manufacturing and service industries. Control charts are used to check for process stability. In this context, a process is said to be "in statistical control" if the probability distribution representing the quality characteristic is constant over time. If there is some change over time in this distribution, the process is said to be "out of control."

As students of production engineering, we are interested in implementing control chart to improve synthetic fibers quality because the process involves several fundamental aspects of production and quality control engineering. The goal here to address the fluctuations and variations of synthetic fiber quality such as strength and tenacity due to temperature and humidity effect in the production processing of synthetic fiber industry, using control chart as an approach to solve these variations which was hardly attempted before.

SYNTHETIC FIBER MANUFACTURING

True synthetics are products of the polymerization of smaller chemical units into long-chain molecular polymers. Fibers are formed by forcing a viscous fluid or solution of the polymer through the small orifices of a spinneret and immediately solidifying or precipitating the resulting filaments. Synthetic fibers are produced typically by two easily distinguishable methods, melt spinning and solvent spinning. [1]

For the common spinning of filaments in the finished range of about 0.1 – 2 tex spinnerets of a diameter 0.1-0.7 mm for melt spinning. Melt spinning is done for most polymers (PET, PP) between 240°C and 320°C. [2]

Polyester fiber spinning is done almost exclusively with extruders, which feed the molten polymer under pressure through the spinnerets. Filament solidification is induced by blowing the filaments with cold air at the top of the spin cell. The filaments are then led down the spin cell through a fiber finishing application, from which they are gathered into tow, hauled off, and coiled into spinning cans. Depending on the desired product, post-spinning operations vary but may include lubrication, drawing, crimping, heat setting, and stapling. [1][3]

Synthetic Fiber Measurement

Various units are used to refer to the measurement of a fiber, such as: the denier and tex (linear mass density of fibers), super S (fineness of wool fiber), worsted count, woollen count, cotton count (or Number English Ne), Number metric (Nm) and yield (the reciprocal of denier and tex). [4]

Denier /'or den (abbreviated D), a unit of measure for the linear mass density of fibers, is defined as the mass in grams per 9000 meters. The denier is based on a natural reference: a single strand of silk is approximately one denier; a 9000-meter strand of silk weighs about one gram.

$$\text{Denier} = (\text{weight of fiber} \times 9000) \div (\text{number of fiber} \times \text{length of fiber}) \quad (1)$$

Tex is a unit of measure for the linear mass density of fibers, yarns and thread and is defined as the mass in grams per 1000 meters. The unit code is "tex". When measuring objects that consist of multiple fibers, the term "filament tex" is sometimes used, referring to the mass in grams per 1000 meters of a single filament. Tex is used for measuring fiber size in many products, including cigarette filters, optical cable, yarn and fabric. [5]

$$\text{Tex} = \text{Denier} \div 9 \quad (2)$$

Temperature and Humidity Effect during Polypropylene Spinning

The rate of crystallization depends on the molecular weight, the history of the PP melt, and the temperature and humidity. In the Spinneret capillary there is a minor pre orientation. The major portion of the orientation is created from the outside filament portion that solidifies first in the border phase between the liquid inside portion and the solidified filament portion. [2] The temperature effect can be described below:

- A hot shroud below the spinneret lengthens the freezing zone, delays the filament thinning and cooling, and increases the yarn tension.
- Cooler quench air and/or higher quench air velocity result in faster filament thinning and higher yarn tension.
- Higher spinneret temperatures result in higher yarn temperatures along the first part of the filament axis, reduce the yarn tension.
- Higher throughputs per spinneret with constant take-up speed increase the cooling time and cooling zone with little influence on the yarn tension.

Case Study

The temperature and humidity effect during polypropylene (pp) spinning is studied at a synthetic fiber manufacturing company named Dird Polytex Limited. Here, the tenacity of the PP fiber increases due to lower temperature and humidity during winter from October to March and the tenacity of the PP fiber decreases due to

higher temperature and humidity during summer from April to September. The data was taken from July, 2014 to May, 2015 of average monthly temperature, humidity and tenacity.

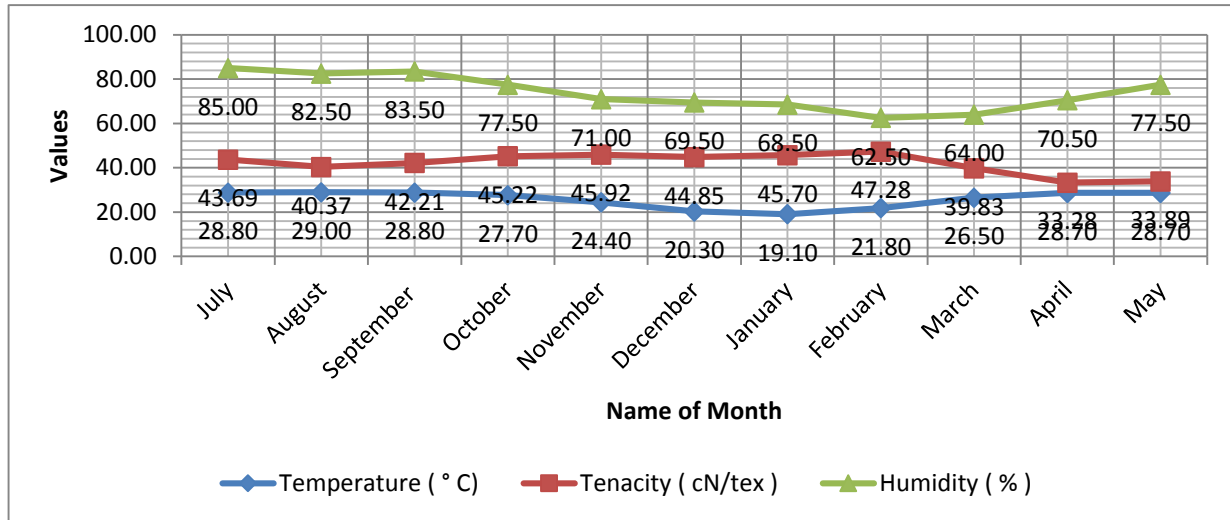


FIGURE. 1. Temperature and humidity effect over PP fiber tenacity.

CONTROL CHART

Control chart is graphical representation of the collected information. A control chart indicates whether a process is in control or out of control. It determines processes variability and detects unusual variations taking place in a process. It provides information about the selection of process and setting of tolerance limits. There are two types of control charts. They are variable and attribute chart. Variable charts involve the measurement of the job dimensions whereas an attribute chart only differentiates between a defective item and a non-defective item. [6]

X-bar and R chart

X-bar and R chart is one kind of variable chart. X-bar chart shows changes in process and is affected by changes in process variability. R chart secures information in establishing or modifying processes, inspection procedures. X-bar and R-bar chart when used together form a powerful instrument for diagnosing quality problems. [6]

$$\bar{X} = (\sum(X_1, X_2 \dots X_n)) / n, n \text{ is the number of observations} \quad (3)$$

$$\bar{X} = (\sum(X_1, X_2 \dots X_k)) / k, k \text{ is the number of subgroups} \quad (4)$$

$$UCL_X = \bar{X} + A_2 \times \bar{R} \quad (5)$$

$$LCL_X = \bar{X} - A_2 \times \bar{R} \quad (6)$$

$$\text{Range} = X_{\max} - X_{\min} \quad (7)$$

$$\bar{R} = (\sum(R_1, R_2 \dots R_k)) / k, k \text{ is the number of subgroups} \quad (8)$$

$$UCL_R = D_4 \times \bar{R} \quad (9)$$

$$LCL_R = D_3 \times \bar{R} \quad (10)$$

Case Study of Control Chart Implementation

Synthetic Fiber Company

Here, Table 1 shows monthly tenacity value of PP white fiber which has been recorded and among them randomly eight days value have been taken for implementation of x-bar and r chart.

TABLE 1. pp fiber tenacity result for eight days and calculation of x double bar and r bar through equation 3, 4, 7, 8.

Month	Tenacity (cN/tex)									
	Day 1	Day 2	Day 3	Day 4	Day 5	Day 6	Day 7	Day 8	X bar	Range
July,14	39.49	47.66	46.91	38.33	45.22	42.71	43.75	45.44	43.69	7.11
August,14	37.73	42.89	35.17	36.62	38.72	42.81	45.41	43.62	40.37	8.79
September,14	36.1	39.05	43.37	43.93	44.94	37.38	43.27	43.54	41.45	8.84
October,14	42.64	45.29	42.88	46.28	47.61	43.73	48.95	41.79	44.90	5.82
November,14	41.25	48.77	42.86	45.00	43.18	45.98	50.22	45.41	45.33	8.97
December,14	45.77	40.03	43.24	44.96	49.56	44.34	43.49	48.31	44.96	9.53
January,15	45.69	41.41	49.25	45.93	46.51	49.97	45.44	41.41	45.70	8.56
February,15	49.47	46.45	55.17	49.93	48.92	43.46	45.22	41.79	47.55	13.38
March,15	44.38	39.45	37.39	38.62	43.33	38.48	38.02	38.93	39.83	6.99
April,15	35.94	26.69	31.06	29.14	30.4	32.6	39.62	40.78	33.28	14.09
May,15	31.78	34.3	34.3	36.43	34.1	34.23	29.64	36.3	33.89	6.79
									X double bar	R bar

TABLE 2. Resultant value of x bar and r chart using previous formula of equation 5,6,9,10.

Bar chart type	Description	Formula
X bar	Upper Control Limit	46.80
	Upper Warning Limit	45.96
	Lower Warning Limit	42.62
	Lower Control Limit	41.79
Range	Upper Control Limit	10.53
	Lower Control Limit	8.53

¹ Warning limit is the two third portion of the corresponding control limit.

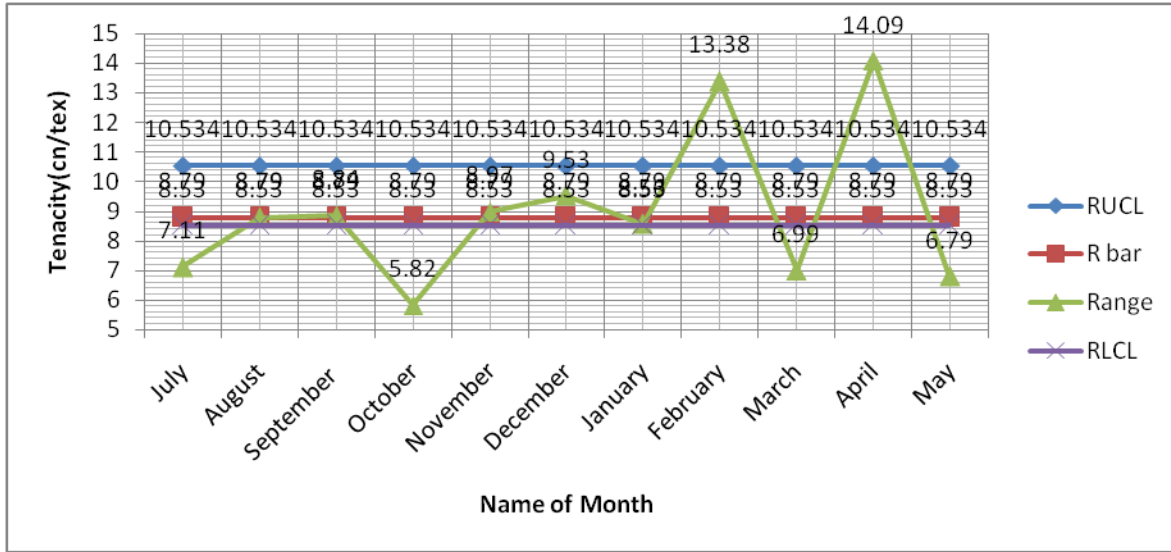


FIGURE 2. X-bar chart for monthly average PP fiber tenacity.

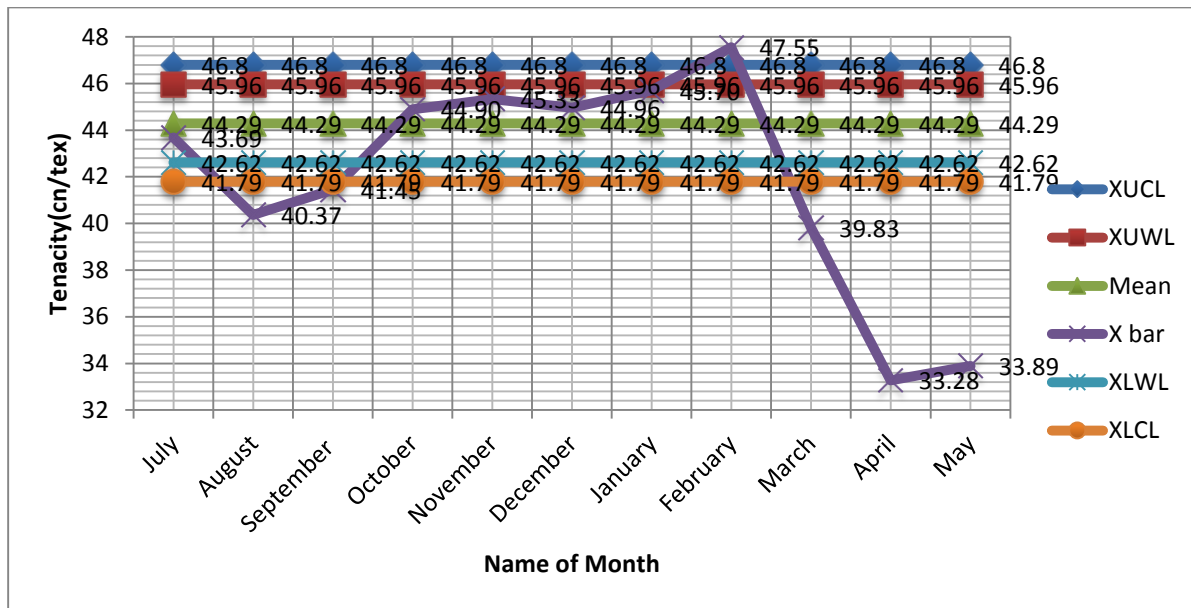


FIGURE 3. R chart of PP fiber tenacity.

RESULT ANALYSIS

Here fig. 2 and 3 depict x bar and r chart in which fig. 2 shows 4 points below lower limit and 1 point above upper limit and fig. 3 shows 4 points below lower limit and 2 points above upper limit. That means both x bar and r chart shows the process is out of control.

As the corresponding figure shows the process is out of control, this happens due to variation of temperature and humidity across the year 2014-15. The weather phenomena cannot be controlled so to solve this problem. A proper grading system is developed for different quality fibers in table 3 according to the x bar chart.

TABLE 3. A grading system of fiber quality

Fiber quality limit	Tenacity(cn/tex)	Fiber grade	Fiber Quality
Above upper limit	>46.8	A	Very good
Between upper warning limit to upper limit	45.96-46.8	B	Good
Between upper warning limit and mean	44.29-45.96	C	Average
Between mean to lower warning limit	42.62-44.29	D	Below Average
Between lower warning limit to lower limit	41.79-42.62	E	Bad
Below lower limit	<41.79	F	Very Bad

CONCLUSION

There is significant effect of temperature and humidity over synthetic staple fiber production process. Control chart is applied to categorize various kinds of synthetic staple fiber considering temperature and humidity effect for establishing statistical quality control over synthetic fiber production process. The paper addresses the fluctuations and variations of synthetic fiber quality such as strength and tenacity due to temperature and humidity effect in the production processing of synthetic fiber industry

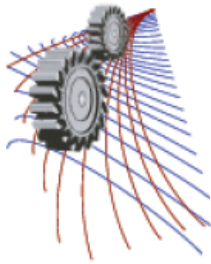
APPENDIX.A

Tabular values for X-bar and range charts

Subgroup Size	A ₂	d ₂	D ₃	D ₄
2	1.880	1.128	-----	3.268
3	1.023	1.693	-----	2.574
4	0.729	2.059	-----	2.282
5	0.577	2.326	-----	2.114
6	0.483	2.534	-----	2.004
7	0.419	2.704	0.076	1.924
8	0.373	2.847	0.136	1.864
9	0.337	2.970	0.184	1.816
10	0.308	3.078	0.223	1.777
11	0.285	3.173	0.256	1.744
12	0.266	3.258	0.283	1.717
13	0.249	3.336	0.307	1.693
14	0.235	3.407	0.328	1.672
15	0.223	3.472	0.347	1.653
16	0.212	3.532	0.363	1.637
17	0.203	3.588	0.378	1.622
18	0.194	3.640	0.391	1.608
19	0.187	3.689	0.403	1.597
20	0.180	3.735	0.415	1.588
21	0.173	3.778	0.426	1.579
22	0.167	3.819	0.434	1.566
23	0.162	3.858	0.443	1.557
24	0.157	3.895	0.451	1.548
25	0.153	3.931	0.459	1.541

REFERENCES

- [1]. "Fibers 540.000", Chemical Economics Handbook, Menlo Park, CA, March 1978.
- [2]. Franz Fourne, Synthetic fibers, Munich : Hanser; Cincinnati : Hanser/Gardner, 1998.
- [3]. Industrial Process Profiles For Environmental Use - Chapter 11 - The Synthetic Fiber Industry, EPA Contract No. 68-02-1310, Aeronautical Research Associates of Princeton, Princeton, NJ, November 1976.
- [4]. Haynes, Williams (1946). "XVII: New Fibres: New Fabrics". This Chemical Age. London: Secker and Warburg. p. 217.
- [5]. Collier, Ann M (1970), A Handbook of Textiles, Pergamon Press, p. 258, ISBN 0-08-018057-4, ISBN 0-08-018056-6, retrieved January 2009.
- [6]. Foster, S. Thomas. Managing Quality. Upper Saddle River: Prentice Hall, Inc. 2001.



Convertible Pattern Template for Design Creation

Md. Mazharul Islam^{1,a)} and Md. Mashiur Rahman Khan^{2,b)}

¹*Department of textile engineering, Northern University Bangladesh, Dhaka-1213, Bangladesh*

²*Department of apparel manufacturing engineering, Bangladesh University of Textiles, Dhaka-1208, Bangladesh*

a) Corresponding author: mazh999@gmail.com

b) mrktex89@gmail.com

Abstract. Technological advances during the past decade have opened many new doors for the textile & apparel industries, especially in the area of garment designing & pattern making by CAD. Fashion industries have been attracted to use this newly available tool in actual product development process to strengthen the collaboration along the supply chain & shorten the product time to the market. In this modern world, fashion & styles are changing frequently. The emergence of fast changes in fashion has given rise to shorten production cycle time in the garment industry. To meet the dynamic customer demands of momentous quantities in shorten lead time, we have to make patterns of different designs in faster way using CAD. Due to design variations, we have to make different patterns which are very time consuming. So our developed method shows the way of making only one single pattern template that are resized & converted to almost any upper body garment pattern according to different buyer's spec sheet.

INTRODUCTION

Pattern making is the centre of attention when talking about the creation of garments. There are three fundamental approaches to pattern creation that have been in practice in the clothing industry over a very long period of time and are still in current use. These are 3D draping (also known as the “haute couture” process), block pattern development and pattern drafting [1]. Pattern drafting is the engineered version of pattern creation, and has proven to be most suitable for targeting the mass production of garments based on standard average size measurements. This process is thus highly dependent on the expertise of the pattern technician to ensure an acceptable fit of the garments on either an individual client, or as a standard size intended for bulk production.

METHODOLOGY

When the two-dimensional pattern is the starting point for creation and lines and shapes are joined together into three-dimensional garments, the pattern can become an effective tool for creating new shapes [2]. Cutting from blocks and designing with the pattern has been promoted as a design method in a number of published titles. The methods have been labeled with different names, such as metric pattern cutting [4], Pattern Magic [5], Subtraction Cutting [6], Transformational Reconstruction [7] and they all have in common that they start out from two-dimensional blocks or shapes and, using a jigsaw puzzle approach to designing, they construct their garments in three-dimensional space. Aldrich [4] claims that the body remains constant and therefore argues that the pattern blocks representing the body are a good starting point for cutting garments. The problem with this argumentation is that the body does not remain constant. It is changeable, varying and inconstant by all means. The body is a moving variable [8] that is constantly shifting its physical appearance. When we working from measurements of spec (specification) sheet, they includes ease allowance along with it. So for spec sheet pattern making we do not need any extra ease allowance. Computer-based solutions are available for fashion drawing and pattern creation. Today's industry prefers to use more and more computer-based techniques as they offer efficiency and time-saving solutions

to many complicated tasks. Specialized CAD packages for drafting and grading flat patterns were introduced into the clothing industry in the 1980s [3] and they have become very popular within the industry.

TABLE 1. Construction figure & their explanations.

Figure	POM	Description	Ref fig.
	HPSF	High Point Shoulder Front	AD, AD2
	HPSB	High Point Shoulder Back	BC, BC2
	CFL	Centre Front Length	GD, GD2, G2D2, G3D3
	CBL	Centre Back Length	HC, HC2
	FND	Front Neck Drop	AG
	BND	Back Neck Drop	BH
	NW	Neck Width or Opening	AI x 2, BI2 x 2
	NC	Neck or Collar Circumference	AI x 5, BI2 x 5
	SD	Shoulder Drop	AE, BE2, FJ, F3J2
	AS	Across Shoulder	AF x 2, BF3 x 2
	S	Shoulder Length	IJ, I2J2
	FS	Forward Shoulder	I1J3, JJ3, I2I4, J2J4
	HC	Half Chest or Chest Width	AB
	HBO	Half Bottom Opening or Bottom Width	D2O, D2F2, D2O3, C2F4, C2O2, C2O4
	AHS	Arm Hole Straight	JL, J2L
	ASD	Arm Scye Depth	KL
	AC	Across Chest or Front	M3N x 2
	AB	Across Back	M4N2 x 2
	NWL	Natural Waist Length	AP
	HW	Half Waist or Waist Width	PP3 x 2, P2P4 x 2
	CD	Curve Distance	ZZ2
	DSp	Dart Spacing	PQ, P2Q6
	DL	Dart Length	Q3Q5, Q8Q10
	DW	Dart Width	Q4Q2, Q9Q7
	PO	Placket Opening	AY
	PW	Placket Width	RD, GR2, G2R4, G3R3, D3R6, D2R5
	YH	Yoke Height	BX
	STL	Shirt Tail Length	DU
	LL	Lapel Length	R3S
	LW	Lapel Width at 90 degree to Break line	SS2
	LWB	Lapel Width from edge to Break line	ST
	VSL	Vent Slit Length	CW
	VSW	Vent Slit Width	CW2
FHS	Front Hem Spacing	V2V x 2	

FIGURE 1. Construction of the template

The aim of this research is to build a pattern template or module which is resized & converted to any possible upper body garment patterns while inputting the measurements. For doing this we used a freeware software named geogebra which supports java & geogebra language to building geometrical shapes. We developed some new tools & using java & geogebra script and geometrical formulas. We also use some existing tools of the geogebra software to build the total construction. Actual construction is far more complex because it contains many shapes & formulas. But we are explaining the basic things of the construction by simple diagram (Fig. 1). During construction we made

some measurement input boxes to input measurements from spec sheet. The system is only works with spec sheet measurements. If we want to use body measurements, then we must add ease allowance with it and then input the total amount in to the measurement in put boxes. The rest part will be done by our module. The system can detect the design and automatically creates the patterns for it.

CONSTRUCTION & CONDITIONS

- **HPS, CBL & CFL:** We start from point A. In fig. 1, $AD = [HPSF] = [FND] + [CFL]$ & $BC = [HPSB] = [BND] + [CBL]$ (except vest & coat). For coat C&D points are shifted to C2&D2 points respectively and for vest D is shifted to D3 point.
- **Front neck point G:** If [FND] is not given, $AG = 1/5$ NC less 0.5 cm. G point is shifted to G2 & G3 points for [FND] of vest & coat respectively.
- **Back neck point H:** If [BND] is not given, $BH = [HPSB] - [CBL]$.
- **Side neck points I & I2:** If [NW] is not given, $AI = BI2 = 1/5$ [NC]
- **Front & back neck curve:** Back neck curve HI2 or HI4 is visible for all patterns. But front neck curve GI or GI3 will be hidden when [LL] is given because coat does not have front neck curve. Front neck curve R4I3 will only visible when [FHS] is given, because this is only measurement point for vest.
- **Shoulder points J & J2:** There are three possible options to get shoulder point if any two of these three: [SD], [S] & [AS] is given. If [AS] & [S] is given, then $AF = BF3 = 1/2$ [AS] and $FJ = F3J2 = [SD]$. If [SD] & [S] is given, then $AE = BE2 = [SD]$ where EE2 is a horizontal line. After that two circles will be drawn from point I & I2 with radius of [S] which will intersect at J & J2 points over EE2 line. If [AS] & [S] is given, then $AF = BF3 = D2F2 = C2F4 = 1/2$ [AS] where FF2 & F3F4 are vertical lines. After that two circles will be drawn from point I & I2 with radius of [S] which will intersect at J & J2 points over FF2 & F3F4 lines respectively.
- **For Forward Shoulder [FS]:** If [FS] is given, then IJ & I2J2 lines are shifted to I3J3 & I4J4 lines respectively.
- **Armpit point L:** There are two possible options to get L point if any one of [AHS] & [ASD] is given. If [AHS] is given then, from point J&J2 two circles will be drawn with radius of [AHS]. Which intersect at L point over KK2 vertical line where $AK = BK = 1/2$ [HC]. If [ASD] is given, then $KL = [ASD]$ is a straight vertical line.
- **[AC] & [AB] points N & N2:** If [AC] & [AB] is given, then a perpendicular line will be drawn from point L over AD & BC line which intersects at M & M2 points respectively. Then $MM3 = M2M4 = 1/3$ of KL measurement and $M3N = 1/2$ [AC] & $M4N2 = 1/2$ [AB].
- **Armhole Curve:** If [AC] & [AB] is not given, then two specially designed curve will be drawn from point J to L and J2 to L. The curve is made by us by modifying a parametric curve equation. But if [AC] & [AB] is given, then another two specially designed curve will be drawn through points JNL & J2N2L. These two curves are also drawn by modifying a parametric curve equation.
- **Bottom Opening Lines:** If [HBO] is not given or equal, then $D2O3 = 1/2$ [HC], but if given and more than [HC]; then O3 & O4 points are shifted to O5 & O6 respectively and if less than [HC]; then O3 & O4 points are shifted to O & O2 points respectively. Other two curve lines R6O & R5VO are only visible when [LL] & [FHS] is given because they are the only measurement points for coat & vest respectively. For shirt tail curve, DO is visible when [STL] is given; where $DU = [STL]$ & $UO = 1/2$ [HBO]
- **Placket:** When [PW] is given, then $RD = GR2 = [PW]$. R & R2 points are shifted to R6 & R3 points and R5 & R4 points respectively for coat & vest.
- **[NWL], [HW] & side seam:** If garments have waist shaping, then $AP = BP2 = [NWL]$ and $PP3 = P2P4 = 1/2$ [HW] + $1/2$ [DW]. If [NWL] & [HW] is not given, the side seam lines are any of the lines: LO, LO3, LO5 for front and LO2, LO4, LO6 for back depending on [HBO] position. If [NWL] & [HW] is given but [CD] is not given, then it will follow LP3O & LP4O2 straight lines and if [CD] is given along with [NWL] & [HW], then side seam will be LZ2P3Z3O & LZ4P4Z5O2.
- **Darts:** Darts are only visible when, [DL], [DW], [DP] are present. The default values for $[DP] = 1/4$ [HW] from center line. In construction, $Q2Q4 = Q9Q7 = [DW]$ & $Q3Q5 = Q8Q10 = [DL]$.
- **Neck opening:** If [NO] is given in case of Polo shirt, then $GY = [PO]$ indicated by an X mark; that means we have to slit the pattern from G to Y before sewing.

RESULT

Final results after creating the patterns are shown in the fig. 2.

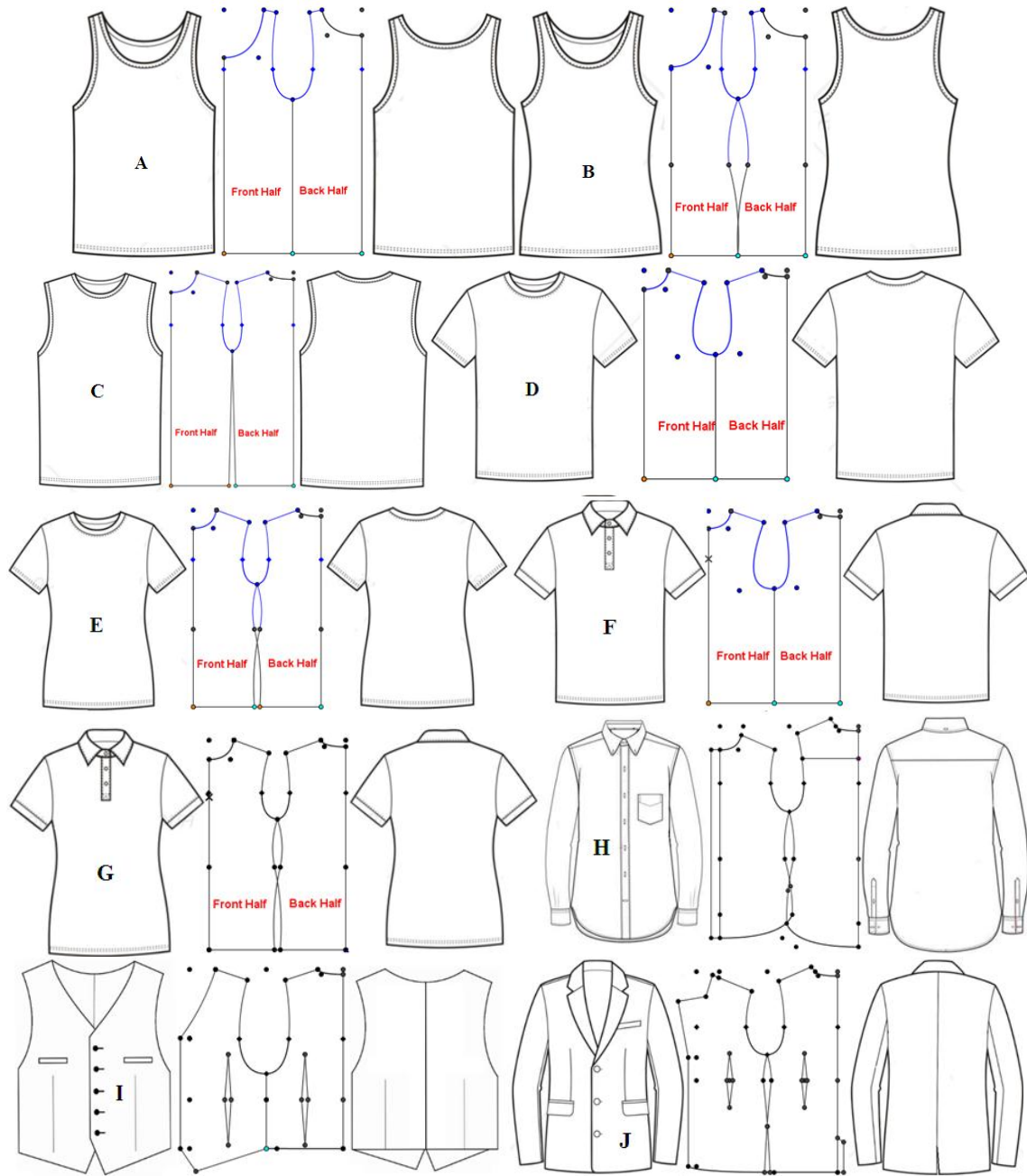
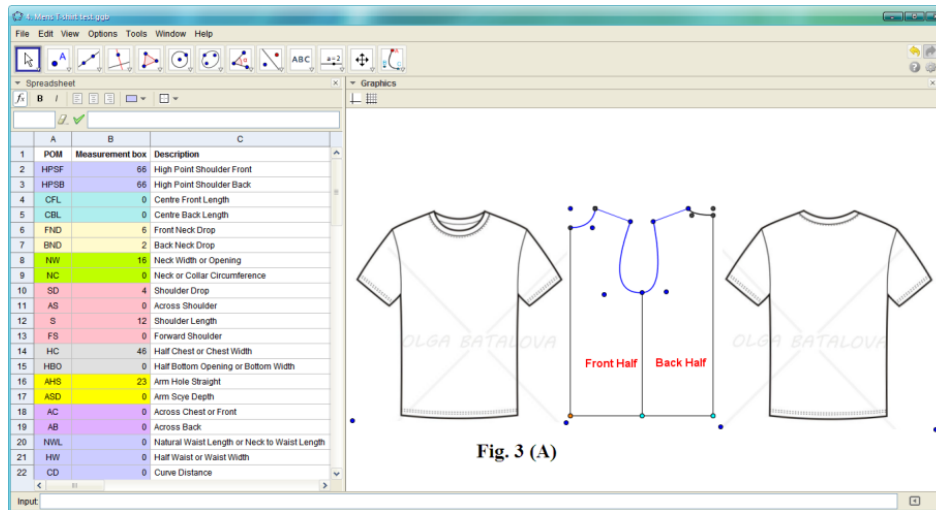
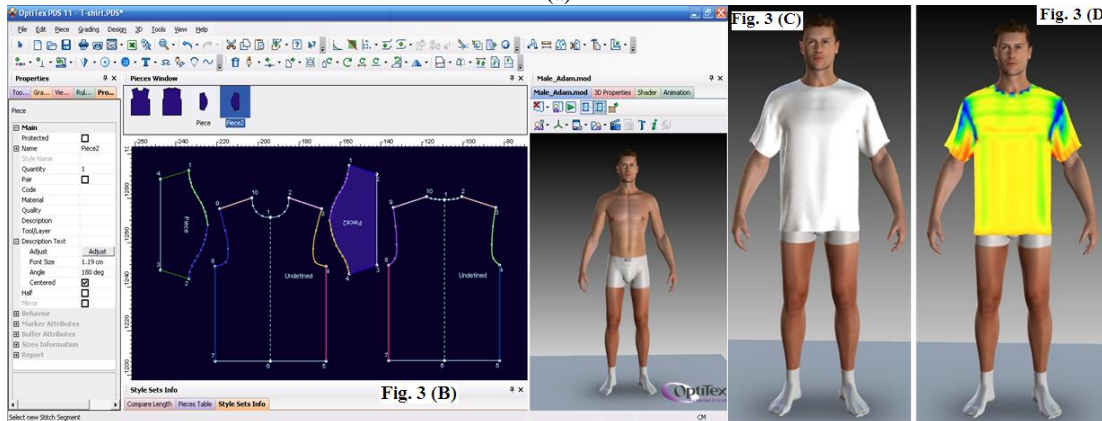


FIGURE 2. Final results of pattern with front & back reference flat spec of garments.

When proper measurements are inputted in Geogebra Template, the patterns are automatically drawn; shown in Fig. 3 (a). If we can export the garment patterns in dxf file format, then it will be supported in any commercial garment CAD. But geogebra cannot export in dxf format. So we have to export it in svg format and then converted to dxf format by a converter or using Adobe Illustrator software. After importing the pattern in commercial CAD (we used Optitex®), the pattern will be look like fig. 3 (b) and if we draped it in 3D, it will looks like fig. 3 (c & d).



(a)



(b)

(c)

(d)

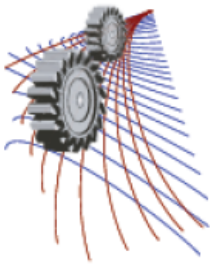
FIGURE 3. (a) Screenshot of our Geogebra Template; (b) Screenshot of Optitex software after importing dxf file of T-Shirt (sleeves are drawn separately); (c) After 3D draping; (d) After stretch mapping.

CONCLUSION

This software module can only generate patterns of symmetrical & basic designs. But we can further add as many designs as we want in the module. In a fast fashion world, we have to make garment patterns of different styles within a short time. So our developed template or module not only saves our valuable time but also can save our money and reduce human effort to make different garment patterns.

REFERENCES

1. Chi, L. Engineering the fit of upper body clothing for non-standard applications. Unpublished thesis (PhD), University of Manchester, (2005).
2. Chi, L. Engineering the fit of upper body clothing. Xi'an (Shaanxi, China): Xi'an Jiaotong University Press, (2007).
3. Burke, S. Fashion Computing - Design Techniques and CAD. UK: Burke Publishing, (2006).
4. Aldrich, W. Metric pattern cutting. Oxford: Blackwell publishing, (1980/2004).
5. Nakamichi, T. Pattern magic 2. London: Laurence King Publishing, (2007).
6. Roberts, J. Subtraction cutting school. St Helena: Centre for pattern design, (2008).
7. Sato, S. Transformational reconstruction. St Helena: Centre for pattern design, (2011).
8. Burnham, D. Cut my cote. Ontario: Royal Ontario Museum, (1973/1997).



Error Reduction of Traditional XY-Point Wise Apparel Pattern Grading System

Md. Mazharul Islam^{1,a)} and Md. Mahbubul Haque^{2,b)}

¹*Department of textile engineering, Northern University Bangladesh, Dhaka-1213, Bangladesh*

²*Department of textile engineering, Daffodil International University, Dhaka-1207, Bangladesh*

^{a)} Corresponding author: mazh999@gmail.com

^{b)} headte@daffodilvarsity.edu.bd

Abstract. Grading is one of the important techniques used in the fashion industry to create different sized clothing from a single pattern. The objectives of the study are to analyze the traditional grading system, find out its problems & finally create solutions for them. In order to grade the pattern, we have to manually calculate the grading increment from body measurements or spec sheet and use not only on manual method but also on CAD method. So problems are the calculation method of traditional system. This study shows how to calculate properly for higher precision grading to fit the cloth on the body. So this study helps us to prevent rejection of graded garment sample approval before production that is very time consuming in some manner.

INTRODUCTION

Apparel grading is the process of increasing or decreasing the base size pattern according to a set of body measurements and proportional relationships to develop a range of sizes for production [1]. Pattern grading can be accomplished using several different techniques: manual, machine, or CAD. In manual grading, pattern pieces are shifted and hand-traced. Machine grading uses a mechanical grading machine. When accurate data is entered into a computer, computerized grading is the most expedient and precise method [2].

The goal of grading is to apply proportional increases or decreases at key locations or cardinal points on the perimeter of the pattern that transform the width and length of the pieces. The changes in growth are made according to a prescribed set of body measurements [3,4]. The earliest example of grading systems for women's clothing were the proportional dressmakers' systems developed between 1820 and 1840 [5]. There are several techniques for implementing manual grading systems in practice. Taylor and Shoben [6] mentioned two techniques: the draft or multi size (nested) grade, and the track or single size grade. Schofield [7] identified three basic types of grading technique: shifting, proportional grading and edge changes.

METHODOLOGY

Grading has long remained a neglected area of research in the clothing industry and the classical size charts used by the industry have evolved over the years by a trial and error method [8]. Today, even with automated computer-based grading techniques, grading still requires a skilled person with an extensive knowledge of garment patterns and an understanding of the expected changes for all sizes in the range. Because we mentioned earlier that when accurate data is entered into a computer, computerized grading is the most expedient and precise method [2]. So, problem is the calculation method; if we calculate them properly and then there will be no error at all.

For experiment we choose three spec sheets of different buyer (Table 1) and combine & draw a single spec (Fig. 1 of Table 1) including all point of measures (POM) because different buyer gives different kinds of spec sheets and

so as to compare them easily. For example shoulder point can be calculated using three POMs combination; if two of “S, SD & AS” is given.

TABLE 1. Measurement points and their descriptions.

Figure	Points	Description	POM
	A	Back Neck Drop or Depth	BND
	B	Front Neck Drop or Depth	FND
	C	Neck Width or Opening	NW
	D	Across Shoulder or Shoulder to Shoulder	AS
	E	Shoulder Length	S
	F	Shoulder Drop or Slant	SD
	G	Arm Hole Straight	AHS
	H	Arm Scye Depth	ASD
	I	Half Chest	HC
	J	Half Bottom Opening	HBO
	M	High Point Shoulder	HPS
	Q	Sleeve Length	SL
	R	Sleeve Opening	SO
	S	Under Sleeve	US
T	Sleeve Width or Upper Arm	SW	

FIGURE 1. Combination of all measurement points of T-shirt.

POM	Reference spec A					Reference spec B					Reference spec C				
	S	M	L	XL	XXL	S	M	L	XL	XXL	S	M	L	XL	XXL
BND	1.5	1.5	1.5	1.5	1.5	3	3	3	3	3	1.5	1.5	1.5	1.5	1.5
FND	8	8.5	9	9.5	10	7	7.5	8	8.5	9	10.2	10.4	10.6	10.8	11
NW	16	17	18	19	20	17	17.5	18	18.5	19	18.2	18.6	19	19.6	20.2
AS	-	-	-	-	-	35	36.5	38	39.5	41	45.3	46.5	47.7	49.5	51.3
S	15	16	17	18	19	-	-	-	-	-	14.5	14.9	15.3	15.9	16.5
SD	5	5	5	5	5	2.4	2.5	2.6	2.7	2.8	-	-	-	-	-
AHS	24	25	26	27	28	18.5	19	19.5	20	20.5	-	-	-	-	-
ASD	-	-	-	-	-	-	-	-	-	-	27.3	27.9	28.5	29.3	30.1
HC	48	51	54	57	60	41	42.5	44	45.5	47	50.9	52.9	54.9	57.9	60.9
HBO	-	-	-	-	-	41	42.5	44	45.5	47	49.5	51.5	53.5	56.5	59.5
HPS	70	72	74	76	78	57	59	61	63	65	70.9	72.6	74.3	76	77.7
SL	21	22	23	24	25	17	17.5	18	18.5	19	20.6	21.3	22	22.7	23.4
SO	18	19	20	21	22	15.5	16	16.5	17	17.5	17.8	18.4	19	20	21
US	14	14.5	15	15.5	16	-	-	-	-	-	7.6	8	8.4	8.8	9.2
SW	-	-	-	-	-	17.5	18	18.5	19	19.5	19.3	20	20.7	21.9	23.1

The edge changes grading forms the foundation of current computer aided grading methods [7]. Traditional incremental grading is based on a Cartesian graph shown in Fig. 2(b), which has a horizontal axis (x) and a vertical axis (y) that intersects at right angles and divides an area in four quadrants. Using a Cartesian graph, patterns are moved left or right on the x-axis and up or down on the y-axis, as dimensional changes occur to create new sizes [4].

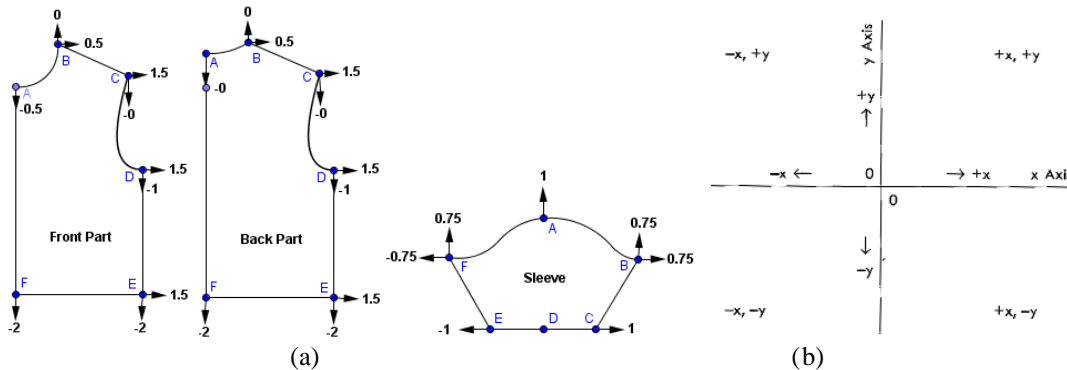


FIGURE 2. (a) Cardinal points and Cartesian coordinate values of T-shirt spec A. and (b) Cartesian graph [4].

TABLE 2. The grade rule table for T-shirt spec A (back, front and sleeve).

Back part		Front Part		Sleeve	
L-M-S	L-XL-XXL	L-M-S	L-XL-XXL	L-M-S	L-XL-XXL
A = (0,0)	A = (0,0)	A = (0,+0.5)	A = (0,-0.5)	A = (0,-1)	A = (0,1)
B = (-0.5,0)	B = (0.5,0)	B = (-0.5,0)	B = (0.5,0)	B = (-1,-1)	B = (1,1)
C = (-1.5,0)	C = (1.5,0)	C = (-1.5,0)	C = (1.5,0)	C = (-1,0)	C = (1,0)
D = (-1.5,+1)	D = (1.5,-1)	D = (-1.5,+1)	D = (1.5,-1)	D = (0,0)	D = (0,0)
E = (-1.5,+2)	E = (1.5,-2)	E = (-1.5,+2)	E = (1.5,-2)	E = (+1,0)	E = (-1,0)
F = (0,+2)	F = (0,-2)	F = (0,+2)	F = (0,-2)	F = (+1,-1)	F = (-1,1)

Problem 1

Some measurements are over the tolerance limits during jumping of sizes from one size to other sizes.

There are basically three methods of recording the growth of the pattern. From S to XXL, XXL to S or middle size (L) to both S & XXL.

TABLE 3. Length Comparisons of spec A (Diagonal measurements).

POM	Measurement comparison	Size					Tol (±)
		S	M	L	XL	XXL	
Shoulder	Length Required	15	16	17	18	19	0.15
	S→XXL	15*	15.95	16.9	17.86	18.82	
	S←L→XXL	15.1	16.05	17*	17.96	18.92	
Armhole Straight	XXL→S	15.18	16.13	17.08	18.04	19*	0.30
	Length Required	24	25	26	27	28	
	S→XXL	24*	25	25.99	26.99	27.99	
Sleeve Armhole straight	S←L→XXL	24	25	26*	27	28	0.30
	XXL→S	24.01	25.01	26	27	28	
	Length Required	24	25	26	27	28	
Under Sleeve	S→XXL	24*	24.79	25.58	26.37	27.16	0.25
	S←L→XXL	24.42	25.21	26*	26.79	27.58	
	XXL→S	24.84	25.63	26.42	27.21	28*	
	Length Required	14	14.5	15	15.5	16	
	S→XXL	14*	14.63	15.28	15.94	16.61	
	S←L→XXL	13.75	14.37	15*	15.65	16.31	
	XXL→S	13.5	14.1	14.72	15.35	16*	

Note: * = Base size, Black = Length required, Blue = exactly same, Green = within tolerance, Red = Over tolerance limit

Solution 1

We observed that horizontal lines & vertical lines lengths are same whatever the size jumping is because they are plotted in X & Y-axis respectively. But some diagonal lines lengths are over the tolerance limit if we graded from S or XXL size. But if we graded from middle size as a base size (e.g. L Size) the diagonal measurements are usually not over the tolerance limit.

Problem 2

Measurements errors occur during grade calculation of inclined lines in traditional XY-point wise grading system.

Even if we use middle size (e.g. L size) as a base size some measurements errors occur even though they are within tolerance limit. This problem occurs due to XY grading system. As we know that X-values are plotted in horizontal direction & Y-values are plotted in vertical direction for both positive & negative values. That's why when we calculate grading increment of horizontal & vertical POMs there are no errors. But if we calculate & plot the grading increment of diagonal lines we must use Pythagoras Law. But in factory they usually do not know the

law & they do not use the law even if they know the law. So if we use the law; then it is not a matter of fact; that which size we take as a base size.

TABLE 4. Length Comparison of graded pattern (Base size = L) (Spec A).

Point of Measure (POM)	Measurement comparison	Size					Tol (±)
		S	M	L	XL	XXL	
Shoulder Length	Length required	15	16	17	18	19	0.15
	Length acquired	15.1	16.05	17*	17.96	18.92	
Armhole Straight	Length required	24	25	26	27	28	0.3
	Length acquired	24	25	26*	27	28	
Sleeve Armhole Straight	Length required	24	25	26	27	28	0.3
	Length acquired	24.42	25.21	26*	26.79	27.58	
Under Sleeve	Length required	14	14.5	15	15.5	16	0.25
	Length acquired	13.75	14.37	15*	15.65	16.31	

Solution 2 (Body part)

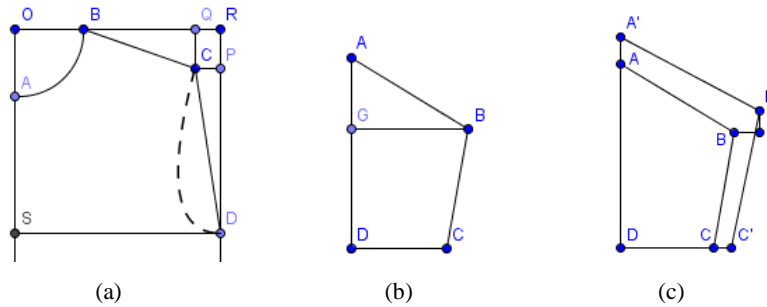


FIGURE 3. (a) Body pattern of t-shirt; (b) & (c) Sleeve pattern.

From ΔBQC (Fig. 3A), we can write according to Pythagoras law, $BQ^2 + QC^2 = BC^2$
 For L size, $BQ_L = \sqrt{17^2 - 5^2} = 16.2480768$ and for XL size, $BQ_{XL} = \sqrt{18^2 - 5^2} = 17.2916165$
 So, X-axis value of Shoulder point C = $(17.2916165 - 16.2480768) = 1.04 + 0.5$ (change in B point) = 1.54
 And, Y-axis value of Shoulder point C = 0 (due to no change in Shoulder drop)
 According to traditional calculation, C = (1.5, 0) which should be replaced by (1.54, 0)
 From (Fig. 3A), $OR = SD = \frac{1}{4}$ Chest; $QC = RP =$ Shoulder Drop;
 $\therefore CP_L = QR_L = OR_L - OB_L - BQ_L = (\frac{1}{4} \text{ Chest})_L - (\frac{1}{2} \text{ Neck width})_L - BQ_L$
 $\therefore CP_L = 27 - 9 - 16.2480768 = 1.7519232$
 And $CP_{XL} = QR_{XL} = OR_{XL} - OB_{XL} - BQ_{XL} = (\frac{1}{4} \text{ Chest})_{XL} - (\frac{1}{2} \text{ Neck width})_{XL} - BQ_{XL}$
 $\therefore CP_L = 29.5 - 9.5 - 17.2916165 = 2.7083835$

From ΔCPD (Fig. 3A), we can write according to Pythagoras law, $PD^2 + CP^2 = CD^2$
 For L size, $PD_L = \sqrt{26^2 - 1.75^2} = 25.92$ and for XL size, $PD_{XL} = \sqrt{27^2 - 2.7^2} = 26.865$
 So, X-axis value of Armpit point D = 1.5 (due to change in $\frac{1}{4}$ Chest)
 And, Y-axis value of Armpit point D = $26.865 - 25.92 = 0.95$
 According to traditional calculation, D = (1.5, -1) which should be replaced by (1.5, -0.95)
 After grading and measuring all values we saw that there is no deviation from the original measurements at all.

Solution 2 (Sleeve)

2.2.3.1 According to spec A (Method 1):

After drawing the pattern we manually measure the length $AG_L = 8.69$ & $GB_L = 24.5$ (Fig. 3B)

For grading of sleeve length, we distribute total amount of grading increment (1 cm) equal in both side of zero point G. So, $AG_{XL} = (8.69+0.5) = 9.19$

From ΔAGB (Fig. 3B), we can write according to Pythagoras law, $AG^2 + GB^2 = AB^2$

For XL size, $GB_{XL} = \sqrt{27^2 - 9.19^2} = 25.388$

So, X-axis value of point B = $(25.388 - 24.5) = 0.89$ and Y-axis value of point B = 0

So, value of point A = (0, 0.5); B = (0.89, 0); C = (1, -0.5); D = (0, -0.5) and G = (0, 0)

TABLE 5. After grading with the above values we found the following measurements (Base size = L) (Spec A).

Point of Measure (POM)	Measurement comparison	Size					Tol (\pm)
		S	M	L	XL	XXL	
Sleeve Armhole Straight	Length required	24	25	26	27	28	0.3
	Length acquired	23.99	24.99	26*	27.01	28.01	
Under Sleeve	Length required	14	14.5	15	15.5	16	0.25
	Length acquired	14.12	14.56	15*	15.45	15.9	

From the table 5 we saw that, all the measurements of sleeve are within tolerance limit but not 100% correct. So to get 100% correct value we can use method 2.

2.2.3.2 According to spec A (method 2)

From point D (Fig. 3C), if we draw pattern of sleeve as AD & A'D = Sleeve length; DC & DC' = Sleeve opening; AB & A'B' = Armhole straight and CB & C'B' = Under sleeve of L & XL size respectively, then we can calculate the value of A = (0,1); D = (0,0); C = (1,0) as like traditional method. But for calculating the increment of B point, we extend the line from B & B' points (as Fig. 3C) that intersect at point P. Now we can manually measure the values of BP & B'P which are actually the X-axis & Y-axis values of B point respectively. So, B = (0.91, 0.55). After grading and measuring all values we saw that there is no deviation from the original measurements at all.

Problem 3

Some inclined or diagonal POMs (point of measures) create measurement errors in traditional XY point wise grading system.

Some pattern points can be calculated using different POMs combination; like Shoulder point can calculate if any two of "S, SD & AS" is given (3 types are given at spec A, B & C).

TABLE 6. Shoulder length comparison of different POMs combination (without using Pythagoras).

Combination of POMs	POM Direction	Reference Spec.	Size→	S	M	L	XL	XXL	Tol (\pm)
If SD & S is given	Vertical & Diagonal	A	Required	15	16	17	18	19	0.15
			Acquired	15.1	16.05	17*	17.96	18.92	
If AS & S is Given	Horizontal & Diagonal	C	Required	14.50	14.90	15.30	15.90	16.50	0.15
			Acquired	14.55	14.93	15.30*	15.86	16.43	
If AS & SD is Given	Horizontal & Vertical	B	Required	7.87	9.1	10.33	11.57	12.81	0.15
			Acquired	7.87	9.1	10.33	11.57	12.81	
N.B. The value of row 3 is not given to spec B, because according to that spec sheet, we need AS & SD to be correct. So compare them to get shoulder.									
If AS & SD is Given	Horizontal	B	Required AS	35	36.5	38	39.5	41	0.2
			Acquired AS	35	36.5	38*	39.5	41	
	Vertical	B	Required SD	2.4	2.5	2.6	2.7	2.8	0
			Acquired SD	2.4	2.5	2.6*	2.7	2.8	

Solution 3

So we can calculate the shoulder point grading without any error if we use horizontal & vertical POM combination which can be plotted in X & Y direction respectively; and so that we don't have to calculate grading using Pythagoras law.

SUGGESTIONS

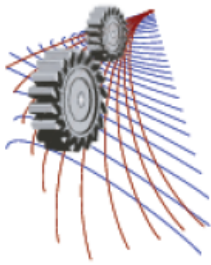
- Always grade from middle size to all sizes to reduce measurement errors.
- Should use Pythagoras Law for inclined line grading.
- Should use horizontal & vertical POMs instead of diagonal or inclined POMs to get the desired shape of pattern wherever possible.

CONCLUSION

Grading is the process used by clothing manufacturers to produce patterns for a garment in a range of sizes for ready-to-wear clothing. Though grading calculating is very complex, but if we successfully grade the pattern; it will not only reduce sample approval time but also helps us to create products that fits well to the body.

REFERENCES

1. Bye, E.K., A Visual Sensory Evaluation of Two Pattern Grading Methods, Unpublished Doctoral Dissertation, University of Minnesota, St Paul, 1990, pp. 10.
2. Mullet, K., Moore, C., & Young, M., Concepts of pattern grading: Techniques for manual and computer grading. New York, NY: Fairchild, 2009.
3. Price, J., & Zamkoff, B., Grading techniques for fashion design. New York, NY: Fairchild Publications, 1996.
4. Sharp, J. R., & Elsasser, V. H., Introduction to AccuMark, pattern design, and product data management. New York, NY: Fairchild Publications, 2007.
5. Kidwell, C., Cutting a Fashionable Fit: Dressmakers' Drafting Systems in the United States, Smithsonian Institution Press, Washington, DC, 1979.
6. Taylor, J. P. and Shoben, M.M., Grading for the fashion industry, the theory and practice. England: Stanley Thomes (Publishers) Ltd., 1990.
7. Schofield, N.A., Pattern grading. In: Ashdown, S.P. Sizing in Clothing. Cambridge (England): Woodhead Publishing Ltd. , pp. 152-201, (2007).
8. Kunick, P., Sizing, Pattern Construction and Grading for Women's and Children's Garments, London: Philip Kunick, Ltd, (1967).



Microstructure and Impedance Spectroscopy of Li Substituted Ni-Mn Ceramics

A.A. Momin^{2,a)} and A.K.M. Akther Hossain¹

¹ Department of Physics, Bangladesh University of Engineering and Technology, Dhaka-1000, Bangladesh

² Department of Physics, Jagannath University, Dhaka-1100, Bangladesh.

^{a)}Corresponding author: Abdulla.al.momin@gmail.com

Abstract. The influences of Li substitution on the microstructure and impedance spectroscopy of $\text{Li}_x\text{Ni}_{0.2}\text{Mn}_{0.8-2x}\text{Fe}_{2+x}\text{O}_4$ have been investigated by scanning electron microscope and impedance analyzer. The surface morphology indicates that average grain size decreases due to Li substitution. The complex impedance analysis has been used to separate the grain and grain boundary resistance and it is found that the real and imaginary part of the impedance decrease with increasing frequency and both are found changing significantly with Li concentration. The complex-plane impedance spectra indicate that the material can be represented by two semicircular arcs (its tendency) which corresponds to the bulk and the grain boundary resistance at high and low frequencies respectively up to $x = 0.1$. Modulus studies also carried out to investigate the effect of grain on the conduction mechanism. From the frequency dependent real and imaginary part of complex modulus show composition dependent space charge release and short range to long range hopping transition. A possible correlation between the observed microstructure and impedance property is discussed on the basis of existing theories.

INTRODUCTION

Ferrites are widely used in many electronic devices because of its high resistivity, high permeability and low losses [1]. Some of the ferrites have spinel type AB_2O_4 crystal structure, where A and B represent tetrahedral and octahedral-sites, respectively. The magnetic and electric properties of a spinel are sensitive to the types of cations and their distribution amongst the two interstitial sites of spinel lattice [2]. Apart from the magnetic properties, studies of electric and dielectric behavior are equally important from both fundamental and applied point of view. The dielectric properties of ferrites depend upon several factors including the method of preparation, chemical composition and grain structure or size [3]. Lithium based ferrites have become important materials for microwave applications such as in circulators, isolators, phase shifters, etc. due to their high resistivity, low dielectric losses, high Curie temperature, squareness of hysteresis loop and low costs [4]. Electrical conductivity is one of the important properties of ferrites, which gives valuable information about conduction mechanism. It depends on the method of preparation, sintering time, types of additives and temperature [5, 6]. It has been reported earlier that ferrites sintered in air are highly characterized by conducting grains separated by poorly conducting grain boundaries [7]. To study the microstructural and electrical properties of polycrystalline oxides complex impedance spectroscopy (CIS) is a useful, well-designed and nondestructive method [8]. This can correlate the structural and electrical characteristics of polycrystalline oxides in a wide range of frequencies and temperatures. CIS also describes the electrical processes occurring in a system by applying an ac signal as input perturbation, which helps to separate the contribution of electroactive regions (such as grain boundary and bulk effects). The output response, when plotted in a complex plane plot, appears in the form of succession of semicircles representing electrical phenomena due to the bulk material, grain boundary effect and interfacial polarization [9].

Many researchers have studied the dielectric properties of Li substituted spinel ferrites such as Li–Ni–Cu [10], Li–Ni–Zn [11], Li–Ni–Mg [12], Li–Cr [13, 14] and Li–Ga [15, 16]. However, no other author had investigated Li substituted Mn–Ni ferrites, therefore, the aim of the present work is to study the effect of adding the Li ions to the nanosamples on their dielectric behavior too.

EXPREIMENTAL

The composites $\text{Li}_x\text{Mn}_{0.8-2x}\text{Ni}_{0.2}\text{Fe}_{2+x}\text{O}_4$ ($x = 0.00, 0.10, 0.20$ and 0.30) were prepared by auto combustion technique. Stoichiometric amounts of LiNO_3 , $\text{MnCl}_2 \cdot 4\text{H}_2\text{O}$, $\text{NiNO}_3 \cdot 6\text{H}_2\text{O}$, $\text{Fe}(\text{NO}_3)_3 \cdot 9\text{H}_2\text{O}$, was dissolved in ethanol. Then the solution was heated at 70°C to transform into gel, the dried gel burnt out to form fluffy loose powders. The powders were calcined at 750°C for 5 h. Following the addition of polyvinyl alcohol (PVA), the milled powders were granulated and pressed into pellets shaped which were finally sintered at 1300°C for 1 h in air. The temperature ramp for sintering was $10^\circ\text{C}/\text{min}$ for heating, and $5^\circ\text{C}/\text{min}$ for cooling. After sintering microstructure and surface morphology of the samples have examined by scanning electron microscope (SEM). Frequency dependent dielectric measurements of the present samples were evaluated with Wayne kerr impedance analyzer (model no 6500B). For dielectric measurements sintered pellets were polished with fine grained sandpaper and coated with high purity silver paste on adjacent faces as electrodes and then dried for 2 h at 150°C to make the parallel plate capacitor geometry. The real (Z') and imaginary (Z'') parts of impedance were calculated using the relation: $Z' = Z \cos\theta$ and $Z'' = Z \sin\theta$. The real (M') and imaginary (M'') parts of complex electric modulus in terms of real (ϵ') and imaginary (ϵ'') parts of dielectric constant were calculated using the relation: $M' = \epsilon' / (\epsilon'^2 + \epsilon''^2)$ and $M'' = \epsilon'' / (\epsilon'^2 + \epsilon''^2)$. The drive voltage of the Impedance Analyzer used in the present work is 0.5 V.

RESULTS AND DISCUSSION

Microstructure (surface morphology)

Figure 1 represents the SEM images of pure and Li substituted ferrite samples (typical) sintered at 1300°C for 1 h. The average grain sizes of the samples are determined from the micrographs by linear intercept technique [17]. From the micrograph it is clear that the average grain size (grain diameter, D_m) noticeably dependent on Li substitution. The D_m gradually decreases with increasing Li content. This is perhaps due to the modified chemical properties as a result of Li substitution. Depending on Li substitution, brand new chemical compositions are produced. The physical and chemical properties of each substituted composition are completely different. The change in grain size as well as grain boundary significantly contributed to impedance and electric modulus spectroscopy.

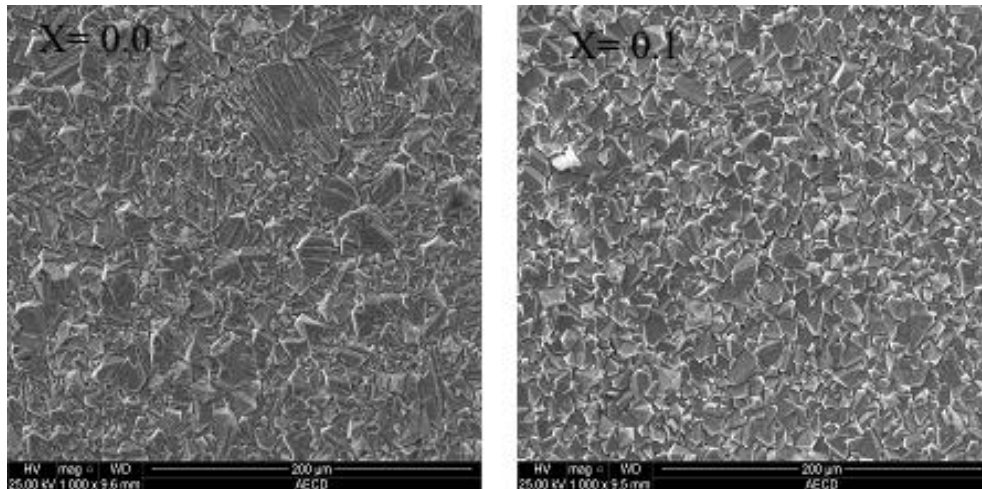


FIGURE 1. SEM micrographs for various $\text{Li}_x\text{Mn}_{0.8-2x}\text{Ni}_{0.2}\text{Fe}_{2+x}\text{O}_4$ sintered at 1300°C .

Modulus study

The variation of real part of electric modulus (M') as a function of frequency for various $\text{Li}_x\text{Mn}_{0.8-2x}\text{Ni}_{0.2}\text{Fe}_{2+x}\text{O}_4$ is given in Fig. 2(a). The value of M' is very low (approaching zero) in the low frequency region and it increases with the increasing frequency. This is probably due to the large value of capacitance at low frequencies. This continuous dispersion on increasing frequency may be contributed to the conduction phenomena due to short range mobility of charge carriers. It is possibly related to the lack of restoring force governing the mobility of the charge carriers under the action of an induced electric field. It is also found that the dispersion region shifts towards higher frequency side which suggests the long-range mobility of charge carriers [18]. The plateau region suggests about the frequency invariant (dc conductivity) electrical properties of the materials.

Figure 2(b) shows the imaginary parts of electric modulus (M'') as a function of frequency at various compositions. The low value of M'' observed at lower frequencies may occur due to the absence of electrode polarization phenomena. M'' possessed a low value at low frequencies for all compositions. It exhibits peak in the high frequency side. This pattern provides wider information relating charge transport processes such as mechanism of electrical transport, conductivity relaxation, and ion dynamics as a function of frequency. The frequency region below the peak maximum determines the range in which charge carriers are mobile over long distances. At the frequency above peak maximum (high-frequency), the carriers are confined to potential wells, being mobile over short distances. Their region where the peak occurs is indicative of the transition from long-range to short-range mobility with increase in frequency. This type of behavior of the modulus spectrum is suggestive of a composition-dependent hopping type mechanism for electrical conduction (charge transport) in the system. The observed asymmetry in peak broadening indicates the spread of relaxation time with different time constant which supports the non-Debye type of relaxation in the materials. It is also observed that the peaks are shifting towards lower frequency side with the increase in Li content. It indicates Li substituting activated behavior of relaxation time.

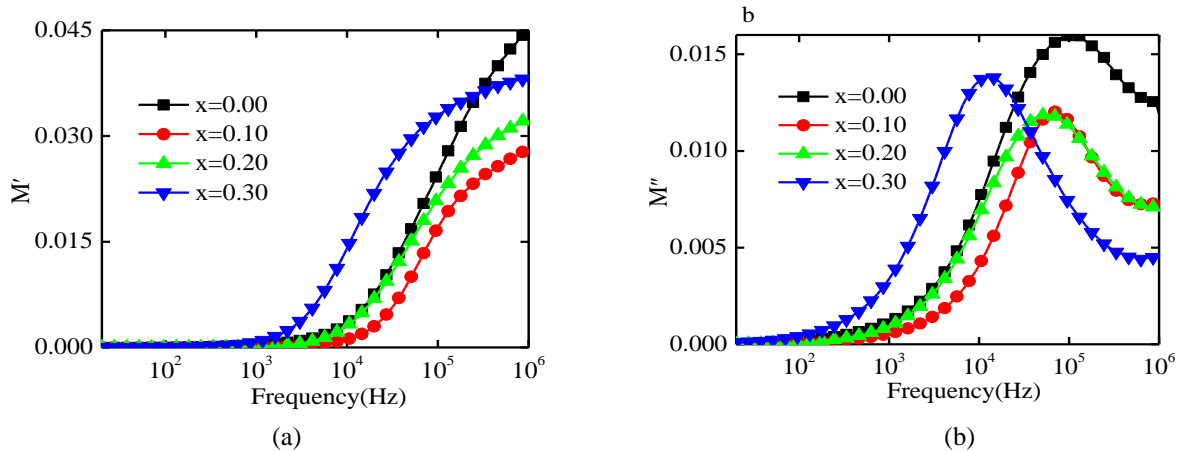


FIGURE 2. Frequency dependence of (a) real part of electric modulus (M') and (b) imaginary parts of electric modulus (M'') of various $\text{Li}_x\text{Mn}_{0.8-2x}\text{Ni}_{0.2}\text{Fe}_{2+x}\text{O}_4$ sintered at 1300°C .

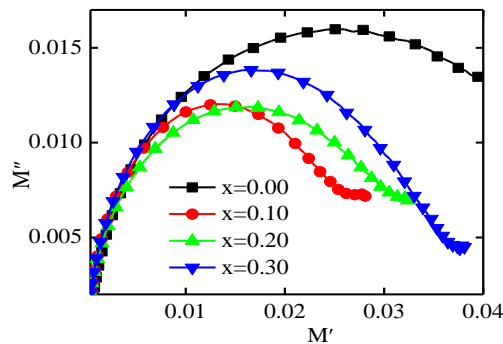


FIGURE 3. Frequency dependence M'' - M' of various $\text{Li}_x\text{Mn}_{0.8-2x}\text{Ni}_{0.2}\text{Fe}_{2+x}\text{O}_4$ sintered at 1300°C .

The modulus plots of M'' versus M' for various compositions shown in Fig. 3. The large semicircle was believed to be induced by the grain effect, due to the smaller capacitance value in the electric modulus spectra, while the small semicircle might be attributed to the grain boundary effect. For clarity, the value of grain capacitance (C_g) can be extracted from the semicircular arc intercepts on the M' axis in Fig. 3., the values of C_g and f_{max} were used to calculate grain resistance. The form of two deformed semi-circles (or their tendency) with their centers lying below the real axis. This indicates spread of relaxation with different (mean) time constant and hence again supports the non-Debye type of relaxation in the materials. In the complex modulus plots two semicircular arcs or their tendency suggest the presence of both the grain and grain boundary contributions in these ferrites.

Impedance study

Impedance spectroscopy is an important method to study the electrical properties of ferrites as the impedance of grains can be separated from the other impedance sources, such as impedance of electrodes and grain boundaries. The impedance measurement gives us information about the resistive (real part) and reactive (imaginary part) components of a material. Complex modulus analysis is suitable when materials have nearly similar resistance but different capacitance [19].

Figure 4(a) shows the variation of real (resistive) part of impedance with frequency for various $\text{Li}_x\text{Mn}_{0.8-2x}\text{Ni}_{0.2}\text{Fe}_{2+x}\text{O}_4$ at room temperature. It is observed that the magnitude of Z' gradually decreases with increasing frequency up to a certain frequency (0.1 MHz). The decrease in Z' indicates that the conduction is increasing with frequency and at a frequency (≥ 0.1 MHz) it becomes almost frequency independent. At lower frequencies the higher values of Z' means the polarization is larger. At higher frequencies the merger of Z' indicates possible release of space charge polarization at the boundaries of homogeneous phases in the samples under the applied external field [20].

Figure 4(b) shows the variation of imaginary part of impedance with frequency. Two peak appeared in Z'' at low and intermediate frequency for $x = 0.0$ and $x = 0.1$. For others sample single pick is observed. It may be due to not much difference of relaxation frequency between grain and grain boundary. This peak proportionately shifted to lower frequency with the increase of Z'' in the low frequency region. The Z'' peak shifts to lower frequencies with increasing Li content, which indicates the presence of composition dependent electrical relaxation phenomenon in the system. The asymmetric broadening of the peaks suggested the presence of electrical processes in the material with a spread of relaxation time [21]. The relaxation phenomenon in the material may be due to the presence of immobile species/electron at low frequencies and in the intermediate frequency range relaxation phenomenon is due to the grain contribution. There was a clear dispersion of the resultant curves in the low and intermediate frequency region at various Li contents and appears to be merging at higher frequency irrespective of composition. This behavior may be because of the presence of the space charge polarization effect at lower frequencies, which is eliminated at higher frequencies [22].

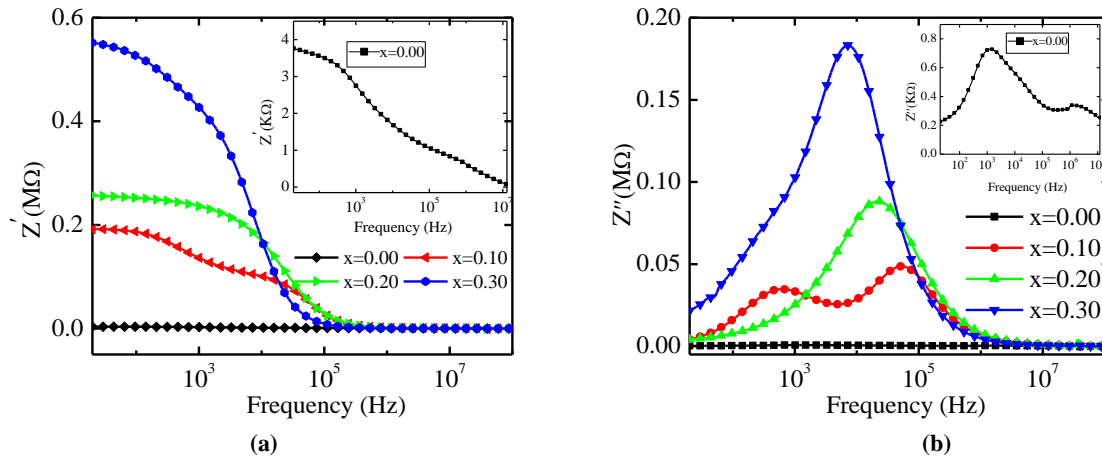


FIGURE 4. Frequency dependence of (a) real part of impedance (Z') and (b) imaginary part of impedance (Z'') of various $\text{Li}_x\text{Mn}_{0.8-2x}\text{Ni}_{0.2}\text{Fe}_{2+x}\text{O}_4$ sintered at 1300°C.

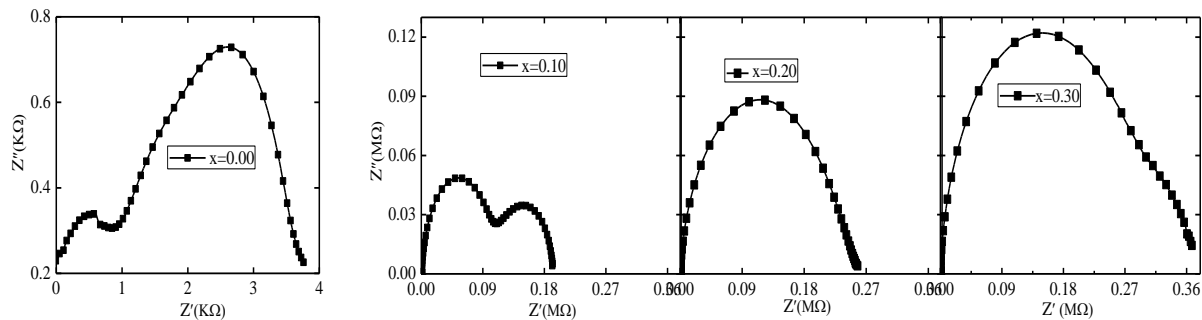


FIGURE 5. Shows Cole–Cole plot for all Li ferrite compositions.

Figure 5 shows the complex impedance or Cole–Cole plot for all the compositions as a function of frequency at room temperature. Two semicircles are found up to $x = 0.1$, indicating a Cole–Cole type of distribution, while only one semicircle has been found for higher compositions ($x \geq 0.2$). Due to the space charge polarization and orientation polarization in the ferrite materials, the two semicircles are observed as shown in Fig. 5. The first semicircle at low frequency represents the resistance of grain boundary. The second one obtained at high-frequency domain corresponds to the resistance of grain or bulk properties. The plot obtained shows only one semi-circular arc ($x \geq 0.2$) corresponding to the conduction due to the grain boundary volume in the low frequency region, which suggests that conduction mechanism takes place predominantly through the grain boundary volume [23].

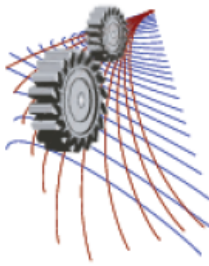
CONCLUSIONS

The $\text{Li}_x\text{Mn}_{0.8-2x}\text{Ni}_{0.2}\text{Fe}_2+x\text{O}_4$ were prepared by auto combustion technique at high temperature. The real and imaginary parts of the impedance have been found to decrease with increasing frequency. The impedance and electric modulus properties of the materials have been investigated with the help of complex impedance spectroscopy technique. Single arc with double semicircles (or tendency) obtained at room temperature corresponding to a certain LiNiMn composition in both the complex impedance and modulus plots suggests the single phase character of the materials. The impedance analysis has indicated the presence of mainly bulk (grain) and interface (grain boundary) contributions in the materials which is found to increase with the increase in Li content. Also, the impedance as well as modulus analysis has confirmed the presence of non-Debye type of relaxation in Li substituted NiMn ferrites.

REFERENCES

1. J.M. Hasting, L.M. Corliss, An Antiferromagnetic Transition in Zinc Ferrite, *Phys. Rev.* **102**, 1460-1463 (1956).
2. B. D. Cullity, Introduction to Magnetic Materials, Addison-Wesley, New York, 1972.
3. S.A Mazen., S.F. Mansour, E. Dhahri, H.M. Zaki, T.A. Elmosalami, The infrared absorption and dielectric properties of Li–Ga ferrite, *J. Alloy. Compd.* **470**, 294–300 (2009).
4. S.T. Assar, H.F. Abosheishasha, M.K. El Nimr, Study of the dielectric behavior of Co–Ni–Li nanoferrites, *J. Magn. Mater.* **350**, 12-18 (2014).
5. A.M. Shaikh, C.M. Kanamadi, B.K. Chougule, Electrical resistivity and thermoelectric power studies on Zn-substituted Li–Mg ferrites, *Mater. Chem. Phys.* **93**, 548–551 (2005).
6. N. Sivakumar, A. Narayanasamy, J.-M. Greneche, R. Murugaraj, Y.S. Lee, Electrical and magnetic behaviour of nanostructured MgFe_2O_4 spinel ferrite, *J. Alloy. Compd.* **504**, 395–402 (2010).
7. A. Dais, R. L. Moreira, Chemical, mechanical and dielectric properties after sintering of hydrothermal nickel–zinc ferrites, *Materials Letters*, **39**, 69–76 (1999).
8. J. R. Wiley, Macdonald, Impedance Spectroscopy: Emphasizing Solid State Materials and Systems, New York, 1987, ch. 2 and 4.

9. D. Dhak, P. Dhak and P. Pramanik, Influence of substitution on dielectric and impedance spectroscopy of $\text{Sr}_{1-x}\text{Bi}_{2+y}\text{Nb}_2\text{O}_9$ ferroelectric ceramics synthesized by chemical route, *Applied Surface Science*, **254**, 3078-3092 (2008).
10. N. Singh, A. Agarwal, S. Sanghi, P. Singh, Synthesis, microstructure, dielectric and magnetic properties of Cu substituted Ni–Li ferrites, *J. Magn. Magn. Mater.* **323**, 486–492 (2011).
11. S.A. Saafan, S.T Assar, Dielectric behavior of nano-structured and bulk Li Ni Zn ferrite samples, *J. Magn. Magn. Mater.* **324**, 2989–3001 (2012).
12. N. Singh, A. Agarwal, S. Sanghi, P. Singh, Dielectric relaxation, conductivity behaviour and magnetic properties of Mg substituted Ni–Li ferrites, *J. Alloy. Compd.* **509**, 7543–7548 (2011).
13. P.P. Hankare, R.P. Patil, U.B. Sankpal, K.M. Garadkar, R. Sasikala, A.K. Tripathi, I. S. Mulla, Magnetic, dielectric and complex impedance spectroscopic studies of nanocrystalline Cr substituted Li-ferrite, *J. Magn. Magn. Mater.* **322**, 2629–2633 (2010).
14. Y.-P. Fu, D.-S. Hung, Y.-D. Yao, Microwave properties of chromium-substituted lithium ferrite, *Ceram. Int.* **35**, 2179–2184 (2009).
15. S.A. Mazen, S.F. Mansour, E. Dhahri, H.M. Zaki, T.A. Elmosalami, The infrared absorption and dielectric properties of Li–Ga ferrite, *J. Alloy. Compd.* **470**, 294–300 (2009).
16. S.A. Mazen, S.F. Mansour, T.A. Elmosalami, H.M. Zaki, The conduction mechanism of Li–Ga ferrite, *J. Alloy. Compd.* **472**, 307–313 (2009).
17. M. I. Mendelson, Average Grain Size in Polycrystalline Ceramics, *J. Am. Ceram. Soc.* **52**, 443 (1967).
18. P. Victor, S. Bhattacharyya, S.B. Krupanidhi, Dielectric relaxation in laser ablated polycrystalline ZrTiO_4 thin films *J. Appl. Phys.* **94**, 5135–5142 (2003).
19. J. Suchanicz, The low-frequency dielectric relaxation $\text{Na}_{0.5}\text{Bi}_{0.5}\text{TiO}_3$ ceramics, *Mat. Sci. Eng. B-Solid.* **55**, 114-118 (1998).
20. Md. D. Rahaman, S.H. Setu, S.K. Saha, A.K.M. Akther Hossain, Synthesis and characterization of $\text{La}_{0.75}\text{Ca}_{0.15}\text{Sr}_{0.05}\text{Ba}_{0.05}\text{MnO}_3\text{--Ni}_{0.9}\text{Zn}_{0.1}\text{Fe}_2\text{O}_4$ multiferroic composites, *J. Magn. Magn. Mater.* **385**, 418-427 (2015).
21. A. K. Jonscher, “The 'universal' dielectric response,” *Nature*, **267**, 673- 679 (1977).
22. S. Sen, R. N. P. Chowdhary and A. Tarafdar, P. Pramanik, Impedance spectroscopy study of strontium modified lead zirconate titanate ceramics, *J. Appl. Phys.* **99**, 124114(1-8) (2006).
23. K.M. Batoor, M.S. Ansari, Low temperature-fired Ni-Cu-Zn ferrite nanoparticles through auto-combustion method for multilayer chip inductor applications, *Nanoscale Res. Lett.* **7**, 112(1-14) (2012).



Measurement of Calorific Values of Tannery Wastages Containing Low and High Chromium and Raw Fleshy Wastages Using Bomb Calorimeter

Md. Naim Jahangir^{1, a)}, Ayesha Kabir Mila¹, Siduzzaman Khan¹, Mohammad Arif Hasan Mamun¹

¹Department of Mechanical Engineering, Bangladesh University of Engineering and Technology, Dhaka 1000, Bangladesh

^{a)} Corresponding author: naim.buet09@gmail.com

Abstract. Industrial wastages have become a major concern for environment considering their slower biodegradability. Tannery wastages with fleshy and harmful low and high chrome wastages are creating imbalance in the environment. Objective of this work is to reuse the wastages those are considered useless. Biomass production and heat generation by burning tannery wastages in an idealized way may serve the purpose of reuse of wastages. Constant-volume type Bomb Calorimeter was used to measure the calorific values of those wastages. Raw fleshy waste and shaving wastages with low and high chromium are the main wastages of tannery industries. As moisture increases, the calorific value of a material decreases due to the heat of vaporization of solid waste [1]. LHV/HHV ratio goes from 0.29 (63.4% of moisture) to 0.44 (45.3% of moisture) [2]. Here calorific values of 5 samples were measured. Calorific values of low and high chromium moisture less shaving wastages were measured 4101.93 cal/ gram and 3276.1 cal/ gram. For low chrome moisturized shaving waste, the value was measured 2537.8 cal/ gram. High chrome shaving waste was kept in the atmosphere for 10 days and its calorific value was measured 3758.1 cal/ gram. Calorific value of raw fleshy tannery waste was measured 5093.1 cal/ gram. Thus wastages that are obtained after tanning process, have reasonable calorific values which fluctuates depending on the moisture content and percentage of their constituents. Heat generated after burning those wastages can be used in heater, furnaces, to produce heat in boiler and in many industries where boiling of water is important.

INTRODUCTION

The energy crisis in the world is increasing with the passage of time and there is a continuous search for new energy sources. In the last 50 years, the ongoing crisis has hindered the path of socio-economic development of a country with the depletion of fossil fuels causing not only economical hazard but also ecological damages [3]. Renewable energy and heat generation from wastages are the more superior ways to cope up with this ongoing energy crisis. The tannery wastages containing fleshy and harmful low and high chrome wastages can be utilized as energy sources in this respect. Waste generated by the tannery industry pose a major challenge to the environment. According to conservative estimate, about 600000 tons/year of solid wastes are generated worldwide from tannery industries and 40-50% of hides are lost to the shaving and trimmings. These wastages can be used as great source of heat energy. The chemical effluents contained in the tannery wastages cause serious environmental pollution such as damage to soil and water bodies, air pollution producing intolerable odor.

If these wastages are converted to efficient energy, it can produce an environmental friendly society with lower emission of CO₂. Tannery wastages can be converted to fuel for cooking in rural areas, biogas for running heat engine, fertilizer for agricultural purpose etc. The energy recovered from the wastages after tanning process can also be directly used as a new energy source in that same industry. Conversion of waste to energy of a tannery industry, can be effective for heat generation and in small power plants.

The properties of this tannery wastages are determined in terms of physical, chemical, biological parameters etc. Calorific value is among these parameters which is very much important in its use as energy. The heating value, calorific value or energy value of a substance, is usually a fuel or food that can be used when heat released during the combustion of a specific amount of it. Calorific value is commonly determined by the use of a bomb calorimeter. The higher heating value (HHV) is defined as the quantity of heat generated by complete combustion in a bomb

calorimeter, of a mass unit sample in an oxygen atmosphere assuming that both the water contained in the sample and that generated from the combined hydrogen remain in liquid form. If it is assumed that the water in the products remain in the form of steam, the lower heating value (LHV) can be calculated [4]. From calorific value, we can get the idea of how these solid wastages can be used in various industrial process to avoid any unusual mishap. First of all, it is important to determine the rank of solid tannery wastes. We have determined the calorific value of 5 samples of tannery wastage. Industrial wastes are usually generated from different chemical processes. As a result the amount and toxicity of waste released from industrial activities varies with the industrial processes. So to convert tannery wastes into beneficial energy form, calorific value determination is an important physical parameter that varies with chemical composition.

NOMENCLATURE

a	time of firing
b	time when temperature reaches 60% of the total rise
c	time at beginning of period in which the rate of temperature change becomes constant
t_a	temperature at time of firing
t_c	temperature at time C
R_1	Rate at which temperature was rising during 5 minutes before firing
R_2	rate of change of temperature after 5 min period after temperature become maximum
t_i	temperature at time $t = 0$
t_e	temperature after 5 min period after temperature become maximum
w	energy equivalent of calorimeter temperature (2426 calories/ °C at standard condition)
m	mass of sample
t	net corrected temperature
e	correction of heat of combustion of fuse wire
H_g	gross heat of combustion

EXPERIMENTAL PROCEDURE

Calorific value has been determined for 5 samples. These samples are mainly tannery wastages collected from tannery industry. Those are collected during various cycles of operations. Each of the samples were kept for at least 10 days before calorific value measurement test was performed. The first sample was shaving wastage with lower chromium content. This was found by shaving the raw fleshy tannery wastage into small pieces. The sample is weighed and dried in the oven at 100°C for 5 hours to remove the moisture content. The 2nd sample is shaving wastage with higher percentage of chromium content.

It was also made moisturize less by drying in the oven at 100°C for about 5 hours. Presence of higher Cr content prevents its use as a fertilizer and conventional handling of tannery waste involves landfills and incineration [5]. The first and third samples were moisturized high and low Cr shaving wastage and the last sample is raw fleshy wastage. These 2 samples are kept normal, without heating. All these samples are properly cut into small pieces to perform operation and those were weighed separately.

EXPERIMENTAL SETUP

The calorific value for these samples were determined using Bomb calorimeter, equipped with a digital thermometer, with a resolution of 0.0001c. Basically there are two main ways to determine calorific value of tannery waste; those are prediction and measurement [6, 7]. Prediction is cheap and convenient but measurement is considered as primary and solid method to ensure the accuracy of heating value [8]. A large scale calorimeter affords greater credibility because kilogram-size samples of MSW should represent the properties of the heterogeneous bulk material more accurately and reliably than the highly processed gram-size samples currently used in bomb calorimetric

determinations. But we used bomb calorimeter because of its quantitative results. One of the most important tests in the evaluation of materials which are burned as fuels is the determination of the heat of combustion, or calorific value. In this experiment, Oxygen Bomb Calorimeter has been adopted for determination of calorific value of tannery wastages. It is a special type of calorimeter which is equipped with a digital thermometer. It is equipped with bomb calorimeter to improve the precision and simplify the procedure for measuring and recording the net temp rise, calculate and report the heat of combustion. The electrical connection is provided from an ignition unit called fuse wire which provides current for firing the oxygen bomb. The fuse wire length was 10 cm. The calorimeter requires no permanent connections. It can be setup and ready to operate in a few minutes, and, when not in use, it is easily disassembled and stored on a shelf. After attaching the fuse wire with the bomb calorimeter, connection was checked. For that, multi meter was used. 1ml water was added in the bomb calorimeter. 1gram wastage was taken in the crucible. Oxygen was flushed in the bomb calorimeter at 300 psi. For safety purpose, there are safety valves that open up when pressure inside increases a lot. Bomb calorimeter was placed in a water bucket. The bucket was kept in the refrigerator so that its temperature remain lower or equal of the calorimeter temperature. A stirrer was rotated with the help of a motor. It was used to ensure proper distribution of temperature.

After the last reading, motor was stopped, electrical connections were switched off, calorimeter bucket is uncovered, knurled knob was opened to release the gas pressure. All unburned pieces of fuse wire were measured and length of burned wire was measured by subtracting the unburned length from the original wire. Here total length used was about 10 cm during experiment. Then Correction in calories for heat of combustion for fuse wire was measured as 2.3 cal/cm. Energy equivalent of calorimeter temp was determined under standardization which was 2426 calories/°C.

CALORIMETRIC MEASUREMENT

Calorific value of 5 different samples were measured considering the effect of both moisture and chromium content. Rate at which temperature was rising during 5 minutes before firing (R_1) and rate at which temperature was changing after 5 min period after temperature reached to maximum were measured using Eq. [1] and Eq. [2].

$$R_1 = (t_a - t_i) / 5 \quad (1)$$

$$R_2 = (t_c - t_b) / 5 \quad (2)$$

Net corrected temperature (t) and correction factor (e) for heat of combustion of fuse wire were measured using Eq. [3] and Eq. [4]

$$t = t_c - t_a - R_1 * (b - a) - R_2 * (c - b) \quad (3)$$

$$e = c * l \quad (4)$$

Finally gross heat of combustion (H_g) was measured where $H_g = (t * w - e) / m$ (5)

RESULT & DISCUSSION

Heat of combustion of an organic compound is nearly equal to the combustion of the elements in it, multiplied by their percentage content in the compound. The total heat produced by an element is the same whether it passes through one or more stages [9]. Measurement of calorific values are usually done in single stage.

TABLE- 1 shows temperature properties of the 5 samples. Increase of temperatures a, b & c and time required to reach the temperatures t_a , t_b , t_c are important parameters as they are used to calculate net corrected temperature using Eq. (3). Table- 2 shows net corrected temperature increases about 1-2.1°C which increases gross calorific values. Correction of heat of combustion of fuse wire is done by subtracting the unburnt fuse wire from the initial size of wire taken. The unburnt portion is due to connecting part with the bomb calorimeter and with the increase of it, gross calorific value decreases according to equation (g). FIGURE-2 shows the obtained calorific values of 5 samples.

The calorific value of raw fleshy tannery wastage is 5093.1 cal/gm. This is quite a moderate heating value whereas the calorific value of coal by proximate analysis is near about 4000-6000 cal/gm. Calorific value of shaving wastage decreases as moisture content increases due to the heat of vaporization of solid waste [1]. Calorific value of shaving wastages with low chromium content with moisture is 2357.8 cal/gm. For moisture less same sample the value is 4105.3 cal/gm. So calorific value of drier sample is much higher. The fact is totally different for high chrome shaving wastages. The calorific value high chrome shaving wastage with moisture content is 3758.09 cal/gm whereas for moisture less sample, calorific value is 3389.28 cal/gm. Thus calorific value is much for the moisturized sample with

high percentage of chromium. Thus it is clear that LHV/HHV decreases with moisture contents. This is required for the need of energy to evaporate water [2]. FIGURE-1 shows the relationship between temperature and time for 5 different samples. From Eq. (5) it is obvious that gross heat of combustion increases if net corrected temperature increases. Temperature after 60% increase of initial has a mix effect on gross calorific value. It depends on other parameters like R_1 , R_2 , c , a . It is suggested that the bond breaking degree for the formation of small gaseous hydrocarbons tended to occur at high temperature, leading to consumption of C & H elements need for HCF production [10]. Calorific value is highly affected by temperature as the percentage of volatile material changes with seasons and the percentage of moisture content changes (55-77 % at summer and 59-00% at winter [12]. During experiment room temperature varied from 20.24 °C to 27.589 °C. Thus operating room temperature has an important impact on the study of calorific value.

TABLE 1: Observed temperature properties and rate of change of temperature with their initial moisture contents

Samples	Moisture State	a (sec)	b (sec)	c (sec)	t_a (°C)	t_c (°C)	R_1 (°C/min)	R_2 (°C/min)
High chrome shaving wastages	Moisturized	300	382	840	22.635	24.22	0.0058	-0.0012
High chrome shaving wastages	Moisture less	300	356	960	19.539	21.004	0.1242	-0.0008
Low chrome shaving wastages	Moisturized	300	378	780	23.7	24.802	0.0472	-0.0018
Low chrome shaving wastages	Moisture less	300	371	840	22.381	24.093	0.0182	-0.0014
Raw fleshy wastage	Moisturized	300	376	840	26.263	28.558	0.1592	-0.0012

TABLE 2: Caloric Values of tannery wastage considering corrected factors

Samples	Moisture State	t (°C)	e (cal)	H_g (cal per gram)
High chrome shaving wastages	Moisturized	1.586	14.95	3758.09
High chrome shaving wastages	Moisture less	1.357	16.33	3276.075
Low chrome shaving wastages	Moisturized	1.0527	15.985	2537.8
Low chrome shaving wastages	Moisture less	1.702	17.48	4101.93
Raw fleshy wastage	Moisturized	2.10	16.79	5093.1

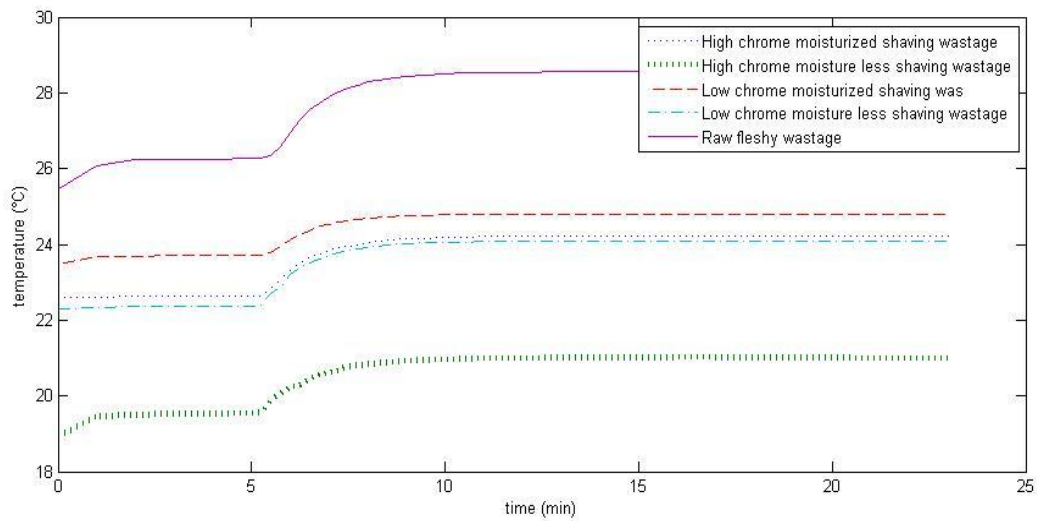


FIGURE 1: temperature properties before and after ignition with time

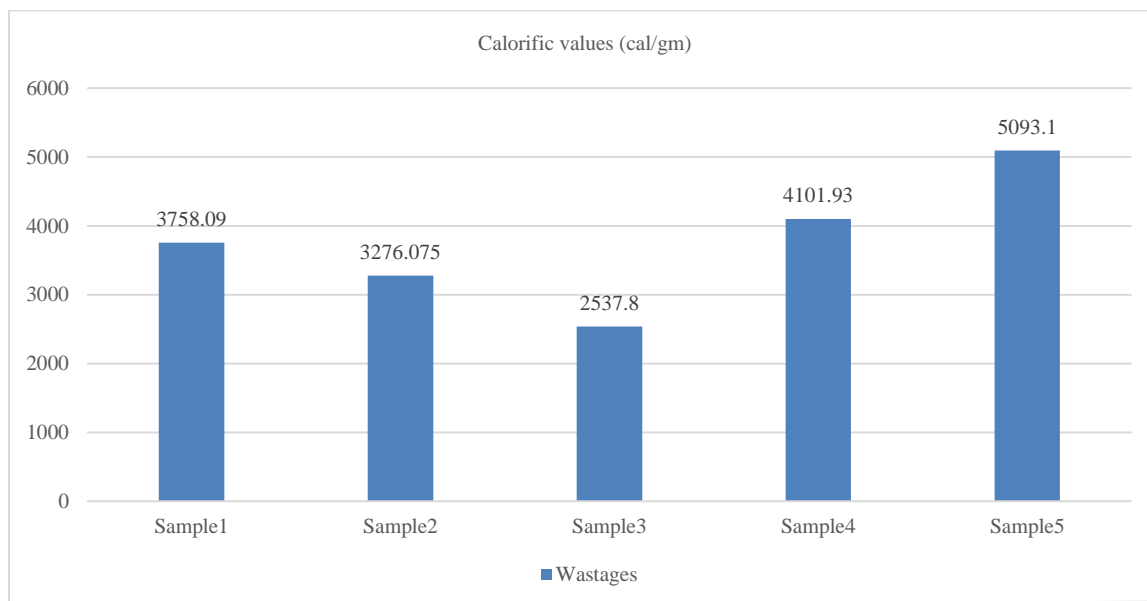


FIGURE 2: Comparison of calorific values of 5 different samples

CONCLUSION

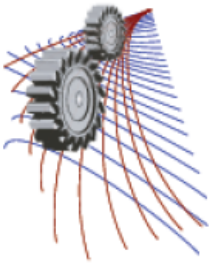
Calorific value is an important physical parameter of any substrate. The data obtained from the bomb calorimeter are different for five samples because of the difference in elements constituting the wastage samples, chemical effluents used in cycling process, presence and absence of moisture content and Cr content, temperature effect etc. Necessary correction has been done to obtain net gross calorific value. Calorific value obtained for these 5 samples are satisfactory and applicable in practical purpose.

ACKNOWLEDGEMENT

The authors wish to acknowledge Mr. Abdur Rahamn and Md. Mahabubur Rahman for their kind assistance during the operations of bomb calorimeter.

REFERENCES

1. D.Komilis,K. Kissas, A. Symeonidis,2014. Effect of organic matter and moisture on the calorific value of solidwastes: An update of the Tanner diagram. *Waste Manage.* 34(2014) 249-255.
2. L.N. Regueira, J.A.Rodríguez-Anon,J.P.Castinneiras,A.V.Diz, N.M.Santoven, 2001. Determination of caloric values of forest waste biomass by static bomb calorimetry.*ThermochimicaActa* 371 (2001) 23-31.
3. Núñez-Regueira, Lisardo, et al. "Determination of calorific values of forest waste biomass by static bomb calorimetry." *Thermochimica Acta* 371.1 (2001): 23-31.
4. Añón, JA Rodríguez, et al. "Calorific values and flammability for forest wastes during the seasons of the year." *Bioresource technology* 52.3 (1995): 269-274.Vindis, P., et al. "The impact of mesophilic and thermophilic anaerobic digestion on biogas production." *Journal of Achievements in Materials and Manufacturing Engineering* 36.2 (2009): 192-198
5. Zupančič, Gregor D., and Anita Jemec. "Anaerobic digestion of tannery waste: Semi-continuous and anaerobic sequencing batch reactor processes." *Bioresource technology* 101.1 (2010): 26-33.
6. A. Demirbağ, "Calculation of higher heating value of biomass fuels," *Fuel*, vol. 76, 1997, pp. 431–434.
7. C. Sheng and J.L.T. Azevedo, "Estimating the higher heating value of biomass fuels from basic analysis data," *Biomass and Bioenergy*, vol. 28, 2005, pp. 499-50.
8. M. Sakiyama and T. Kiyobayashi, "Micro-bomb combustion calorimeter equipped with an electric heater for aiding complete combustion," *Journal of Chemical Thermodynamics*, vol. 32, 2000, pp. 269-279.
9. P.H Given,D Weldon,J H Zoeller.Calculation of calorific values of coals from ultimate analysis: theoretical basis and geochemical implications. *Fuel* (1986) vol 65.
10. W. Lu, M. Ma, X. Jhang, B. Ghang, Y. Guo, C. Wang. Comparison of high calorific fuels obtained from flesh and dried hydrilla verticillata. *Journal of Analytical and applied pyrolysis* 111(2015) 76-87.
11. J. Anon, F. Lopez,J. Castineiras, J. Ledo, L. Regueira. Calorific values and flammability for forest wastes during the seasons of the year. *Bioresource technology* 52 (1995) 269-274.



A Novel Computational Language-Based Image Analysis Approach for Surveying and Statistical Applications

Tanvir Ahmed, Muhammad Shafiul Munir and Shoeb Ahmed^{a)}

Department of Chemical Engineering, Bangladesh University of Engineering and Technology, Dhaka-1000, Bangladesh

^{a)}Corresponding author: shoebahmed@che.buet.ac.bd

Abstract: With technology evolving every day, imaging is also emerging as a significant tool in wide range of applications such as medical science, biological research and industrial safety. However, these images are useful only if analyzed properly. There being many available tools for analyzing images; most of them lacks universal suitability, appropriateness and flexibility for varying applications. Considering simplicity, widespread applicability and customization options image analysis using MATLAB-based custom codes has already gained popularity in many perspectives. Being a customizable tool, MATLAB offers its benefits to different arena of users and applications. Geographical surveying is one of the applications where image analysis can cater the requirements of the user faster and with a lesser investment. This study deals with statistical analysis of Google map using MATLAB to exhibit how a customized application can perform individual mapping of various objects and areas, measurement of different terrain properties and statistical surveying of the region of interest. This program takes Google map as input, segments the image in various maps like road map, field map etc. and provides necessary statistical data for the segments. The program can be modified as required to facilitate any further need as well as can be applied in different color-based image analysis applications. However, coding knowledge and techniques being unfamiliar to many people, lessens its user-friendliness too some extent. To address this issue a graphical interface of the program has been developed for the users possessing no MATLAB or computational language experience. That executable file with graphical interface can be operated in any computer regardless of the technical background of the user. The program is also customized to work on Google map snapshots in different zooms. Possible applications of the program include geographical survey, surveillance and tracking, urban planning and design etc.

INTRODUCTION

Image analysis has been an important tool in analyzing and evaluating various geographical and biological images to extract information from them in order to utilize in further studies [1,2,3,4]. In medical and biological sciences, image analysis has been proven extremely significant to elaborate the diverse images taken from laboratory experiments, internal and external body parts in diagnosis and treatment of diseases [1,5,6,7,8]. It is also important in geological survey and research, considering the requirement of analysis of geographical maps and images repeatedly [9,10,11,12]. Systematic image analysis also provides valuable data extracted from images to be utilized in statistical analysis [7,13,14]. There being many available tools for analyzing images; most of them lacks universal suitability, appropriateness and flexibility for varying applications. Computational language-based image analysis approach offers the flexibilities without the limitations of the commercial software. Because of the simplicity, widespread applicability and customization options, image analysis using MATLAB-based custom codes has already gained popularity in many perspectives [7,15,16,17]. Wide range of images can be analyzed using algebraic theories and functions building up particular unique algorithm for each task. The main feature that makes MATLAB the most ideal tool is its capability to address any sorts of needs due to its unparalleled flexibility and its functional inventory, which is able to provide diversified methods to deal with problems within a great range.

Nowadays, satellite and mapping systems can provide large volumes of data that are invaluable in monitoring earth resources and the impacts of human activities. Images obtained by satellites are useful in many environmental applications such as geographical mapping, prediction of agricultural crops, urban growth, weather, flood and fire control etc. [9,12]. Analysis of high resolution satellite images has been an important tool to acquire accurate and up-to-date road network information essential for urban planning. One of the major information that can be extracted from the images obtained from Google map is the roads that constitute an important layer of vector maps. However, along with roads, field, water and residential areas are also the points of interest to different users. Road network information is required for a variety of applications. Manual extraction of roads and other zones directly from Google map imagery is very time-consuming and not straight forwards. It becomes even more complicated for road network in regions that consists of larger parts of desert or dry mountainous areas, e.g., northern Africa. Because of the complexity and considering the volume of work, it is convenient to use automated image analysis approaches [10]. These extraction methods can be of many different forms according to purposes, sources and applications of the images. Considering simplicity, widespread applicability and customization options image analysis using MATLAB-based custom codes has already gained popularity in many perspectives. Here, a MATLAB-based approach has been proposed and implemented for detailed statistical analysis of satellite maps. A typical Google map was analyzed using MATLAB to exhibit how a customized application can perform individual mapping of various objects and areas, measurement of different terrain properties and statistical surveying of the region of interest.

IMAGE ANALYSIS WITH MATLAB

There are large number of studies reported regarding image analysis techniques. Some of them explained the basic techniques behind the image analysis methods while others showed various functions and tools of analysis. Justyna Inglot discussed the basic uses and applications of MATLAB in image processing and segmentation [16]. Graphical User Interface mostly known as GUI is important to present the complicated codes in an easily understandable, executable format which is essential for the non-technical people to be able to use it. Sharma *et al.* summarize the automated segmentation methods, specifically discussed in the context of Computed topography (CT) and Magnetic resonance (MR) images [8]. Accurate segmentation of medical images is a key step in contouring during radiotherapy planning. CT and MR imaging are the most widely used radiographic techniques in diagnosis, clinical studies and treatment planning. Cloppet *et al.* proposed a new segmentation method of complex nucleus configurations [1]. The developed method is based on the marker based watershed algorithm which is one of the most widely accepted solutions in biomedical imaging. Gonzalez *et al.* summarizes substantial amount of works and techniques for image segmentation [18].

Image segmentation can be classified in to three categories such as Threshold technique, Region-based image segmentation, and Edge-based image segmentation [19]. The threshold technique is the simplest of segmenting methods. If an image $f(x,y)$ is composed of light objects on a dark background, in such a way that object and background pixels have intensity levels grouped into two dominant modes, one obvious way to extract the objects from the background is to select a threshold T that separates these modes. Then any point (x,y) for which $f(x,y) \geq T$ is called an object point; otherwise the point is called a background point. In other words, the thresholded image $g(x,y)$ is defined as

$$g(x, y) = \begin{cases} 1; & f(x, y) \geq T \\ 0; & f(x, y) < T \end{cases} \quad (1)$$

Data clustering is one method of Region-based image segmentation, and it is popularly used in mathematics and statistics. Centroids or prototypes are used to present the great numbers of cluster to achieve the two goals of reducing the computational time and providing a better condition to compress it [19]. Edge detection and corner detection are getting utilized recently in digital image processing. The watershed image segmentation is an example of edge-based image segmentation [19].

Mangala *et al.* proposed a new automatic road extraction technique using gradient operation and skeletal ray formation [11]. Considering the usage of satellite images and the significance of road extraction from imagery the authors found a more suitable and effective way to isolate road from satellite images. Jens Rittscher reviewed

necessary image analysis techniques as well as applied these techniques to deliver the data that will enable systems-level biology [6]. Some recent studies demonstrated another significant facet of image analysis to parse intra-cellular signaling during cell migration, a hallmark of cancer cell [7,15,17]. Application of MATLAB in image analysis makes it more convenient, customized and affordable, thus making it one of the most popular approaches for analyzing industrial, medical and biological images.

METHODOLOGY

The most prominent aspect of the approach is that it is relatively flexible and open to changes according to the needs and is quite user friendly despite being totally dependent on MATLAB programming. This program takes Google map as an input and segregate the regions to shows segmented road, field and water area maps as necessary. It also provides quantitative information of the region as bar and pie charts. Raw values are stored in excel files by default. Because of the flexible nature of the code it is able to provide more information extracted from the original map if designed by the user based on requirements.

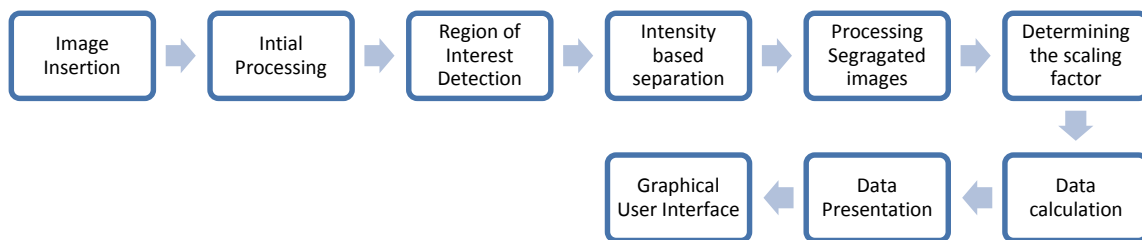


FIGURE 1. Flowchart of Google map segmentation and statistical analysis.

The program has two sections designed for two different situations; one for zoomed out maps and another for zoomed in maps. Two separate parts are displayed in simple graphical user interfaces [20] which indicates that in order to operate the program the user does not need to have MATLAB basics. The main algorithm is also different for two types of maps. For the zoomed in ones the input image is processed through intensity based thresholding followed by various spatial filters using specificity based on particular property geometry. The processed image is then further undergone through some morphological operations to obtain the desired output map. In case of the zoomed out ones after extracting the individual maps of roads, fields, water ways and residential areas through intensity based segmentation utilizing the scaling factor in the map the area of individual areas are found out through algebraic equations.

Finally the segmented images and extracted data are presented in pie chart, bar chart and excel sheet for further calculation and analysis. The calculation and data extraction has been done only for the second part but it can be performed for the first part as well by modifying the code.

The user manual for the program is as follows:

As the user starts the program a graphical user interface will appear just like FIGURE 2(a)

1. GUI starts at the beginning
2. User needs to insert two pictures
 - i) As 'input image'- the Google map on which the program would operate
 - ii) As 'scale image'- image containing the scale bar of the bottom left corner of Google map
3. User needs to specify the requirements entering 'code number' indicating what kind of output is desired
4. The scaling factor value in the scale bar image needs to be inserted.

As the 'OK' button is pressed the program initiates processing and shows desired output

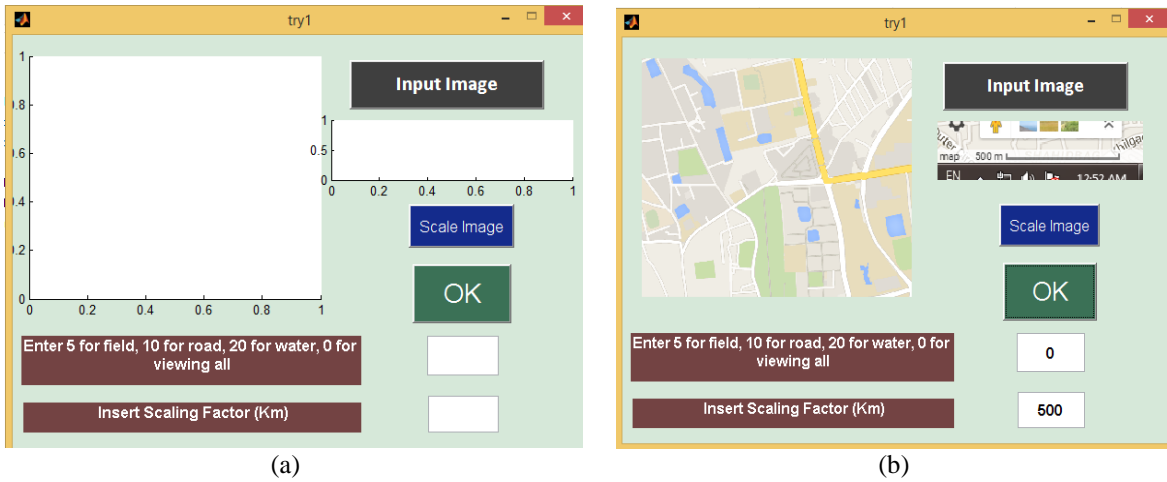
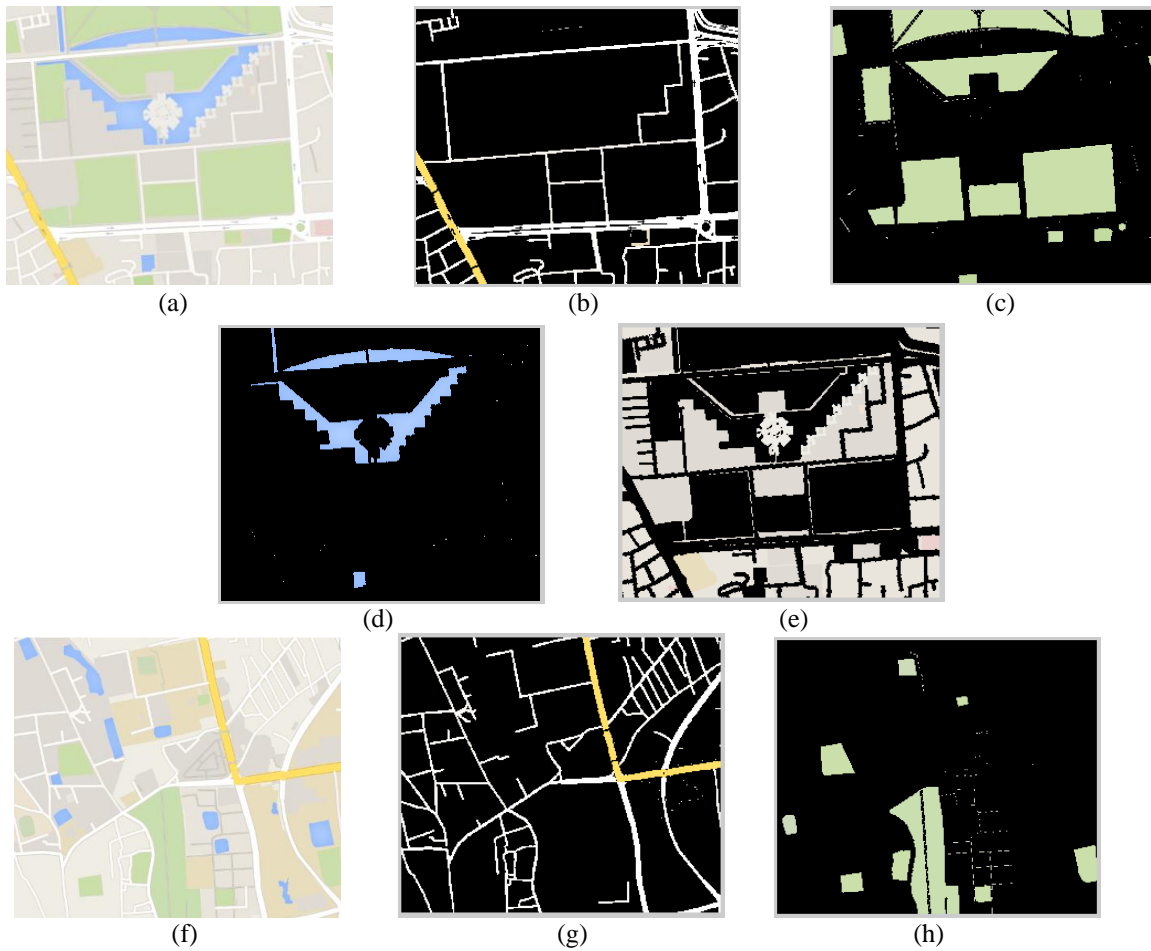


FIGURE 2. (a) Graphical user interface for Google map segmentation; (b) Graphical user interface after giving input.

RESULTS & DISCUSSIONS

The program is designed to generate various maps from the input images. The currently designed code can generate four types of segmented maps from Google map containing only roads, fields, water ways and residential areas.



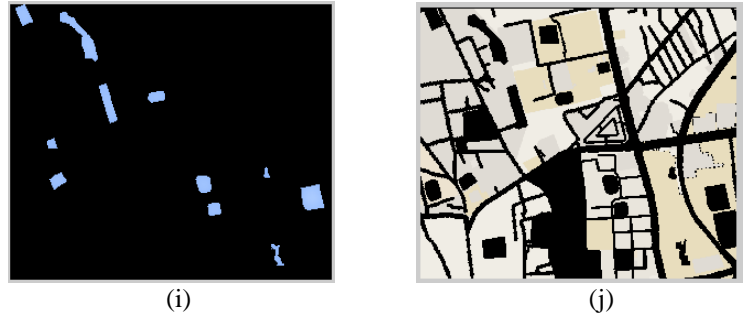


FIGURE 3. (a, f) Google map, (b, g) processed map showing only roads, (c, h) processed map showing only fields, (d, i) processed map showing only water bodies, and (e, j) processed map showing remaining land area.

Once the input image is processed, the program generates separate maps for roads, fields, and water ways as shown in Fig. 3. After the maps are being generated the program starts the calculation based on the input scale and initial map images. After calculating the areas of different regions it displays the data as pie chart and bar chart as below (FIGURE. 4).

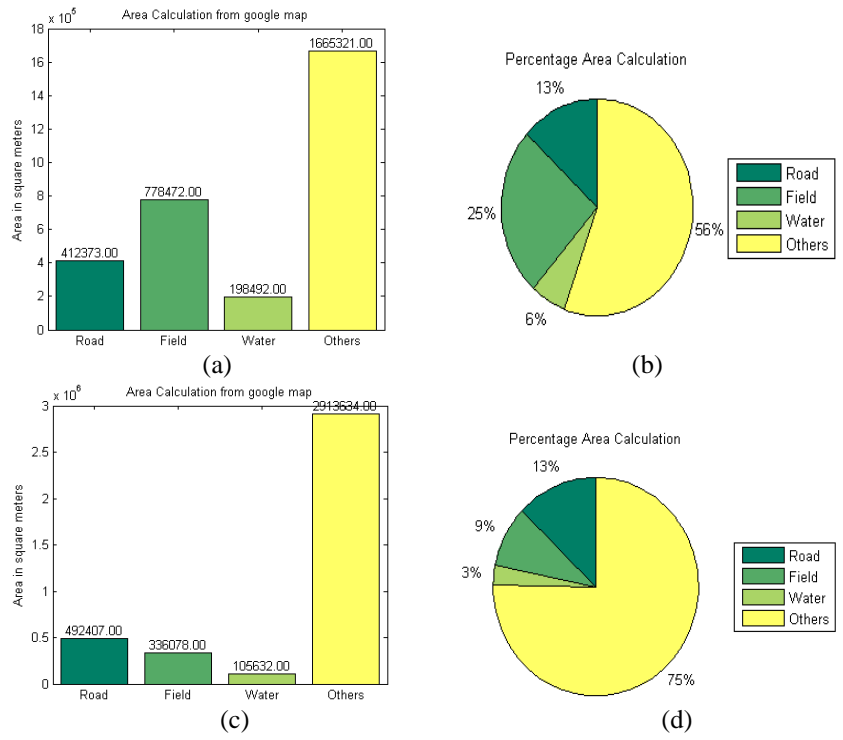


FIGURE 4. (a) Bar chart showing the total area of each type of regions for image 3(a), (b) pie chart shows the percentage of total area occupied by each section for image 3(a). (c, d) shows similar data for image 3(f).

For this case, a pie chart exhibits how much area of a certain region is occupied by roads, fields, water bodies, individually. There approximate areas are also shown in bar charts. Raw data is also saved in excel file for further use. However, these options can be changed by the users based on their requirements. Presently the program only provides the area statistics on the maps that has been extracted but it can be modified to attain data based on many other geometrical properties. This procedure of road or field map extraction is very accurate and thus the data found from the maps are also quite accurate. In order to compare the accuracy of the program a comparison with the manually calculated area data is planned to be performed, which will certainly prove the effectiveness and accuracy of the program.

CONCLUSION

In this paper we have proposed an algorithm to segment typical map images to separate road, field, water and other areas with high accuracy. The user friendly graphic interface provides a platform to the users who lack proper computational language expertise. This algorithm generates very accurate results and is pretty flexible for further changes. Some other segmentation techniques like K-mean segmentation, Canny edge base segmentation, and Watershed segmentation were also applied for the same purpose, however, this technique provide most satisfactory and accurate result. This program can further be used for urban planning, rural development, annual surveys and any landscape planning and development.

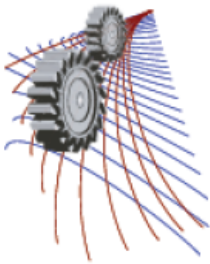
ACKNOWLEDGEMENT

The authors gratefully acknowledge the financial support by BUET Chemical Engineering Forum (BCEF) during this work.

REFERENCES

1. A.B. F. Cloppet Segmentation of complex nucleus configurations in biological images, *elsevier* (2010) 755–761.
2. M.W. Khan, A Survey: Image Segmentation Techniques, *International Journal of Future Computer and Communication* 3 (2014).
3. U. Zakir, A.N.J. Leonce, E.A. Edirisinghe, Road sign segmentation based on colour spaces: A comparative study, 11th IASTED International Conference Computer Graphics and Imaging, Innsbruck, Austria, 2010.
4. K.K.L. Wong, Z. Sun, J. Tu, S.G. Worthley, J. Mazumdar, D. Abbott, Medical image diagnostics based on computer-aided flow analysis using magnetic resonance images, *Computerized Medical Imaging and Graphics* 36 (2012) 527– 541.
5. F.P.M. Oliveira, J.M.R.S. Tavares, Medical image registration: a review, *Computer Methods in Biomechanics and Biomedical Engineering* (2012).
6. J. Rittscher, Characterization of Biological Processes through Automated Image Analysis, *Annual Review of Biomedical Engineering* (2010) 315-344.
7. M.C. Weiger, S. Ahmed, E.S. Welf, J.M. Haugh, Directional Persistence of Cell Migration Coincides with Stability of Asymmetric Intracellular Signaling, *Biophysical Journal* 98 (2010) 67-75.
8. A.K.R. Neeraj Sharma, K. K. Shukla, Shiru Sharma, Satyajit Pradhan, Arvind Srivastva, Lalit M. Aggarwal, Automated medical image segmentation techniques, *Journal of Medical Physics* 35 (2010).
9. D.B.L. Bong, K.C. Lai, A. Joseph, Automatic Road Network Recognition and Extraction for Urban Planning, *International Journal of Computer, Information, Systems and Control Engineering* 3 (2009).
10. S.a.A. Hameed, Automatic Road Extraction from Satellite Image, In *Proceedings of the National Conference on Communications, 2007*, pp. 42-47.
11. T.R. Mangala, S.G. Bhirud, A New Automatic Road Extraction Technique using Gradient Operation and Skeletal Ray Formation, *International Journal of Computer Applications* 29 (2011).
12. D.P.R.G. Rohit Maurya, Ajay Shankar Shukla, Road Extraction Using K-Means Clustering and Morphological Operations, 2011 International Conference on Image Information Processing (ICIIP 2011), 2011.
13. M. KATHLEEN KERR, G. A. CHURCHILL, Statistical design and the analysis of gene expression microarray data, *Genetics Research* 77 (2001) 123-128.
14. C.J. Veenman, M. J. T. Reinders, and E. Backer., Resolving motion correspondence for densely moving points., *IEEE Trans. Pattern Analysis and Machine Intelligence* (2001) 54–72.
15. S. Ahmed, H.-k. Yang, A.E. Ozcam, K. Efimenko, M.C. Weiger, J. Genzer, J.M. Haugh, Poly(vinylmethylsiloxane) Elastomer Networks as Functional Materials for Cell Adhesion and Migration Studies, *Biomacromolecules* 12 (2011) 1265-1271.
16. J. Inglot, *Advanced Image Processing with Matlab*, Mikkeli University of Applied Sciences, May 2012, pp. 65.
17. E.S. Welf, S. Ahmed, H.E. Johnson, A.T. Melvin, J.M. Haugh, Migrating fibroblasts reorient directionality by a metastable, PI3K-dependent mechanism, *The journal of cell biology* 197 (2012) 105-114.
18. R.E.W. Rafael C. Gonzalez, *Digital Image Processing, Second Edition ed.*, Prentice Hall, Upper Saddle River, New Jersey, 2002.

19. Y.-H.W. Chia -Hao Tsai, Segmentation, Graduate Institute of Communication Engineering, National Taiwan University, Taipei, Taiwan, 2010, pp. 36.
20. T. MathWorks, Building GUIs with MATLAB, The MathWorks, 1996.



In Vitro Analysis of Dental Erosion Potential of Soft Drinks and Bottled Drinking Water

Nayer Sultana Nisha, Afrin Ahsan, Fatima Enam, Mehnaz Mursalat, Muzahidul Islam Anik, Mohidus Samad Khan^{a)}

Department of Chemical Engineering, Bangladesh University of Engineering & Technology, Dhaka – 1000, Bangladesh

^{a)} Corresponding author: mohid@buet.ac.bd

Abstract. Dental erosion is a non-carious, pathological loss of tooth surface, distinct from abrasion and attrition, and is defined as an irreversible loss of dental hard tissues as a result of exposure to nonbacterial acids. Drinks having pH lower than the critical erosive pH of enamel (5.2~5.5) and root dentin (~6.7) are mainly responsible for dental erosion. The types of beverages that may cause erosion are carbonated beverages, fruit juices, diluting juices, squash drinks and bottled drinking waters. The potential of a soft drink or a fruit juice to erode dental enamel depends not only on the pH of the drink, but also on its buffering capacity, total dissolved solids (TDS), calcium and phosphate concentrations. In Bangladesh, there is limited scientific information available to assess the potential of dental erosion of the commercially available beverages and drinking water. The aim of this experimental study is to analyze dental erosion potential of various soft drinks and bottled drinking water, and to perform in vitro analysis to measure erosion rate of dental samples exposed to selected drinks. Dental samples (infant incisor) covered with hydrophobic varnish except for 4mmx4mm windows were exposed to some selected drinks, and dental erosion was measured for 7 days. Characteristics of dental erosion were analyzed using SEM (Scanning Electron Microscopy) images. The experimental results of this study will be highly useful for the consumers, health professionals, regulatory authorities, and government policy makers for quality control of the available soft drinks, energy drinks, fruit juices, and bottled drinking water commercially available in the local market.

INTRODUCTION

Dental erosion refers to the dissolution of tooth structure under continuous exposure to low pH, while not being associated with bacterial infection [1-3]. Replacement of minerals, primarily calcium from enamel or hydroxyapatite $\text{Ca}_5(\text{PO}_4)_3(\text{OH})$ [4], can trigger degradation of teeth structure and upon long-term exposure can lead to severe harmful impacts on dental aesthetics and functionality [2].

In dental erosion the amount of mineral dissolved from enamel can be appreciated from pH and titratable acidity (TA) values of beverages and foods [5-7]. The pH value corresponds to the equilibrium measure of the hydrogen ion concentration, but it gives no indication of the overall acidic content of the beverage or food, whereas, TA gives a measure of all free hydrogen ions available to cause erosion. The concentrations of calcium (Ca^{2+}) and phosphate (PO_4^{3-}) ions, and total dissolved solids (TDS) in the exposure media (ingested drinks or food and saliva) dictate the degree of dissolution of enamel. Presence of suitable concentration of fluoride may also counteract the dissolution. Besides, other factors such as acid type, acid concentration, frequency of consumption, buffering capacity of saliva, temperature of the drinks, and oral hygiene also have shown to impact the absolute erosion caused by the drinks.

There are three main groups of people at risk of dental erosion: a) teenage males primarily as a result of the consumption of large amounts of acidic beverages, b) teenage females (bulimia), and c) the adults.

Soft drinks, beverages, and juices commonly consumed by the people of Bangladesh are acidic and might be related to dental erosion issues. Dental erosion is also caused by poor oral hygiene practice, lack of dental education

and affordable dental care among general population of Bangladesh. Therefore, it has become essential to evaluate the erosive potential of commonly consumed food and beverages in Bangladesh.

The objective of this study is to experimentally analyze different dental erosion indicating parameters, such as pH, TTA, TDS, PO₄³⁻, and Ca²⁺ of the soft drinks, energy drinks, fruit juices and bottled drinking water available in the local market, and to evaluate the potential hazard associated with these drinks that leads to dental erosion, and to perform in vitro analysis to find out the degree of dissolution of dental samples (infant incisor).

EXPERIMENTATION

Materials

Beverages and bottled drinking water samples were collected from different super shops of Dhaka, Bangladesh. All the chemicals used were reagent grade. To measure pH of the samples a calibrated bench top pH meter (Hanna HI2211) was used. A HACH Model 44600 Conductivity/TDS Meter was used to measure the TDS of the samples. For carbonated samples, the samples were allowed to sit for 30 minutes so that some of the gas escaped. The effervescing gas keeps the meter from giving a steady reading. The titratable acidity of each sample was measured by titrating 10 mL of each sample with 0.1N NaOH, with phenolphthalein as the indicator. For the drink samples with an intense color, the samples were diluted for accuracy in determining the endpoint. The calcium levels in the beverages were determined using complexometric titration method. EDTA solution was prepared by dissolving 9.306g of reagent grade EDTA (Sigma Aldrich) in 500ml of solution to prepare a 0.1N solution. A pH 11 buffer solution was prepared to maintain an alkaline environment which would help any magnesium precipitate; otherwise the EDTA would simultaneously complex with the magnesium ions resulting in a reading concomitant with total hardness readings. 10ml of the samples were titrated with the EDTA solution, with Calcon as the indicator. The phosphate contents of the samples were measured using spectrophotometer (Hach UV/vis spectrophotometer, DR4000) and phosphate reagent (PhosVer, HACH). 10 mL samples of the beverages were taken into cuvettes, diluted as required..

Method

Dental Erosion Potential of Beverages and Bottled Drinking Water

The samples were classified into four categories: a) soft drinks (17 brands), b) energy drinks (8 brands), c) fruit juices (13 brands), and d) bottled drinking water (9 brands). Each test were carried out for three times (n=3) and the average results were used for further analysis. All the tests were performed at room temperature.

In Vitro Analysis of Dental Erosion

One soft drink (Sprite), one energy drink (Speed) and one fruit juice (Frutika) were used to conduct the experiment. Dental samples (infant incisor) covered with hydrophobic varnish except for 4mmx4mm windows were exposed to the selected drinks. It was found that the nail polish did not affect dental erosive potential of beverages. The change of key parameters of beverages with time was analyzed (with and without tooth).

150 ml of each drink were taken in 3 different conical flasks. After measuring the initial parameters of the drinks, 3 tooth samples (infant incisor) covered with hydrophobic varnish except for 4mmx4mm windows were immersed into 3 drinks samples and kept for 7 days (168 hours). Weight of the tooth samples were measured before immersing into the solutions by drying into an oven for 5 minutes at 100°C temperature. After 7 days, all the parameters of the drinks samples (with tooth sample) along with weight of the tooth samples were measured. In other 3 conical flasks, 150 ml of each drink were taken and all the parameters were measured at t=0, and t=7 days. Each test were carried out for three times (n=3) and the average results were used for further analysis. All the tests were performed at room temperature.

RESULTS AND DISCUSSION

TABLE 1. Key parameters of soft drinks, energy drinks, fruit juices and bottled water: TDS, pH, TTA, phosphate and calcium.

	Sample	Total Dissolved Solids (TDS), mg/L	pH	Titrateable Acidity (TA), mg/L as CaCO ₃	Phosphate (PO ₄ ³⁻), (ppm)	Calcium (Ca ⁺⁺), (ppm)
Soft Drinks	CocaCola	590.3	2.5	1647.5	555.8	120.24
	Fanta	312.7	2.9	1773.8	240.3	30.06
	Sprite	230.0	3.1	1490.3	0.1	50.10
	Pepsi	521.3	2.9	1663.0	462.5	40.08
	Mirinda Orange	330.7	2.9	2356.5	1.3	90.18
	7Up	333.3	3.4	2168.0	0.1	30.06
	Mountain Dew	275.0	3.0	1572.3	0.7	80.16
	RC Cola	416.7	2.7	1534.3	418.5	20.04
	Uro Orange	319.5	2.8	1560.0	1.0	60.12
	Virgin Red	674.0	2.4	1785.2	1017.7	80.16
	Mojo	590.7	2.5	1551.7	2259.7	120.24
	Clemon	423.0	3.5	1843.3	0.5	80.16
	Appy Fizz	618.7	3.5	1921.3	2.3	40.08
	Diet Pepsi	478.0	3.12	5000.0	367.0	400.80
	Diet Coke	578.0	2.84	4166.7	635.0	400.80
	Diet Mojo	699.0	2.64	5000.0	678.0	400.80
Energy Drinks	Red Bull	832.3	3.5	5283.5	0.2	390.78
	Speed	408.3	3.0	2155.8	0.2	70.14
	Tiger	284.7	3.1	3321.5	1.2	90.18
	Power	290.7	3.2	2519.7	0.6	70.14
	Black horse	436.0	2.8	5833.3	7.7	400.8
	Wild brew	432.0	3.9	2500.0	63.4	514.36
Royal dutch	569.0	4.0	5000.0	71.8	267.20	
Braver	427.0	2.9	4166.7	5.9	400.80	
Fruit Juices	SunDrop Mango	664.3	3.5	1308.9	3.1	160.32
	Ceres Mango	1279.3	3.7	3810.5	1.9	90.18
	Danish Mango	565.7	3.8	1472.5	1.9	120.24
	Frooto Mango	618.3	3.4	1601.3	2.3	100.20
	Fruitika Mango	502.3	3.9	1134.9	2.5	140.28
	Mangolee mango	713.7	3.9	1370.6	0.5	110.22
	Shezan Mango	615.3	3.9	1368.0	1.2	150.30
	Pran Mango	596.7	3.7	1712.5	0.7	80.16
	Pran apple	529.0	3.1	5000.0	61.8	400.80
	Juicy	281.0	3.5	4000.0	32.8	400.80
	Lichigo	288.0	3.2	2000.0	6.2	400.80
Frutella	653.0	3.5	5000.0	27.0	400.80	
Foster clark's	638.0	3.1	3000.0	124.4	801.60	
Bottled Water	Aquafina	11.6	7.0	51.5	0.2	3.01
	Mum	118.7	7.1	25.8	0.3	32.06
	Ifad	46.1	7.2	51.5	0.4	26.05
	Acme	50.2	7.3	34.3	0.2	9.70
	Evian	234.0	7.8	25.8	0.6	163.33
	Spa	325.7	7.1	59.2	3.7	92.18
	Fresh	113.8	7.1	25.8	0.2	13.03
	Pran	73.0	7.6	25.8	0.2	6.01
	Jibon	57.5	4.9	34.3	0.2	15.03

Dental Erosion Potential of Beverages and Bottled Drinking Water

The average values of the experimental results of TDS, pH, TA, phosphate and calcium contents of soft drinks, energy drinks, fruit juices and bottled drinking water are shown in Table 1.

Experimental results (Table 1) show that all the beverages locally available were acidic. The soft drink samples had the lowest pH values, with the black cola drinks having the minimum, all below pH 3. The energy drinks category had slightly higher pH than the soft drinks. Fruit juices have a considerable higher pH (>3) but with similar titratable acidity as soft drinks. It is noticeable that most of the samples had a pH below 4.5 which is way below the critical erosive pH values for enamel (5.2-5.5) and dentin (6.5), indicating high erosive potential upon continuous or recurrent consumption with the exception of bottled water samples [8]. TA was the highest for the energy drinks. All the bottled water samples had a pH over 6.7, most of them having a pH over 7, and with almost negligible TA.

The black cola drinks had the highest levels of phosphate (PO_4^{3-})-compared to other samples (Table 1). Amongst the black colas 'Mojo' exhibited high PO_4^{3-} content, while both 'Mojo' and 'CocaCola' contain relatively high calcium (Ca^{2+}) content compared to other soft drinks. The phosphate levels in energy drinks were found to be lower than that of the soft drinks, especially, black cola drinks. The concentrations of phosphate were low but calcium content of fruit juices was found higher as compared to other beverages (Table 1). With the exception of spring water (Evian), bottled water samples had negligible amounts of calcium and phosphate. Among the samples, Spa and Evian showed greater phosphate and calcium content respectively than any other sample (Table 1). Presence of minerals (Ca^{2+}) and dissolved solids (TDS) can induce resistance to dissolution, which can somewhat alter the erosive potential [9].

Change of Key Parameters of Beverages within 7 Days (With & Without Tooth)

Dental samples were exposed to Sprite, Speed and Frutika for 7 days. The mean values of pH, TDS, phosphate, TTA, and calcium contents of the beverages (at $t = 0$ and $t = 7$ days) in presence and absence of dental samples are shown in Table 2. The weight change of dental samples (at $t=0$ and $t=7$ days) because of the presence of beverages are also enlisted in Table 2. The decay rate of tooth samples and the change of physiochemical parameters (pH, TDS, phosphate, TTA, and calcium) of beverages are graphically shown in Figures 1. The dental decay rate was found higher for Sprite followed by Speed and Frutika (Figure 1a). Change of pH, TDS and TTA of beverages were found insignificant in presence of dental sample (Figures 1b, c, e). Change of phosphate and calcium of beverages were found higher in presence of dental sample (Figures 1d, f), which indicates dissolution of phosphate and calcium contents of dental samples exposed to beverages.

TABLE 2. Change of key parameters of beverages (with and without tooth).

Drinks	Weight of tooth		pH		TDS (mg/l)		PO_4^{3-} (mg/l)		TTA (mg/l)		Ca^{2+} (mg/l)	
	t=0 day	t=7 day	t=0 day	t=7 day	t=0 day	t=7 day	t=0 day	t=7 day	t=0 day	t=7 day	t=0 day	t=7 day
Sprite with tooth	0.23	0.17	3	3.1	196	211	0.02	0.32	1085	1162.50	10.69	122.24
Sprite without tooth	--	--	3	3	196	202	0.02	0.03	1085	1139.25	10.69	63.46
Speedwith tooth	0.18	0.21	2.9	2.9	427	449	0.09	2.69	3100	3487.5	106.88	634.60
Speed without tooth	--	--	2.9	2.9	427	443	0.09	0.90	3100	3255	80.16	200.40
Frutika with tooth	0.26	0.25	3.7	3.8	508	516	46.20	96.30	1240	2790	601.20	1603.20
Frutika without tooth	--	--	3.7	3.6	508	495	46.20	58.60	1240	1860	601.20	1402.80

SEM Image of Dental Sample

SEM images were taken before and after dissolution of dental samples in beverages for 10 days. It was found that dental samples exposed to Fanta, Speed and Tiger were eroded and lost the shiny upper layer. Figure 2 showed that exposure of dental sample to Sprite for 10 days caused the tooth surface eroded and cracked. The reason could be the dissolution of enamel of dental sample in beverage.

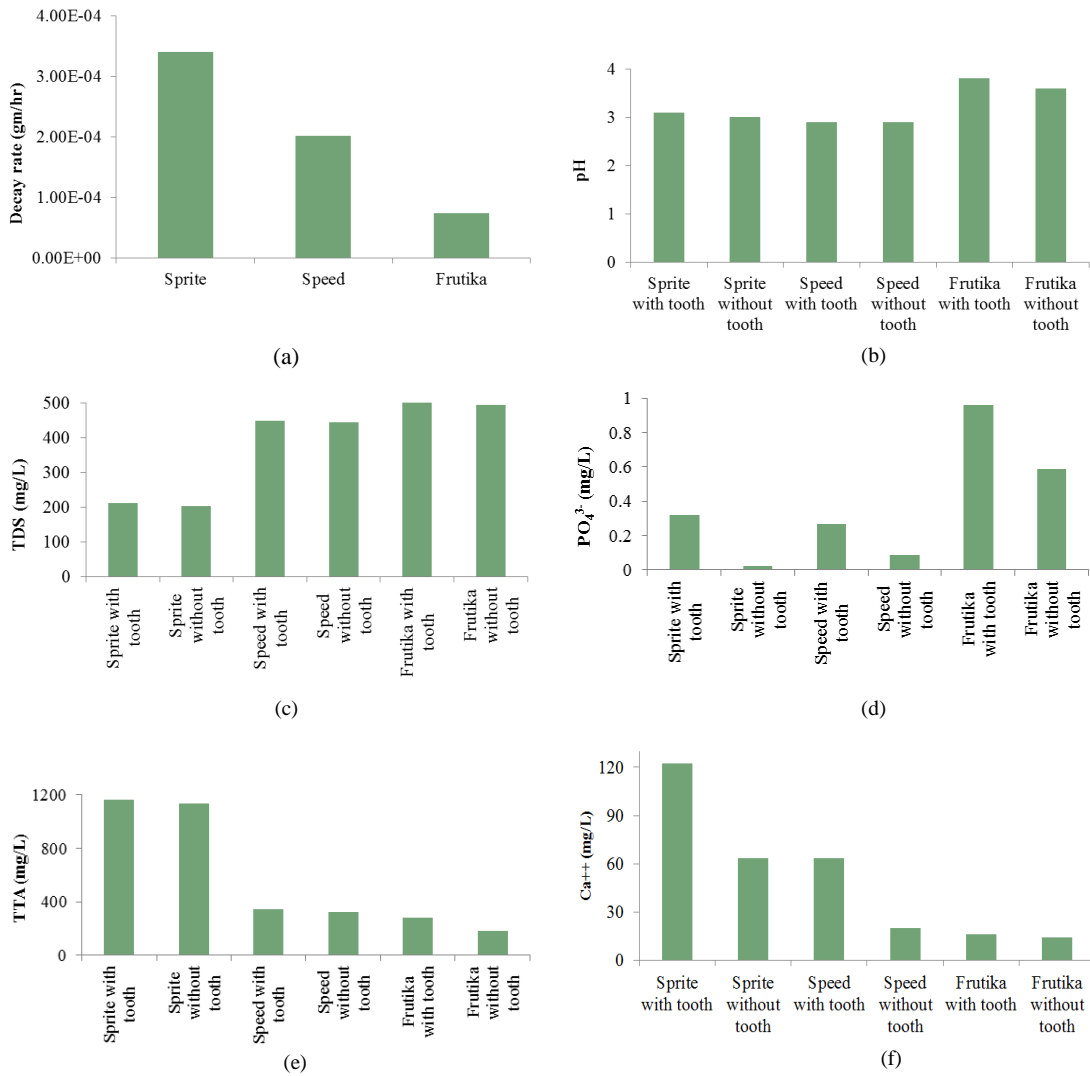


FIGURE 1. Change of dental erosion indicating parameters of beverages for 7 days (with and without dental samples exposed to beverages): a) decay of dental sample in presence of beverages, b) change of pH of beverages, c) change of TDS of beverages, d) change of PO₄³⁻ of beverages, e) change of TTA of beverages, f) change of Ca²⁺ of beverages.

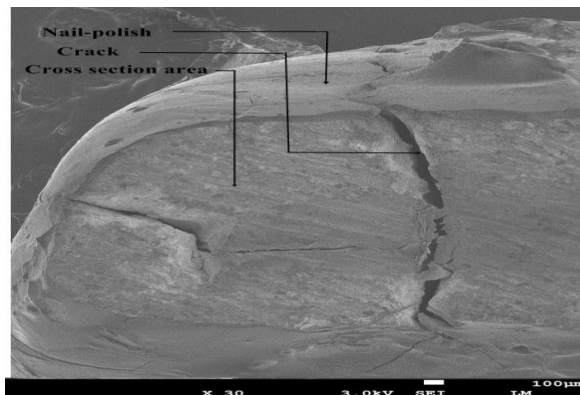


FIGURE 2. SEM image of cross section of eroded tooth sample in Sprite.

CONCLUSION

The experimental results showed that all the beverages analysed in this study were mostly acidic, with the soft drinks category having the lowest pH values, followed by the energy drinks, the fruit juices and finally the bottled water samples having a pH close to 7. Most of the samples had a pH below 4.5 which is way below the critical erosive pH values for enamel (5.2-5.5) and dentin (6.5), indicating high erosive potential upon continuous or recurrent consumption with the exception of bottled water samples. In vitro analysis also investigated the erosive potential of selected beverages. In vitro analysis demonstrated that prolong exposure of dental sample to beverage could cause the tooth surface eroded and cracked. The experimental results showed that erosive beverages could cause dissolution of phosphate and calcium contents of dental samples exposed to beverages.

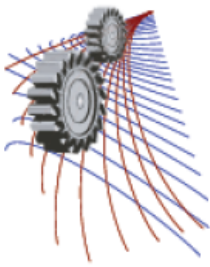
The relationship of foods and drinks to dental caries is a very complex one. Conducting in vitro analysis with representative dental samples: in terms of size, age and nature of the dental samples, is laborious and time staking. This experimental study may serve as the basis for determining the potential dental erosion risk towards the population of Bangladesh and other countries with similar socio-economic conditions.

ACKNOWLEDGMENTS

This research was supported by BCEF Academic Research Fund, CASR Research Fund, and financial support from the Department of Chemical Engineering, BUET. The authors acknowledge Dr. N. Ahsan and Dr. A. Sultana for dental samples, and Mr. M. S. Rana of GCE Department, BUET for technical support, and Mr. N. Aich and Ms. U. Guha for technical discussion.

REFERENCES

1. A. Lussi, Dental Erosion: From Diagnosis to Therapy, in Dental Erosion. Monogr Oral Sci. Basel, A. Lussi, Editor. 2006, Karger. pp. 66-76.
2. A. Lussi, M. Schaffner and T. Jaeggi, Dental erosion - diagnosis and prevention in children and adults*. International Dental Journal, 2007. 57(S6): pp. 385-398.
3. T. Imfeld, Dental erosion. Definition, classification and links. European Journal of Oral Sciences, 1996. 104(2): pp. 151-155.
4. A. S. Dawes, A three-dimensional contact algorithm for sliding surfaces. International Journal for Numerical Methods in Fluids, 2003. 42(11): pp. 1189-1210.
5. C. J. Brown, et al., The erosive potential of flavoured sparkling water drinks. International Journal of Paediatric Dentistry, 2007. 17(2): pp. 86-91.
6. M. Kitchens and B. Owens, Effect of Carbonated Beverages, Coffee, Sports and High Energy Drinks, and Bottled Water on the in vitro Erosion Characteristics of Dental Enamel. Journal of Clinical Pediatric Dentistry, 2007. 31(3): pp. 153-159.
7. N. J. Cochrane, et al., Erosive potential of sports beverages. Australian Dental Journal, 2012. 57(3): pp. 359-364.
8. J. Featherstone and A. Lussi, Understanding the chemistry of dental erosion. 2006.
9. N. Cochrane, et al., Erosive potential of sports beverages. Australian dental journal, 2012. 57(3): pp. 359-364.



CFD Analysis of Temperature Distribution and Thermal Comfort of Complete Footwear for Hot and Cold Country

Abu Jor¹, Md. Rafiul Hashar², Md. Samsul Arefin^{3,a)}

^{1,2,3}Department of Leather Engineering, Khulna University of Engineering & Technology, Khulna-9203, BANGLADESH

^{a)}Corresponding author: arefinkuet@gmail.com ,arefin@le.kuet.ac.bd

Abstract. Computational fluid dynamics (CFD) has become an elemental tool for analyzing various phenomena of footwear comfort nature during wear like temperature distribution and velocity magnitude within the footwear and find out its thermal comfort level. The goals of this study were to analyze the temperature distribution and the level of thermal comfort for complete footwear during wear through predicted mean vote (PMV) & percentage person's dissatisfaction (PPD) model by using CFD techniques. This makes establishing heat transfer-thermal-comfort relationships easier to approximate. For this analysis, environmental conditions of cold (-20°C) and hot (50°C) countries were considered and also considered the upper materials as leather. The occupant (human foot) felt neutral to slightly cool in the cold country and felt very hot in the hot country within the footwear and their PPD is more than 25% and 99.1% respectively that means 75% persons will be satisfied in the cold country and only of 0.99% persons will be satisfied in the hot country. Thus the effectiveness of the footwear design for keeping the human foot comfortable for any kind of design and region can be assessed.

INTRODUCTION

Nowadays, the footwear and textile manufacturers are focused not only on the quality and design of their products, but also on customer comfort, which has also been one of the primary functions of most of textile products [1]. The climate inside a shoe is controlled by thermal and moisture conditions and is important to attain comfort. Development of thermal models that are capable of predicting in-shoe temperature distributions is an effective way forward to undertake extensive parametric studies to assist optimized design [2]. Regarding foot comfort, the movement adaptability of the material, waterproof qualities, weight and the thermal as well as moisture control would be the main parameters to be taken into account during footwear design & development [3]. According to the inquiry performed by Kuklane et al. [4] about the main problems related to feet comfort, up to 43% of customers dislike having cold feet and 12% are concerned about sweat problems. Therefore, thermal comfort is an important key when considering comfortable footwear, and it can be achieved by keeping the footwear temperature in the range from 27 °C to 33°C [3, 5]. The aims of this study were to investigate the temperature distribution across the footwear during wear using CFD technique and analyzed their thermal comfort level using PMV and PPD model for cold and hot country perspective.

MATHEMATICAL FORMULATION

The commercial code Autodesk® Simulation CFD 2015 was used to simulate a three-dimensional steady state turbulent flow and heat transfer in the computational model. The partial differential equations governing fluid flow and heat transfer include the continuity equation, the Navier-Stokes equations and the energy equation [6]. A continuity equation describes the transport of a conserved quantity. The continuity equation is given below:

$$\frac{\partial u}{\partial t} + \frac{\partial u}{\partial x} + \frac{\partial u}{\partial y} + \frac{\partial u}{\partial z} = 0 \quad (1)$$

Navier-Stokes equations are the basic governing equations for a viscous, heat conducting fluid. The Navier-Stokes equations are given below:

$$\rho\left(\frac{\partial v}{\partial t} + v \cdot \nabla v\right) = -\nabla p + \mu \nabla^2 v + f \quad (2)$$

For incompressible and subsonic compressible flow, the energy equation is written in terms of static temperature:

$$\rho C_p \left(\frac{\partial T}{\partial t} + u \frac{\partial T}{\partial x} + v \frac{\partial T}{\partial y} + w \frac{\partial T}{\partial z} \right) = \frac{\partial}{\partial x} \left[k \frac{\partial T}{\partial x} \right] + \frac{\partial}{\partial x} \left[k \frac{\partial T}{\partial x} \right] + \frac{\partial}{\partial x} \left[k \frac{\partial T}{\partial x} \right] + qv \quad (3)$$

MATERIAL PROPERTIES

The material properties required for a transient heat transfer footwear model include mass density, specific heat, thermal conductivity, emissivity, transmissivity, electrical resistivity and wall roughness; a list of the material properties used in the heat transfer footwear models and their sources can be seen in Table 1.

Table 1. Material properties used to assign the CAD model for simulation.

Model part	Thermal conductivity (W/m-k)	Specific heat (J/Kg-K)	Mass density (Kg/m ³)	Emissivity	Transmissivity	Electrical resistivity (ohm-cm)	Wall roughness (mm)
Footwear upper(leather)	0.16 ^[7]	1500 ^[8]	998 ^[9]	0.95 ^[10]	0.02 ^[10]	1e+16 ^[11]	0.000874 ^[12]
Insole (particle board) ^[13]	0.078	1300	590	0.8	0	3e+17	0
Occupant(human foot) ^[13]	50	4182	998	0.98	0	0	0
Air volume ^[13]	0.02563	1004	--	1	--	--	0

These properties are also only of importance in transient models, where the change in temperature with respect to time is not zero. The thermal property that defines the contact between materials determines the continuity of temperature distributions and the degree of heat flow between separate materials.

IMPLEMENTATION OF THE SIMULATION MODEL

For this analysis considered two different temperature regions such as cold and hot country temperatures and also considered the upper material as leather. The process is done by generating a geometric model and specifying material properties along with boundary conditions. Next, the model is divided into smaller elements connected at nodes through a process known as meshing and then solved the model (Fig. 1). Finally, plots and numerical results are output to provide engineers with insights to the behavior of the model. All the boundary conditions have been assigned for cold country temperature (-20°C) [14] and hot country temperature (50°C) [15].

A 3D footwear model with human foot inside it was modeled for this study using solid works software. Table 2 represents the detail dimensions of the model. Leather was assigned as upper materials, taxon/particle board as insole, human material as foot and air was assigned to internal gap. By assigning boundary conditions such as heat flux, heat generation, film coefficient, velocity, pressure and temperature to the openings and other specific locations of a complete footwear, it was effectively "connected" the design with the physical world. Air velocity was assigned at the inlet surface of 0.15 m/s [16] to flow air inside the footwear and a temperature of about -20°C and 50°C was assigned at the inlet section respectively for cold and hot country weather. The outlet surface was defined with atmospheric pressure which allowed the air to move within model boundary. To simulate heat transfer to the surroundings, a film coefficient boundary condition was applied to the external surfaces.

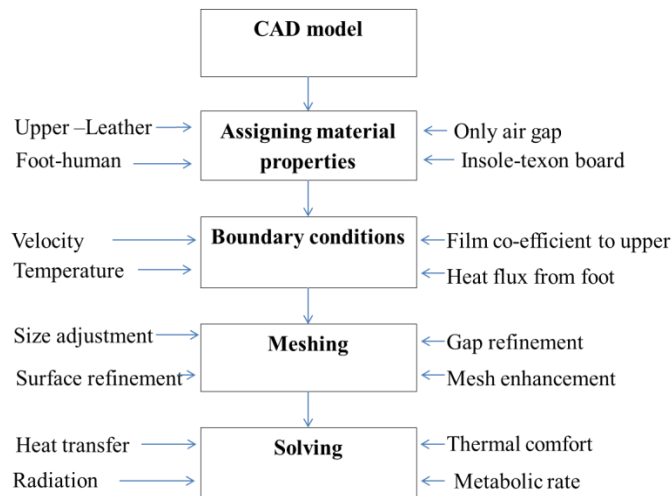


Fig. 1. Implementation of the simulation model

Considering the surrounding air is still, a film coefficient value of 5 W/m² K was used [17]. Reference temperature for film coefficient was equal to ambient temperature of the respective areas which was of around -20°C and 50°C respectively. Heat flux put into the system to represent the heat provided by blood flow. To consider the value of heat flux in CFD simulation, heat flux boundary condition was used on the surface of the human foot model. The value for the heat flux was taken from estimated whole body values of walking (at 1.3 m/s) 150 W/m² as presented by Cengel [18]. Here the foot surface area was about 7 percent of the whole body surface area.

Table 2. Detail dimensions of the CAD model

Shoe	Dimension	Unit
Size	43	Paris point

length	28.66	cm
width	9.25	cm
Upper(leather) thickness	0.08	cm
Insole(particle board) thickness	0.20	cm

Prior to running an Autodesk Simulation CFD analysis, the geometry is broken up into small pieces called elements. The corner of each element is a node. The calculation is performed at the nodes. These elements and nodes make up the mesh. The solution accuracy of any simulation largely depends on grid generation. Automatic mesh scheme followed by advanced mesh enhancement was used to generate fine mesh (Fig.2).

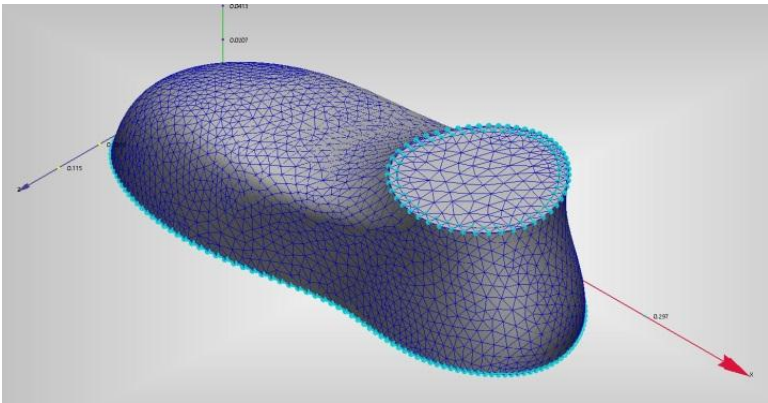


Fig. 2. Meshing view of the CAD model

To define how the simulation runs, the physics tab was used to enable physical models such as flow and heat transfer, the control tab to specify analysis parameters such as steady state or transient and to set the number of iterations and the adaptation tab was used to progressively improve the mesh by running the simulation multiple times. At the end of each run, Adaptation modifies the mesh based on the results, and uses the new mesh for the next cycle. The result is a mesh that is optimized for the particular simulation. Table 3 represents the solver settings.

Table 3. Solver settings

Solution parameters	Settings/Values
---------------------	-----------------

Heat transfer	On
Radiation	On
Thermal comfort	On
Metabolic rate	150 W/m ²
Humidity	50%
Clothing(socks)	0.74 clo
Iterations run	100

RESULTS AND DISCUSSION

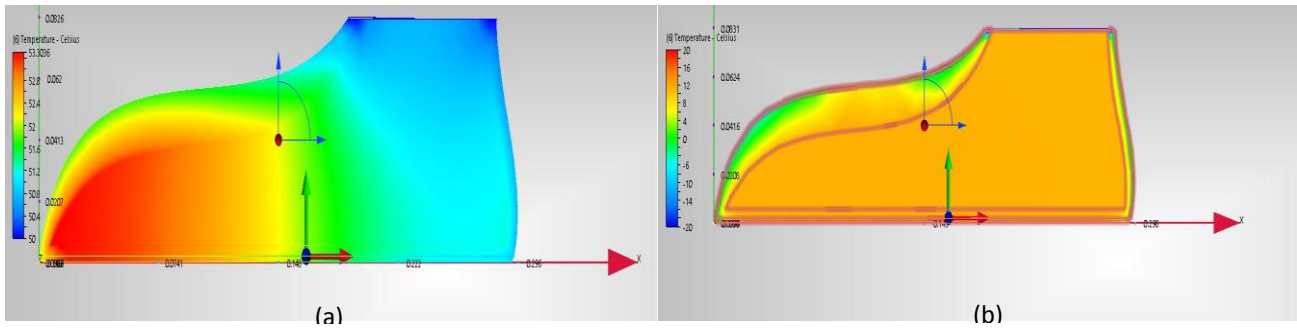


Fig. 3. Temperature distribution cut plane (a) for hot country (50°C) and (b) for cold country (-20°C) temperature

Assigned air of -20°C and 50°C temperature entered into the footwear and came in contact with the heat generating source (i.e. human foot) and got heated (Fig. 3). In this way temperature was distributed inside the footwear and increased due to the insulating property of footwear and remained between 11.1°C to 12.3°C and 51°C to 53.3°C respectively. In figure 3(a) continuous air flow from the opening of the footwear but in figure 3(b) no air flows within the footwear resulting from the close air tight opening of the footwear during wear in cold country.

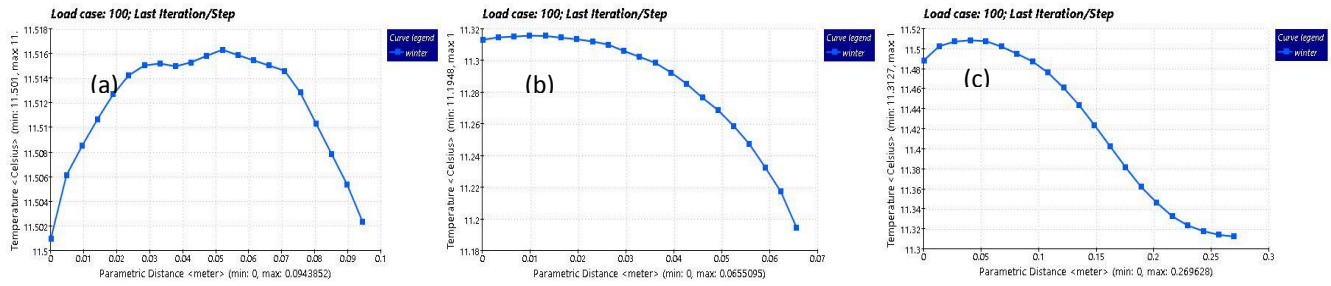


Fig. 4. Temperature profile at (a) toe portion, (b) heel portion and (c) bottom portion in case of cold country.

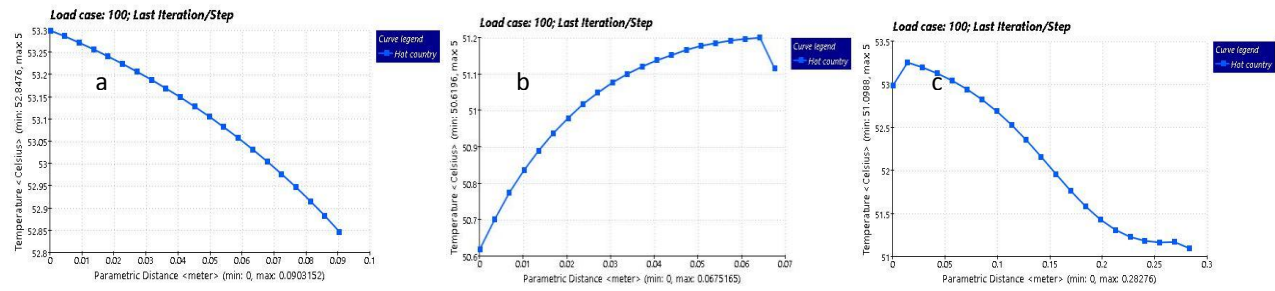


Fig. 5. Temperature profile at (a) toe portion, (b) heel portion, (c) bottom portion in case of hot country

The temperature profile at the toe, heel and bottom portion on XY plane (Fig.4) in case of cold country. It showed the vertical thermal stratification in the footwear. At the toe, heel and bottom portion the temperature was in the range of 11.50°C to 11.51°C, 11.20°C to 11.30°C and 11.32°C to 11.50°C respectively. The temperatures within the footwear were near the same in the entire toe, heel and bottom portion because of close air tight opening of the footwear and unavailability of air circulation. In the same way, the temperature profile at the toe, heel and bottom portion on XY plane (Fig.5) in case of hot country. At the toe, heel and bottom portion the temperature was in the range of 52.85°C to 53.3°C, 50.6°C to 51.2°C and 51.2°C to 53.3°C respectively whereas optimum and acceptable ranges of operative temperature for people during 50% relative humidity and mean air speed (≤ 0.15 m/s) are 22°C and 24.5°C according to ASHRAE [19]. The intensity of temperature within the footwear was much more at the toe portion than in the heel portion results due to the variation of air circulation at the opening of the footwear.

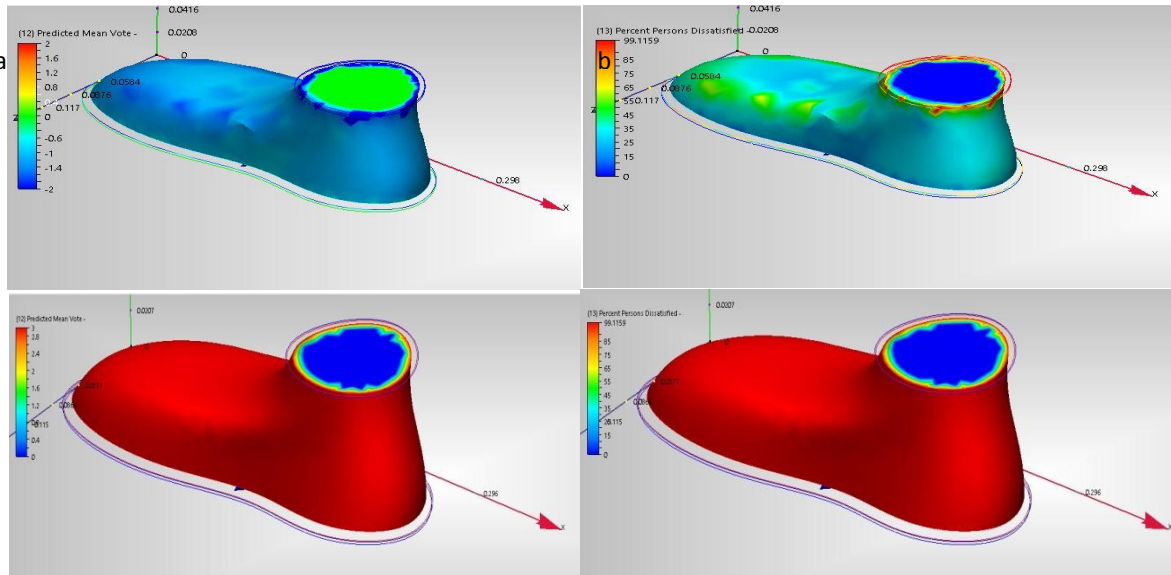


Fig. 6. Comparison of (a) PMV and (b) PPD among two different temperature regions

According to PMV, the occupant (human foot) felt very hot in the hot country, neutral to slightly cool in the cold country within the footwear according to ASHRAE thermal sensation scale (Table 4) and their PPD is up to 99.1% in hot country but up to 24% in cold country temperature (Fig. 6), whereas the acceptable thermal environment for general comfort are PMV, -0.5 to +0.5 and PPD, <10% [20] that means the footwear is near the comfort range only in cold country regions with closed air tight at the opening of the footwear.

Table 4. ASHRAE Thermal sensation scale

Value	Sensation
+3	Hot
+2	Warm
+1	Slightly warm
0	Neutral
-1	Slightly cool
-2	Cool
-3	Cold

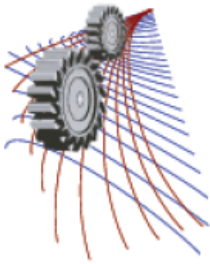
CONCLUSIONS

A simple 3D model has been developed successfully to simulate in-footwear temperatures in various locations using CFD simulation. These models covered two different temperature regions as boundary conditions. Predicted temperature distributions in the foot and shoe indicate greater heat transfer in the toe region in case of hot country but in the cold region temperatures were increased and distributed evenly. This model demonstrated a powerful approach to simulating in-footwear microclimate conditions, with promising results. The modeling results were then linked to the thermal comfort index to assist footwear manufacturers to design footwear with better thermal comfort. Occupant's (human foot) PMV and PPD values were not acceptable according to ASHRAE thermal sensation scale when used in hot country temperature due to felt hot in this

region. Because of very high temperature around the human foot experienced approximately 99.1% discomfort in this region. On the other hand PMV and PPD values were quite acceptable when the footwear was used in cold country temperature; hence the human foot felt neutral to slightly cool in this region according to ASHRAE thermal sensation scale. Here the human foot experienced only 25% discomfort which showed good option according to the foot comfort range. Now it can be concluded that the designed footwear model is comparatively best for use in cold country. This work will establish a base to develop more complex 3D thermal models, further to the coupled models, to cover both temperature and moisture. The techniques developed are also useful for modeling other microclimate conditions, such as in-glove, helmet and in-clothing environments.

REFERENCES

- [1] N. Sarier, E. Onder, Organic phase change materials and their textile applications: an overview, *Thermochim Acta* 2012; 540: 7–60.
- [2] D. Covill, Z. W. Guan, M. Bailey, H. Raval, Development of thermal models of footwear using finite element analysis, *Proc. IMechE, Engineering in Medicine*, 2 August 2010, Vol. 225 Part H: J.
- [3] K. Kuklane, Protection of feet in cold exposure, *Ind Health* 2009; 47: 242–253.
- [4] K. Kuklane, Y. Holmer, G. Giesbrecht, Change foot-wear insulation at various sweating rates, *J Physiol Anthropol Appl Hum Sci* 1999, 18: 161–168.
- [5] G. S. Song, Effect of floor surface temperature on blood flow and skin temperature in the foot, *Indoor Air* 2008, 18: 511–520.
- [6] D Cüneyt Sert, Governing Equations of Fluid Flow and Heat Transfer, *Finite Element Analysis in Thermo fluids*, ME 582.
- [7] Isidoro Martinez, *Properties of solids*, 1995-2015.
- [8] R. Joseph Kanagy, Specific Heats of Collagen and Leather, October 1955, Vol. 55, No. 4.
- [9] H. Ishii, Y. Sakurai, T. Maruyama, Effect of soccer shoe upper on ball behavior in curve kicks, *Scientific reports*, 14 August 2014.
- [10] D Brownleigh, Raleigh, Basics of non-contact temperature measurement, MICRO-EPSILON, 8120, NC 27617 / USA.
- [11] E. Charles Weir, Influence of Temperature and Moisture on the Electrical Properties of Leather, *Journal of Research of the National Bureau of Standards*, May 1952, Vol. 48, No. 5,.
- [12] XLiu, ZYue, Z Cai, D. G. Chetwynd, S. T. Smith, Quantifying touch–feel perception: tribological aspects, *Meas. Sci. Technol.*, February 2008.
- [13] Autodesk® Simulation CFD 2015, Commercial CFD Software, Student Version, © 2014 Autodesk Inc.
- [14] S. Samant, TRAVEL Top 10 Coldest Countries in the World, January 6, 2014.
- [15] S. Samant, TRAVEL Top 10 Hottest Countries in the World, June 13, 2014.
- [16] ANSI/ASHRAE Standard 55, Thermal Environmental Conditions for Human Occupancy, American Society of Heating, Refrigerating and Air-Conditioning Engineers, Inc., 1791 Tullie Circle NE, Atlanta, GA 30329, 2004.
- [17] Boundary Conditions in Simulation CFD, Intro to Simulation CFD for AEC Applications, Published on Autodesk University Workshop, Design Academy, Autodesk, Inc., 2014.
- [18] D. Covill, Z. W. Guan, M. Bailey, H. Raval, Development of thermal models of footwear using finite element analysis, *Proc. IMechE, Engineering in Medicine*, 2 August 2010, Vol. 225 Part H: J.
- [19] J. F. Kreider, *Handbook of Heating, Ventilation, and Air Conditioning*, CRC Press, Technology & Engineering - 680 pages, 26 Dec, 2000.
- [20] Proposed Addendum d to Standard 55-2004, Thermal Environmental Conditions for Human Occupancy, First Public Review, Sep 2008.



A Combined Process of Algal Bio-sorption and Chemical Coagulation Aided by Natural Coagulant: A New Approach of Tannery Waste Water Treatment

Subrata Paul^{a)}, Thuhin Kumar Dey and Rajan Kumar Raha

Department of Leather Engineering, Khulna University of Engineering & Technology, Khulna-9203, Bangladesh

^{a)} Corresponding author: skpaul.2k10@gmail.com

Abstract. Tannery in Bangladesh seems a source of pollution load and waste water to all because there are 270 registered tanneries where approximately 220MT raw hides and skins are taking for the production of leather in Bangladesh [1]. The leather industry has crossed the record \$1-billion mark in exports in 2013-2014 [2]. According to the Department of Environment, the tanneries discharge 22,000 cubic meters of untreated liquid toxic waste daily [3]. These pollution load and waste water should need treatment to make environment sustainable and living. From this point of view, we worked on tannery waste water processing. The paper highlights the initiation of Algal treatment with chemical coagulation process aided by natural coagulant in waste water processing in Bangladesh. The methodology of this process starts with mixing of waste water from different section of beam house operations at a definite ratio. The mixer takes nearly six hours to settle down. After sedimentation, the turbidity decreases at a reasonable amount i.e. 1428 NTU whereas before sedimentation it was 9050 NTU (2100P Turbid Meter of HACH). Later the supernatant was collected for algal treatment. After algal treatment the turbidity reduced to 530 NTU from 1428 NTU and the DO level increased up to 4.48 mg/L at 33.6 °C (HQ 40d of HACH) where DO level was 0.24 mg/L at 33.6°C in raw mixer. In addition, the amount of alum was reduced in tannery waste water treatment by using snail shell powder as coagulant aid in conjunction with alum [4]. In case of untreated sample after sedimentation required alum dosing was 6mL/40 mL sample. After algal treatment, required alum dosing reduced to 4 mL/40 mL sample. By adding 3mL/40mL natural coagulant as coagulant aid, alum dosing was further minimized to 1mL/40mL sample. The odour was more tolerable than raw mixer after algal treatment but after adding alum aided by natural coagulant, the odour was more acceptable than before. The diversified technique can hopefully reduce a reliable chemical cost in treatment process, considerable amount of pollution load & increase DO level and thus make effluent environment friendly to discharge. Finally the DO level increases up to 6.56 mg/L at 33.7 °C and turbidity reduces to 183 NTU, pH reduces to 7.6, odour turns to be tolerable limit.

INTRODUCTION

Tanning is one of the oldest leather manufacturing processes which is highly complex and is characterized by high suspended solids, settleable solids, sulphide, chloride and chromium etc. When untreated tannery effluents are discharged directly into the water bodies or into the open lands, they cause irreversible damage to the environment. As a result, the Tanning Industry is one of the industries which is considered as a highly polluting industry [5]. Tanneries generate wastewater in the range of 30 - 35 L/kg skin or hide processed with variable pH and high concentrations of suspended solids. Major problems are due to wastewater containing heavy metals, toxic chemicals, chloride, lime with high dissolved and suspended salts and other pollutants [6]. Due to the inherent characteristics of tannery effluents, various physico-chemical techniques have been studied for their applicability to the treatment of tannery wastewater. Among these are coagulation, flocculation, ozonation, reverse osmosis, ion exchange and adsorption [7].

Biosorption of heavy metals by algal biomass is an advantageous alternative, an appropriate and economically feasible method used for wastewater and waste clean-up, because it uses algal biomass, sometimes considered waste from some biotechnological processes or simply its high availability in coastal areas, which makes it suitable for

developing new by-products for wastewater treatment plants[8]. The use of the dead cells offers several advantages: metal removal system is not subjected to metal toxicity, limitations, there is no requirement for growth media and nutrients, and adsorbed heavy metals can easily be desorbed and the biomass can be reused [9]. Algae have proved to possess high metal binding capacities due to the presence of polysaccharides, proteins or lipid on the surface of their cell walls containing some functional groups such as amino, hydroxyl, carboxyl and sulphate, which can act as binding sites for metals [10].

Coagulation indicates the process which colloidal particles and very fine solid suspensions are destabilized, so that they can begin to agglomerate if the conditions are appropriate. Flocculation refers to the process by which destabilized particles actually conglomerate into larger aggregates so that they can be separated from the wastewater [11]. Coagulant chemicals with charges opposite those of the suspended solids are added to the water to neutralize the negative charges on non-settleable solids (such as clay and color-producing organic substances). Once the charge is neutralized, the small suspended particles are capable of sticking together. These slightly larger particles are called microflocs, and are not visible to the naked eye [12]. Aluminum sulfate (alum), ferrous sulfate, ferric chloride and ferric chloro-sulfate were commonly used as coagulants [11].

While the effectiveness of these chemicals as coagulants is well-recognized, there are, nonetheless, disadvantages associated with usage of these coagulants such as ineffectiveness in low-temperature water, relatively high procurement costs, detrimental effects on human health, production of large sludge volumes and the fact that they significantly affect pH of treated water. There is also strong evidence linking aluminum-based coagulants to the development of Alzheimer’s disease in human beings [13]. It is therefore desirable to reduce the amount of chemical coagulant for wastewater treatment. In this paper this is done by combining coagulation with biosorption.

Coagulant aids are chemicals which are added to water during coagulation to improve coagulation, build a stronger, more settleable floc, reduce the amount of coagulant required and reduce the amount of sludge produced [14]. Here the amount of chemical coagulant is further reduced by using snail shell powder as a natural coagulant.

METHODOLOGY

Sample Collection

Samples were collected from a renowned tannery nearby KUET campus. Collected samples were different sections of beamhouse operations i.e. soaking, liming, delimiting & bating, pickling & chrome tanning.

Beamhouse Operations

Beamhouse operations are the initial stage of leather processing in tannery. The steps in the production of leather between curing to tanning are collectively referred to as beamhouse operations. The stepwise processes namely pre-soaking, soaking, liming, delimiting, bating, pickling and tanning are considered as beamhouse operation. The beamhouse operation has great importance for leather production. The flow chart for beamhouse operations from wet salted hide or skin is shown in below [15].

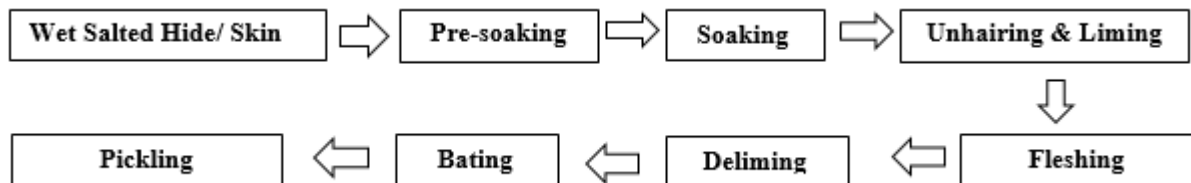


FIGURE 1. Flow chart of beam house operations.

Settling of Suspended and Insoluble Materials

Settling operation was the preliminary operation of this work. In this stage, samples were mixed in a beaker with a definite ratio 2:1:1:1 of different waste liquors i.e. soaking, liming, delimiting & bating and pickle & chrome liquor.

They were agitated properly to mix up well and kept up to 5-6 hours maximum for significant settling down. A continuous study represents that approximately 700 mL supernatant liquid was collected from the 1000 mL beaker where 300 mL was liquid & suspended mixture (Sludge). By considering the settled sample as raw, different environmental parameters of the raw sample were measured.



FIGURE 2. Before settling.



FIGURE 3. After settling.

Materials

The materials used for the desired treatment process are micro algae of Chlorophyta group, alum as coagulant and snail shell powder as coagulant aid. This algae is highly available in the rural area, urban area, ponds, lakes, rivers etc. The green algae are a large, informal grouping of algae consisting of the Chlorophyte and Charophyte algae. The algae were collected near KUET campus from a lake. The algae were washed well thoroughly by continuous water flow. They were dried for two days in an oven at 50-60 °C for conditioning to protect from fungal attack and putrefaction. After conditioning they were grinded carefully and isolated micro particles by sieving. The alum used in the treatment process was reagent grade. Alum is grinded well and prepared a solution of alum in the concentration of 10 g/L. Snail shell is collected from rural area. It was washed well with continuous water flow and dried well. Then it was grinded well and prepared snail shell power solution in the concentration of 10 g/L. In this way, materials were prepared for the treatment process.

Algal Dosing

Algal dosing is the process of choosing optimum amount of required algae and given best performance on the basis of pH, time and some essential parameters. Optimum dose of algae was selected on the basis of percentage adsorption of suspended solids by different amount of algae at different pH and time. To do so firstly, 6 beakers each of 50 mL volume were taken and each of all the beakers was poured to 40 mL of raw sample. Then 0.1 g, 0.2 g, 0.3 g, 0.4 g, 0.5 g algae were taken in different beakers and kept them for 2.5hrs. After that percentage adsorption of suspended solids by different amount of algae was calculated and was selected the best one. Secondly, 4beakers each of 50ml size was filled by 40 mL of raw sample each was taken and was maintained different pH like 5.0, 6.0, 7.0 and 8.0 by using desired quantity of 0.1 N hydrochloric acid. After that all the samples were treated with the above selected optimum amount of algae for 2.5 hours and percentage adsorption of suspended solids at different pH was calculated and was selected the best one. The selected dose of algae is 0.3 g/ 40 mL i.e. 7.5 g per one liter of raw sample at pH 6.0 and time duration is 2.5 hours.

Algal Treatment Process

The algal treatment process starts with the application of definite amount of algae in the supernatant liquid (waste water) obtained from settling operation. The treatment process was run into normal condition. In this process, the required essentials are

- Algae
- Beaker (50 mL)
- Analytical balance
- Filter (Locally available)
- pH meter
- Oven
- Measuring Cylinder (10 mL & 50 mL)
- Stirrer

At the beginning of treatment process, 40 mL of waste water was taken by the help of measuring cylinder (50 mL capacity) and poured into a beaker (50 mL capacity). Then adding hydrochloric acid to maintain solution pH 6.0. The optimum dose of algae selected for the 40 ml waste water processing is 0.3 g. That amount of algae was measured with the help of analytical balance. The measured amount of algae was poured into the waste water and mixed with the waste water by the help of stirrer. The mixture was kept for two and half hours for the treatment process. After treatment, turbidity, DO level, pH were measured. A pretty good result was obtained.

Coagulant Dosing for Raw Sample

After settling operation, raw sample maintaining pH 6.0 was treated with different amount of alum as chemical coagulant to select dosing. From raw sample, 40 mL of raw sample was taken for each beaker. Alum solution was added to each beaker in sequential manner 3 mL, 4 mL, 5 mL, 6 mL and 7 mL and vigorously stirred the sample for five minutes. Then stirred the sample slowly for 10 minutes. After stirring, provided rest for thirty minutes and checked out whether settling starts or not. Then 10 mL of upper solution was taken for suspended solids measurement.

Coagulant Dosing for Algal Treated Sample

At first five beakers about 50 mL were taken. Then the beakers were conditioned in oven and measure the weight of each beaker after drying. About 40 mL algal treated sample was taken in each beaker. Then alum dosing were made in the treated sample in each beaker. Then 1mL, 2mL, 3mL, 4mL, 5mL solution of alum were added sequentially in the five beakers and vigorously stirred the sample for five minutes. Then the sample was stirred slowly for 10 minutes. After stirring, provided rest for thirty minutes and checked out whether settling starts or not. Then 10 mL of upper solution was taken for the measurement of suspended solids.

Optimization of Chemical by Using Snail Shell Powder as Natural Coagulant

The amount of alum for the processing of algal treated waste water can be partially reduced by adding snail shell powder as coagulant aid. Three beakers were taken and conditioned properly. In first beaker, 40 mL treated sample was taken and add Alum with snail shell powder with the ratio of 50:50 (Alum: snail shell powder). In second beaker, Alum with snail shell powder solution was added in 40 ml sample with the ratio of 45:55 (Alum: snail shell powder). In third beaker, Alum with snail shell powder solution was added in 40 ml sample with the ratio of 33:67 (Alum: snail shell powder). Then 10 mL of upper solution was taken for the measurement of suspended solids. Equation for the calculation of percentage of absorbance.

RESULTS AND DISCUSSION

The amount of suspended solid was 47550 mg/L without algal treatment. The following tables represent the optimization of algal dosing for 40 mL solution.

TABLE 1. Effect of amount of algae.

No of Beaker	Amount of Algae (g)	Absorbed (mg/L)	Percentage of absorbance (%)	Remarks
1	0.1	20680	43.49	Accepted
2	0.2	11070	23.28	
3	0.3	28450	60.00	
4	0.4	8580	18.00	
5	0.5	23360	49.13	

TABLE 2. Effect of pH on algae.

No of Beaker	pH	Absorbed (mg/L)	Percentage of absorbance (%)	Amount of algae (g)	Remarks
1	5.0	23890	50.00	0.3	Accepted
2	6.0	30250	63.00	0.3	
3	7.0	20640	43.00	0.3	
4	8.0	24550	51.63	0.3	
5	Raw	25100	52.78	0.3	

From table 1, 2 it is noticed that the percentage absorbance of suspended solids by algae is fluctuated. There may be different reasons: algal bleeding, optimum condition, pH range, time and so on and the selected dose of algae is 0.3 g/ 40 mL of raw sample at pH 6 and time duration two and half hours.

The total amounts of suspended solids for different dosing of alum are given below:

TABLE 3. Coagulant dosing for raw sample.

No of Beaker	Amount of Alum (mL)/ 40 mL [Solution Concentration 10 g/L]	Amount of Suspended Solids (mg/L)	Remarks
1	3 mL	29046	Accepted
2	4 mL	28356	
3	5 mL	26750	
4	6 mL	24900	
5	7 mL	24578	

The total amounts of suspended solids for different dosing of alum after algal treatment are given below:

TABLE 4. Coagulant Dosing after Algal Treatment.

No of beaker	Amount of alum (mL)/ 40 mL [Solution Concentration 10 g/L]	Amount of Suspended Solids (mg/L)	Remarks
1	1 mL	14370	accepted
2	2 mL	12890	
3	3 mL	11050	
4	4 mL	9920	
5	5 mL	9610	

The total amounts of suspended solids through optimization of chemical coagulant by using natural coagulant are given below:

TABLE 5. Optimization of chemical coagulant by using snail shell powder as natural coagulant.

No of beaker	Amount of Alum with snail shell powder (mL)/ 40 mL [Solution Concentration 10 g/L]	Alum: Snail Shell Powder Solution	Amount of Suspended Solid (mg/L)	Remarks
1	2.0 mL + 2.0 mL	50:50	8425	
2	1.4 mL + 2.6 mL	44:56	8100	
3	1mL + 3mL	33:67	7820	Accepted

From table 3, 4, 5 it is noticed that the amount of suspended solids reduced in a sequential manner. Finally the amount of suspended solids reduced to 7820 mg/ L from 47550 mg/ L.

Different environmental parameters are measured of raw sample by the utilization of different devices. Some environmental parameters of raw sample and the devices used for the measurement are given in the table 6.

TABLE 6. Environmental parameters (raw sample) and devices.

Parameter	DO	Turbidity	pH	Salinity	Conductivity
Raw Sample	0.25 mg/L at 33.7 °C	873 NTU	9.1	24.4 ppt. at 33.7 °C	45.00 mS/ m at 33.6 °C
Device	HQ 40d of HACH	2100P Turbid Meter of HACH	EZDO PH5011	BOECO CT-676	BOECO CT-676

After combination treatment i.e. algal treatment and chemical coagulation aided by natural coagulant some environmental parameters are measured of treated sample by the utilization of different devices. Some environmental parameters of treated sample and used devices for measurement are given in table 7.

TABLE 7. Environmental parameters (treated sample) and devices.

Parameter	DO	Turbidity	pH	Salinity	Conductivity
Treated Sample	6.56 mg/L at 33.6 °C	183 NTU	7.6	18.1 ppt. at 33.7 °C	33.46 mS/m at 33.6 °C
Device	HQ 40d of HACH	2100P Turbid Meter of HACH	EZDO PH5011	BOECO CT-676	BOECO CT-676

By comparing table 6 & 7, it is observed that a pretty good result is obtained. The DO level of treated sample is increased 6.56 mg/ L at 20 °C from 0.25 mg/L at 20 °C of raw sample (waste liquor). Another two parameters measured are also reduced to a significant amount; i.e. the former turbidity was 873 NTU and after treatment it is reduced to 183 NTU. The pH is measured i.e. 7.6 which is in a safe level. The discharge limit of water to environment is 6-9 pH [16].

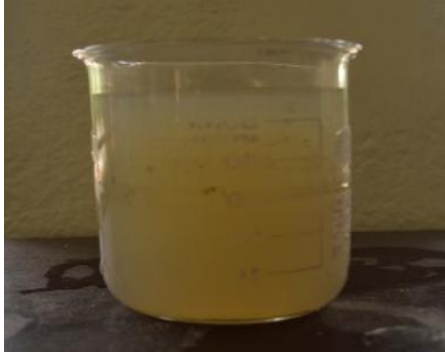


FIGURE 4. Before Treatment.



FIGURE 5. After Treatment.

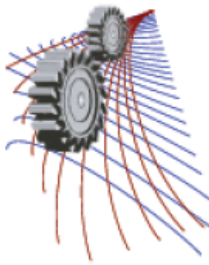
CONCLUSIONS

Dead algal biomass is a useful alternative to conventional adsorption products for heavy metal uptake from tannery effluents. But the development of bio-sorption processes using algal biomass requires further investigation, with particular attention to: Selectivity of algal species, Regeneration and reusability of algal biomass, Simulation and modelling of processes etc. After the usage of green algae as bio-sorbents with chemical coagulation process aided by snail shell powder as natural coagulant shows good efficiency of reducing pollution load from tannery waste water. During the thesis work, we use 0.3 g algae at pH 6.0 within 2.5 hours duration for treating 40 mL sample. After treatment of sample with algae, amount of waste particles reduced from 47550 mg/L to 28880 mg/L. That means 60.73% absorbance obtained by using such amount of algae. Therefore, it can be concluded that green algae can be used as bio-sorbents in treatment process. Moreover, snail shell powder can be used as coagulating aid with alum in waste water treatment process. In the thesis work, we select 4mL alum solution as optimum dosing. By using such amount in algal treated sample, the amount of total waste particles reduced to 9920 mg/L. For the purpose of aiding the coagulation process, we select 1mL alum with 3 mL snail shell powder solution as optimum dosing of aiding solution. Such amount reduces the amount of waste particles to 7820 mg/L. Thus, the dosage of alum used originally for treatment can be reduced during waste water treatment. The use of this approach overall can provide solution to the need for reduction of pollution load from waste water of tannery without being exposed to potential health hazard.

REFERENCES

1. http://www.worstpolluted.org/projects_reports/display/111(Nov 21, 2015)
2. <http://www.thedailystar.net/leather-industry-hits-record-exports-1b-23968>(Nov 21, 2015)
3. <http://ourworld.unu.edu/en/colours-of-water-bangladeshs-leather-tanneries>(Nov 21, 2015)
4. B. Bina, M. H. Mehdinejad, M. Nikaeen and H. Movahedian Attar, Effectiveness of Chitosan as Natural Coagulant Aid in Treating Turbid Waters, Iranian Journal of Environmental Health Science & Engineering, 2009, 6 (4), pp. 247-252.
5. <http://ourworld.unu.edu/en/colours-of-water-bangladeshs-leather-tanneries>(Nov 21, 2015)
6. G. Durai, M. Rajasimman and N. Rajamohan, Kinetic Studies on Biodegradation of Tannery Wastewater in a Sequential Batch Bioreactor, Journal of Biotech Research, 2011, 3, pp. 19-26.
7. M. A. Aboulhassan, S. Souabi and A. Yaacoubi, Pollution Reduction and Biodegradability Index Improvement of Tannery Effluents, International Journal Environment Science and Technology, 2008, 5 (1), pp. 11-16.
8. L. Brinza, M. J. Dring and M. Gavrileskul, Marine Micro and Macro Algal Species as Biosorbents for Heavy Metals, Environmental Engineering and Management Journal, 2007, 6 (3), pp. 237-251.
9. A. Wike, R. Buchholz and G. Bunke, Selective Biosorption of Heavy Metals by Algae, Environmental Biotechnology, 2006, 2 (2), pp. 47-56.
10. V. K. Gupta and A. Rastogi, Biosorption of Lead from Aqueous Solutions by Green Algae Spirogyra Species: Kinetics and Equilibrium Studies, Journal of Hazardous Materials, 2008, 152, pp. 407-414.

11. H. Farajnezhad and P. Gharbani, Coagulation Treatment of Wastewater in Petroleum Industry Using Poly Aluminium Chloride and Ferric Chloride, International Journal of Recent Research and Applied Studies, 2012, 13 (1), pp. 306-310.
12. N. B. Prakash, V. Sockan and P. Jayakaran, Waste Water Treatment by Coagulation and Flocculation, International Journal of Engineering Science and Innovative Technology, 2014, 3 (2), pp. 479-484.
13. T. Kazi1 and A. Virupakshi, Treatment of Tannery Wastewater Using Natural Coagulants, International Journal of Innovative Research in ScienceEngineering and Technology, 2013, 2 (8), pp. 4061-4068.
14. http://water.me.vccs.edu/exam_prep/coagulants.htm(Nov 21, 2015)
15. M. A. Hashem, A. Islam, S. Paul and S. Nasrin, Generation of Ammonia in Deliming Operation from Tannery and Its Environmental Effect: Bangladesh Perspective, International Journal of Renewable Energy and Environmental Engineering, 2014, 2 (4), pp.266-270.
16. <http://www.nea.gov.sg/anti-pollution-radiation-protection/water-pollution-control/allowable-limits>(Nov21,2015)



Effect of Mn on Microstructure and Mechanical properties of Al-2wt%Zn-2wt%Mg alloy

Md. Sarower Hossain Tareq^{a)}, Dr. HMMA Rashed^{b)} Roisul Hasan Galib^{c)}
Tanzilur Rahman^{d)} Md. Abdul Aziz Antor^{e)} Md. Asif Anowar^{f)}

*Department of Materials and Metallurgical Engineering, Bangladesh University of Engineering & Technology,
Dhaka 1000.*

^{a)}Corresponding author: tareqsarower30@gmail.com

^{b)}hrashed@mme.buet.ac.bd

^{c)}roybds@gmail.com

^{d)}tanzil.mmebuet@gmail.com

^{e)}antormme@gmail.com

^{f)}asifanwaraman91@gmail.com

Abstract. The effects of Mn (up to 0.8 wt.%) on microstructure and mechanical properties of Al-2wt% Zn-2 wt% Mg alloy was investigated. It was found that Mn modifies the microstructure by changing shapes and distribution of intermetallic particles in matrix phase. The amount of intermetallic particles were also reduced. Mn transformed the distribution of intermetallic particles from continuous network to dispersed phase. These changes in microstructure were examined by optical microscope and scanning electron microscope (SEM). Combining of these effects, the mechanical properties were enhanced, as confirmed by hardness and tensile testing. With the increment of Mn up to 0.8 wt% in the base alloy the ultimate tensile strength gradually increased while percentage of elongation reduced significantly. Addition of Mn also gradually increased the hardness of the alloy. These increment in strength and hardness and reduction in ductility occurred due to the changes of distribution of intermetallic phase.

INTRODUCTION

Al alloys are beneficial in both automobile and aerospace industries mostly due to their inherent lightness and ability of precipitation hardening to obtain a good weight-to-strength ratio [1]. As alloying elements, silicon, copper, zinc and magnesium are being used for the last couples of decades in Al base alloys to enhance mechanical properties and corrosion resistance [2-5]. The required window for heat treatment alloys limits the amounts of alloying elements that can be added to modify the composition [5]. Addition of Zn and Mg in Al helps to improve mechanical properties and makes the alloy weldable [6-8]. Al-Zn-Mg alloys are mostly used for Light weight military bridge, Aircraft construction, Motor cycle and other structural components. Research have been carried out to increase mechanical and other chemical properties by adding different alloying elements. It has high industrial important to find out the effect of different alloying element in the alloy to find the best combination of desired properties in application. This research work was carried out to investigate the influence of Mn addition in microstructure and mechanical properties in Al-Zn-Mg alloy.

EXPERIMENTAL

To make the respective alloys commercially pure Al, Zn, Mg and 99.9% pure Mn powder were used. Base alloy was prepared by taking 2wt% Zn, 2wt%Mg and rest Al. To investigate the effect of Mn three different alloys were prepared by changing the wt% of Mn content i.e, 0.2wt% (alloy-1), 0.6wt% (alloy-2) and 0.8% (alloy-3). The compositions used in the experiment are shown in Table-1

Table-1: Composition of different alloys used in the experiment

	Wt.% Al	Wt.% Zn	Wt. % Mg	Wt. % Mn
Base alloy	Balance	2.0	2.0	0
Alloy-1	Balance	2.0	2.0	0.2
Alloy-2	Balance	2.0	2.0	0.6
Alloy-3	Balance	2.0	2.0	0.8

At first Zn was placed into a graphite crucible and melted in a gas fired pit furnace. Then Al pieces and at last Mg were mixed slowly in the melted Zn. The melt was stirred slowly to homogenize at about 6000c. For alloys except base alloy Mn powder was added and stirred slowly to distribute Mn in whole melt. Before adding Mn upper layer of melt was skimmed off. Then the melt was poured in a preheated rectangular shaped metal mold. Composition of the alloys were investigated by OES. Cubic samples were prepared for microstructure analysis. The as-cast alloys were fine polished on a polishing wheel using γ -alumina powder as polishing medium. Non-ferrous metallographic fine polishing standard technique was carried out with 0.5 μ m γ -Al₂O₃ particles in order to obtain the microstructure. Keller's reagent was used as etching reagent. The samples were observed by an optical microscope (LEICA-MZFLIII, Italy). Polished cubic samples were used to measure Rockwell hardness in F scale. The ingots were mechanically machined into tensile specimens with a gauge length marked 25.00 mm for each sample as per sub-standard size of the ASTM E8/E8M-11 and the width and thickness of the samples were 6.00 mm and 5.00 mm respectively. Tensile tests were carried out with a universal testing machine (Instron 3369 Universal Testing Machine) at a strain rate of 3.00 mm/min at 25°C to obtain data on the stress–strain curves containing information of elongation at fracture and UTS.

RESULT AND DISCUSSION

OES analysis

The actual composition of the alloys were ensured by OES analysis. The composition found rom OES are given below in Table-2

TABLE-2: OES analysis result

Sample	Al (%)	Zn (%)	Mg (%)	Mn (%)	Si (%)	Fe (%)
Commercially Pure Al	98.9	-	-	-	0.89	0.35
Commercially Pure Zn	-	99.05	-	-	0.67	0.21
Commercially Pure Mg	0.04	-	99.82	-	0.15	-
Base alloy	95.6	2.20	1.85	-	0.09	0.04
Alloy-1	94.8	2.1	1.74	0.16	0.15	0.06
Alloy-2	96.02	1.95	1.87	0.63	0.06	0.04

Alloy-3	95.78	2.26	1.74	0.76	0.03	0.02
---------	-------	------	------	------	------	------

From the table it is seen that there are some loss of Mg %wt for each alloy compositions. It might be due to its high reactivity.

Microstructural Changes

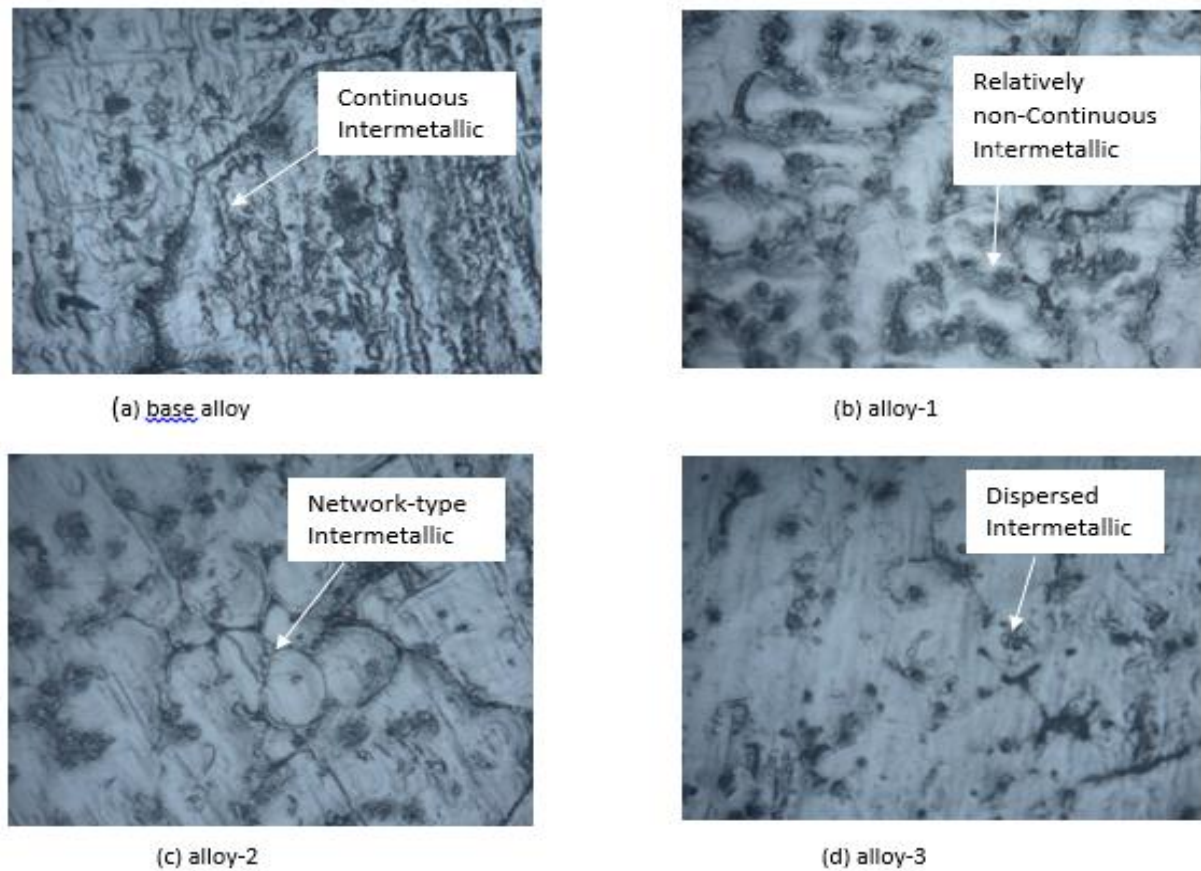


FIGURE 1. Optical micrograph of (a) base alloy, (b) alloy-1, (c) alloy-2, (c) alloy-3

Microstructure of the cast alloy contains intermetallic compound in Al matrix phase. As in most other Al alloys, Al solid solution forms the matrix, into which the other phases are dispersed. The region where the ratio of Zn to Mg is over 2, $MgZn_2$ intermetallic forms and where the ratio is lower, $Mg_3Zn_3Al_2$ forms. With the addition of Mn in the base alloy a changes in size and distribution has been observed. Addition of Mn changed the distribution of intermetallic particles from continuous to dispersed phase in the matrix. In base alloy (Fig.1,a) intermetallic are seen to be continuous whereas with addition of Mn the intermetallic gradually transformed into dispersed phase in alloy-3 (Fig.1,d) through network form in alloy-2 (Fig.1,c). Finally for 0.8% Mn the intermetallic are seen to be completely dispersed.

Changes in Mechanical properties

Addition of Mn gradually increased tensile strength of the alloys. Table-3 shows the changes of tensile strength with increment of wt. %Mn.

TABLE-3: changes of UTS with wt. % Mn

	Base alloy	Alloy-1	Alloy-2	Alloy-3
%Mn	0	0.2	0.6	0.8
UTS (MPa)	164.1	182	194	205

From above table it is seen that in base alloy tensile strength was 164.1 MPa whereas it increased up to 205 MPa in alloy-3 for 0.08% Mn. With the increment of Mn ductility of the materials also decreased considerably. Table-4 depicts the reduction of ductility of the alloy with increment of Mn.

TABLE-4: Changes of max. elongation before fracture with wt. %Mn

	Base alloy	Alloy-1	Alloy-2	Alloy-3
%Mn	0	0.2	0.6	0.8
%Strain	20.6	12.17	8.89	7.14

Base alloy showed maximum elongation up to 20.6% strain. Which with the addition of Mn decreased to 7.14% strain until 0.8% manganese in alloy-3.

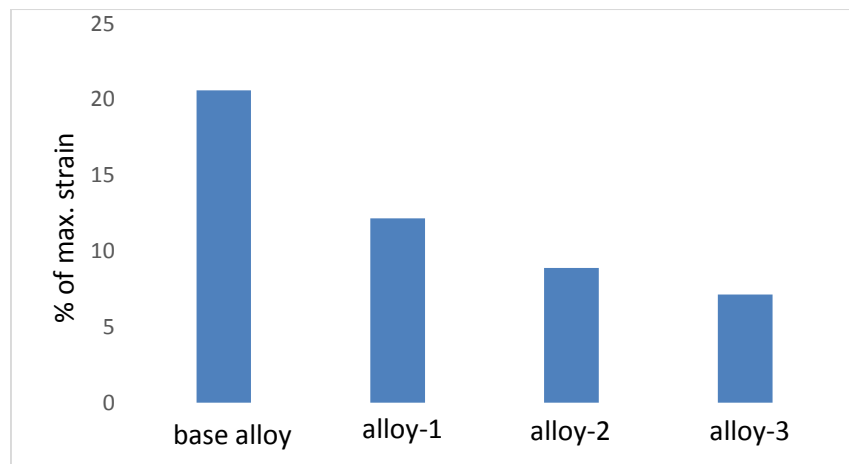


FIGURE 2. Changes of max. elongation before fracture with wt%Mn

From Fig.2 it is seen that initially this reduction of maximum elongation was more abrupt from base alloy to alloy-1 and then it decreased gradually until alloy-3. The reason of increasing strength and decreasing ductility can be related with the changes in microstructure. Science with the addition of Mn intermetallic compounds gradually changed into

dispersed phase they hindered dislocation motion more effectively by pinning effect. Thus the movement of dislocation became more difficult and increased the strength of the alloy. This difficulties in movement of dislocation reduced the maximum elongation of the alloy before fracture and reduced its ductility. Addition of Mn also increased the hardness of the alloys gradually as obtained by Rockwell hardness testing machine. The changes of hardness with increment of wt. %Mn in base alloy are given in table-5

TABLE-5: Changes of Rockwell hardness with wt. %Mn

	Base alloy	Alloy-1	Alloy-2	Alloy-3
%Mn	0	0.2	0.6	0.8
Hardness (HRF)				
Load: 60 kg	61.2	80.2	82.5	90.2

CONCLUSION

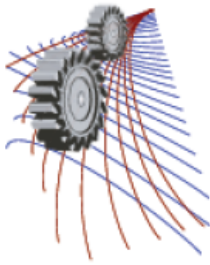
Changes of microstructure and mechanical properties due to addition of Mn in Al-2wt% Zn-2 wt% Mg were studied in the work. It was found that Addition of Mn has significant effect in microstructure and mechanical properties of the alloy. Addition of Mn changed the microstructure by changing distribution of the intermetallic in the matrix phase. This change in microstructure due to addition of Mn considerably increased tensile strength and reduced its maximum elongation before fracture by effective pinning action of dislocation. Hardness of the alloys also increased with increment of wt. %Mn.

ACKNOWLEDGEMENTS

The authors would like to thank Bangladesh University of Engineering and Technology (BUET) in funding the present research.

REFERENCE

1. Davis, J. R. (1993). Aluminum and aluminum alloys. J. R. Davis (Ed.). ASM international.
2. Kim, Y. W. (1989). Intermetallic alloys based on gamma titanium aluminide. *Jom*, 41(7), 24-30.
3. Kulekci, M. K. (2008). Magnesium and its alloys applications in automotive industry. *The International Journal of Advanced Manufacturing Technology*, 39(9-10), 851-865.
4. Davis, J. R. (Ed.). (1999). Corrosion of aluminum and aluminum alloys. Asm International.
5. Vargel, C. (2004). Corrosion of aluminium. Elsevier.
6. Aluminum Association. (1984). Aluminum: properties and physical metallurgy. J. E. Hatch (Ed.). ASM International.
7. Zhao, L. M., & Zhang, Z. D. (2008). Effect of Zn alloy interlayer on interface microstructure and strength of diffusion-bonded Mg–Al joints. *Scripta Materialia*, 58(4), 283-286.
8. Honma, T., Ohkubo, T., Kamado, S., & Hono, K. (2007). Effect of Zn additions on the age-hardening of Mg–2.0 Gd–1.2 Y–0.2 Zr alloys. *Acta Materialia*, 55(12), 4137-4150.
9. Yuan, G. Y., Liu, Z. L., Wang, Q. D., & Ding, W. J. (2002). Microstructure refinement of Mg–Al–Zn–Si alloys. *Materials Letters*, 56(1), 53-58.



A Comprehensive Review of Soot Formation in Diffusion Flame at Microgravity Conditions

Avik Ray^{1, a)}, Arup Jyoti Bhowal^{2, b)} and Bijan Kumar Mandal^{3, c)}

^{1,3}Department of Mechanical Engineering, Indian Institute of Engineering Science and Technology, Shibpur, Howrah – 711103, West Bengal, India.

²Department of Mechanical Engineering, Heritage Institute of Technology, Chowbaga Road, Anandapur, Kolkata-700 107, West Bengal, India.

^{c)}Corresponding author: bkm375@yahoo.co.in

^{a)} ray.avik2014@gmail.com

^{b)} arupjyoti.bhowal@heritageit.edu

Abstract. This paper is the outcome of the literature survey on soot formation in diffusion flames under reduced gravity conditions. The analysis of the results of different studies shows that the soot volume fraction in microgravity flame is nearly a factor of two higher than that at normal gravity flame. Microgravity flames are brighter and produce more soot because the residence time for soot formation is longer. Axial velocity along the flame centerline decreases by more than 50% in microgravity flame compared to buoyant flame. Microgravity flame is momentum controlled whereas normal gravity diffusion flame is buoyancy controlled. Peak soot temperature under lower gravity is found to be lower than normal gravity flame by a magnitude of around 200 K. In case of microgravity heat loss through radiation is higher mainly due to the higher occurrence of soot.

INTRODUCTION

In recent times, more than eighty percent of the worldwide used energy is generated by the combustion of fossil fuels. The emissions of soot particles, NO_x and other pollutants formed during combustion lead to global warming and health hazard. Fundamental understanding of combustion process is required to design efficient combustion device with minimum emission. Combustion takes place in non-premixed (also called diffusion) flame and premixed flame modes. Diffusion flame is one of the most commonly used flames where oxidizer combines with fuel in the combustion chamber by diffusion. The main problem with diffusion flame is the soot formation. Three distinct zones in diffusion flame are observed as demonstrated by Warnatz *et al.* [1]. The three zones are soot free zone, soot growth zone and soot oxidation zone as shown in Fig.1.

MICROGRAVITY

Now-a-days, the combustion under microgravity has drawn attention of the combustion researchers. In microgravity condition, the gravity force is almost zero. That is why combustion phenomenon is very much different in microgravity compared to normal gravity combustion. The absence of the buoyancy induced flow in microgravity environment results in an increase in the reactant residence time, which also has effects on the processes like stability, radiation, soot formation and soot oxidation in the flame. Combustion research in this area is essential for improving spacecraft safety. With this in the background, the authors have attempted to review the progress in microgravity combustion based on the recent experimental as well as numerical studies available in the literature. Although the main focus of the review work is on soot formation, other relevant parameters of diffusion flame such as flame length, temperature and velocity have also been looked in to get a better understanding of soot formation.

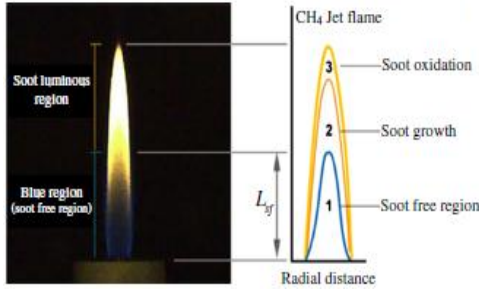


FIGURE 1. Schematic diagram of three zones of laminar methane and air diffusion flame [1]

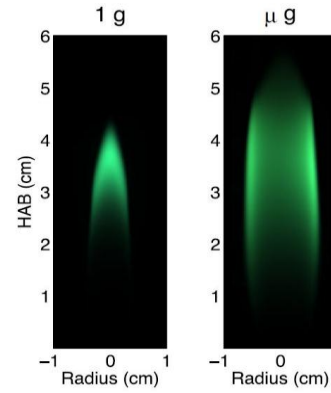


FIGURE 2. Normal gravity (left) and microgravity (right) flames of methane and air [6]

FLAME GEOMETRY

Most of the researchers have reported that diffusion flame under microgravity is longer and wider compared to normal gravity due to the lack of buoyancy driven flow. Charest *et al.* [2] numerically predicted a 50% increase of flame length of laminar ethylene-air diffusion flame under lower gravity condition compared to normal gravity condition. Based on computational and experimental studies, with CH₄/air diffusion flame Cao *et al.* [3] reported that flame length is proportional to the mass flow rate and the non-buoyant flame was found to be 28% longer than normal gravity flame for the same mass flow rate. Bhowal and Mandal [4] numerically predicted that flame height decreased by around 20% when the gravity decreased from 1g (normal gravity) to 0.1g. Datta [5] also reported that the flame height decreased and the flame width increased with decrease of gravity levels. Bin *et al.* [6] presented digital colour images of normal gravity and microgravity as shown in Fig. 2. It can see from the figure that the microgravity flame is longer and also wider compared to normal gravity flame.

TEMPERATURE

Temperature distribution plays a very important role in flames because of the fact that both soot and NO_x formations are dependent on it. It is observed that the peak temperature in microgravity flame is lower than normal gravity flame. Longer residence time and higher soot formation are thought to be the main reason behind this. Based on the theoretical studies, Kaplan *et al.* [7] predicted similar results. They also suggested that larger soot volume fraction is the main reason for more radiative heat losses from microgravity diffusion flame. Charest *et al.* [8] computed the values of radiative heat losses at different pressures in lower gravity environment. The isotherms for different pressures at normal gravity and zero gravity have been shown in Fig. 3. They found that peak temperature of 0g flame gradually increased from 2045 K to 2083 K when pressure was varied from 1 atm to 60 atm. Reimann and Will [9] worked with propane air diffusion flame and reported that peak temperature decreases from 2070 K to 1850 K as the gravity level changes from normal to zero. Cao *et al.* [3] reported that peak temperature along the flame centreline dropped around 300 K when buoyancy is eliminated. Bin *et al.* [6] observed that peak soot temperature in microgravity flame was 200 K lower than normal gravity flame for CH₄-air diffusion flame. Bhowal and Mandal [4] worked with CH₄ – air co-flow diffusion flame and predicted that at lower axial height temperature distribution not too much affected by gravity changes. But at higher heights temperature distribution was influenced by radiation and they observed flat temperature distribution at lower gravity levels. The centreline temperature decreased around 400 K when gravity level was changed from 1g to 0.1g. Zhang *et al.* [10] found that the temperature decreased at microgravity because of more radiative heat loss. They also proposed a formula for the estimation of radiative heat loss which is given by the following equation

$$q_{rad} = a[1 - \exp(-\tau_r L/c)] \quad (1)$$

where τ_r is centerline residence time (in ms), L is characteristics optical length of flame given by $L = 3.6(V_f/S_f)$ V_f and S_f being the flame volume surface and area of the flame respectively.

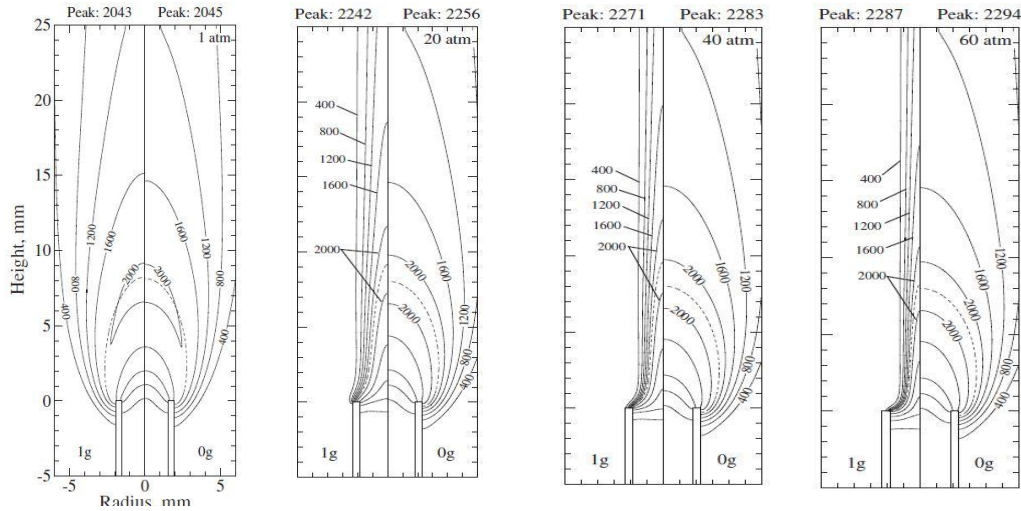


FIGURE 3. Predicted temperature (in K) contours for the normal-gravity (left) and zero-gravity (right) flames at different pressures [8].

Kong and Liu [11] conducted a numerical investigation of temperature distribution and soot formation in a methane air diffusion flame at normal gravity and also at 0.5 g and microgravity levels. Their predicted results showed a decrease in peak temperature with the lowering of gravity level. The peak temperature was found to be around 1941 K at normal gravity level whereas the corresponding values were found to be 1939 K and 1937 K at 0.5 g and zero gravity respectively. The variation has been in figure 4 based on their numerical data for better illustration of the fact. The centreline temperature shows no difference upto a certain axial height with the variation of gravity level. However, at higher heights the centreline temperature becomes much lower at microgravity than that at normal gravity.

AXIAL VELOCITY

It is clear that the axial velocity will be lower at lower gravity levels due to the reduction in buoyancy force or complete absence of buoyancy force at zero gravity level. Kaplan *et al.* [7] reported that maximum axial flow velocity decreased from 120 cm/s to 22 cm/s when gravity level was reduced from normal to 0.001 g in case of laminar ethylene – air diffusion flame. Charest *et al.* [2] observed 65% reductions in the centreline axial velocity at zero gravity level compared to normal gravity in a co-flow CH₄-air diffusion flame. Cao *et al.* [3] investigated both experimentally and numerically co-flow laminar CH₄-air diffusion flame in microgravity environment. They also reported that velocity decreased when the gravity level was lowered. Bhowal and Mandal [4] numerically predicted that centreline velocity distribution become flat after a certain height above the burner in case of microgravity condition. They also reported 75% reduction in axial velocity at a lower gravity of 0.1G compared to normal gravity. Bin *et al.* [6] carried out experiments on CH₄ - air diffusion flame and reported 55 % velocity decrease when gravity level was lowered from normal gravity to zero gravity. Kong and Liu [11] proposed that buoyancy induced velocity is proportional to the $(az)^{0.5}$, where a is the effective value of the acceleration due to gravity and z is the axial height above the burner. They found that the axial velocity decreased by 100% at zero gravity compared to the normal gravity flame at a height of 4 cm above the burner.

Zhang *et al.* [12] worked with laminar ethylene / air flame using axisymmetric co-flow diffusion flame burner. They observed peak axial velocities to be 260.8 cm/s, 182.2 cm/s and 50.9 cm/s for 1.0 g, 0.5 g, and 0.0 g flames respectively. The centreline velocity profile as obtained by Zhang *et al.* [12] has been reproduced in Fig. 5 for better understanding. For gravity levels of 1.0 g and 0.5 g, velocity increases very sharply close to the burner, but after that it maintains constant increasing trend. But in case of 0.0 g, velocity is much lower compared to the previous cases and after a certain height of burner it becomes flat.

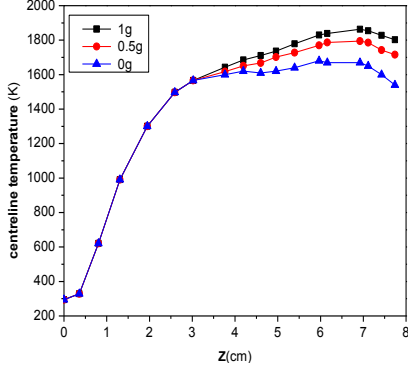


FIGURE 4. Centerline temperature distributions under different gravity levels of methane-air diffusion flame [11]

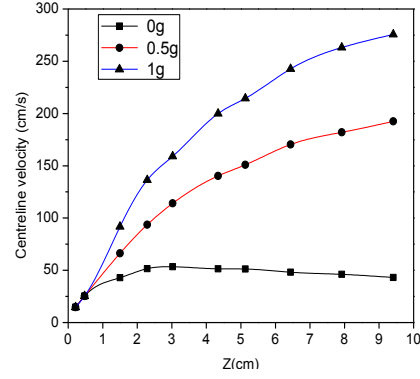


FIGURE 5. Centreline velocity at three gravity levels for ethylene-air diffusion flame [12]

SOOT

Incomplete combustion of hydrocarbon fuels in practical combustion devices such as industrial furnaces, gas turbine combustors and diesel engines, generates nanometer sized carbon particulates called soot. However, the mechanism of soot formation is not yet fully understood. Normally soot is formed in the fuel side of the reaction zone and gets consumed as it is moves into oxidizing zone. The soot formation mainly depends upon fuel type, temperature and fuel residence time. It is experimentally observed that soot formation starts beyond a temperature of about 1300K. Sunderland and Faeth [13] carried out experiments with different fuels and reported that C₂H₂ is the main precursor for the soot formation. Megaridis *et al.* [14] found two times the value of maximum soot volume fraction at zero gravity than that at normal gravity from their experiments at 2.2s drop tower of the NASA Lewis research centre. Panek and Gülder [15] experimentally measured the position of peak soot volume fraction above the burner at sub atmospheric pressure in microgravity environment. The position of the peak soot formation region moved towards burner tip with the decrease of pressure. Jeon and Choi [16] conducted experiments based on High-temperature Air Combustion Technology (HiCOT) at lower gravity using ethylene as fuel. They found a two-fold increase in soot volume fraction when the gravity level was lowered from normal gravity to 0.3 g. The reduction in soot oxidation rate in reduced gravity flames was due to the decrease of air entrainment in non-buoyant flames. They also reported that with decreasing gravity level the maximum position of soot volume fraction moved downstream to burner. Konsur *et al.* [17] carried out an experiment with nitrogen diluted acetylene fuel burning in quiescent air at atmospheric pressure under reduced gravity environment. Panek and Gülder [15] experimented with ethylene-air laminar diffusion flame under microgravity environment at sub atmospheric condition for different fuel flow rates. They reported that the fraction of carbon in the fuel converted into soot was between 0.1 % and 1.2 % in the sub-atmospheric pressure range from 0.2 atm to 1 atm for a fuel flow rate of at 0.48 mg/s.

As the experiments with flame under reduced gravity conditions are difficult and also the measurement of soot and other related parameters needs very sophisticated instruments, researchers have tried to develop mathematical models for the reacting flows and soot formation. Some of the soot models available in the literature are due to Moss *et al.* [18], Lautenberger *et al.* [19], Delichatsios *et al.* [20] and Leung *et al.* [21]. No model is yet to describe the complex phenomenon of soot formation completely. However, Leung *et al.* model is often used by the combustion research community. This model takes care of different processes and steps such as soot nucleation, surface growth and oxidation. The transport equations for soot mass fraction and soot number density as given by Leung *et al.* are as follows:

$$\rho V_r \frac{\partial Y_s}{\partial r} + \rho V_z \frac{\partial Y_s}{\partial z} = -\frac{1}{r} \frac{\partial}{\partial r} (r \rho V_{T,r} Y_s) - \frac{\partial}{\partial z} (\rho V_{T,z} Y_s) + S_m \quad (2)$$

$$\rho V_r \frac{\partial N}{\partial r} + \rho V_z \frac{\partial N}{\partial z} = -\frac{1}{r} \frac{\partial}{\partial r} (r \rho V_{T,r} N) - \frac{\partial}{\partial z} (\rho V_{T,z} N) + S_N \quad (3)$$

where, Y_s is soot mass fraction, N is soot number density and $V_{T,r}$ and $V_{T,z}$ are soot thermophoretic velocities in r and z direction. The thermophoretic velocities are calculated as

$$V_{T,x_i} = -0.65 \frac{\mu}{\rho T} \frac{\partial T}{\partial x_i} (x_i = r, z) \quad (4)$$

The source term S_m in Eq. (2) accounts for the contributions due to soot nucleation, surface growth and oxidation (with a negative sign). The source term SN in Eq. (3) represents the production and destruction of soot particles due to nucleation and agglomeration. This semi-empirical soot model assumes that C_2H_2 is the only chemical species responsible for soot nucleation and surface growth processes.

Zhang *et al.* [12] computationally investigated ethylene/air diffusion flame and found peak soot volumes of 11.2 ppm, 15.7 ppm, and 29.9 ppm at gravity levels of 1g, 0.5g, and 0g respectively. Kaplan *et al.* [7] predicted a ten-fold increase in peak soot volume fraction for ethylene flame due to decrease of gravity from normal to microgravity. Charest *et al.* [8] observed that peak soot volume fraction in ethylene flame became almost twice at microgravity.

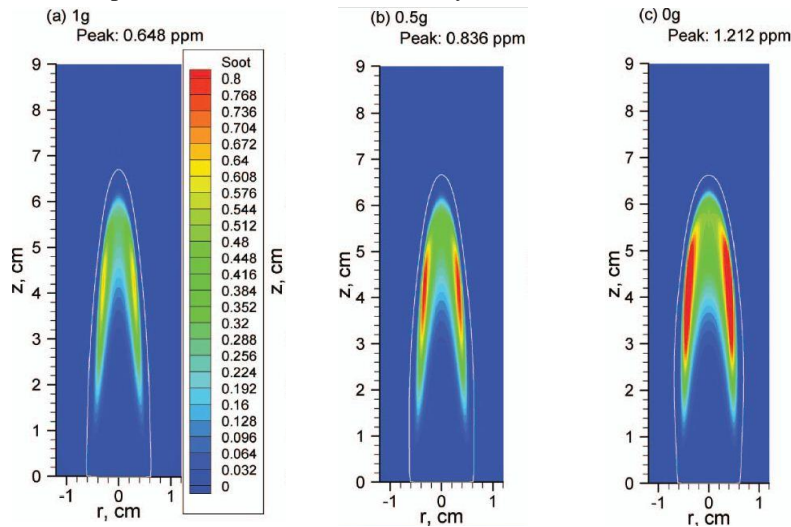


FIGURE 6. Distributions of soot volume fraction (in ppm) for $V_A = 77.6$ cm/s at (a) 1g, (b) 0.5g and (c) 0g. The white curves indicate the stoichiometric mixture fraction. [22]

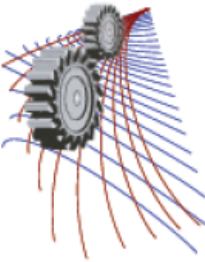
Kong and Liu [22] conducted a numerical experiment to predict the soot volume fraction in laminar co-flow CH_4 -air diffusion flames using different air stream velocities and fixed mean fuel stream velocity (6.5 cm/s) under different reduced gravity conditions. The results from the above study for co-flow air flow velocity of 77.6 cm/s have been presented as a case study. The soot volume fraction contours at the gravity levels of 1g, 0.5g and 0g have been shown in figures 6 (a)-(c) respectively. The figures show that soot laden zone is extending radially with the lowering of gravity levels and the peak soot volume fraction are 0.648, 0.836, 1.212 ppm under normal gravity, 0.5g and zero gravity respectively. They also found that at a lower air flow velocity of 30 cm/s, the peak soot volume fraction increases for all gravity levels and the maximum being for zero gravity.

CONCLUSION

The following conclusions can be drawn from this review work on soot formation under microgravity conditions. The flame geometry, flame temperature and sooting behavior are significantly changed at reduced gravity and particularly at microgravity condition. The microgravity flame is longer and wider than normal gravity flame. Axial velocity is much lower in case of microgravity flame due to negligible buoyancy force. The residence time becomes larger and more soot is formed at microgravity. The maximum soot volume fraction at microgravity becomes two times that of normal gravity flames. This causes more radiation heat loss from soot and the flame temperature is reduced compared to normal gravity diffusion flame.

REFERENCES

1. J. Warnatz, U. Maas, R. W. Dibble, Physical And Chemical Fundamentals, modeling and simulation, experiments, pollutant formation. 4th Ed. Springer-Verlag Berlin and Heidelberg GmbH & Co.; (2010)
2. M. R. J Charest, C. P.T. Groth., Ö. L. Gülder, Effects of gravity and pressure on laminar co flow methane–air diffusion flames at pressures from 1 to 60 atmospheres, *Combustion and Flame*, **158** 860–875 (2011).
3. S. Cao, B. Ma., B. A. V. Bennett, D. Giassi, D. P. Stocker, F. Takahashi, M. B. Long and M. D. Smooke. A computational and experimental study of co flow laminar methane/air diffusion flames: effects of dilution, inlet velocity, and gravity, *Proceedings of the Combustion Institute*, **35** 897-903 (2015).
4. A. J. Bhowal and B. K. Mandal, Radiation effect on temperature distribution and soot formation in a diffusion flame under reduced gravity Conditions, *Heat and Mass Transfer*, DOI 10.1007/s00231-015-1552-0 (2015)
5. A. Datta, Effect of gravity on structure and entropy generation of confined laminar diffusion flames, *International Journal of Thermal Sciences*, **44** 429-440 (2005).
6. B. Ma, S. Cao, D. Giassi, D. P. Stocker, F. Takahashi, B. A. V. Bennett, M. D. Smooke and M. B. Long, An experimental and computational study of soot formation in a coflow jet flame under microgravity and normal gravity, *Proceedings of the Combustion Institute*, **35**, 839–846 (2015).
7. C. R. Kaplan, E. S. Oran and K. Kailasanath, Gravitational effects on sooting diffusion flames, 26th Symposium (International) on Combustion/The Combustion Institute, 1301–1309 (1996).
8. M. R. J. Charest, C. P. T. Groth, Ö. L. Gülder, A numerical study on the effects of pressure and gravity in laminar ethylene diffusion flames, *Combustion and Flame*, **158** 1933–1945 (2011).
9. J. Reimann, S. Will, Optical Diagnostics on sooting laminar Diffusion Flames in Microgravity, *Microgravity Sci. technol.* XVI, 333-337 (2005).
10. D Zhang, J Fang, J. Guan, J. Wang, Y. Zeng, J. Wang, Y. Zhang, Laminar jet methane/air diffusion flame shapes and radiation of low air velocity coflow in microgravity, *Fuel* **130** 25-33 (2014).
11. W. Kong and F. Liu, Effects of Gravity on Soot Formation in a Coflow Laminar Methane/Air Diffusion Flame, *Microgravity Sci. Technol* **22** 205-214 (2010).
12. Y. Zhang, D. Liu, S. Li, Y. Li and C. Lou, The Influence of Gravity Levels on Soot Formation for the Combustion of Ethylene – air Mixture, *Chemical Kinetics and Catalysis*, **88** 2300-2307 (2014).
13. P. B. Sunderland and G.M. Faeth, Soot Formation In Hydrocarbon / Air Laminar Jet Diffusion Flames. *Combustion and flame* **105** 132-146 (1996).
14. C. M. Megaridis, D W. Griffin and B Konsur, Soot-field structure in laminar soot-emitting microgravity nonpremixed flames, *Proceedings of the 26th symposium (International) on combustion / the combustion Institute*, 1292-1299 (1996).
15. N. Panek and Ö. L. Gülder, Simulation of microgravity diffusion flames using sub-atmospheric pressures, *Proceedings of the 48th ALAA Aerospace Sciences Meeting Including the New Horizons Forum and Aerospace Exposition*, (AIAA2010-1477) (2010).
16. B-H Jeon and J H Choi, Effect of buoyancy on soot formation in gas-jet diffusion flame, *Journal of mechanical science and technology* **24** (7) 1537-1543 (2010).
17. B. Konsur, C. M. Megaridis and D. W. Griffin, Soot Aerosol Properties in Laminar Soot-Emitting Microgravity Nonpremixed Flames, *Combustion and Flame* **118** 509-520 (1999).
18. J. B. Moss, C. D. Stewart and K. J. Young, Modeling Soot Formation and Burnout in a High Temperature Laminar Diffusion Flame Burning under Oxygen-Enriched Conditions, *Combustion and Flame* **101** 491-500 (1995).
19. C. W. Lautenberger, J. De Ris, N. A. Dembsey, J. R. Barnett and H. R. Baum, A simplified model for soot formation and oxidation in CFD simulation on non-premixed hydrocarbon flames, *Fire saf. J.***40** 141-176 (2005).
20. M. A. Delichatsios, A phenomenological model for smoke- point and soot formation in laminar flames, *Combustion Science Technology*, **100** 283-298 (1994).
21. K. M. Leung, R. P. Lindstedt and W. P. Jones, a simplified reaction mechanism for soot formation in nonpremixed flames, *Combustion and Flame* **87** 289-305 (1991).
22. W. Kong and F. Liu, Numerical study of the effects of gravity on soot formation in laminar coflow methane/air diffusion flames under different air stream velocities, *Combustion Theory and Modeling*, **13**(6) 993–1023 (2009).



Performance improvement of local automotive industry by adopting JMM

A.K.M. Mohiuddin¹, Julia Bt Haji A. Jabbar²

¹*Department of Mechanical Engineering, International Islamic University Malaysia, Kuala Lumpur 53100, Malaysia*

²*Department of Manufacturing and Materials Engineering, International Islamic University Malaysia, Kuala Lumpur 53100, Malaysia*

^aCorresponding author: mohiuddin@iium.edu.my

Abstract. In the era of globalization, most companies all over the world are constantly looking for ways to increase productivity and at the same time to remain competitive to reduce cost. Companies in automotive manufacturing industry are no exceptions. Substantial evidence suggests that practices associated with Japanese Manufacturing Management (JMM) can yield a superior competitive advantage in terms of productivity, quality and provide overall successful business performance. This paper discusses the transfer of the best practice of the JMM locally and obtain the impact of the adoption and adaptation of the JMM in a Malaysian automotive company. An in-depth case study was conducted to identify what are the changes in terms of the philosophy and practices undertaken by the automotive company and ascertain the impact of the JMM on its manufacturing and financial performances. The elements of business performance from the viewpoint of manufacturing based on safety, quality, cost and delivery were quantified and examined. These elements are safety, Parts per Million (PPM), in-line Defect per Unit (DPU), First Time Quality (FTQ), cycle time, productivity, efficiency and stock level. The results show a positive impact to the automotive plant manufacturing performance. For example, safety index has reduced to 0 major accident occurrences. The PPM and In-line DPU have improved by 98% and 91% respectively. The FTQ has improved by 167% and cycle time was reduced from 20 minutes to 6 minutes. The productivity has increased up to 43% whilst the efficiency was at 99.9%. The stock level was reduced from half month to 3 days after the adoption of the JMM. The results of the financial performance also show the profitability of the plant.

INTRODUCTION

Most companies all over the world are constantly looking for ways to increase productivity and at the same time to remain competitive to reduce cost. Companies in automotive manufacturing industry are no exceptions.

Automotive companies are looking for ways and means to produce quality and competitive products and services to the market. Toyota Motors Corporation is currently the largest auto maker in the world beating the sales records of the giant automotive companies such as General Motors (GM) and Ford. In 2012, Toyota sold 9.75 million vehicles in the United States compared with 9.29 million for GM [1]. There still remains a wide gap in profitability between the giant American automotive manufacturers and their Japanese automotive counterparts. While Toyota continues to be the industry benchmark of automakers, American automakers have been facing with various problems including bankruptcy, reorganization, declining demand, high operational costs, and overproduction [2].

The success for Toyota starts since post World War II (WWII). The company has developed its own principles in excellent manufacturing practices and philosophy. With scarce materials and resources after WWII, Toyota has utilized different techniques of manufacturing rather than mass production introduced by Ford in the USA, and formally copied by other Japanese manufacturers during the period. Unlike mass production with high inventory level to cater for big production volume to take advantage of economy of scale, the manufacturing practices by Toyota emphasizes on Lean Production. Generally, Lean Production focuses on producing high quality finished goods satisfactory to customer demand by means

of eliminating waste (muda). The Lean Production approach includes a wide variety of management practices, including just-in-time (JIT), continuous improvement (Kaizen), quality systems, quality circles, work teams, cellular manufacturing, supplier management, etc. in an integrated system [3,4]. These practices, which later referred to the best practices when applied to manufacturing scenarios, are continuously improved and tied to form a management system such as Toyota Production System (TPS). Due to its effectiveness, the technique turned out to be used by most of other Japanese automotive companies in the 70s and later was adapted and implemented in the USA, Europe and other parts of the world. Other example of Japanese company which practices Lean Production and the Japanese way of manufacturing includes Isuzu with its philosophy and practice called Isuzu Manufacturing Management (IMM). IMM is implemented by its parent company in Japan and similar best practices are adopted and shared by its overseas plants throughout the world. The TPS, IMM and JIT have been adopted and adapted in various developed and developing countries to the extent they form what is known as “The Japanese Way” [5]. Until now, the Japanese has continuously perfected their manufacturing strategy in automotive industry [6]. Japanese production management or in other word Japanese Manufacturing Management (JMM) has evolved over the last thirty years and it continues to evolve. There are significant numbers of studies that examined the transfer of Japanese production practice and its impact on the company performance in the US [5,6,7]. Also, in the UK and Japan, the manufacturing practice and its relationship with performance have been studied extensively. Phan et al. [8] conducted two surveys with twenty seven Japanese manufacturing companies in the 1990s and 2000s to compare the degree of implementation of eleven quality management practices and their impact on different dimensions of competitive performance during the period. This paper provides a case study of similarities and differences before and after the implementation of JMM in a local automotive plant which assembles vehicles under a Japanese marque reveals the adoption and adaptation of JMM as well as its success in Malaysia.

AUTOMOTIVE MANUFACTURING IN MALAYSIA

The economic policy of Malaysia has shifted previously from the focus on agriculture sector to that on manufacturing. Until today, the manufacturing sector in Malaysia continues to play a significant role in the financial health of the nation. In 2011, the manufacturing sector contributed 27.9% of Malaysia Gross Domestic Product (GDP) compared to other sectors i.e. agriculture (7.4%), mining (7.1%), construction (3.2%) and services (57.3%). The percentage had also steadily increased from 26.6% to 27.6% for 2009 and 2010 respectively [9]. The automotive industry is viewed as one of the most pertinent contributors for the economy since it is directly correlated with manufacturing and service sectors. More than half of the population in Malaysia owns a vehicle. The presence of Japanese influence in Malaysian automotive industry has existed for quite some time. The ‘Look East’ policy by the former Prime Minister Tun Mahathir Mohamad has resulted in the establishment of Proton, the first national car company in Malaysia, in 1983 which jointly collaborated with Mitsubishi Motors Corporation and Mitsubishi Corporation. The second national car company was established in 1992 under the name PERODUA. The company is a joint venture between a Malaysian company and Daihatsu Motor Corporation.

JAPANESE MANUFACTURING MANAGEMENT

Manufacturing management involves managing the main activities of an organization which concerns with the conversion of an organization's inputs into its outputs, from production to delivery and distribution of the goods. The common role of manufacturing or operations management is the responsibility for managing the resources, known as the 4Ms which are Materials, Machines, Manpower and Method.

The objective of manufacturing management is to manage these resources effectively and contribute significantly to the achievement of corporate objectives. The main target of manufacturing management is productivity, meaning manufacturing or production effectiveness. Manufacturing requires integration with other management functions to ensure that the manufacturing objectives can be accomplished. This includes the running of production processes, quality management, logistics, maintenance, industrial engineering, procurement as well as human resources.

In order to operate effectively, top management must acknowledge that the organization as a whole needs to develop an integrated approach to the business and its activities. This involves recognizing and understanding the interactions between different functions that are necessary for the organization to be effective. All of the different management functions must be involved in setting the corporate strategy of the organization. Each function will then set its own functional objectives and develop a functional strategy to achieve those objectives.

JMM places a great emphasis on mission and vision of a company. In the Executive Summary of the 14 Toyota Way Principles extracted from the book ‘The Toyota Way’ written by Liker [10], it is stated that companies should base the management decisions on a long-term philosophy, even at the expense of short-term financial goals. Company should

also have a philosophical sense of purpose that supersedes any short-term decision making. Work, grow, and align the whole organization toward a common purpose that is more important than making profit.

TOYOTA PRODUCTION SYSTEM (TPS)

TPS can be seen as a technology-based, comprehensive production management system with the primary goals of increasing productivity and reducing costs. This is achieved by reducing cycle time, increasing flexibility, reducing stock levels and shortening machine changeover times.

It is generally agreed that the best word to describe TPS is Lean Production. The use of the term "Lean", in a business or manufacturing environment, describes a philosophy that incorporates a collection of tools and techniques into the business processes to optimize time, human resources, assets, and productivity, while improving the quality level of products and services to their customers. Becoming "Lean" is a commitment to a process with a tremendous learning that goes with the implementation of Lean principles and practices into an organization.

Womack and Jones [11] define lean manufacturing as a five-step process: defining customer value, defining the value stream, making it "flow", "pulling" from the customer back, and striving for excellence. To be a lean manufacturer requires a way of thinking that focuses on the product flow through value-adding processes without interruption, a "pull" system that cascades back from customer demand by replenishing only what the next operation takes away at short intervals, and a culture in which everyone is striving continuously to improve [10].

From an industrial engineering perspective, the basic features of TPS are identified as follows [12]:

- It achieves cost reductions by eliminating waste, be it staff time, materials, or other resources.
- It reduces the likelihood of overproduction by maintaining low inventories ("non-stock") and keeps labor costs low by using minimal manpower.
- It reduces production cycle time drastically with innovations like the Single-Minute Exchange of Die (SMED) system, which cuts downtime and enables small-lot production.

The driving force behind the Japanese system of production is eliminating waste, thereby maximizing process efficiency and the returns on resources. After waste is targeted, new processes or practices can be devised to deal with it. While low inventory levels are a key outcome of the TPS, an important element of the philosophy behind its system is to work intelligently and eliminate waste so that inventory is no longer needed.

The management philosophy for the TPS is further described in 'The 14 Principles of the Toyota Way'. The main ideas are to base management decisions on a 'philosophical sense of purpose' and think long term, to have a process for solving problems, to add value to the organization by developing its people, and to recognize that continuously solving root problems that drives the organisation learning. Liker [10] further added that in the Toyota Way, it's the people who bring the system to life: working, communicating, resolving issues, and growing together. From the first look at excellent companies in Japan practicing lean manufacturing, it was clear that the workers were active in making improvement suggestions. But the Toyota Way goes well beyond this; it encourages, supports, and in fact demands employee involvement. It is a system designed to provide the tools for people to continually improve their work. The Toyota Way means more dependence on people, not less. It is a culture, even more than a set of efficiency and improvement techniques

ADOPTION OF JMM

The findings from Laosirihongthong et al. [5] on Japanese auto companies show that six pillars to support JMM implementation are the key enabler to success in adopting JMM. They are as follows:

Cultural change: Local employees are encouraged to adapt and familiar with JMM by providing on job training and education.

Quality at the shop floor: Assembly line employees practice quality check point to ensure they do not receive defects, make any defects or transfer the defects to the next workstation. Morning briefing is held daily as part of quality circle to improve production process.

Consensus: Top Down and Bottom Up approaches are present in JMM companies.

Incremental continuous improvement: Implementation of Kaizen at shop floor including open concept office layout with no partitions for easy communication and access. Gemba (Go see problem at source) are conducted every day by managers to better understand issues at workplace and to develop relations with subordinates.

Benchmarking: All cases studied use benchmarking techniques for quality, delivery, cost, flexibility and innovation metrics.

Backward-forward integration: The relationship integration exists among the suppliers, the auto company itself and customers.

IMPLEMENTATION OF JMM

During the restructuring exercise in late 2007, the local company had taken massive improvement activities under JMM umbrella. In line with the implementation of JMM, the improvement activities can be listed as follows:

Plant Layout Improvement: the initial improvement in plant layout was conducted by rearranging the original layout to fit the lean requirement. All of the plant reengineering and relocation activities are performed under a project called J-Project.

Quality Improvement: Among the quality improvement activities conducted are workshop quality improvement, open space concept for the offices and supplier quality management. The workshop quality improvement is dedicated to minimize wrong assembly and defects in production line and most detection are performed by production operators. This self-check activity has empowered operators to ensure the quality of the vehicle manufactured is in line with the standard required by JMM.

The JMM adopted by the local company necessitates the changes in quality activities implemented in accordance to JMM requirement. The activities for workshop improvement consist of daily quality audit meeting; two (2) minutes parts check; two (2) minutes tips check; defect parts management; work stop rule; torque analyser usage; daily inspection of torque wrench and torque meter; daily checking of inspection tools; fallen bolt, torque wrench and meter; 4M change control point at QC inspection points; QC in-line inspection and process matrix; QC quality agreements; feedback rule among production lines and from QC to production; abnormalities guidelines; maintenance agreements; joint operation manual; purchase of new torque; colour code etc.

RESULTS AND DISCUSSIONS

Implementation of JMM in the local company results in the process performance based on safety, quality, cost and delivery (SQCD).

Safety: Implementation of JMM shows the improvement of the safety index. In financial year 2007/2008, the local company registered 6 occurrences of recordable major accidents with medical leave and 8 minor accidents. The accident rate dropped sharply in FY2011/2012 with no occurrence of recordable major accident and 6 occurrences of minor accident. This was the best accident record ever achieved for the major accident. Although in early implementation of JMM, the minor accidents were above the plant target of 8 occurrences per year, the rate dropped below the target of 8 occurrences in FY2008/2010 onwards.

Parts per Million (PPM): PPM is used by the local company to measure quality performance of parts received from suppliers. The plant originally recorded 6,500 PPM in FY2007/2008 and then improved by 97.8% at 141 PPM and 98.1% at 121 PPM for FY2010/2011 and FY2011/2012 respectively. It shows a significant reduction of defective parts supply.

In-Line Defect per Unit (DPU) and First Time Quality (FTQ): The In-line DPU is simply the number of defects found in assembly line divided by the number of units inspected. Since the implementation of the JMM, the In-line DPU had shown a consistent downward trend from 5.7 DPU to 0.49 DPU in Y2007/2008 to FY2011/2012.

First Time Quality (FTQ) is a lean metric that indicates to what extent parts are manufactured correctly the first time without need for inspection, rework, or replacement. The FTQ in percentage also indicated an improvement trend beginning FY2009/2010. In FY2011/2012, the FTQ improved at 84.97% as compared to 31.8% before the JMM implementation.

Cycle Time: Beginning with more than 20 minutes prior to the adoption of JMM, the cycle time was improved to 6 minutes in financial year 2012/2013. The cycle time had improved by 70% after implementation of JMM. The improvement was due to the improved process, skill upgrading, kaizen activities undertaken by all process owners i.e. supervisor, foremen and operators, and improved manpower skill.

Productivity: During the early year of JMM in FY2008/2009, Body Shop and General Assembly employees produced an average of 0.23 units per hour and 0.05 units per hours respectively. In FY2011/12, over 3 years later after JMM, Body Shop productivity improved by 43% at 0.33 units per hour. The General Assembly performance is quite stable at 0.07 units due to conveyerized system. Therefore, both shops had shown improvement in subsequent years after the introduction of JMM which exceeded or at par with the targets.

Efficiency: It measures how well a factory operates in production. The plant recorded an increase in efficiency for the past few years as compared to the first year of the JMM implementation in FY2008/2009. Although the efficiency performance at Body Shop recorded a mixed trend due to introduction of new models, new manpower etc., the

performance was above the target of 96% set by the plant. The highest achievement was 99.9% efficiency accomplished in 2009/2010, an improvement of 4% against the target.

Stock Level: One of the important aspects of lean manufacturing is the control of stock level. It was found that the CKD stock level for the local company was steadily controlled from 1.7 months prior to the JMM to 1.5 months after the JMM implementation. The stock level for the local parts also was reduced from 0.5 months to 3 days before delivery from the local suppliers.

FINANCIAL PERFORMANCE

The financial results were taken in FY2007/2008, a year before the full implementation of the JMM and assess throughout the adaptation period for the following 4 years. The local company began with RM189.7 million business turnover during the midst of the JMM implementation in FY2007/2008 but had significantly increased by 47.6% from RM189.7 million in FY2007/2008 to RM280.189 million in FY2008/2009. The revenue however had

Table 1. Financial Performance.

JMM started

	2007/08	2008/09	2009/10	2010/11	2011/12
	RM'000	RM'000	RM'000	RM'000	RM'000
Revenue	189,726	280,189	232,211	316,327	364,059
Profit after taxation	10,111	10,640	17,149	38,453	29,670
Total assets	72,974	142,228	137,059	206,042	248,822
Inventory	27,454	36,531	22,007	30,084	77,517
Total s/equity	49,285	59,925	77,074	113,373	143,043
Net profit margin (%)	5.33	3.80	7.39	12.16	8.15
Return on asset ROA (%)	13.86	7.48	12.51	18.66	11.92
Return on equity ROE (%)	20.52	17.76	22.25	33.92	20.74
Inventory Turnover Ratio	6.91	7.67	10.55	10.51	4.70

decreased to RM232.2 in FY2009/2010 as a result of Tsunami calamity in Japan and Thailand flood which had disrupted the parts supply. Even so, the figure was still more than the revenue before the JMM implementation. The revenue continued to improve by 36% at RM316.3 million in the following financial year due to the increase in the volume of vehicles sold to the market, manufacturing efficiency and the acquisition of product ownership for the heavy-duty model. In FY2011/2012, the plant recorded an increase in revenue by 15% at RM364 million compared to the previous financial year. The financial performance of the local company is indicated in Table 1 which shows that the financial performance of the local company has improved after the adoption of JMM.

CONCLUSIONS

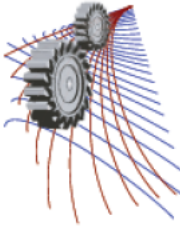
The research shows that through the JMM adoption and adaptation, the manufacturing performance improves in terms of the following aspects:

- i) Safety index reduction from 6 major accidents to 0 accident,
- ii) PPM reduction of 98%,
- iii) In line DPU improvement of 91%,
- iv) FTQ up from 31.8% to 84.97% giving an improvement of 167%
- v) Cycle time improvement from 20 minutes to 6 minutes.
- vi) Productivity improvement up to 43% at Body Shop and at par for General Assembly
- vii) Efficiency improvement up to 4% against the target for Body Shop.
- viii) Stock level of local parts from half month to 3 days and CKD from 1.7 months to 1.5 months.

The results of this study also show that the implementation of JMM increases the firm's profitability and revenue besides maintaining the stability of expenses. The revenue has increased from 22% to 92% after the JMM adoption and the net profit has increased from 5.33% to 8.15%.

REFERENCES

- [1] C. Dawson, Toyota Takes Top Car-Maker Title Back from GM. Wall Street Journal, (2013) Retrieved March 2013, <http://blogs.wsj.com/drivers-seat/2013/01/28/toyota-takes-top-car-maker-title-back-from-gm>.
- [2] A. L. Bergenwall, C. Chen and R. E. White, TPS's process design in American Automotive Plants and its Effects on the Triple Bottom Line and Sustainability, *Int. Journal of Production Economics*, 140(1) (2012) 374-384.
- [3] R. Shah and P.T. Ward, Lean Manufacturing: Context, Practice Bundles, and performance, *Journal of Operation Management*, 21 (2003) 129-149.
- [4] R. R. Fullerton, C. S. McWatters, and C. Fawson, An Examination of the Relationship Between JIT and Financial Performance, *Journal of Operations Management*, 21(4) (2003) 383-404.
- [5] T. Laosirihongthong, M. W. McLean, P. Leabsuetrakool, T. Chongjareonjai, and S. Leedhirakul, Technology Strategy: Findings from Adoption and Adaptation of Japanese Manufacturing Management (JMM) to ASEAN and Australasian Automotive Manufacturers, 4th IEEE International Conference on Management of Innovation and Technology, (2008) 1325-1330.
- [6] R. J. Schonberger, Japanese Production Management: An Evolution-With Mixed Success, *Journal of Operations Management*, 25(2) (2007) 403-419.
- [7] F. K. Pil, Thrive: Managing the Transfer of "Best Practice" at Japanese Auto Plants in North America, *Journal of World Business*, 34(4) (2000) 372-390.
- [8] A. C. Phan, A. B. Abdallah and Y. Matsui, Quality Management Practices and Competitive Performance: Empirical Evidence from Japanese Manufacturing Companies, *International Journal of Production Economics*, 133(2) (2011) 518-529.
- [9] Economic Report 2010/2011. (2010). Official Website of Ministry of Finance Malaysia. Retrieved March, 2013. <http://www.treasury.gov.my>.
- [10] J. K. Liker, *The Toyota Way: 14 Management Principles from the world's greatest manufacturer*, McGraw- Hill, USA, 2004.
- [11] J. P. Womack and D. T. Jones, *Lean Thinking*, revised ed., Free Press, New York, 2003.
- [12] S. Shingo, *A Study of the Toyota Production System*, rev. ed., Productivity Press, Cambridge, 1989.



Stresses and Displacements in Basic Fracture Modes: A Comparison between Near-tip and Global Solutions

M. Chowdhury^{a)}

¹*School of Mechanical and Manufacturing Engineering University of New South Wales, Sydney NSW 2052, Australia*

^{a)}Corresponding author: m.chowdhury@unsw.edu.au

Abstract. The solutions for stresses and displacements in an infinite elastic plane with a centre crack under equal bi-axial loads is re-visited. The main thrust in this paper is to present the materials in an easy to follow format suitable for beginners with limited mathematical background. After presenting the *global* solution using complex potential function, the equations are simplified to local *near-tip* solutions. Both *near-tip* and *general* solutions are useful in the study of crack extension behaviour. After giving a brief description of the three basic Modes of fracture, the derivation is given only for Mode I or opening mode. The analysis for the other two modes are almost identical and not elaborated here but all results are presented.

INTRODUCTION

There are two basic approaches to establish criteria of failure of solids by crack initiation and propagation. One is the global energy balance approach based on Griffith's [1] pioneering work on brittle fracture of glass. The other one is based on local *near-tip* stresses and displacements. Almost all of the fracture properties of a solid are characterized using a couple of parameters from the *near-tip* stress and displacement fields [2]. The theory of plane elasticity may be used to derive these fields.

As an extension of Griffith's work the concept of energy release rate was introduced. This concept is valid for studies of both linear elastic and elastic-plastic fracture mechanics [3]. The energy release rate can be calculated numerically with stress and displacement fields away from the crack tip, that is, from *global* analysis. Both *global* and *near-tip* fields are developed here.

An effective way of dealing with many plane elasticity problems is to introduce a new "unknown", the Airy stress function, ϕ . One way to solve this bi-harmonic function is to express ϕ in terms of another complex function $Z_I(z)$ for Mode I crack problems. In other words $Z_I(z)$ is an intermediate solution which satisfies the bi-harmonic equation. It was chosen appropriately by Westergaard [4] to suit the general characteristics of Mode I problems. Credit is due to Westergaard for finding a simple expression for $Z_I(z)$. Similar functions $Z_{II}(z)$ and $Z_{III}(z)$ were also proposed for the other two fracture modes.

It may be mentioned that the Westergaard approach adopted here is not the most general way of solving plane elasticity problems. To solve more general problems, such as, arbitrary plate shape and crack geometry [5] developed the complex potential approach applicable to more versatile plane elasticity problems.

BASIC MODES OF FRACTURE

A crack in a solid consists of disjointed upper and lower faces. When the cracked body is subjected to external loads, remotely or at crack surfaces, the crack faces move with respect to each other causing displacements (u_x , u_y and u_z) between two surfaces. There are three independent movements corresponding to three fundamental fracture modes as pointed out by Irwin and which are schematically illustrated in Figure 1.

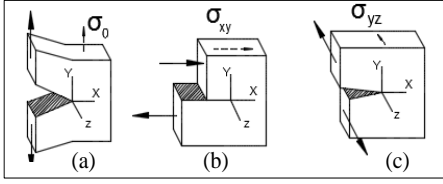


Fig. 2. Schematic of the basic fracture modes: (a) Mode I (opening), (b) Mode II (sliding), (c) Mode III (tearing).

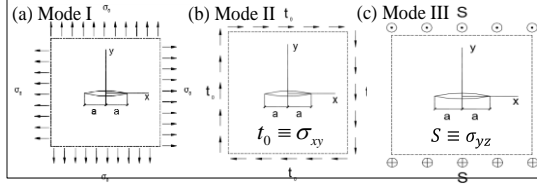


Fig. 1. A crack in an infinite elastic plane subjected to (a) bi-axial tension (Mode I), (b) pure in-plane shear (Mode II) and (c) anti-plane shear (Mode III)

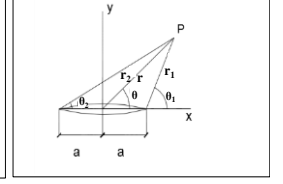


Fig.3. Polar Coordinate system to define a point (Mode III)

The remote loads for these modes may be viewed as axial tension, σ_o in-plane shear $\sigma_{yx} = \sigma_{xy}$, and anti-plane shear σ_{yz} for Modes I, II and III respectively. The projected views of these loads on an infinite centre-cracked plate are shown in Figures 2 (a, b and c). The derivation of stresses and displacements will be based on the polar coordinate system shown in Figure 3.

DERIVATION OF STRESSES AND DISPLACEMENTS

The derivation of stresses and displacements at any point, P is given in the Appendix. First, the derivation is given for *global* solution and then these are simplified for *near-tip* solutions.

Non-dimensional Presentation of Stresses and Displacement

The results obtained in the Appendix will now be presented in non-dimensional form using symbols with a bar as follows:

$$\bar{\sigma}_{xx} = \frac{\sigma_{xx}}{F}, \quad \bar{\sigma}_{yy} = \frac{\sigma_{yy}}{F} \quad \text{and} \quad \bar{\sigma}_{xy} = \frac{\sigma_{xy}}{F}, \quad \text{where } F = \sigma_o, \tau_o \text{ and } S \text{ respectively for modes I, II and III.} \quad (3.1)$$

$$\text{Also } \bar{r} = \frac{r}{a}, \quad \bar{r}_1 = \frac{r_1}{a}, \quad \bar{r}_2 = \frac{r_2}{a}, \quad \bar{x} = \frac{x}{a}, \quad \bar{u}_x = \frac{u_x}{a}, \quad \bar{u}_y = \frac{u_y}{a} \quad \text{and} \quad \bar{u}_z = \frac{u_z}{a}$$

$$\text{Also, } \bar{r} = \left[(1 + \bar{r}_1^2) + 2\bar{r}_1 \cos \theta_1 \right]^{\frac{1}{2}}; \quad \theta = \sin^{-1} \left(\frac{\bar{r}_1 \sin \theta_1}{\bar{r}} \right) \quad \text{and} \quad \bar{r}_2 = \left[(4 + \bar{r}_1^2) + 4\bar{r}_1 \cos \theta_1 \right]^{\frac{1}{2}}; \quad \theta_2 = \sin^{-1} \left(\frac{\bar{r}_1 \sin \theta_1}{\bar{r}_2} \right) \quad (3.2)$$

Tables 3.1(I), 3.1(II) and 3.1(III) summarises the results for *global* and *near-tip solutions* for Mode I, II and III respectively.

TABLE 3.1 (I) - Non-dimensional Equations for Mode I Problems

Parameter	$\bar{\sigma}_{xx}$	$\bar{\sigma}_{yy}$	$\bar{\sigma}_{xy}$	\bar{u}_x	\bar{u}_y
Global Solutions	$\frac{\bar{r}}{\sqrt{r_1 r_2}} \left[\cos \phi - \frac{1}{r_1 r_2} \sin \theta \sin 3\psi \right]$	$\frac{\bar{r}}{\sqrt{r_1 r_2}} \left[\cos \phi + \frac{1}{r_1 r_2} \sin \theta \sin 3\psi \right]$	$\frac{\bar{r}}{(r_1 r_2)^{\frac{1}{2}}} \left[\sin \theta \cos 3\psi \right]$	$\frac{\sigma_o \sqrt{r_1 r_2}}{2\mu} \left[\frac{k-1}{2} \cos \psi - \frac{r^2}{r_1 r_2} \sin \theta \sin \phi \right]$	$\frac{\sigma_o \sqrt{r_1 r_2}}{2\mu} \left[\frac{k+1}{2} \sin \psi - \frac{r^2}{r_1 r_2} \sin \theta \cos \phi \right]$
Near-tip Solutions	$\frac{1}{\sqrt{2r_1}} \cos \frac{\theta}{2} \left(1 - \sin \frac{\theta_1}{2} \sin \frac{3\theta_1}{2} \right)$	$\frac{1}{\sqrt{2r_1}} \cos \frac{\theta}{2} \left(1 + \sin \frac{\theta_1}{2} \sin \frac{3\theta_1}{2} \right)$	$\frac{1}{\sqrt{2r_1}} \sin \frac{\theta}{2} \cos \frac{\theta_1}{2} \cos \frac{3\theta_1}{2}$	$\frac{\sigma_o \sqrt{r_1}}{2\mu} \sqrt{\frac{\theta}{2}} \left[(k-1) + 2 \sin^2 \frac{\theta_1}{2} \right]$	$\frac{\sigma_o \sqrt{r_1}}{2\mu} \sqrt{\frac{\theta}{2}} \left[(k+1) - 2 \cos^2 \frac{\theta_1}{2} \right]$

TABLE 3.1 (II) - Non-dimensional Equations for Mode II Problems

Paramete	Global Solutions	Near-tip Solutions
$\bar{\sigma}_{xx}$	$\frac{\bar{r}}{\sqrt{r_1 r_2}} \left[2 \sin \phi - \frac{1}{r_1 r_2} \sin \theta \cos 3\psi \right]$	$-\frac{1}{\sqrt{2r_1}} \sin \frac{\theta}{2} \left[2 + \cos \frac{\theta_1}{2} \cos \frac{3\theta_1}{2} \right]$
$\bar{\sigma}_{yy}$	$\frac{\bar{r}}{\sqrt{r_1 r_2}} \cdot \frac{1}{r_1 r_2} \sin \theta \cos 3\psi$	$\frac{1}{\sqrt{2r_1}} \sin \frac{\theta}{2} \cos \frac{\theta_1}{2} \cos \frac{3\theta_1}{2}$
$\bar{\sigma}_{xy}$	$\frac{\bar{r}}{\sqrt{r_1 r_2}} \left[\cos \phi - \frac{1}{r_1 r_2} \sin \theta \sin 3\psi \right]$	$\frac{1}{\sqrt{2r_1}} \cos \frac{\theta}{2} \left[1 - \sin \frac{\theta_1}{2} \sin \frac{3\theta_1}{2} \right]$
\bar{u}_x	$\frac{\tau_o \sqrt{r_1 r_2}}{2\mu} \left[\frac{k+1}{2} \sin \psi + \frac{r^2}{r_1 r_2} \sin \theta \cos \phi \right]$	$\frac{\tau_o \sqrt{r_1}}{2\mu} \sqrt{\frac{\theta}{2}} \left[(k+1) + 2 \cos^2 \frac{\theta_1}{2} \right]$

TABLE 3.1 (III) - Non-dimensional Equations for Mode III Problems

Parameter	Global Solutions	Near-tip Solutions
$\bar{\sigma}_{yz}$	$\frac{\bar{r}}{\sqrt{r_1 r_2}} \cos \phi$	$\frac{1}{\sqrt{2r_1}} \cos \frac{\theta}{2}$
$\bar{\sigma}_{xz}$	$-\frac{\bar{r}}{\sqrt{r_1 r_2}} \sin \phi$	$\frac{-1}{\sqrt{2r_1}} \sin \frac{\theta}{2}$
\bar{u}_z	$\frac{S}{\mu} \sqrt{r_1 r_2} \sin \psi$	$\frac{S}{\mu} \sqrt{2r_1} \sin \frac{\theta}{2}$

Other in-plane stresses and displacements are zero. In the above tables $\phi = \theta - \frac{\theta_1}{2} - \frac{\theta_2}{2}$ and $\psi = \frac{1}{2}(\theta_1 + \theta_2)$

The Equations in Table 3.1(I), (II) and (III) may be used to compute the stresses and displacements at any point, P specified by (\bar{r}_1, θ_1) alone. Use of (\bar{r}_1, θ_1) imply shifting the coordinate origin to crack-tip.

Some Interesting Analytical Results along the Crack axis

Since the angles are either 0 or 180 degrees, the expressions for stresses and displacements are independent of trigonometric functions and can be vastly simplified.

Non-dimensional Stresses ahead of right crack-tip

Ahead of (right) crack-tip along x-axis: For $\bar{r}_1 \geq 0$, $\theta_1 = \theta = \theta_2 = 0$, also $\bar{x} = 1 + \bar{r}_1$

Tables 3.2(I), 3.2(II) and 3.2(III) listed the stresses ahead of right crack tip; behind the left crack-tip the stresses will be identical by virtue of symmetry. In addition to non-dimensional stresses, the ratio of stresses using *near-tip* solution to that using *global* solution are also included in these tables.

Table 3.2 (I) Mode I stresses ahead of right-tip along x-axis ($\bar{\sigma}_{xx} = \bar{\sigma}_{yy}$)			Table 3.2 (II) Mode II stresses ahead of right-tip along x-axis ($\bar{\sigma}_{xy}$)			Table 3.2(III) Mode III stresses ahead of right-tip along x-axis ($\bar{\sigma}_{xz}$)		
Global Solution	Near-tip Solution	Ratio of Near-tip/Global	Global Solution	Near-tip Solution	Ratio of Near-tip/Global	Global Solution	Near-tip Solution	Ratio of Near-tip/Global
$\frac{1 + \bar{r}_1}{\sqrt{\bar{r}_1(2 + \bar{r}_1)}}$	$\frac{1}{\sqrt{2\bar{r}_1}}$	$\frac{\sqrt{(2 + \bar{r}_1)/2}}{1 + \bar{r}_1}$	$\frac{1 + \bar{r}_1}{\sqrt{\bar{r}_1(2 + \bar{r}_1)}}$	$\frac{1}{\sqrt{2\bar{r}_1}}$	$\frac{\sqrt{(2 + \bar{r}_1)/2}}{1 + \bar{r}_1}$	$\frac{1 + \bar{r}_1}{\sqrt{\bar{r}_1(2 + \bar{r}_1)}}$	$\frac{1}{\sqrt{2\bar{r}_1}}$	$\frac{\sqrt{(2 + \bar{r}_1)/2}}{1 + \bar{r}_1}$
Or $\frac{\bar{x}}{\sqrt{\bar{x}^2 - 1}}$	Or $\frac{1}{\sqrt{2(\bar{x} - 1)}}$	Or $\frac{\sqrt{(1 + \bar{x})/2}}{\bar{x}}$	Or $\frac{\bar{x}}{\sqrt{\bar{x}^2 - 1}}$	Or $\frac{1}{\sqrt{2(\bar{x} - 1)}}$	Or $\frac{\sqrt{(1 + \bar{x})/2}}{\bar{x}}$	Or $\frac{\bar{x}}{\sqrt{\bar{x}^2 - 1}}$	Or $\frac{1}{\sqrt{2(\bar{x} - 1)}}$	Or $\frac{\sqrt{(1 + \bar{x})/2}}{\bar{x}}$
Here, $\bar{\sigma}_{xy} = 0$ by symmetry.			Here, $\bar{\sigma}_{xx} = \bar{\sigma}_{yy} = 0$			Here, $\bar{\sigma}_{xz} = 0$		

Non-dimensional Displacements ahead of right crack-tip

Tables 3.3(I) and 3.3(II) listed the displacements ahead of right crack tip; behind the left crack-tip the displacements will be identical by virtue of symmetry. Again, the ratio of displacements using *near-tip* solution to that of *global* solution are included in these tables. Note that there is no such displacement along x-axis for Mode III.

Table 3.3 (I) Mode I displacements ahead of right tip along x-axis (\bar{u}_x): $\theta_1 = 0, \bar{r}_1 > 0, \bar{x} = 1 + \bar{r}_1$

Table 3.4 (I) – Mode I displacements inside crack surfaces (\bar{u}_y)

	Global Solution	Near-tip Solution	Ratio of Near-tip/Global		Global solution	Near-tip Solution	Ratio of Near-tip/Global
Plane Stress	(1) $-\nu \frac{\sigma_0}{E} \sqrt{\bar{r}_1(2 + \bar{r}_1)}$	$(1 - \nu) \frac{\sigma_0}{E} \sqrt{2\bar{r}_1}$	$\sqrt{\frac{2}{2 + \bar{r}_1}}$	Or	$2 \frac{\sigma_0}{E} \sqrt{\bar{r}_1(2 - \bar{r}_1)}$	$2 \frac{\sigma_0}{E} \sqrt{2\bar{r}_1}$	$\sqrt{\frac{2}{2 - \bar{r}_1}}$
	Or $(1 - \nu) \frac{\sigma_0}{E} \sqrt{\bar{x}^2 - 1}$	$(1 - \nu) \frac{\sigma_0}{E} \sqrt{2(\bar{x} - 1)}$	Or $\sqrt{\frac{2}{1 + \bar{x}}}$		Or $2 \frac{\sigma_0}{E} \sqrt{(1 - \bar{x}^2)}$	Or $2 \frac{\sigma_0}{E} \sqrt{2(1 - \bar{x})}$	Or $\sqrt{\frac{2}{1 + \bar{x}}}$
Plane Strain	$(1 + \nu)(1 - 2\nu) \frac{\sigma_0}{E} \sqrt{\bar{r}_1(2 + \bar{r}_1)}$	$(1 + \nu)(1 - 2\nu) \frac{\sigma_0}{E} \sqrt{2\bar{r}_1}$	$\sqrt{\frac{2}{2 + \bar{r}_1}}$	Or	$2(1 - \nu^2) \frac{\sigma_0}{E} \sqrt{\bar{r}_1(2 - \bar{r}_1)}$	$2(1 - \nu^2) \frac{\sigma_0}{E} \sqrt{2\bar{r}_1}$	$\sqrt{\frac{2}{2 - \bar{r}_1}}$
	Or $(1 + \nu)(1 - 2\nu) \frac{\sigma_0}{E} \sqrt{\bar{x}^2 - 1}$	Or $(1 + \nu)(1 - 2\nu) \frac{\sigma_0}{E} \sqrt{2(\bar{x} - 1)}$	Or $\sqrt{\frac{2}{1 + \bar{x}}}$		Or $2(1 - \nu^2) \frac{\sigma_0}{E} \sqrt{(1 - \bar{x}^2)}$	Or $2(1 - \nu^2) \frac{\sigma_0}{E} \sqrt{2(1 - \bar{x})}$	Or $\sqrt{\frac{2}{1 + \bar{x}}}$
Here $\bar{u}_y = 0$ by symmetry				Here $\bar{u}_x = 0$ by symmetry			

TABLE 3.3 (II) Mode II displacements ahead of right tip along x-axis (\bar{u}_y) Here $\bar{u}_x = 0$

TABLE 3.4 (II) Mode II displacements inside crack surfaces (\bar{u}_x) Here $\bar{u}_y = 0$

Global Solution	Near-tip Solution	Ratio of Near-tip/Global	Global Solution	Near-tip Solution	Ratio of Near-tip/Global
$\frac{-\tau_0}{2\mu} \sqrt{\bar{r}_1(2 + \bar{r}_1)} \left(\frac{k-1}{2}\right)$	$\frac{-\tau_0}{2\mu} \sqrt{2\bar{r}_1} \left(\frac{k-1}{2}\right)$	$\sqrt{\frac{2}{2 + \bar{r}_1}}$	$\frac{\tau_0}{2\mu} \sqrt{\bar{r}_1(2 - \bar{r}_1)} \left(\frac{k+1}{2}\right)$	$\frac{\tau_0}{2\mu} \sqrt{2\bar{r}_1} \left(\frac{k+1}{2}\right)$	$\sqrt{\frac{2}{2 - \bar{r}_1}}$

TABLE 3.4 (III) – Mode III displacements inside crack surfaces (\bar{u}_z) Here $\bar{u}_x = \bar{u}_y = 0$

Global Solution	Near-tip Solution	Ratio of Near-tip/Global
$\frac{S}{\mu} \sqrt{\bar{r}_1(2-\bar{r}_1)}$	$\frac{S}{\mu} \sqrt{2\bar{r}_1}$	$\sqrt{\frac{2}{2-\bar{r}_1}}$

Non-Dimensional Displacements Inside Crack Surfaces

Inside crack surfaces along x-axis:

For $0 \leq \bar{r}_1 \leq 1$, $\theta_1 = \pi, \theta = \theta_2 = 0$, also $\bar{x} = 1 - \bar{r}_1$

Tables 3.4(I), 3.4(II) and 3.4(III) list the displacements inside crack surfaces, from right crack tip to crack centre.

Stresses And Displacements Along A Vertical Line At Crack-Tip ($\Theta_1 = 90^\circ$)

Although the near-tip equations are free from trigonometric terms, the global equations cannot be written without trigonometric terms. Hence, the ratios are not simple functions of \bar{r}_1 alone and omitted.

Summary of Stress and Displacement ratios

From Tables 3.2 (I-III) the ratios of near-tip to global values are summarised as follows:

Parameter			Ratio	Comment
Mode I	Mode II	Mode III		
$\bar{\sigma}_{xx} = \bar{\sigma}_{yy}$	$\bar{\sigma}_{xy}$	$\bar{\sigma}_{yz}$	$\frac{\sqrt{(2+\bar{r}_1)/2}}{1+\bar{r}_1}$ Or $\frac{\sqrt{(1+\bar{x})/2}}{x}$	ahead of crack tip, same for all modes
\bar{u}_x	\bar{u}_y		$\sqrt{\frac{2}{2+\bar{r}_1}}$ or $\sqrt{\frac{2}{1+\bar{x}}}$	ahead of crack tip, same for all modes
\bar{u}_y	\bar{u}_x	\bar{u}_z	$\sqrt{\frac{2}{2-\bar{r}_1}}$ or $\sqrt{\frac{2}{1+\bar{x}}}$	inside crack tip, same for all modes

SOME NUMERICAL COMPARISONS FOR MODE I

From numerical computation, as expected the error in $\bar{\sigma}_{yy}$ increases with \bar{r}_1 ; around 3.6% for $\bar{r}_1 = 0.05$ and $\theta_1 = 0$.

Similar error magnitude are expected for $\bar{\sigma}_{xx}$ and $\bar{\sigma}_{xy}$.

In the calculation of displacements we need information about the material properties, E and ν .

Numerical values are based on Al6061-T6 for which E= 68.9GPa and $\nu = 0.33$. We also assumed $\sigma_0 = 100$ MPa.

The *near-tip* solution underestimates \bar{u}_x ahead of (right) crack-tip. But the magnitude of underestimation is much larger compared to stress comparisons.

Whereas \bar{u}_y inside the crack surfaces are overestimated by the *near-tip* solution; it could be as much as +41.2% at the crack centre.

DISCUSSIONS AND CONCLUSIONS

The materials presented here are intended for beginners who wish to investigate the stress and displacement fields in a centre-cracked plate subjected to bi-linear remote stresses.

The emphasis is on the original Westergaard solutions, its context to the more versatile solution methods and is derived in a manner suitable for the beginners with limited mathematical background.

The *general* solutions for stresses and displacements are then converted to the so-called *near-tip* solutions, valid only in the vicinity of crack tips. The accuracy of the near-tip solutions are quantified to highlight what constitutes near-tip conditions. This will give a clear picture of stresses and displacements in any cracked plate which resembles any of the three basic modes of cracking.

In addition to providing assistance in learning and teaching the subject at a basic undergraduate level, this paper may be of some benefit to the developer of ‘crack-tip finite element methods’. The modelling accuracy of any finite element solution can be validated using the general solution. However, in Mode I and Mode II crack problems, the stresses at the crack front may be three dimensional. For instance, even in a thin plate containing a through-thickness crack, high stress gradients near the crack tips are present. This plane elasticity (or 2-D) solutions as established here and in the literature [6, 7] may not be the perfect solution.

Appendix

The Derivation of General Solutions

As mention before, the solution of plane elasticity problems are based on Airy’s bi-harmonic equation $\nabla^2(\nabla^2\phi) = 0$.

Once the correct expression for the stress function $\phi(x,y)$ which satisfies both the bi-harmonic equation and the boundary conditions of any given problem is found, the stresses and displacements can be easily determined.

During 1950s, Kolosov and Mushkhelishvili introduced a very powerful complex potential function method to solve general plane elasticity problems. Basically this method is the complex representation of the Airy stress function. They derived the following explicit equations for the stresses and displacements in terms of two complex functions:

$$\sigma_{xx} + \sigma_{yy} = 4\text{Re}\{\psi'(z)\}, \quad \sigma_{yy} - \sigma_{xx} + 2i\sigma_{xy} = 2\{\bar{z}\psi''(z)\} + \chi''(z), \quad 2\mu(u_x + iu_y) = \kappa\psi(z) - z\bar{\psi}'(z) - \bar{\chi}'(z) \quad (\text{A-1})$$

We will base our derivation on this solution without explaining these equations.

A.1. Symmetric Problems (bi-axial tension)

For symmetric problems, $\sigma_{xy} = 0$ along $y=0$. Using this symmetry condition, Equations (A-1) can be expressed in terms of, as yet unknown, single complex function rather than two. Mode I crack is a symmetric problem and we will use $Z_I(z)$ as the desired complex function which is linearly related to $\psi(z)$. After somewhat difficult complex function manipulations (not elaborated here) it can be shown that for Mode I crack problems:

$$\sigma_{xx} = \text{Re}\{Z_I\} - y\text{Im}\{Z_I'\}, \quad \sigma_{yy} = \text{Re}\{Z_I\} + y\text{Im}\{Z_I'\}, \quad \sigma_{xy} = -y\text{Re}\{Z_I'\} \quad (\text{A-2})$$

$$2\mu u_x = \frac{\kappa-1}{2}\text{Re}\{Z_I\} - y\text{Im}\{Z_I'\}, \quad 2\mu u_y = \frac{\kappa+1}{2}\text{Im}\{Z_I\} - y\text{Re}\{Z_I'\}$$

Where $Z_I'(z) = \frac{\delta Z_I}{\delta z}$, $Z_I(z) = \int Z_I(z)\delta z$ and $\text{Re}\{ \}$ & $\text{Im}\{ \}$ are respectively the real and imaginary part of the complex function.

$$\text{Also } \mu = \frac{E}{2(1+\nu)} \text{ and } \kappa = 3-4\nu \text{ for plane strain and } \kappa = \frac{3-\nu}{1+\nu} \text{ for plane stress} \quad (\text{A-3})$$

To solve any symmetric problem, in our case Mode I crack problem, all we need is to search for $Z_I(z)$ which satisfies the general conditions of the problem.

Westergaard Solution – Mode I Crack problem

Westergaard used the following function in his solutions of contact stresses and some crack problems.

$$Z_I(z) = \frac{\sigma_0 z}{\sqrt{z^2 - a^2}} \quad (\text{A-4})$$

which satisfies the following boundary conditions relevant to mode I crack problems. Referred to Figure-3

$$\sigma_{xy} = \sigma_{yy} = 0 \text{ at } |x| \leq a \text{ and } y=0 \text{ and } \sigma_{xx} = \sigma_{yy} = \sigma_0, \quad \sigma_{xy} = 0 \text{ as } x^2 + y^2 \rightarrow \infty \quad (\text{A-5})$$

We will use Equations (A-2) together with (A-4) to derive the *general* solution of Mode I crack problems.

A.2. Skew-symmetric Problems (in-plane shear)

For skew-symmetric problems, $\sigma_{yy} = 0$ along the y-axis. Mode II crack problems is one of the skew-symmetric type and again using Equations (A-1) the following solutions can be derived for stresses and displacements of Mode II crack problems.

$$\sigma_{xx} = 2\text{Im}\{Z_{II}\} + y\text{Re}\{Z_{II}'\}, \quad \sigma_{yy} = -y\text{Re}\{Z_{II}'\}, \quad \sigma_{xy} = \text{Re}\{Z_{II}\} - y\text{Im}\{Z_{II}'\} \quad (\text{A-6})$$

$$2\mu u_x = \frac{\kappa+1}{2}\text{Im}\{Z_{II}\} + y\text{Re}\{Z_{II}'\}, \quad 2\mu u_y = -\frac{\kappa-1}{2}\text{Re}\{Z_{II}\} - y\text{Im}\{Z_{II}'\}$$

Westergaard Solution – Mode II Crack problem

The proposed complex function in this case is:

$$Z_{II} = \frac{\tau_0 z}{\sqrt{z^2 - a^2}} \quad (\text{A-7})$$

which satisfies the following boundary conditions related to Mode II crack problems. Again referred to Figure-3.

$$\sigma_{xy} = \sigma_{yy} = 0 \text{ at } |x| \leq a \text{ and } y=0 \text{ and } \sigma_{xx} = \sigma_{yy} = 0, \quad \sigma_{xy} = \tau_0 \text{ as } x^2 + y^2 \rightarrow \infty \quad (\text{A-8})$$

We will use Equations (A-6) together with (A-7) to derive the *general* solution for Mode II crack problems.

Although it is not important here, it may be verified that for any plane elasticity problem having collinear cracks in an infinite plate

$$\phi = \text{Re}\{Z_I\} + y\text{Im}\{Z_I'\} - y\text{Re}\{Z_{II}\} + Ay^2, \quad \text{where } Z_I = \int \int Z_I(z)\delta z \delta z \quad (\text{A-9})$$

A.3. Westergaard Solution of Mode III crack problems (anti-plane shear)

This type of problems are associated with anti-plane deformation for which

$$u_x = 0, \quad u_y = 0 \text{ and } u_z = u_z(x, y)$$

Note that Mode III crack problem is of a different type from other two modes.

Nonetheless, the appropriate Westergaard complex function is: $Z_{III} = S\sqrt{z^2 - a^2}$ (A-10)

which satisfies the Mode III boundary conditions and the non-zero stresses and deformations are given as follows:

$$\sigma_{yz} = \text{Re}\{Z'_{III}\}, \quad \sigma_{xz} = \text{Im}\{Z'_{III}\}, \quad \mu u_z = \text{Im}\{Z_{III}\} \quad (\text{A-11})$$

We will use Equations (A-11) with (A-10) to derive the stresses and displacements in Mode III crack problems.

A.4. Sample Derivation of Stresses and Displacements

There are thirteen stresses and displacements related to three crack modes. But to keep the presentation within reasonable limits we will only show the derivation of stresses and displacements for Mode I problem. However, the complete list of all thirteen stresses and displacements will be presented in the main body of this paper. The equations are listed in three tables in non-dimensional forms.

A.4.1. General Solution for Mode I crack problem

Referred to Figure-3, we express the coordinates of a point, P in vector forms:

$$z = re^{i\theta}, \quad z - a = r_1 e^{i\theta_1} \quad \text{and} \quad z + a = r_2 e^{i\theta_2}; \quad i = \sqrt{-1} \quad (\text{A-12})$$

Substitution of (A-12) in A-4 will produce the $\text{Re}\{\}$ and $\text{Im}\{\}$ parts of various complex functions required for 5 stresses and displacements in (A-2). The explicit solutions are given below.

Noting that $y = r \sin \theta$

$$\sigma_{xx} = \frac{\sigma_0}{\sqrt{r_1 r_2}} \left[\cos \phi - \frac{a^2}{r_1 r_2} \sin \theta \sin 3\psi \right], \quad \sigma_{yy} = \frac{\sigma_0}{\sqrt{r_1 r_2}} \left[\cos \phi + \frac{a^2}{r_1 r_2} \sin \theta \sin 3\psi \right], \quad \sigma_{xy} = \frac{\sigma_0}{\sqrt{r_1 r_2}} \left[\frac{a^2}{r_1 r_2} \sin \theta \cos 3\psi \right] \quad (\text{A-13})$$

$$2\mu u_x = \sigma_0 \sqrt{r_1 r_2} \left[\frac{k-1}{2} \cos \psi - \frac{r^2}{r_1 r_2} \sin \theta \sin \phi \right], \quad 2\mu u_y = \sigma_0 \sqrt{r_1 r_2} \left[\frac{k+1}{2} \sin \psi - \frac{r^2}{r_1 r_2} \sin \theta \cos \phi \right]$$

Similarly (A-12) can be used with (A-7) and then (A-10) to derive stresses and displacements for Mode II and Mode III, respectively. All thirteen stresses and displacements pertinent to three basic fracture modes are listed in Tables 3.1 (I-III) in the main text. These tables also include the *near-tip* solutions as shown below.

A4.2. Near-tip Solution for Mode I Crack problem

In the study of crack growth behaviour using Irwin's Stress Intensity Factor (K_I), the stresses and displacements around the crack-tip is useful. In the vicinity of (right) crack-tip we use the following special conditions. Referred to Figure-3:

$$\text{For } \frac{r_1}{a} \square 1, \quad \theta \approx 0, \quad \theta_2 \approx 0, \quad r \approx a, \quad r_2 \approx 2a \quad \text{and} \quad \sin \theta = \frac{r_1 \sin \theta_1}{r} \quad (\text{A-14})$$

Applying these near-tip conditions to the general solutions, Equations (A-13) may be re-written as:

$$\sigma_{xx} = \sigma_0 \sqrt{\frac{a}{2r_1}} \cos \frac{\theta_1}{2} \left(1 - \sin \frac{\theta_1}{2} \sin \frac{3\theta_1}{2} \right), \quad \sigma_{yy} = \sigma_0 \sqrt{\frac{a}{2r_1}} \cos \frac{\theta_1}{2} \left(1 + \sin \frac{\theta_1}{2} \sin \frac{3\theta_1}{2} \right), \quad \sigma_{xy} = \sigma_0 \sqrt{\frac{a}{2r_1}} \sin \frac{\theta_1}{2} \cos \frac{\theta_1}{2} \cos \frac{3\theta_1}{2} \quad (\text{A-15})$$

$$2\mu u_x = \sigma_0 \sqrt{\frac{ar_1}{2}} \cos \frac{\theta_1}{2} \left[(\kappa-1) + 2 \sin^2 \frac{\theta_1}{2} \right], \quad 2\mu u_y = \sigma_0 \sqrt{\frac{ar_1}{2}} \sin \frac{\theta_1}{2} \left[(\kappa+1) - 2 \cos^2 \frac{\theta_1}{2} \right]$$

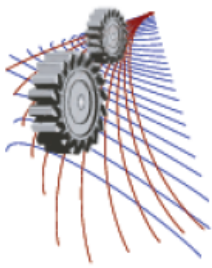
In all of the Equations (A-15), we may convert the non-angular factors in terms of the so-called stress intensity factor $K_I = \sigma_0 \sqrt{\pi a}$. For example, $\sigma_0 \sqrt{\frac{a}{2r_1}} = \frac{K_I}{\sqrt{2\pi r_1}}$ and $\sigma_0 \sqrt{\frac{ar_1}{2}} = K_I \sqrt{\frac{r_1}{2\pi}}$ for stresses and displacements, respectively.

Following the procedures outlined above, both general and near-tip solutions for the other two modes can be easily derived. It may be noted that for other two modes: $K_{II} = \tau_0 \sqrt{\pi a}$ and $K_{III} = S\sqrt{\pi a}$.

REFERENCES

1. A.A. Griffith, The Phenomena of Rupture and Flow in Solids, Philosophical Transactions of Royal Society, A, Math. Phys. Eng. Sci. 221(1921) 582-593.
2. G.R. Irwin, Analysis of stresses and strains near the end of a crack traversing a plate, J. Appl. Mech. 24 (1957) 361-364.
3. J.R. Rice, A path independent integral and approximate analysis of strain concentration by notches and cracks, J. Appl. Mech. 35 (1968) 379-386.
4. H.M. Westergaard, Bearing Pressure and Cracks, J. Appl. Mech. 10 (1939) 77.
5. N.I. Muskhelishvili, Some Basic Problems of the Mathematical Theory of Elasticity, 4th ed., P. Noorhoff, Göttingen (1953)

6. C.H. Wang, Introduction to Fracture Mechanics, Defence Science and Technology Organisation (DSTO), Australia (1996).
7. C.T. Sun, Z.-H. Jin, Fracture Mechanics, Academic Press, Elsevier Inc. (2012).



Physio-Mechanical Properties of Pineapple Leaf Fiber and its Spinning Performance

Mohammad Abdul Jalil^{1,a}, A.K.M.Mahabubuzzaman^{2,b}, Md. Nasir Uddin^{3,c},
Md.Tanjim Hossain^{3,d} and Md. Moshir Rahman^{3,e}

¹Mawlana Bhashani Science and Technology University, Tangail-1902, Bangladesh

²Bangladesh Jute Research Institute, Dhaka, Bangladesh

³Northern University Bangladesh, Banani, Dhaka-1213, Bangladesh

^aCorresponding author: jalil.mbstu@gmail.com

^bdrmahabu.bjri@yahoo.com

^cenr.nasir_rony@yahoo.com

^dtanjimseu@yahoo.com

^emoshiur_txt01@yahoo.com

Abstract. The physio-mechanical properties such as strength, fineness, tenacity and elongation of Pineapple Leaf Fiber (PALF) have been studied and compared. It was found that physio-mechanical properties of PALF were similar to jute fiber. PALF contained relatively greater diameter (fewer fine) compared with that for jute fiber and consequently, the quality ratio value of yarn for PALF was much smaller than that of jute yarn.

INTRODUCTION

Pineapple is one kind of fruit which is mainly used for making jam and juice. In many countries of the world there exist a lot of industries involved in processing jam and juice. From one pineapple fruit, only 52% is used for jam and juice production, remaining 48% consists of fruit peel and leaves forming the waste. These wastes are rich in lignin and cellulose and thus form a very good raw material for allied fibers. Also waste disposal is a major problem in these industries because of very high lignin and cellulose content of the waste leaves which is difficult to be degraded thus resulting in pollution and affecting the environment [1].

Pineapple Leaf Fiber (PALF) serving as reinforcement fiber in most of the plastic matrix has shown its significant role as it is cheap, exhibiting superior properties when compared to other natural fiber as well as encouraging agriculture based economy. Natural fibers like sisal, banana, jute, oil palm, kenaf and coir have been used as reinforcement in thermoplastic composites for application in consumer goods, furniture, low cost housing and civil structures. PALF is one of these natural fibers that also have the potential to be used as reinforcement in thermoplastic composites [2]. PALF is multi-cellular and lignocelluloses materials extracted from the leave of plant *Ananas cosomus* belonging to the *Bromeliaceae* family by retting (separation of fabric bundles from the cortex). PALF has a ribbon-like structure and is cemented together by lignin, pentose-like materials, which contribute to the strength of the fiber [3]. The excellent mechanical properties of PALF are associated with this high cellulose and low microfibrillar angel. This fiber can be obtained for industrial purposes without any additional cost [4]. Pineapple

leave fiber is an agro-waste which is rich in cellulose, relatively inexpensive and has a potential for polymer reinforcement [5].

The available traditional methods of fiber extraction involve the processes viz. retting, decortications, combing etc., which takes 6 to 10 days. During decortications it is difficult to extract the fibers as they are sticky due to the presence of pith thus bow to necessary the use of chemicals which is not eco-safe. So the aim of this study is to develop an eco-friendly, cost effective technology for processing the pineapple leave fiber (PALF) and identify the spinning performance of this fiber. These fibers are used for diverse commercial application including value-added handicraft and handloom products [6, 7, 8].

MATERIALS AND METHODS

The Pineapple Leaf was collected from Modhupur Upazilla, Tangail Bangladesh. Pineapple Leaf Fiber (PALF) extracted from the leave of plant *Ananascosomus* belonging to the *Bromeliaceae* family by retting (separation of bundle of fibers from the cortex). Jute plant of variety C-145, Bangla White B (*Corchorus Capsularies*) jute fibers were collected from the experimental plot of Bangladesh Jute Research Institute (BJRI), Dhaka and retted under fresh water for 18 days. The fibers were separated and sun dried. The resulting fibers were used as the fibrous raw materials.

Fiber Properties

Physical properties such as strength, fineness, tenacity and elongation of jute fibers and Pineapple Leaf Fibers have been determined in the BJRI testing laboratory. BS 3411 method is used for this purpose. All the tests are performed in the standard testing atmosphere i.e. 65 ± 2 % R.H and $20 \pm 2^\circ$ C [9]. Measured physical properties of the fibers are furnished below.

TABLE 1: Physical Properties of Bangla White B (BWB) Jute Fiber.

Grade	Statistics	Fineness (tex)	Bundle Strength (Pressly index, kg/mg)	Breaking Tenacity (gf/tex)	Breaking Elongation (%)
BWB	Mean	2.60	4.03	33.40	1.60
	Range	1.3-4.0	3.0-5.16	30-45	1.0-1.8
	CV%	19.30	20.11	25.09	20.50

TABLE 2: Physical Properties of Pineapple Leaf Fiber (PALF).

Grade	Statistics	Fineness (tex)	Bundle Strength (Pressly index, kg/mg)	Breaking Tenacity (gf/tex)	Breaking Elongation (%)
PALF	Mean	3.20	4.89	31.32	3.25
	Range	2.5-6.0	2.5-5.0	25-45	2.5-4.0
	CV%	20.30	24.06	30.11	25.60

Yarn Preparation

Samples were prepared in Mechanical Processing Division, Bangladesh Jute Research Institute (BJRI), Manik Mia Avenue, Dhaka, Bangladesh. The raw Pineapple Leaf Fibers 100 kg was softened in the softener machine with an application of 25% emulsion on the weight of fibers. Then the soften fibers were stored in a bin for pilling or conditioning for a period of 48 hours as commonly practiced in jute mills and these pilled fibers were processed through conventional jute processing sequence i.e. breaker card, finisher card, 1st, 2nd and 3rd drawing frame machines. The output of 3rd draw frame sliver was spun through apron draft ring spinning frame for producing yarns of 5 and 7 lbs/spy.

Yarn Properties

Yarn properties like tensile strength and extension at break was measured by the Universal Strength Tester Model Titan² which applies the principle of constant rate of extension (CRE) for testing. The procedure is adopted ASTM, D2256. The count of yarn is measured according to ASTM D 1907. A mechanical Shirley twist tester was used for measuring the inserted twist in the yarn. The quality ratio is calculated using the following relationship.

$$\text{Quality ratio (\%)} = \frac{\text{Tensile Strength in lbs}}{\text{Count of yarn } \left(\frac{\text{lbs}}{\text{spy}}\right)} \times 100 \quad (1)$$

TABLE 3: Physical Properties of PALF Yarn.

Fiber	Nominal Count ¹ tex (lbs/spy)	Actual Count ¹ tex (lbs/spy)	Twist tpm	Tensile Strength Kg (lbs)				Quality Ratio %	Reference value of Quality Ratio %
				Mean	SD	CV %	Extension at break %		
									100% BWB jute fiber
PALF	173(5)	176 (5.11)	314	2.05 (4.51)	0.22 3	13.11	2.10	88.25	93.02
PALF	241(7)	242 (7.02)	276	2.64 (5.82)	0.29 1	10.65	2.22	82.91	90.13

$$^1 \text{tex} = \text{Jute count (lbs/spy)} \times 34.45$$

RESULTS AND DISCUSSION

Pineapple Leaf Fiber contain very big diameter compared with other textile fibers like jute fiber and mainly due to this bigger diameter pineapple leaf fiber produces low percent quality ratios (table 3).

The higher breaking load or tenacity or tensile strength may be due to the tight packing of the crystalline and amorphous regions and higher intermolecular forces in the fibers [10]. The mean tenacity values obtained for PALF was 31.32 gf/tex (table 2). This value as obtained for Bangla White B (BWB) jute fiber is 33.40 gf/tex. Again, the mean values of bundle strength and elongation percentage for Bangla White B jute fiber are 4.03 kg/mg and 1.60 % respectively. Referring to the table 2, it is observed that jute fiber shows better performance compare to pineapple leaf fiber (PALF). The linear density (fineness) for Bangla White B jute fiber is 2.60 tex. But the linear density for pineapple leaf fiber is much higher (3.20 tex) than that of jute fiber (table 2). Thus pineapple leaf fiber content relatively greater diameter (less fine) compared with jute.

The quality ratio (reference value) 100% BWB jute fiber for 173 tex (5 lbs/spy) and 241 tex (7 lbs/spy) count of yarns are 98.20 and 93.71% respectively. These values (table 3) for pineapple leaf fiber at 173 tex (5 lbs/spy) and 241 tex (7 lbs/spy) count of yarns are 88.25 and 82.91% respectively. This quality ratio value is less mainly due to the bigger diameter contained by the pineapple leaf fiber. Thus pineapple leaf fiber cannot be spun alone for quality yarn manufacturing purpose but diameter being greater and fiber being cheaper compared to jute, this fiber could have better application in jute industries.

In conclusion, a fiber having good strength cannot produce a good quality of yarn unless it's diameter is small i.e. a small and even diameter is necessary for producing good quality yarn.

COST ANALYSIS

As mention earlier, PALF yarn can easily be prepared in conventional jute processing machine. So, manufacturing of PALF yarn does not require any new or extra machine. Thus capital investment for making the yarn is much less. The raw material cost is also very low. Considering the price of PALF yarn in the range of Tk.40 to 60 per kg and that of 100% jute and cotton yarn in the range of Tk. 40 to 80 and Tk.250 to 500 per kg respectively. It may be

stated that manufacturing of PALF yarn in existing conventional jute processing machine would be highly cost effective as this value added high performing yarn/fabric may be marketed at a much higher price and also the use of cotton fiber can be minimized by use this fiber.

APPLICATIONS

This new type of PALF yarn opened up some new areas of use for jute and PALF fiber for which jute and PALF have never been thought off. Disposable decorative and fancy carry bags with different color effects for i) school bag ii) shopping bag iii) ladies purse iv) traveling luggage bag v) curtains vi) placement sheet vii) table cloth viii) cushions fabric etc. can be made from this yarn/fabric. Presently, these items are made from 100% synthetic material.

CONCLUSIONS

- The findings will have a direct impact on the jute industry and may be able to produce better quality yarn by adopting the method suggested.
- Consequently the use of PALF yarn will be increased, which is to bio-degradable and therefore environment friendly.
- Valuable foreign currency can be saved by encouraging the use of PALF yarn in place of synthetic yarn.
- Pineapple Leaf Fiber can be obtained for industrial purposes without any additional cost. So, capital investment is low.
- Pineapple Leave Fiber is an agro-waste which is rich in cellulose, relatively inexpensive. So, use this fiber we could reach the zero waste management.

Nomenclature

lbs/spy: Pounds per spyndle indicates the fineness or coarseness of yarn and determined by the weight of 14400 yards (= 1 spyndle) length of yarn in pound (lb).

Tex: Tex is the mass of yarn in gram per kilometer of its length

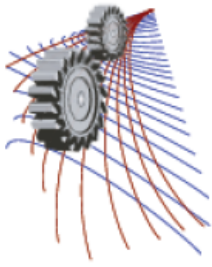
TPM: Twist per meter

CV%: Co-efficient of Variation %

REFERENCES

1. Yasodha Thirumal , Advantages of Pineapple Fiber, Available at [www. Fibre2fashion.com](http://www.Fibre2fashion.com), 2010.
2. Ms. Munirah Mokhtar, Abdul Razak Rahmat, Azman Hassan , Suriani Abdul Samat Characterization and Treatments of Pineapple Leaf Fibre Thermoplastic Composite for Construction Application,2007,Research vot. no.75147, UTM, p. iii.
3. George, J., Bhagawan, S.S., Prabhakaran, N. and Thomas, S, Short Pineapple-leaf-fiber-reinforced Low-density Polyethylene Composites. *Journal of Applied Polymer Science*. 1995, 57: 843-854.
4. Folkes, M.J. *Short Fibre Reinforced Thermoplastics*. John Wiley & Sons Ltd., Great Britain, 1982.
5. Mishra, S., Misra, M., Tripathy, S.S., Nayak, S.K. and Mohanty, A.K. Potentiality of Pineapple Leaf Fibre as Reinforcement in PALF-Polyester Composite: Surface Modification and Mechanical Performance. *Journal of Reinforced Plastics and Composites*, 2001, 20(4): 321-334
6. Gurumurthy G. SITRA to Commission Pineapple Fibre Plant Agartala,Textile Research Association (SITRA), Coimbatore, India, 2010.
7. Roy A N, Basu G and Bhattacharya G K, An Approach to Engineer Jute Based Yarn for Improvement of its Property Performance, IE(I) Journal-TX, February 2003, Vol 89, pp. 1-5.

8. Sengupta S, Ganguly P K and Bhattacharyya G K, Mechanical Behavior of Jute Ply Yarns, IE(I) Journal-TX, August 2003, Vol 84, pp. 1-5.
9. Booth, J.E. "Principle of Textile Testing" 3rd edition, CBS Publishers & Distributers, 4596, 1-A, 11 Darya Ganj, New Delhi, 1968, p.101.
10. Gohl, E.P.G. & Vilensky, L.D. 1983, *Textile Science: An explanation of fiber Properties*, 2nd edn, CBS Publishers and Distributers, New Delhi, pp.14-18.



Hazardous Effects on Health and Environment due to Coal Dust Producing in Pigment Production Factories: A Case Study of Chittagong City

Liton Chandra^{a)} and Asiful Hoque^{b)}

Department of Civil Engineering, Chittagong University of Engineering and Technology (CUET), Chittagong-4349, Bangladesh

^{a)} Corresponding author: litondas91@gmail.com

^{b)} masifulcuet@gmail.com

Abstract: Chittagong is the port city of Bangladesh. Due to export and import business there have developed many industries where a huge number of people are working for producing various manufacturing products. Among these industries some are producing pigment which is used for dado of building. Due to rapid urbanization the demand of this pigment is increasing highly across the country. During the process of pigment producing a lot of coal dusts are evolved in those factories environment. The internal environment of those factories has not developed properly to minimise the production of the coal dust and health risk of workers as well as nearby living people. That's why those are causing hazardous effects on health of workers and surrounding environment of the factory. Coal is toxic because elements such as arsenic, mercury, lead, nickel, cadmium, selenium, vanadium, and copper are accumulated and concentrated within coal. During producing the fine particulate nature of coal dust and its toxic constituents are readily inhaled by the workers. In that cases workers as well as people living in nearby environment faces many health problems such as lodge in the lungs, cardiopulmonary disease, chronic obstructive pulmonary disease, high blood pressure, lung disease, and kidney disease. The main aim of this study is to find out whether people working inside pigment factory and living in nearby environment are exposed to coal dust that may cause which sorts of health risks. This study also aimed to find the variation and intensity of diseases suffered by workers due to work there with respect of working time duration and by the people who live in surrounding environment. In order to study the health hazards of pigment producing factory on workers and nearby living people, about six factories were considered for the studies. Among these six factories, three were north side of Karnaphuli River, at Kalurghat industrial area and other three were south side at CEPZ industrial area. The workers as well as nearby people were administered with the standard format questionnaire which was followed by personal interviews. The results indicate a visible impact on health of workers and the health related problems increases. Long time inhaling of coal dust will exacerbate this problem which could increase fatality of those diseases as well as mortality further in future. This study would emphasize the urgent need for prevention measures of health risks and improving the internal production mechanism of those factories

INTRODUCTION

Pigment is important for wall painting all over the world. In building construction, for colouring the skirting of superstructure wall, a blackish pigment is mostly used in all over Bangladesh. Fifteen to twenty years ago this pigment was imported from other countries. Among these countries India was first one when there was no factory in Bangladesh. When pigment using were increasing day by day then few entrepreneurs started to manufacture this pigment locally at Dhaka, Chittagong and Khulna. There have many pigment production factories in Bangladesh. In Chittagong City six factories are identified for research work. Among these six factories, three were north side of Karnaphuli River, at Kalurghat industrial area and other three were south side at CEPZ industrial area. The processes of manufacturing pigment have not been developed as required to prevent health risks of workers and ambient air pollution. Coal is a brown to black combustible material made from decayed plant matter that has been

compressed by rock formations over a long period of time. It is found throughout the world and is the most abundant of the fossil fuels [1]. Coal dust is powdered form of coal which contains toxic heavy metals including arsenic, lead, thallium, barium, cadmium, chromium, mercury, and nickel. The pigment is produced mainly from iron splinter, coal and chemicals. When these ingredients are pulverized huge amount of dust, gases, noise and vibration are emitted from machinery. The impacts of pigment industry are countless and adverse to health of workers.

METHODOLOGY

Six factories were taken in consideration for survey. At first Kalurghat industrial area were surveyed and secondly CEPZ industrial area. All subjects were served with a questionnaire which was made by help of doctor. Firstly some probable diseases caused by coal dust were selected and their symptoms are noted in English. Then the English disease name and symptoms were translated into Bengali to make it easily understandable to the workers. The workers working in the pigment factories were administered with the questionnaire and total of 80% of employees in pigment factories were studied. Later interviews were conducted. The questionnaire and interview question are as bellow.

WORKER'S AND RESIDENCY'S INTERVIEW ABOUT HEALTH QUESTIONNAIRE:

Name :
 Age :
 No. of years since working in the factory :
 Marital status :

1. Do you smoke tobacco?	<input type="checkbox"/> Yes	<input type="checkbox"/> No
---------------------------------	-------------------------------------	------------------------------------

2. If yes, how many packs per day? _____ Number of years _____

3. Have you ever had any of the following conditions? (indicate yes or no for each)	<input type="checkbox"/> Yes	<input type="checkbox"/> No
a. Seizures (fits)		
b. Diabetes (sugar disease)		
c. Allergic reactions that interfere with your breathing		
d. Trouble smelling odors		

4. Have you ever had any of the following pulmonary or lung problems?	<input type="checkbox"/> Yes	<input type="checkbox"/> No
a. Asbestosis		
b. Chronic bronchitis more than 3 episodes in the last year		
c. Emphysema		
d. Lung cancer		
e. Silicosis		
f. Chest injuries or surgeries		

g. Asthma as an adult
h. Pneumonia in the last month
i. Tuberculosis (active disease)
j. Any other lung problem

5. Do you currently have any of these symptoms of pulmonary or Lung illness?	<input type="checkbox"/> Yes	<input type="checkbox"/> No
a. Shortness of breath		
b. Shortness of breath with light activity		
c. Shortness of breath with strenuous activity		
d. Cough that produces thick sputum or blood		
e. Cough lasting longer than 3 weeks		
f. Wheezing		
g. Wheezing that interferes with work		
h. Any other symptoms that may be related to lung problems:		

6. Have you ever had any of the following cardiovascular or heart problems?	<input type="checkbox"/> Yes	<input type="checkbox"/> No
a. Heart Attack		
b. Stroke		
c. Angina (chest pain)		
d. Heart failure		
e. Irregular heart beat		
f. Swelling in your legs or feet (not caused by walking)		
g. High blood pressure		
h. Any other heart problems:		

7. Have you ever had any of the following cardiovascular or heart symptoms?	<input type="checkbox"/> Yes	<input type="checkbox"/> No
a. Frequent pain or tightness in your chest		
b. In the past two years, have you noticed your heart skipping or missing a beat?		
c. Heartburn or indigestion that is not related to eating		
d. Any other symptoms that may be related to heart or circulation problems		

8. Do you currently take medication for any of the following problems?	<input type="checkbox"/> Yes	<input type="checkbox"/> No
a. Breathing or lung problems		
b. Heart trouble		
c. Blood pressure		
d. Seizures (fits)		

9. Do you use respirator during work.	<input type="checkbox"/> Yes	<input type="checkbox"/> No
--	-------------------------------------	------------------------------------

10. If you've used a respirator, have you ever had any kind of problem?	<input type="checkbox"/> Yes	<input type="checkbox"/> No
a. Eye irritation		
b. Skin allergies or rashes		
c. Anxiety		
d. General weakness or fatigue		
e. Any other problem that interferes with your use of a respirator		

11. Which health specialist do you visit most frequently? A) What kind of medicine do you use mostly?
--

12. How much a day.
Date: _____ Comments: _____

Thank you for your help!

Another Interview Questions asked to workers

1. Do you use any safety devices such as masks, respirator etc.

<input type="checkbox"/> If yes, what?	<input type="checkbox"/> If no, why?
Answer:	Answer:

2. Does the owner provide you with safety devices?

If yes, what?	<input type="checkbox"/> If no, why?
Answer:	Answer:

3. You have any family history for any diseases?

<input type="checkbox"/> If yes, How the symptom?	<input type="checkbox"/> If no.
---	---------------------------------

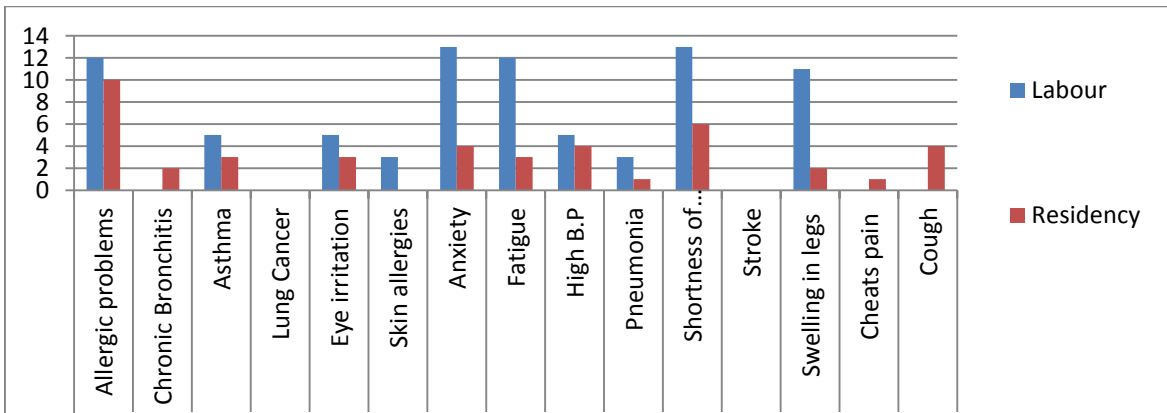
RESULT

At first Kalurghat industrial area was selected. Labourer and residency were being interviewed for surveying. Kalurghat area's surveying results are bellow :

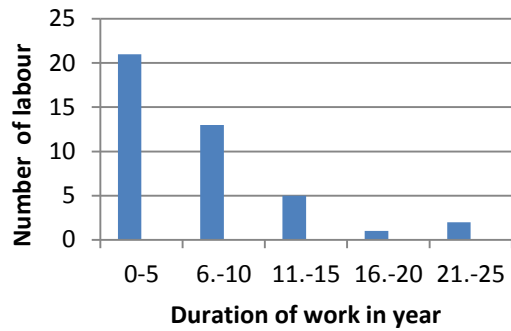
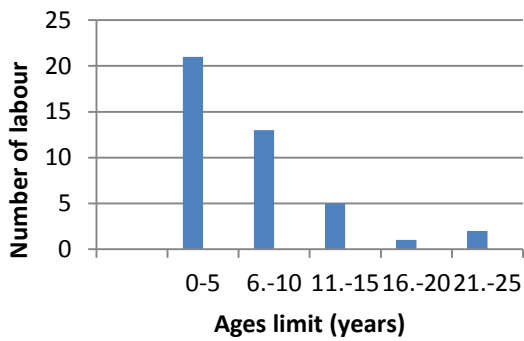
TABLE 1. Survey results of pigment producing factories from Kalurghat industrial area.

Kalurghat industrial area	Diseases											Ages limit (years)					Duration of work in years(years)								
	Allergic problems	Chronic Bronchitis	Asthma	Lung Cancer	Eye irritation	Skin allergies	Anxiety	Fatigue	High B.P	Pneumonia	Shortness of breath	Stroke	Swelling in legs	Cheats pain	Cough	20-30	31-40	41-50	51-60	61-70	0-5	6-10	11-15	16-20	21-25
No. of labour	15	0	5	0	5	4	10	10	5	0	15	0	10	0	0	30	5	4	4	2	26	14	6	4	2
No. of Resident	7	1	1	0	2	1	6	4	4	0	6	0	3	1	2	-	-	-	-	-	-	-	-	-	-

According to questionnaire and interview following results are found which has been described in graphical way



(a)



(b)

(c)

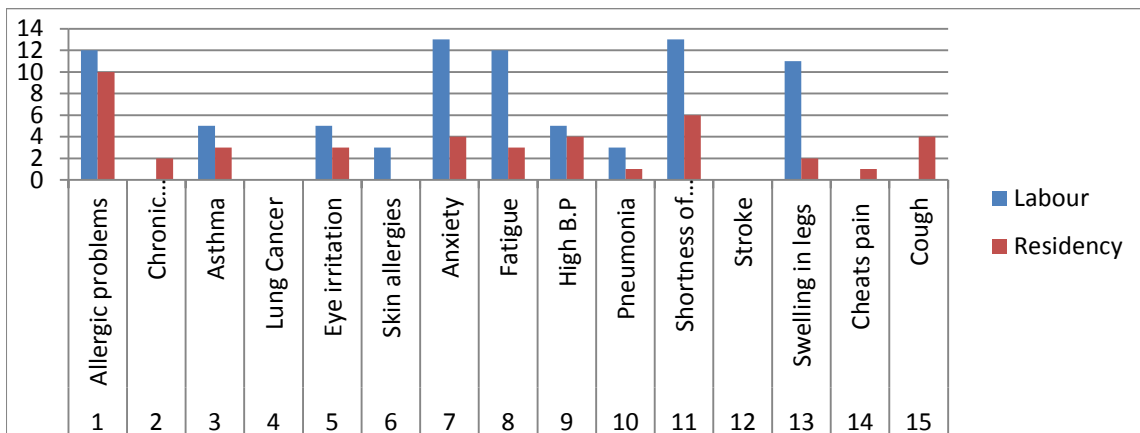
FIGURE 1. (a) Diseases caused by labour and resident; (b) Labours based on different ages; (c) Labours based on duration of work in year.

Secondly CEPZ industrial area was surveyed for this research purpose. These results are given below.

TABLE 2. Survey results of pigment producing factories from CEPZ industrial area.

CEPZ industrial area	Diseases														Ages limit (years)					Duration of work in years(years)					
	Allergic problems	Chronic Bronchitis	Asthma	Lung Cancer	Eye irritation	Skin allergies	Anxiety	Fatigue	High B.P	Pneumonia	Shortness of breath	Stroke	Swelling in legs	Cheats pain	Cough	20-30	31-40	41-50	51-60	61-70	0-5	6-10	11-15	16-20	21-25
No. of labour	12	0	5	0	5	3	13	12	5	3	13	0	11	0	0	28	7	3	4	1	21	13	5	1	2
No. of Resident	10	2	3	0	3	0	4	3	4	1	6	0	2	1	4	-	-	-	-	-	-	-	-	-	-

According to questionnaire and interview following results are found which has been described in graphical way.



(a)

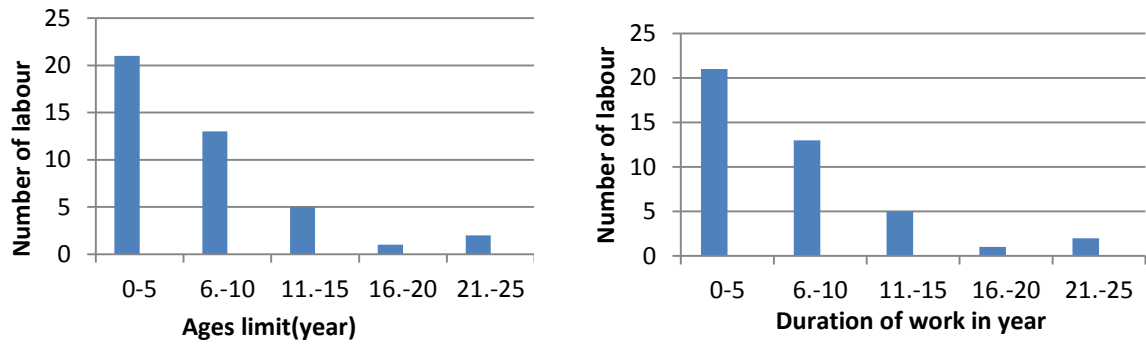


FIGURE 2. (a) Diseases caused by labour and resident; (b) Labours based on different ages; (c) Labours based on duration of work in years.

There are fifteen kinds of diseases [Fig:1(a)] and [Fig:2(b)] were recorded from the labors in the pigment production in Chittagong city. These included: Allergic problem, chronic bronchitis, asthma, emphysema, Lung cancer, pneumonia, tuberculosis, shortness of breath, cough, wheezing, stroke, chest pain, swelling in legs and feet, eye irritation, skin allergies, anxiety and fatigue, High B.P. Ages of greater part of labors were within the limit 20-25 years and duration of work within 0-5 years [Fig.1(a)], [Fig.2(b)] & [Fig.1(c)], [Fig.2(c)].



DISCUSSION

We have gathered some experience during the execution of this work. They are mentioned below.

- Workers were illiterate and unwilling to provide authentic information of some cases.
- Workers do not go to doctor if they suffer in allergic problem.
- The effects of working in this factory would cause fatal problem to health when worker will be old in age.
- There were no pollution control devices installed in factories.

Workers use tube well installed in those factories but the underground water may have heavy metal due to infiltration of coal slurry.

CONCLUSION

Majority diseases were found in labors that were old in age and working for long period. But the numbers of old labors were considerably less than that of young labors. All of them were not conscious about the diseases that may occur due to inhaling coal dust. The study shows that the workers work in those factories for few years and then

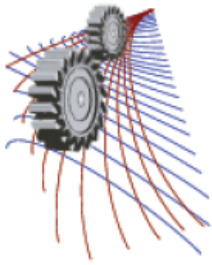
change their job to anywhere. So the effect of coal dust on health could not detect as assumed from another study. If some tests on health were executed the accurate effect of coal dust could be determined. Another point of concerning that the infrastructures of those factories are not good. There was not enough shade and wall around the factories. For this reason they pollute ambient air very much. Some studies have shown that the slurry of coal dust can infiltrate into ground water and can contaminate that ground water with the presence of heavy metal. People who lives around these pigment producing factories also suffering same diseases but rate remain lower than labor.

ACKNOWLEDGEMENTS

The authors thank all medical staffs of medical center of CUET for their frequent support to run this study, specially to Dr. Md. Yusuf Miah, Chief Medical Officer and Dr. Mir Murtaza Reza Khan ,Medical Officer CUET. The authors also thank to factory workers of the pigment production factories who participated in this study and shared their perceptions, as well as those who helped to recruit participants and who offered help through various stages of the study. We would also like to thank Dr. Md. Reaz Akter Mollick, Researcher, CUET Green for Peace (GP) for his cordial support for conducting this research.

REFERENCES

1. S, Sana, GA;Bhat, HM; Balkhi. 2013. Health Risks Associated With Workers in Cement Factories. International Journal of Scientific and Research Publications, Volume 3, Issue 5, May 2013 ISSN 2250-315.
2. SD; Azad, MA; Khan, MI; Ghaznavi, S; Khan. 2013. STUDY OF THE HEALTH EFFECTS OF COAL MINING ON COAL MINE WORKERS OF BALUCHISTAN. International Journal of Asian Social Science,2013, 3(7):1572-1590.
4. Workplace Health and Safety Bulletin, CH063-Chemical Hazards Revised April 2010. [online]. Available at:
5. Biping, S. 2012. Occupational heat stress and health impact assessment at a shoe factory in China. Available at: http://www.phmed.umu.se/digitalAssets/104/104570_biping-song.pdf [Accessed 12 August 2014].
6. Vijai, SS; Deep, NP. 2011. Human Health Risk due to Cement Dust Exposure. Policy-Brief. [online]. Available at:http://www.rpcb.rajasthan.gov.in/rpcbweb/ReportsAndPaper/RSPCB_CEMENT_DUST_PolicyBrief.pdf [Accessed 12 August 2014]
8. Barbara, G; Steven, GG and Lisa, GE. 2010. Coal Ash The toxic threat to our health and environment.
9. A Report From physicians for social Responsibility and Earthjustice. [online]. Available at: <http://www.psr.org/assets/pdfs/coal-ash.pdf>.
10. Coal Mine Dust Exposures and Associated Health Outcomes. A Review of Information Published Since 1995. Department Of Health And Human Services Centers for Disease Control and Prevention National Institute for Occupational Safety and Health. [online]. Available at: <http://www.cdc.gov/niosh/docs/2011-172/pdfs/2011-172.pdf>



MHD Mixed Convection in Two-Sided Lid Driven Open Cavity Including Partition Heat Sources

Anwarul Karim^{a)}

Department of Mechanical Engineering, Bangladesh University of Engineering and Technology, Dhaka-1000, Bangladesh

^{a)}Corresponding author: anwarul2buet@gmail.com

Abstract. The effect of magnetic field on mixed convection is numerically investigated in a two-sided lid-driven open cavity including partition heat sources. The heated partition walls are located at the middle of the upper half of the cavity. The vertical moving walls are at constant low temperature while the bottom wall is at constant high temperature. The inclined inlet and outlet are placed at the top corner. The cool air is injected into the cavity at an angle of 45°. Steady, laminar, two-dimensional model based on the Galerkin weighted residual finite-element method is used for solving the governing equations. The flow and thermal fields (represented by streamline and isotherm contour) are investigated for fixed Reynolds number ($Re=100$) with varying Richardson number ($Ri = 0.1 \sim 10$) and Hartmann number ($Ha = 10 \sim 50$). The quantitative heat transfer is measured by average Nusselt number (Nu) along the heated surfaces. The computational results indicate that the heat transfer coefficient is strongly affected by Richardson number and Hartmann number. It is observed that convection heat transfer increases with Richardson number while Hartmann number retards it.

INTRODUCTION

The interaction between free and forced convection is termed as mixed convection. Mixed convection flow in a cavity or in a channel in the presence of a magnetic field is of special technical significance as it is frequently used in many industrial applications such as geothermal reservoirs, cooling of nuclear reactors, thermal insulations, petroleum reservoirs, electronic packages and microelectronic devices. Several analytical, numerical and experimental studies have been carried out to investigate the heat transfer and fluid flow in mixed convection in different open cavities and channels. One of the common shapes is horizontal open channel [1 and 2]. Other shapes like square, rectangular, T-shape, vertical channels etc are also investigated [3-6]. Saeidi and Khodadadi [5] presented finite-volume based computational study of steady laminar forced convection inside a square cavity with inlet and outlet ports. Porous and vented enclosures [7 and 8] have also significant importance in mixed convection. Sumon Saha et al. [9] showed influence of different inlet outlet configuration on mixed convection in a vented enclosure. Magneto-hydrodynamics (MHD) studies the dynamics of electrically conducting fluids in the presence of electromagnetic fields and has many applications such as liquid-metal cooling of nuclear reactors, electromagnetic casting etc. Rahman et al. [2] studied magneto-hydrodynamic mixed convection using Galerkin weighted residual method in a horizontal channel with an open cavity. Other investigations were also done for different configurations of cavities and channels [4, 6 and 10].

In this present paper MHD mixed convection in side lid-driven cavity with partition is investigated. The objective of this article is to investigate the mixed convection subjected to magnetic field and partition heat source in a side lid-driven cavity. The analysis focuses the effect of Richardson number and Hartmann number on characteristics of mixed convection inside cavity.

NOMENCLATURE

g	acceleration due to gravity (m/s^2)	Nu	Nusselt number
k	thermal conductivity ($W m^{-1}K^{-1}$)	<i>Greek symbol</i>	
T	temperature (K)	ρ	density (kgm^{-3})
L	length of the cavity (m)	α	thermal diffusivity (m^2s^{-1})
p	pressure (Pa)	β	volume expansion coefficient (K^{-1})
P	dimensionless pressure	ν	kinematic viscosity (m^2s^{-1})
(u, v)	velocity components ($m \cdot s^{-1}$)	σ	electrical conductivity ($(\Omega \cdot m)^{-1}$)
(U, V)	dimensionless velocity components	Ψ	streamfunction
(x, y)	dimensional coordinates (m)	Θ	dimensionless temperature
(X, Y)	dimensionless coordinates	<i>Subscript</i>	
Ri	Richardson number	h	hot
Pr	Prandtl number	c	cold
Gr	Grashof number	i	inlet

PROBLEM FORMULATION

Physical Modeling

The geometry of the problem is depicted in *Fig.1*. The system consists of a two-dimensional cavity of sides L with partition heat source of length $0.5L$ and width w . The inclined inlet and outlet have sides of b with the ratio of $b/L=0.05$ at the top corners. The partition walls and the horizontal bottom wall are kept at constant high temperature of T_h where the vertical side walls at constant low temperature T_c ($<T_h$). Moreover, the vertical cold walls move in negative y direction with velocity v_o . The cold air jet enters in to the cavity at a velocity of $u_i \sin 45^\circ$ through inclined inlet at top left corner and leaves through outlet at top right corner. The gravity is acting in the negative y -direction. A magnetic field with strength B_o is applied on the right side of the cavity. The radiation effect and viscous dissipation are neglected for the simplification of the problem.

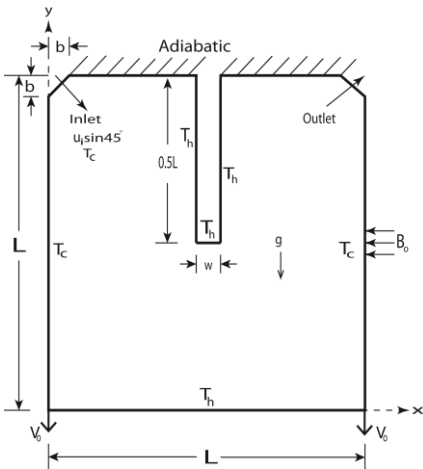


FIGURE 1. Schematic diagram of cavity with partition heat source.

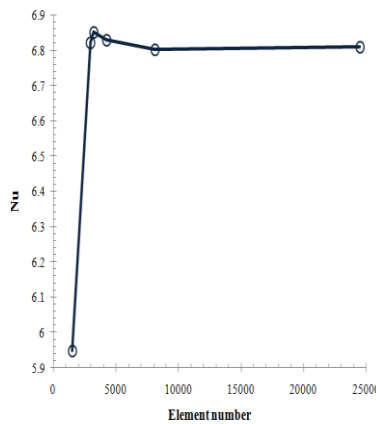


FIGURE 2. Grid refinement test on average Nusselt number for $Ri=1$, $Ha=20$.

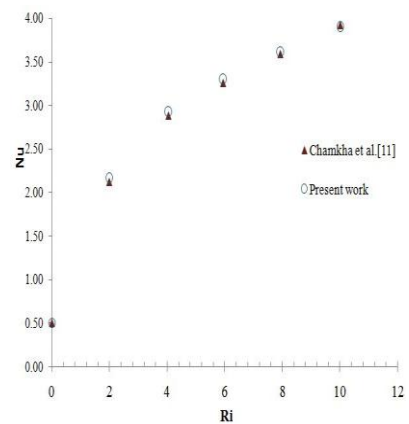


FIGURE 3. Comparison of Present work with Chamkha et al. [11] for $Ar=0.2$ and $Re=200$.

Mathematical Formulation

The flow is considered to be two dimensional, steady and laminar, and the physical properties are assumed to be constant except for the density in the buoyancy term of the momentum equation in the vertical direction, which is treated by using the Boussinesq approximation. The viscous dissipation and joule heating in the energy equation is neglected. The working fluid is assumed to be air ($Pr= 0.71$). Taking into account the above mentioned assumptions, the governing equations can be written in non-dimensional form as follows:

$$\frac{\partial U}{\partial X} + \frac{\partial V}{\partial Y} = 0 \quad (1)$$

$$U \frac{\partial U}{\partial X} + V \frac{\partial U}{\partial Y} = -\frac{\partial P}{\partial X} + \frac{1}{Re} \left(\frac{\partial^2 U}{\partial X^2} + \frac{\partial^2 U}{\partial Y^2} \right) \quad (2)$$

$$U \frac{\partial V}{\partial X} + V \frac{\partial V}{\partial Y} = -\frac{\partial P}{\partial Y} + \frac{1}{Re} \left(\frac{\partial^2 V}{\partial X^2} + \frac{\partial^2 V}{\partial Y^2} \right) + Ri\Theta - \frac{Ha^2}{Re} V \quad (3)$$

$$U \frac{\partial \Theta}{\partial X} + V \frac{\partial \Theta}{\partial Y} = \frac{1}{Re Pr} \left(\frac{\partial^2 \Theta}{\partial X^2} + \frac{\partial^2 \Theta}{\partial Y^2} \right) \quad (4)$$

The mixed convection parameter is Richardson number (Ri) can be written as $Ri = \frac{Gr}{Re^2}$. The other non-dimensional numbers, Reynolds number (Re), Grashof number (Gr), Prandtl number (Pr) and Hartmann number (Ha) can be defined as:

$$Re = \frac{u_i L}{\nu}, Gr = \frac{g \beta (T_h - T_c) L^3}{\nu^2}, Pr = \frac{\nu}{\alpha}, Ha = B_0 L \sqrt{\frac{\sigma}{\rho \nu}} \quad (5)$$

The dimensionless parameters in equations above are defined as follows: $X = \frac{x}{L}, Y = \frac{y}{L}, U = \frac{u}{u_i}, V = \frac{v}{u_i}, P = \frac{P}{\rho u_i^2}, \Theta = \frac{T - T_c}{T_h - T_c}$. (6)

Boundary conditions in the dimensionless form for the present problems are given in Table 1.

Table 1. Non-dimensional boundary conditions.

	Temperature, Θ	Horizontal velocity, U	Vertical velocity, V
Inlet	0	$\cos 45^\circ$	$\sin 45^\circ$
Outlet	$\partial \Theta / \partial X = \partial \Theta / \partial Y = 0$	Convective boundary condition, $P=0$.	
Top wall	$\partial \Theta / \partial Y = 0$	0	0
Bottom wall	1	0	0
Vertical side walls	0	0	-1
Partition walls	1	0	0

The average Nusselt number at the heated vertical side walls and partition walls can be expressed by

$$Nu = -\frac{1}{L} \int_0^L \frac{\partial \Theta}{\partial n} dn, \text{ where } \frac{\partial \Theta}{\partial n} = \left(\frac{\partial \Theta}{\partial X} + \frac{\partial \Theta}{\partial Y} \right) \text{ and } n \text{ is normal to surface.}$$

Flow field of the present problem is visualized through streamline which is obtained from stream function. Stream function is defined from velocity components U and V . Relation between the stream function and velocity components for a two-dimensional flow is given by, $U = \frac{\partial \psi}{\partial Y}, V = -\frac{\partial \psi}{\partial X}$.

NUMERICAL PROCEDURE AND GRID INDEPENDENCY TEST

Galerkin weighted residual method of finite element analysis is applied study to obtain the numerical solution. The entire domain is discretized into triangular mesh elements of different size. Non-dimensional governing equations are transformed into a set of algebraic equations. $P_2 - P_1$ Lagrange finite elements are used to discretize pressure and velocity components and Lagrange-quadratic finite elements are chosen for temperature. Iteration technique is employed to find the converged solution. The convergence criterion is set to 10^{-6} , so that $|z^{p+1} - z^p| \leq 10^{-6}$, where z is the general dependent variable and p is the number of iteration.

A grid sensitivity test is performed for $Ri=1$ and $Ha=20$ to ensure the numerical accuracy of this computation. The test is performed for different element numbers as 1485, 2996, 3212, 4236, 8114 and 24486. It is evident from *Fig.2* that after reaching element number 8114, average Nusselt number becomes insensitive. So for the present problem, grid having element number 8114 is taken as the optimum grid and all the simulations are carried out at this specified grid.

CODE VALIDATION

A code validation is necessary for checking the reliability of the present code. The present code is compared with the results of Chamkha et al. [11] on the basis of average Nusselt number for CC configuration at $AR=0.2$ and $Re=200$. As indicated from *Fig.3*, obtained result shows good agreement with literature result.

RESULT AND DISCUSSION

The main objective of investigation is to analyze mixed convection inside an open cavity in the presence of external magnetic field. The relative parameters, Richardson number and Hartmann number are varied to compare heat transfer performance in terms of streamline and isotherm contours, average Nusselt number (Nu) and mid plane velocity of the fluid inside cavity. In present study Richardson numbers (Ri) are varied from 0.1 to 10 and Hartmann numbers (Ha) from 10 to 50 .

Effect of Richardson Number

Effect of Richardson number on flow and thermal fields is depicted in terms of stream function and isothermal contours in *Fig.4*. The study is carried out for $Ha=20$, $Re=100$ and varying Ri of 0.1 , 1 and 10 . Due to cold vertical moving walls and heated partition walls, external cold air from top left corner moves along the left vertical wall and forms a counter clockwise (CCW) vortex in the left half and almost equal clockwise (CW) vortex in the right half of the cavity. A small recirculation is also developed at the inlet where heat is carried out by conduction. In *Fig.4(a)* for $Ri=0.1$, forced convection begetting from inertia force due to lid velocity v_o and air velocity u_i , is dominant. The increment of Ri number to 1 provides the stretching of vortices in horizontally confirming the presence of buoyancy force. *Figure.4(c)* depicts that further increase of Ri number ($Ri=10$) spreads vortices more with thicker velocity boundary layer. These vortices absorb more energy from heat source and become enlarged. The dominating buoyancy force at higher Ri number increases mixing of cold and hot fluids and thus increases heat transfer. The isotherms are stratified in parallel lines in both left and right sides of partition for $Ri=0.1$ in *Fig.4(d)*. Below the partition the isotherm contours look like irregular dome. For increasing Richardson number ($Ri=1$), the parallel pattern starts to distort. Further increase of Ri to 10 presents more distorted and dense isotherms inside cavity in *Fig.4(f)*. Moreover, thermal boundary layer near hot walls becomes thinner due to increasing buoyancy force which indicates increasing heat transfer. The influence of Richardson number on average Nusselt number at heated surfaces is shown in *Fig.5(a)*. It is observed that Nu increases as the Ri value rises. Nu increases rapidly in the range of $Ri=0.1$ to 5 . Later on the steepness becomes dull up to $Ri=10$. As Nusselt number defines the effectiveness of convection compared to conduction, the higher Nusselt number indicates more convection heat transfer with the increase of Richardson number. *Fig.5(b)* depicts the variation of y-velocity (V) along horizontal mid-plane (X) for various Richardson number ($Ri=0.1, 1, 5, 10$). Velocity profiles are symmetric about partition and along the partition wall velocity is zero for all Ri values. It is Observed that V increases more rapidly for $Ri=10$ in left

symmetric profiles and decreases same way for the opposite. This indicates the effect of buoyancy force is high near the partition walls for all Ri and maximum for $Ri=10$.

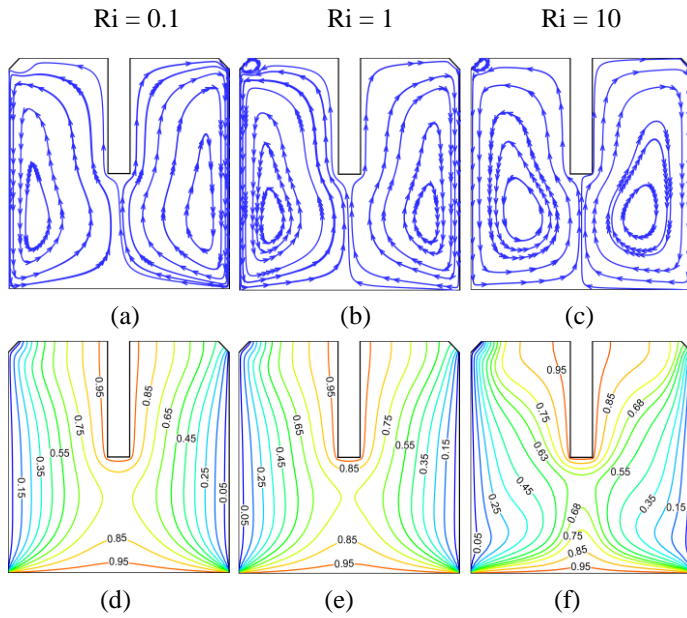


Figure.4. Variation of streamlines at (a), (b), (c) and isotherms at (d), (e), (f) for $Ri=0.1$, $Ri=1$ and $Ri=10$ respectively.

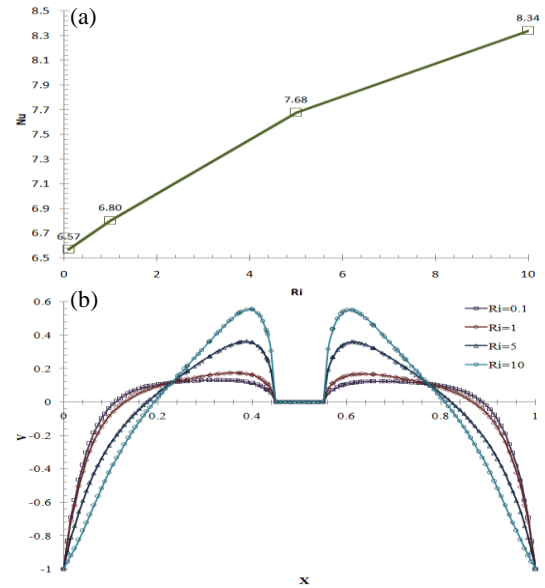


Figure.5. (a) Variation of average Nu number with Ri number, (b) Variation of y -velocity along

Effect of Hartmann Number

Effect of Hartmann number on the streamline and the isotherm contours is presented in *Fig.6*. Here Hartmann number is varied from 10 to 50 at $Ri=4$. For $Ha=0$ in *Fig.6(a)*, a counter clockwise (CCW) circular vortex at the left half and a clockwise (CW) circular vortex at the right half of the partition cover the cavity. The increment of Ha to 25 introduces a secondary vortex near inlet and primary vortices are elongated vertically. Further increase of Ha to 50 in *Fig.6(c)* presents more elongated vortices along the vertical walls. The small recirculation near inlet enlarges which indicates the decrease in kinetic energy of flow. The vortices become weaker with lower stream function value and less dense stream lines. The increasing effectiveness of Lorentz force produced from magnetic field restricts strength of flow as the Ha value increases. The isotherm contours in *Fig.6(d)* for $Ha=10$ are parallel to each other near hot and cold walls and irregularly distributed at middle, near partition. With the increase of Ha value to 25 and 50, isothermal lines are distributed almost parallel to vertical side walls. This indicates the dominance of conduction compared to convection. It is also noticeable that the thermal boundary layer becomes thicker which represents less heat transfer. The impact of Ha on average Nusselt number at heated surfaces is shown in *Fig.7(a)*. It is observed that Nu number is decreasing with increasing Ha . Nusselt number decreases more steeply up to $Ha=50$ and after that the magnitude of the slope becomes small. The variation of y -velocity (V) along horizontal mid-plane (X) for various Hartmann number ($Ha=10, 25, 50, 100$) is depicted in *Fig.7(b)*. It is interesting to see that the velocity profiles are symmetric about partition wall. The velocity profile shows that $Ha=10$ has higher increasing rate of V at left and decreases in same way at right side. This velocity profile denotes the reduction in strength of flow due to magnetic effect as Ha increases.

CONCLUSION

The results of numerical analysis on flow field, thermal field and effectiveness of heat transfer with varying Richardson number and Hartmann number is computationally analyzed in a two-sided lid driven open cavity with heated partition. The outcomes are listed as follows:

- Increment in Richardson number increases heat transfer rate by buoyancy effect. Rate of increase in average Nusselt number is higher at high value of Richardson numbers.
- The effect of magnetic field reduces strength of flow. As a result higher Hartmann number weakens convection and also lessens Nusselt number.

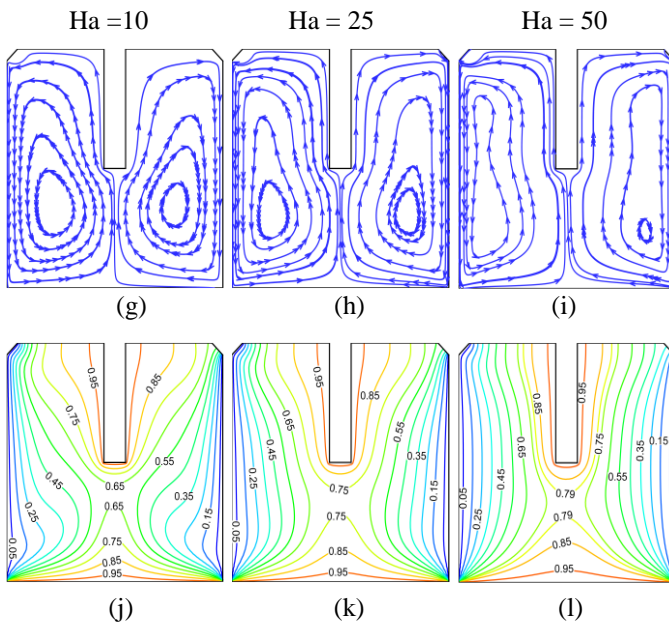


Figure 6. Variation of streamlines at (a), (b), (c) and isotherms at (d), (e), (f) for $Ha=10$, $Ha=25$ and $Ha=50$ respectively.

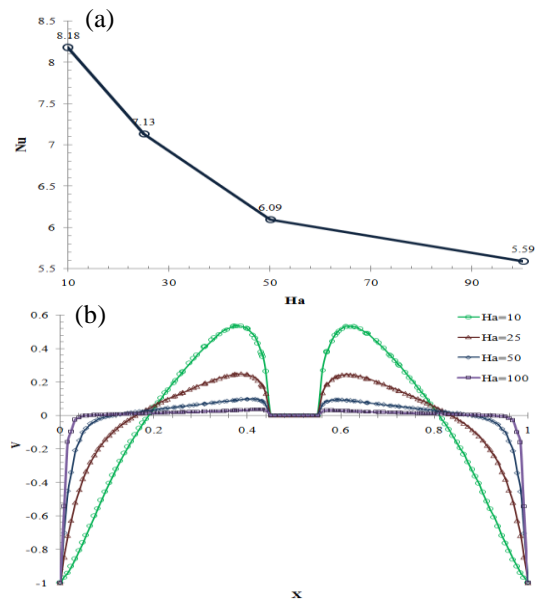


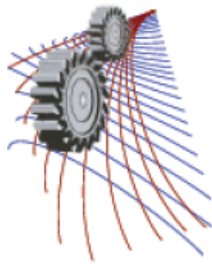
Figure 7. (a) Variation of average Nu number with Ha number and (b) Variation of y -velocity along horizontal mid-plane.

This open cavity is compared to the shape of IC engine cylinder which can be a promising research topic in future.

REFERENCES

1. S.M. Aminossadati, B. Ghasemib, A numerical study of mixed convection in a horizontal channel with a discrete heat source in an open cavity, *Eur. J. Mech. B. Fluids* 28 (2009) 590–598. R. T.
2. Rahman, M. M., et al. "Magnetohydrodynamic mixed convection in a horizontal channel with an open cavity." *International Communications in Heat and Mass Transfer* 38.2 (2011): 184-193.
3. Wei-Mon, Yan. "Effects of film evaporation on laminar mixed convection heat and mass transfer in a vertical channel." *International journal of heat and mass transfer* 35.12 (1992): 3419-3429.
4. N. Rudraiah, M. Venkatachalappa, C.K. Subbaraya, Combined surface tension and buoyancy-driven convection in a rectangular open cavity in the presence of magnetic field, *Int. J. Non-linear Mech.* 30 (5) (1995) 759–770.
5. S.M. Saeidi, J.M. Khodadadi, Forced convection in a square cavity with inlet and outlet ports, *Int. J. Heat Mass Transfer* 49 (2006) 1896–1906.
6. Kasaeipoor, A., B. Ghasemi, and S. M. Aminossadati. "Convection of Cu-water nanofluid in a vented T-shaped cavity in the presence of magnetic field." *International Journal of Thermal Sciences* 94 (2015): 50-60.
7. Ahmad, Syakila, and Ioan Pop. "Mixed convection boundary layer flow from a vertical flat plate embedded in a porous medium filled with nanofluids." *International Communications in Heat and Mass Transfer* 37.8 (2010): 987-991.
8. Mahmud, Shohel, and Ioan Pop. "Mixed convection in a square vented enclosure filled with a porous medium." *International journal of heat and mass transfer* 49.13 (2006): 2190-2206.
9. Saha, Sumon, et al. "Mixed convection in an enclosure with different inlet and exit configurations." *Journal of Applied Fluid Mechanics* 1.1 (2008): 78-93.

10. G. Sposito, M. Ciofalo, Fully developed mixed magnetohydrodynamic convection in a vertical square duct, *Numer. Heat Transfer A* 53 (9) (2008) 907–924.
11. Chamkha, Ali J., Salam Hadi Hussain, and Qusay Rashid Abd-Amer. "Mixed convection heat transfer of air inside a square vented cavity with a heated horizontal square cylinder." *Numerical Heat Transfer, Part A: Applications* 59.1 (2011): 58-79.



Measurement of particulate pollution in Rajshahi city and draw particulate pollution curve in different areas.

Abu Salek^{1, a)} and Abdullah Al Mamun^{1, b)}

¹Dept. of Mechanical Engineering, Rajshahi University of Engineering & Technology, Rajshahi-6204, Bangladesh

^{a)}Corresponding author: saleksohag@yahoo.com

^{b)}mamun102018@gmail.com

Abstract. Particulate pollution is a great threat to the human health. One of the major causes of the particulate pollution is the emission from the various vehicles, which are running by the burning of the fossil fuels in different Internal Combustion (I.C) Engines. Objectives of this thesis: To measure particulate emission in different areas of the Rajshahi metropolitan city of Bangladesh, draw particulate pollution profile of this area, identify the causes of harmful particulate emission, and recommend steps to reduce the particulate pollution. We have used “portable airborne particle counter” incorporate extreme life laser diode technology sensor on this purpose to determine the amount of particulate per cubic foot in the air. We determined the average amount of particulate per cubic foot of air (count/ft³) of different points of the Rajshahi city. We also determined the air quality of the class room, the teacher’s quarters and an air conditioned room and a normal environmental condition room of Rajshahi University of Engineering & Technology. We have taken the data for several times of each of a point and then made an average result. Then we made tables and chart to make the comparison of the gathered data. After analyzing all the data we have made a result of how much polluted those points were. We have also find that, using the air condition (A.C) with air filter we can improve the air quality of a room, reducing the amount of particulate in the air, as the A.C filters the air that entering the room. From our thesis work, the following conclusion can be drawn: It is not possible to eliminate the particulate pollution completely, because it is produced naturally and produced in the time when we run the all types vehicles, which are running by the diesel and petrol fuel. But our sincerity and some measured ways can reduce the amount of particulate pollution in our daily life. Some steps may as: Use better quality fuel, Run the vehicles at proper engine tuning, Use better lubricants, Use better crank case ventilation system, Use catalytic converter to reduce the amount of particle remains in the exhaust gases, Do not use the fuels in which Sulphur is mixed, Plant more trees, Control the population increasing rate, Remove the older vehicles from the road of Rajshahi, Construct the roads well, so they can sustain in the rainy season and do not break, Implements required rules and regulations reducing pollution from Industrial Chimney etc.

PARTICULATE MATTER

A particulate matter is defined as mixture of solid particles and liquid droplets found in air. Particulate matter is the term for particles found in the air including dust, dust soot, smoke and liquid droplets. This pollutant comes in a variety of size and composed of many types of materials and chemicals. Some particles can be suspended in the air for long periods of time. Some particles are large or dark enough to be seen as soot or smoke. Others are so small that individually they can only be detected with an electron microscope. Particles that are small enough to be inhaled have the potential to causes health effects.

Particulate matter is primarily formed from chemical reactions in the atmosphere and through fuel combustion with insufficient oxygen in motor vehicles, power generation, industrial facilities, residential fire places, wood stoves, and agricultural burning.

INSTRUMENTATION AND METHODOLOGY

- Particulate of fixed aerodynamic diameter of 0.3, 0.5, 1, 3, 5, 10, 25 μm was taken under consideration.
- Laser Particle Counter was used for counting particulate matter in different locations. The data of this thesis were taken in terms of count per cubic foot.
- Data was taken in different locations
- With the help of the particle counter, measurement of the amount of the particle count (CNT) that present in per cubic foot of air (Count/ ft^3) of those areas being done .Also able to measure the humidity and air velocity of those areas.

Equipment required

1. Network enabled personal computer(IBM-compatible)
2. SOLAIR Portable Airborne Particle Counter
3. Small 5-port hub or switch and two 3-foot long straight- through cat5 Ethernet cables Or one 3 foot crossover cats Ethernet cable.

MEASUREMENT METHOD

There are basically two modes of measurement of operation in the “SOLAIR 1.0 CFM airborne particle counter”. These are:

Manual counting mode: In manual counting mode, the sample is based on when the counter is instructed to stop counting. At this point, a data record is recorded and the sample time is the interval between the command to start counting and the command to stop counting.

Automatic counting mode: In automatic counting mode, the instrument uses the configured sample time, hold time and initial delay to record samples.

The instrument will continue running samples until it receives a sop command .when the stop command is given, since the device will not have completed a full sample cycle, the most current data will not record to the buffer.

IMPROVING AIR QUALITY IN INDOOR

- Source Control: Usually the most effective way to improve indoor air quality is to eliminate individual sources of pollution or to reduce their emissions. Some sources, like those that contain asbestos, can be sealed or enclosed; others, like gas stoves, can be adjusted to decrease the amount of emissions. In many cases, source control is also a more cost-efficient approach to protecting indoor air quality than increasing ventilation because increasing ventilation can increase energy costs.
- Ventilation Improvements: For most indoor air quality problems in the home, source control is the most effective solution. Another approach to lowering the concentrations of indoor air pollutants in our home is to increase the amount of outdoor air coming indoors. Most home heating and cooling systems, including forced air heating systems, do not mechanically bring fresh air into the house. Opening windows and doors, operating window or attic fans, when the weather permits, or running a window air conditioner with the vent control open increases the outdoor ventilation rate. Local bathroom or kitchen fans that exhaust outdoors remove contaminants directly from the room where the fan is located and also increase the outdoor air ventilation rate. It is particularly important to take as many of these steps as possible while we are involved in short-term activities that can generate high levels of pollutants. For example painting, paint stripping, heating with kerosene heaters, cooking or engaging in maintenance and hobby activities such as welding, soldering or sanding. We might also choose to do some of these activities outdoors, if we can and if weather permits.

- **Air Cleaners:** There are many types and sizes of air cleaners on the market, ranging from relatively inexpensive table-top models to sophisticated and expensive whole-house systems. Some air cleaners are highly effective at particle removal, while others, including most table-top models, are much less so. Air cleaners are generally not designed to remove gaseous pollutants. The effectiveness of an air cleaner depends on how well it collects pollutants from indoor air (expressed as a percentage efficiency rate) and how much air it draws through the cleaning or filtering element (expressed in cubic foot per minute). A very efficient collector with a low air-circulation rate will not be effective, nor will a cleaner with a high air-circulation rate but a less efficient collector. The long-term performance of any air cleaner depends on maintaining it according to the manufacturer's directions. Another important factor in determining the effectiveness of an air cleaner is the strength of the pollutant source. Table-top air cleaners, in particular, may not remove satisfactory amounts of pollutants from strong nearby sources. People with a sensitivity to particular sources may find that air cleaners are helpful only in conjunction with concerted efforts to remove the source.

PARTICULATE MATTER EMISSION IN DIFFERENT LOCATIONS FOR OUTDOOR AIR QUALITY

Motor vehicles in urban areas are the main source of ultrafine particles (diameters $< 0.1\mu\text{m}$). Ultrafine particles are generally measured in terms of particle number because they have little mass and are prolific in terms of their numbers. These sized particles are of particular interest because of their ability to enter deep into the human respiratory system and contribute to negative health effects. In the development of transport the internal combustion engines, both petrol and diesel engines, occupy a very important position. However, in recent times the internal combustion engine powered vehicles have come under heavy attack due to creation of particulate pollution along with other atmospheric pollution, such as sound pollution. Vehicles are the major factor in atmospheric particulate pollution. Figures show the particle size distribution in different locations of Rajshahi city for outdoor air quality. From the figures it is clear that Maximum PM was found at Rail gate.

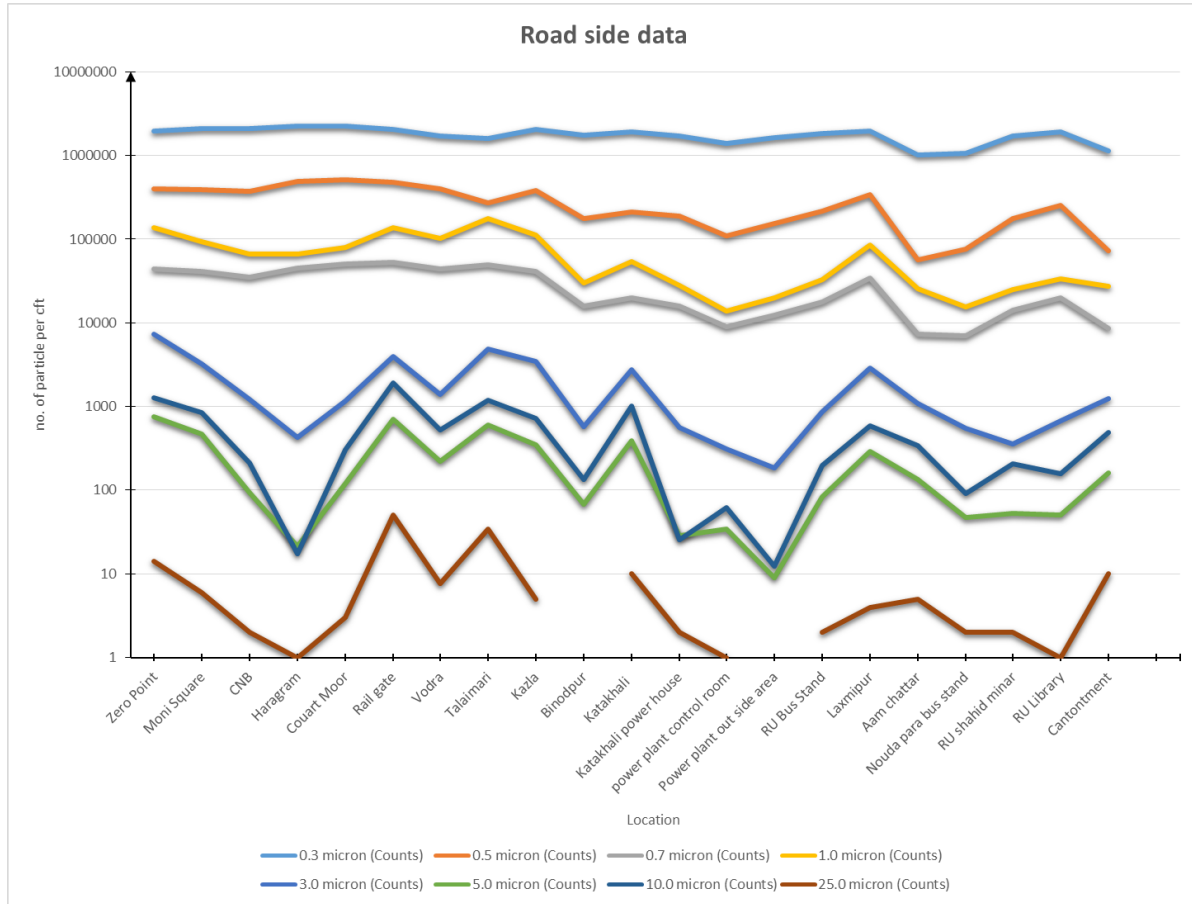
COMPARISON OF PARTICLE SIZE AT DIFFERENT LOCATIONS

The size of particles is directly linked to their potential for causing health problems. Small particles less than $10\mu\text{m}$ in diameter pose the greatest problem, because they can get deep in the lungs and some may even get in the blood stream. $0.3\mu\text{m}$ is categorized as fine particles and are very dangerous to human health. These particles are mostly found in smoke and haze. The Coarse ($3\mu\text{m}$, $5\mu\text{m}$) are very low in number in comparison with finer particles. PM is generated by the burning of wood, fossil fuels, industrial processes, power generation, residential burning etc. both natural and human activities are responsible for the PM emission. Other variables responsible for PM emissions are-

- Number of vehicles
- Humidity in air
- Air velocity
- Construction and demolition work

Windblown dust and wild fires are the natural causes that help to generate PM. Number of vehicle plays an important role in generating PM. Traffic particulates are not only directly emitted as exhaust particles from engines, they include particulates wear on road, tires and brakes and also re-suspension from road surfaces. Also the type of vehicle determines the type of PM to be generated. Such as diesel engine produce very fine PM than Petrol engine.

Figures



ACKNOWLEDGEMENT

It is great pleasure and privilege for the authors to present this report on “Measurement of particulate pollution in Rajshahi city and draw particulate pollution curve in different areas”. The Authors also wish to acknowledge with appreciation and pleasure the Department of Mechanical Engineering, RUET, Rajshahi for full support and co-operation.

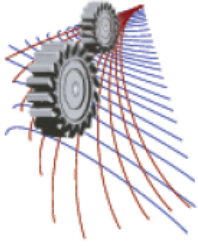
The authors wish to express their deepest sense to Professor Dr. Md. Shamim Akhter, Department of Mechanical Engineering, Rajshahi University of Engineering and Technology (RUET), for his constant guidance, inspiration, suggestion and support in performing and completing the thesis work.

At last but not the least, authors are indebted to those, who have directly or indirectly helped to complete the work.

Authors

August, 2015

Rajshahi University of Engineering and Technology (RUET), Rajshahi-6204, Bangladesh.



Computational Technique to Determine Deflected System State of One End Fixed Cable-Stayed Cantilever Beam

Adnan Shahriar^{1, a)}, Kh. Md. Faisal¹ and Moosfika Haque Treesha¹

¹*Department of Aeronautical Engineering, Military Institute of Science and Technology,
Dhaka, Bangladesh*

^{a)}Corresponding author: shahriar.adnan@yahoo.com

Abstract. This paper represents the development of a computational technique to determine the properties of one end fixed cable-stayed cantilever beam. This type of beam of linear elastic material under the action of external vertical concentrated load near the free end is analyzed. Equations have been derived to find out the properties of beam and cable for definite vertical loading and vertical deflection at the free end of beam. As the beam is one end fixed and another end is cable stayed with an inclination the system is indeterminate and complex. Analytical approaches with some approximations are not exact. Energy method such as potential energy method offers an exact solution but it is a long iterative process. We introduce a new approach to solve this case. Although we made some approximations, this approach gives satisfactory results. To analyze behavior of the system we use the governing differential equation and force vectors. Though the equation is a 2nd order non linear differential equation it has similarity with a known system, simple pendulum, so it is solvable. Finally we designed an algorithm to solve the system using MATLAB. Later we have presented various numerical applications. Finally we use Energy method to verify our procedure.

INTRODUCTION

The objective of this paper is to study cable stayed beam. One end of beam is fixed end and another one is cable stayed. As the fixed end generates moment the system gets indeterminate. Some simple approaches may give result with approximation, but this is not exact and for large deflection of beam those results are not satisfactory. There are energy methods and finite element methods to find out exact or satisfactory solution but they are very tough and

long iterative process.

Here a new computational approach will be made to find out a satisfactory solution of this type of systems. Beam and Cables both have uniform cross section and material is linear elastic homogeneous and isotropic and subjected to only vertical load. Initial step is Mathematical modeling. For Mathematical modeling first we shall separate forces into only vertical and horizontal components and then derive equations to find out the exact deformation of beam. Deflection of this type of beam of linear elastic material is analyzed in Landau's book on elasticity [1]. In this paper for exact deformation, we shall have a equation of 2nd order non linear differential equation. As it has similarity with a very known system 'simple pendulum' it is solvable [2]. We shall include "nodal eccentricity" in those equations which is a result of manufacturing defects. Then we shall use force vectors to take contribution of cable to this system in account. Second step is designing algorithm to solve equations using computer programs. We shall use iterative method. For application of this algorithm we shall use MATLAB. To solve complex integrals 'simpson's integration' shall be used. Finally a verification using energy method shall be done for 'Gradual loading'.

Nomenclature

E	Modulus of elasticity of beam material
E_2	Modulus of elasticity of cable material
I	2nd moment of inertia of beam
A_2	Cross sectional area of cable
θ	Slope angle of beam at any point
θ_0	Initial slope angle at beam at tip
T_x	Horizontal force from cable
T_y	Vertical force from cable
L	Load at beam end
L_1	Beam length
L_2	Cable length
n,a	Distance from Neutral axis and points where forces are acting

2. Mathematical modeling:

The cable stayed cantilever beam system is depicted in figure 1. Cable is attached at beam tip $s=0$ and at point $s=S$ beam is fixed. All loadings are at node $s=0$ with nodal eccentricity n and a .

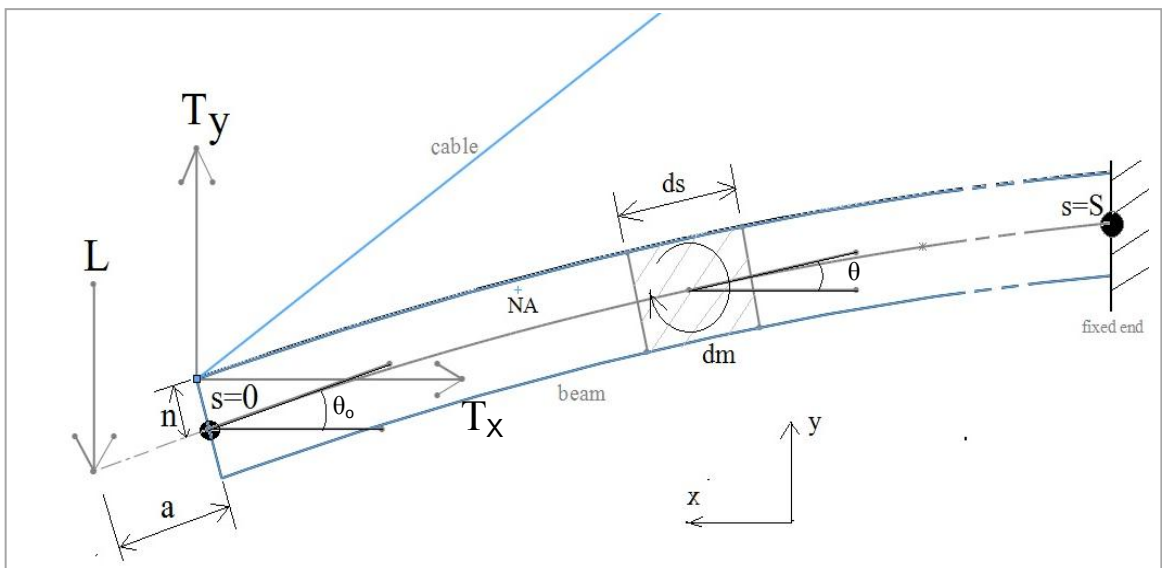


Fig. 1. One end fixed cable-stayed cantilever beam

2.1 Beam section:

This beam follows Bernoulli-Euler hypothesis [3,7].

Initial moment is a function of n and a and denoted by C_0 . Initial moment can be manipulated into,

$$- \frac{d\theta}{ds} = n \theta_0 \cos s \theta_0 - \theta_0 \sin s \theta_0$$

Differential moment at ds distance from beam tip from figure 1 is,

Integrating and then differentiating equation(2) w.r.t s the governing non linear differential equation,

—

This has similarity with the result that can be found in the study of simple pendulum [2]. After some manipulation with the end conditions, at $s=0, \theta=\theta_0$,

—

Integrating equation (4) to determine total moment,

$$- \frac{d\theta}{ds} = \frac{1}{\sin \theta} \frac{d\theta}{ds} = \theta_0 \cos s \theta_0$$

Using equation(1), manipulating and integrating equation(5) and considering axial deformation negligible, beam arc length [6],

—
—

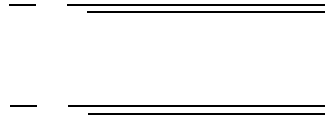
x and y coordinate and axial deformation Δ of beam respectively [6,8]

—
—
—
—

—

2.2 Cable section:

For only one cable, Tension force along x and y axis respectively,



2.3 Stored energy:

As axial deformation & energy stored in beam is negligible. This is avoided in calculation. Energy stored due to gradual loading in cable follows conventional equation [4, 8]. Energy stored in beam due to instantaneous loading without nodal eccentricity is [4]

$$\int_{\theta_0}^{\theta} \frac{\cos\theta - \cos\theta_0}{\sin\theta} d\theta$$

3. Development of algorithm:

Only one cable is considered. For input values of $L, L_2, E_2, (x_1, y_1), L_1, E, n, a, I, A_2$ a flow chart is presented to describe the algorithm named “Algorithm to find out deflected system state” to solve deflected beam tip coordinate (x, y) is shown below. (x_1, y_1) is the cable joint point with rigid support coordinate.

i is the number of iterations from step 2 to step 8, to avoid step for checking convergence characteristics. P is the maximum value of i allowed. ΔT_x and ΔT_y is the difference between guessed and solved values of T_x and T_y .

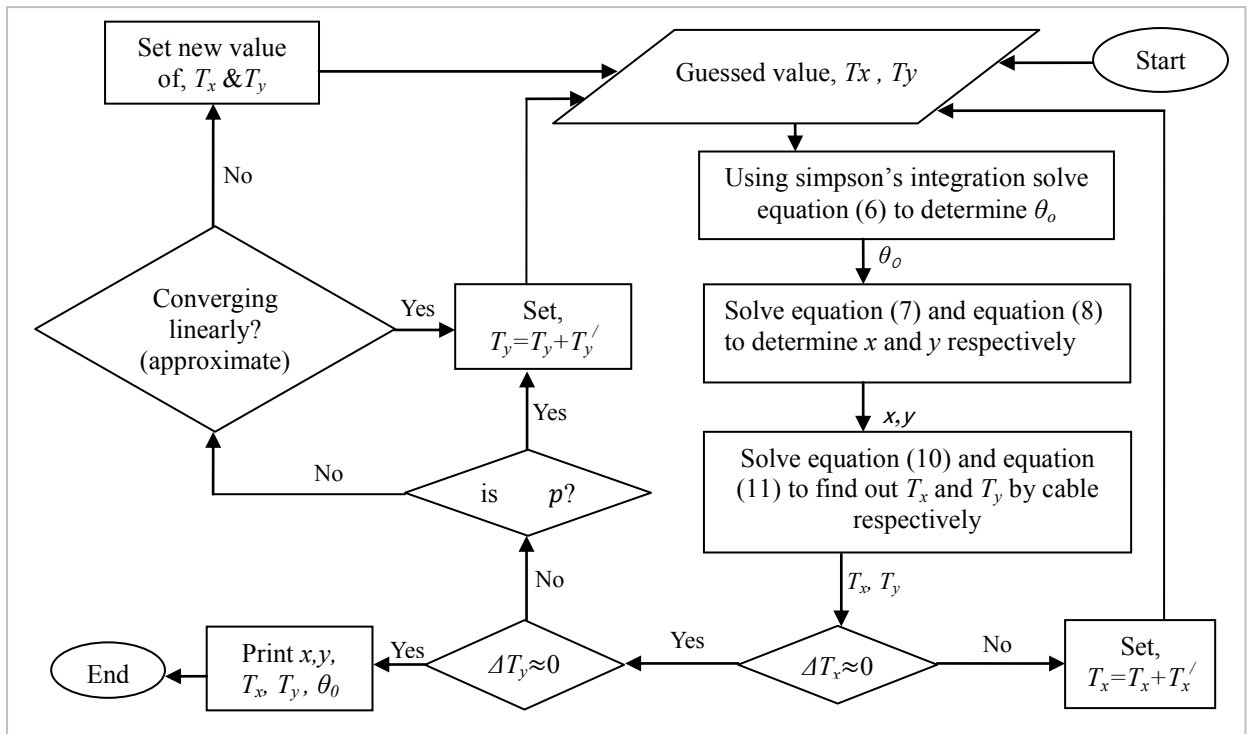


Fig. 3. Flowchart showing Algorithm to find out deflected system state

4. Numerical result:

Problem:

In numerical example given values,
 Geometric data of beam: Beam initial length, $L_1 = 1.5248\text{m}$, Beam moment of inertia, $I = \text{m}^4$, Cross sectional area = approximately $.00045\text{ m}^2$
 Geometric data of cable: Cable initial length, $L_2 = 1.5419\text{m}$, Cross sectional area, $A_2 = 1\text{ m}^2$
 Material data: Beam material elasticity modulus $E = 69\text{ GPa}$, Cable material elasticity modulus $E_2 = 112400\text{ MPa}$
 Coordinate data: If beam fixed end point coordinate is $(0,0)$, Then cable joint point with rigid support coordinate is $(0, .2286\text{m})$

Solution:

To avoid singularity equations (6),(7), (8) are integrated from 0 to $(\theta_0 - 10^{-10})$ and tolerance is 10^{-10} in MATLAB. Values smaller than .10 mm are neglected. Nodal eccentricity is not considered. Axial deformation is neglected.

Following "Algorithm to find out deflected system state" for 200N, 40 N and 50N vertical loading, results found are shown in Table 1, Table 2 and Table 3 respectively.

Table 1. Properties of deflected system state for 200 N vertical loading

<i>Property for 200 N</i>	<i>symbol</i>	<i>value</i>	<i>error</i>
x coordinate of beam tip	x	1.5238m	0
y coordinate of beam tip	y	-.0502m	0
Horizontal force by cable	T_x	980N	.6648N
Vertical force by cable	T_y	179.4048N	0
Vertical external load	L	199.6648N	.3352N
Tip slope angle	θ_0	.05085 rad	0

Table 2. Properties of deflected system state for 40 N vertical loading

<i>Property for 40N</i>	<i>symbol</i>	<i>value</i>	<i>error</i>
x coordinate of beam tip	x	1.5248m	0
y coordinate of beam tip	y	-.00978m	0
Horizontal force by cable	T_x	195N	.20155N
Vertical force by cable	T_y	30.4384N	0
Vertical external load	L	40.4384N	.4384N
Tip slope angle	θ_0	.009679 rad	0

Table 3. Properties of deflected system state for 50 N vertical loading

<i>Property for 50 N</i>	<i>symbol</i>	<i>value</i>	<i>error</i>
x coordinate of beam tip	x	1.5247m	0
y coordinate of beam tip	y	-.0121m	0
Horizontal force by cable	T_x	235.5N	.62195N
Vertical force by cable	T_y	37.1416N	0
Vertical external load	L	49.1416N	.8584N
Tip slope angle	θ_0	.012006 rad	0

5. Verification using Energy method:

For verification with energy method we use the basic of "Clapeyron's law"[5]. It states, total amount of work generated by the external forces will be stored as strain energy. So Internal work done = External work done.

For gradual loading, when external force is 0, deformation is also 0.

Energy stored in cable is obtained manipulating conventional equation [8] for instantaneous loading and converted into a product of Tension and elongation.

Energy stored in beam for each loading condition is obtained solving integration of equation(12) from 0 to $(\theta_0 - 10^{-10})$ with tolerance 10^{-10} using simpson's integration in MATLAB. Result is converted into a product of θ_0 , and equivalent bending moment. Taking slope angle(rad) along x axis and moment(Nm) along y axis coordinate points are (0,0), (.001432,197.061), (.00173,238.41) and (.007248,996.94) for 0N, 40N, 50N and 200N load respectively.

External work done is converted into a product of external Force and deformation directly using data from tables. Finally graph is drawn using MATLAB. All units follow International System of Units.

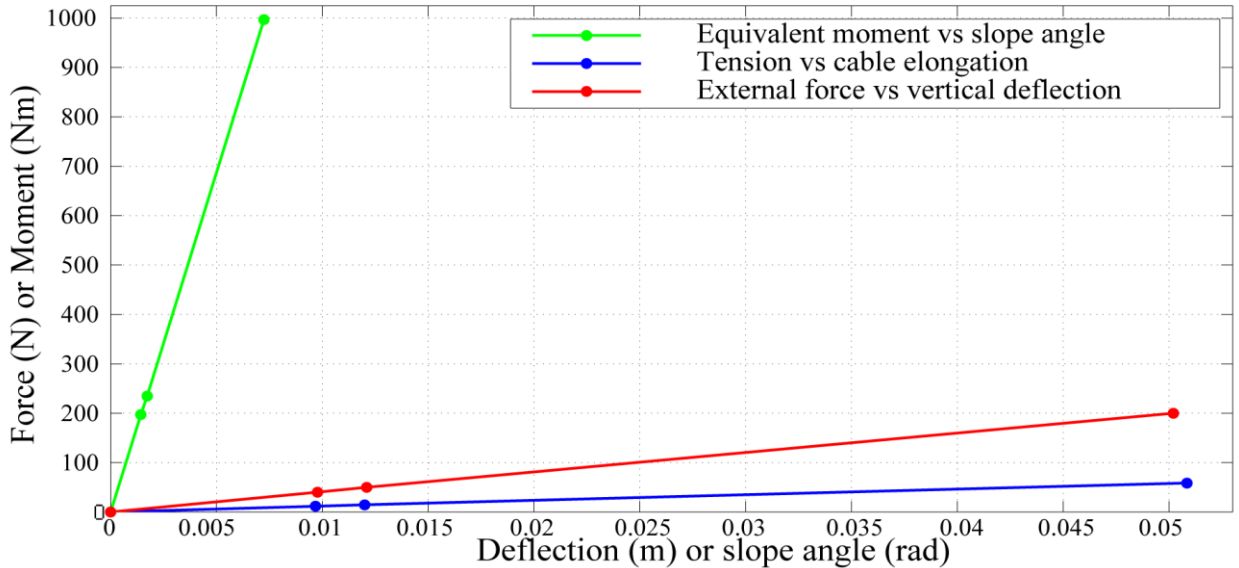


Fig. 4. Force or Equivalent Moment vs deflection or slope angle graph

Graph is showing straight line which was expected.

Internal work done= Area under Tension vs cable elongation curve + Area under Equivalent moment vs slope angle curve= $(3.6162+ 1.5029)J = 5.1171 J$

External work done= Area under external force vs vertical deformation curve= 5.05 J

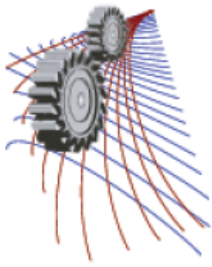
So, taking Internal work done as 'measured value' and external work done as 'actual value', Error= 1.33%.

6. Conclusions:

We have studied cable stayed fixed end beam theoretically. Firstly we have obtained equations for exact deflection of beam tip. We had a non-linear differential equation to be solved. As the system is indeterminate we have designed Algorithm and implemented the equations derived to obtain deflected system state. We have solved problem numerically for three cases. Algorithm and numerical integrations are done using MATLAB. We validate our results using energy method. There is error. First of all the problem was very sensitive due to very high elasticity modulus of cable, secondly we have neglected values lower than .1 mm, thirdly we did not calculate Energy stored due to compression in beam and finally we used numerical integration which never give exact value. We did not take any experimental approach.

References:

- [1] Landau Ld and Lifshitz Em 1986 Course of theoretical physics, Vol 7: Theory of Elasticity (Oxford: Pergamon Press) Chap. 17
- [2] Alonso M and Finn E J 1992 *Physics* (Massachusetts: Addison-Wesley Publishing) Chap. 10
- [3] Anderson Pytel and Ferdinand L.Singer *Strength of materials*, Chap. 6, equation (6-1)
- [4] Hans Welleman *Structural mechanics 4 CIE3109*, Chap. 3
- [5] Hans Welleman *Structural mechanics 4 CIE3109*, Chap. 2(2.4)
- [6] T. Beléndez, Augusto Beléndez, Cristian Neipp *Large and small deflection of a cantilever beam*
- [7] Anderson Pytel and Ferdinand L.Singer *Strength of materials*, Chap. 5
- [8] T.H.G. Megson *Structural and Stress Analysis, Chapter 7*, equation 7.29



Design of A Model House with Zero Conventional Energy Demand

Nirendra Nath Mustafi ^{a)}, Shimul Barua^{b)}, Md. Alauddin^{c)} and Md.Ariful Islam^{d)}

Department of Mechanical Engineering, Rajshahi University of Engineering & Technology, Bangladesh.

^{a)}Corresponding author: shimulbarua.ruet@gmail.com

^{b)}nnmustafi@gmail.com

^{c)} alauddin102006@gmail.com@gmail.com

^{d)}arifruet.me10@gmail.com

Abstract. Energy problem is now a burning question in the world. In universe, there is limited source of conventional energy and maximum people of the world depend on this energy. Eventually they are decaying day by day. Moreover, after burning them the product of combustion are not reversible. Consequently they are causing harmful effect to the environment such as global climate change, environmental degradation and various human health problem and so on. To overcome the energy crisis and to protect the environment from harmful products one of the best way is to utilization of renewable energy resources. This project will exhibit how a family can survive without any conventional energy for household work. A suitable solar panel, solar collector and a biogas plant can supply efficient energy to performing household work. Besides, by placing a water turbine on the way of water flow inside any pipe line used in habitation area, industry, factory, power plants or other where water flow is present, the potential energy of water may be used to generate electrical power without distributing his daily work for which the water is employed. Thus the energy problem can be solved as well as the pollution of environment will automatically minimize.

INTRODUCTION

The sun radiates the energy uniformly in the form of electromagnetic waves. Solar energy has the greatest potential of all the sources of renewable energy and if only a small amount of this form of energy can be utilized, it will be one of the most important supplies of energy. The photovoltaic solar (PV) cell is a semiconductor device that generates electricity when light falls on it. The PV cells have one or more electric fields whose purpose is to force the loose electrons in one direction, similar to how a diode works, hence the formation of current.

One of the well-known solar thermal applications is solar water heating. A Solar Water Heating System (SWHS) utilizes the incident solar energy and convert it into thermal energy for heating the water to use in various applications. The Solar Water Heating System consists of solar thermal collectors, water tanks, interconnecting pipelines, and the water, which gets circulated within the solar water heating system. Sun rays falling on the collector tube which then heats the tube, thereby transferring the heat energy to water flowing through it.

Biogas refers to a gas which is produced by break down of organic matter substance by bacteria, yeasts or other micro-organisms in the absence of oxygen i.e. by anaerobic digesters. Organic wastes like kitchen wastes, animal, plant, human wastes etc can be converted in to biogas. During the process, as an air-tight tank transforms biomass waste into methane producing renewable energy that can be used for heating, electricity and many other operations.

Biogas contains mainly methane (50-70%), carbon dioxide (20-40%) and traces of other gases such as nitrogen, hydrogen, ammonia, hydrogen sulphide, water vapour etc[1].

The calorific value of biogas is appreciably high (around 4700 kcal or 20 MJ at around 55% methane content) [2]. Among all the renewable energy sources available, small hydropower is considered as the most promising

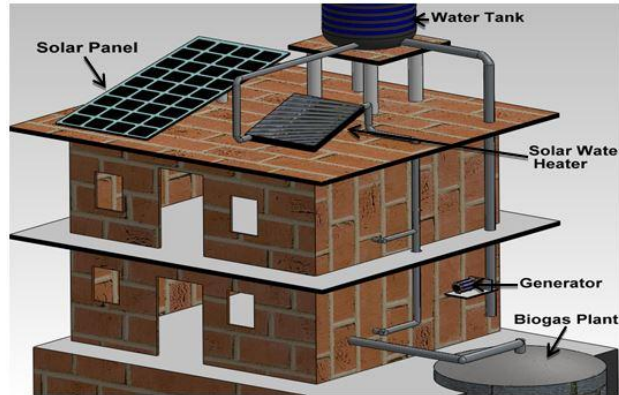


FIGURE 1. Complete arrangement of model house.

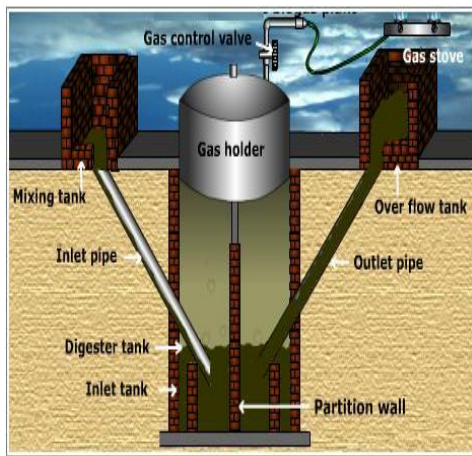


FIGURE 2. Biogas plant.

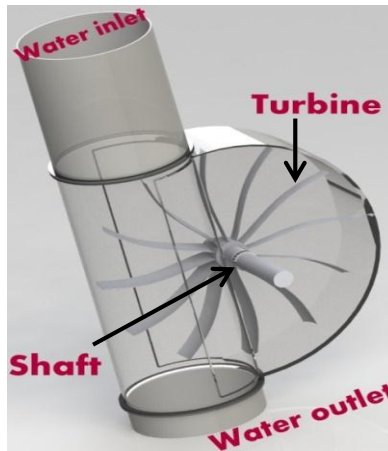


FIGURE 3. Water turbine.



FIGURE 4. Solar water heater.

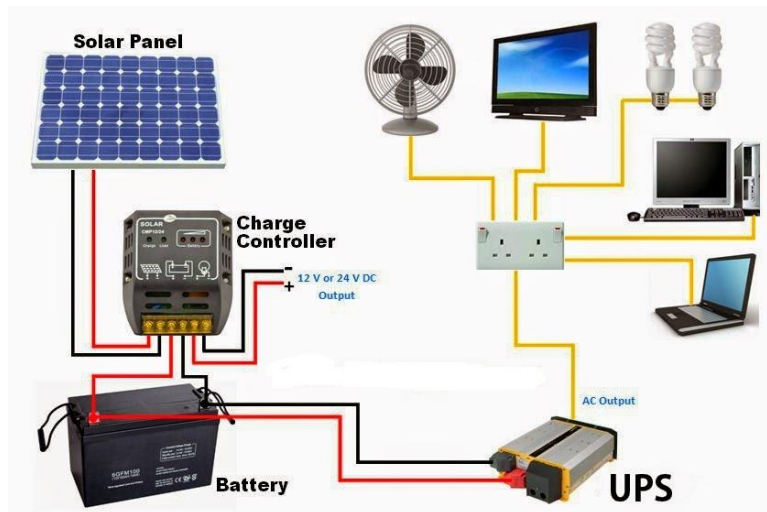


FIGURE 5. Using power from Solar panel.

source of energy. In home, Industry, Factory and others, the hydraulic turbine may use to convert the potential energy of water to mechanical energy. The water stored in storage on a certain height from ground level contains

potential energy which converted to kinetic energy when flowing water is directed on the blades of a turbine and creating force on the blades. Since the runner is spinning, the force acts through a distance (force acting through a distance is the definition of work), in this way energy is transferred from the flowing water to the turbine. Hence, rotates turbine shaft which is coupled with generator shaft to produce electricity. By this method energy can be utilized without environmental disturbances.

The aim of this project is to combining the four topics above discussed in household sector especially in rural area to conserve energy and minimizing cost and indirectly reducing the pollution.

METHODOLOGY

The device in which the digestion process occurs is called Biogas digester. The organic matter are supplied into the digester and permitted to undergo degradation in a sealed oxygen-free chamber. The main parts of the digester are: hopper, through which slurry is introduced in the digester; inlet pipe which carries slurry from hopper to the digester or fermentation chamber where fermentation processes occurred. It has two parts: one is upper part which is used for the storage of biogas known as gas tank and the lower part that connected with upper part by nut-bolt arrangement for easy discharging of sludge. There is a pipe for the delivery of the gas from the fermentation chamber. A gas control valve is used to control the gas flow.

It was observed that biogas production from cow dung, poultry waste and water hyacinth is 0.034 m³/kg, 0.058 m³/kg and 0.014 m³/kg respectively. Poultry waste produced maximum gas 0.026m³ at the 8th day whereas cow dung and water hyacinth produced maximum gas of 0.0263 m³ and 0.012m³ respectively at the 26th day[3].

In average, approximately 0.034 m³ gas is produced per kg of organic matter. To dilute the cow dung a required amount of water is needed. The mixture ratio of water to the cow dung is about 2:1.

$$\text{Total volume (V)} = \text{quantity of cow dung (kg)} + \text{quantity of water (litre)} \quad (1)$$

There is an optimum relation between the diameter(D) of the digester and the total volume(V) [4],

$$D = 1.3078\sqrt[3]{V} \quad (2)$$

$$\text{Where, } f_1/D = 1/5; f_2/D = 1/8 \text{ and } H = D/2.5 \quad (3)$$

The solar panel converts sunlight into DC electricity to charge the battery. This DC electricity is fed to the battery via a solar regulator which ensures the battery is charged properly and not damaged. DC appliances can be powered directly from the battery but AC appliances require an inverter to convert the DC electricity into 220Volt AC power.

$$\begin{aligned} \text{Energy produced from a solar panel} &= (\text{rated power} \times \text{hour} \times \text{efficiency}) \text{ Wh/day} [5] \\ &= (\text{rated power} \times \text{hour} \times \text{efficiency} \times 3600)/1000 \text{ kJ/day} \quad (4) \end{aligned}$$

A solar water heater absorbs solar radiation comes from sun and heat energy is transferred to the water circulated inside the water tube. In a flat plate collector the cold water flows inside the tube and warm up by sunshine and flows upward as it becomes lighter than cold water and supplied to the household work.

The energy produced from the solar collector is calculated by following formula [6].

$$\text{Energy production from solar collector per second} = m \times C_p \times (T_{\text{outlet}} - T_{\text{inlet}}) \text{ joule} \quad (5)$$

Hydraulic power can be captured wherever a flow of water falls from a higher level to a lower level. The vertical fall of water is known as the "Head", is essential for hydropower generation. Hence two quantities are required: Flow rate of water (Q), and Head of water (H). With the increase of water head (H), the flow rate (Q) also increases. The power available from falling water can be calculated from the flow rate and density of water, the height of fall, and the local acceleration due to gravity [7]

$$P = \eta \rho g Q H \quad (6)$$

Nomenclature

m	mass flow rate of water (kg/s)
C _p	specific heat of water (4200 J/kg.K)
T _{outlet}	outlet temperature of water (°C)
T _{inlet}	inlet temperature of water (°C)
P	mechanical power produced at the turbine shaft (Watts).

H	hydraulic efficiency of the turbine.
ρ	density of water (1000 kg/m ³).
g	acceleration due to gravity (9.81 m/s ²).
Q	water flow rate passing through the turbine (m ³ /s).
H	effective pressure head of water across the turbine (m).

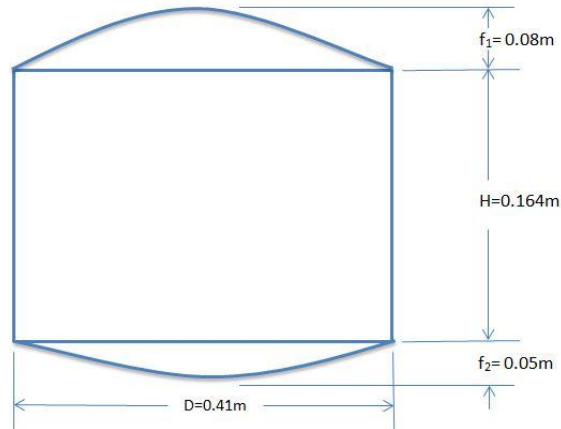


FIGURE 6. Digester dimension.

CALCULATION

If one family of 4-5 members use three 20watt energy saving bulb for 3 hours, watch a 50watt television for 2 hours and use a 20watt fan for two hours then electric energy consumption is shown in table 1.

TABLE 1. Table for estimating electric energy requirement

Serial no.	Name	Power (watt)	No of device	Effective hours	Energy consumption (Wh/day)
1	Bulb	20	3	3	180
2	Television	50	1	2	100
3	Fan	20	1	2	40
Total electric energy consumption					320

For this family daily needs about 0.35 litre LPG(liquefied petroleum gas) i.e. Butane gas for cooking.

Heat energy needed for cooking per day = 0.35×28700 kJ [1 litre butane gas produce 28700 kJ heat energy] [8]
=10045 kJ

Though hot water needs for a family for domestic purpose but it is difficult to calculate. The gas production from cow dung shown in fig.7. The average temperature of the digester was about 33.5°C. It shows that gas produced from 5th day and lasts to 40th day. Maximum gas is produced at the 26th day which is 0.0263 m³ [9].

It shows that the total gas production from 13.5kg of cow dung is 0.46 m³. This means that 0.034 m³/kg of biogas is produced from cow dung.

1 m³ natural gas = 31736 kJ [10]

If 10kg cow dung or organic matter is supplied daily, then

Natural gas production per day = 10×0.034 m³ = 0.34 m³ = 0.34×31736 kJ = 10790 kJ

Water needed = 10×2 kg/day = 20 kg/day [Since water : Cow dung = 2 : 1]

From equation (1), Total volume (V) = quantity of cow dung (kg) + quantity of water (liter) [1kg = 1 liter]
= 10+20 liter = 30 liter = 0.03 m³ [1m³ = 1000 liter]

From equation (2), $D = 1.3078 V^{1/3} = 1.3078 \times (0.03)^{1/3} = 0.41$ metre

In equation (3), substituting the value of D by 0.41; Hence $f_1=0.08$ metre; $f_2=0.05$ metre; $H=0.164$ metre.

If a "solar panel" of 280 Watt runs averagely for 5 hours per day with efficiency 20% [11].

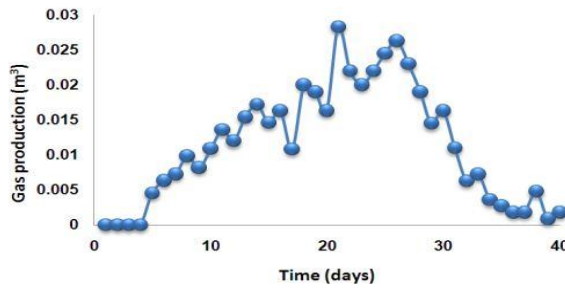


FIGURE 7. Gas production from cow dung

From equation (4), Energy produced from a solar panel = (rated power × hour × efficiency) Wh/day
 = (280 × 5 × 0.20) Wh/day
 = 280 Wh/day

TABLE 2. Table for calculating temperature difference.

For 30% efficiency of flat plate solar collector, the data table is shown in table.							
No.	Time	Inlet temp (in °C)	Outlet temp (in °C)	Temp difference (in °C)	Average temp difference (in °C)	Mass flow rate (kg/s)	Solar intensity (w/m²)
1	11.10AM		30	6			
2	11.27AM		32	8			
3	11.32AM	24	33	9	8	0.0072	11640
4	11.45AM		33	9			
5	12.00PM		34	10			
6	12.15PM		33	9			

From equation (5), Energy production from solar collector per second = $m \times C_p \times (T_{outlet} - T_{inlet})$ joule
 = $0.0072 \times 4200 \times 8$ joule
 = 0.242 kJ

If in average, the solar collector runs for 3 hours per day with efficiency 30%.

Energy production from solar collector = $0.242 \times 3600 \times 3 \times 0.30$ kJ/day = 784 kJ/day

In “experiment”, water was flowing in the pipeline about 380cm³/sec to 420 cm³/sec with 50% efficiency of turbine blade and effective pressure head of 10 m.

From equation (6), $P = 0.50 \times 1000 \times 9.81 \times 0.00040 \times 10$ Watt = 19.6 Watt

If in average, continuously water flow is found 3 hours per day, then conversion of power to energy is similar to solar panel.

From equation (4), Energy produced from water flow through pipe = (rated power × hour) Wh/day
 = (19.6 × 3)Wh/day
 = 59 Wh/day

RESULT

Natural gas production is 10790 kJ/day.

Total electricity produced by solar panel and water turbine=(280+59) Wh/day =339 Wh/day

Energy production from solar collector is 784 kJ/day.

TABLE 3. Table for energy needed and output per day

Serial no.	Name of the energy	Energy needed	Energy output
1	Electricity	320 Wh	339 Wh
2	Biogas	10045 kJ	10790 kJ

DISCUSSION

Though power generation from utilizing hydraulic energy is small quantity but it is quiet economical and environment friendly. In contrast, the renewable energy cannot produce large amount of energy like traditional fossil fuels. Installation of biogas plant is applicable for rural area because in urban area, installation of bio gas plant is quite impossible in most of the case. Since, solar panel and solar water heater depends on solar intensity. Hence in rainy season the efficiency of them becomes lower because of the deficiency of solar intensity.

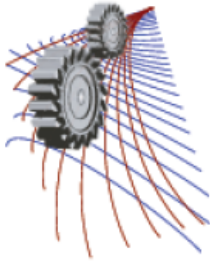
CONCLUSION AND FUTURE RECOMMENDATION

Renewable energy reduces the dependence on conventional energy. Though the initial cost to set up the biogas plant and solar panel is high but they require less operation cost and maintenance cost and to operate them no extra fuel is needed. Besides such type of energy protect the environment from toxic pollution. In remote area, where electricity and gas supply are not available, this project will be more beneficial for such type of area.

For better performance of solar panel, auto tracking system can be used to accumulate more solar energy.

REFERENCES

1. S. M. Maishanu, M.Musa, A. S. Sambo, Nigerian Journal of Solar Energy, 9 (1990) 183-194.
2. Ravi Agrahari, G. N. Tiwari. The Production of Biogas Using Kitchen Waste. International Journal of Energy Science, 2013, 3(6), 408-413.
3. Md. Forhad Ibne Al Imam, M. Z. H. Khan, M. A. R. Sarkar Development of Biogas Processing from Cow dung, Poultry waste, and Water Hyacinth ,International Journal of Natural and Applied Science 2013; 2(1): 13-17
4. S. M. Maishanu, M.Musa, A. S. Sambo, Nigerian Journal of Solar Energy, 9 (1990) 183-194.
5. https://www.solaronline.com.au/solar_system_basics.html
6. Professor Ashok Gadgil “Design for Sustainable Communities” ;Solar Water Heater Project; <http://energy.lbl.gov/staff/gadgil/docs/2009/swh-rpt-2009.pdf>
7. RK Kapuria. Journal of Energy in Southern Africa, 2009, 20, 19-29
8. <http://www.natural-gas.com.au/about/references.html>
9. Md. Forhad Ibne Al Imam, M. Z. H. Khan, M. A. R. Sarkar Development of Biogas Processing from Cow dung, Poultry waste, and Water Hyacinth ,International Journal of Natural and Applied Science 2013; 2(1): 13-17
10. http://www.volker-quaschning.de/dataserv/faktoren/index_e.php
11. http://www.volker-quaschning.de/datserv/faktoren/index_e.php



Industrial pollution and various ways to control pollution in aspect of Bangladesh

Md. Abdul Mannan Akanda^{1, a)} and A. K. M. Enamul Hoque^{1, b)}

¹Department of Mechanical Engineering, Rajshahi University of Engineering & Technology, Bangladesh.

^{a)}Corresponding author: mannandinner@gmail.com

^{b)}shovo.ruet102021@gmail.com

Abstract. At the contemporary each countries of the world are focused on own development and consequently increasing living standards of her inhabitants. With the industrial revolution, humans were able to advance further into the 21st century. Technology developed rapidly, science became advanced and the manufacturing age came into view. With all of these came one more effect, industrial pollution. For the paradigm Bangladesh is a developing country and her industries are growing rapidly as well as industrial pollution. Different industrial pollutants that released from the industries in the form of solid, liquid and gaseous. It contaminates many sources of drinking water, releases unwanted toxins into the air and reduces the fertility of the soil all over the country. Because of solid, liquid and gaseous pollutants associated with noise and radioactive pollution causes environmental imbalance which may give rise to various environmental problems. Lack of policies to control pollution, unplanned industrial growth, use of outdated technologies, presence of large number of small scale industries, inefficient waste disposal, leaching of resources from our natural world are the important factors for the industrial pollution. Pollution is more prone in case of Bangladesh. The present environmental condition of Bangladesh is not at all equilibrium. Severe air, water, soil and noise pollution are threatening human health, ecosystems and economic growth of Bangladesh. This paper analyses solid, liquid and gaseous pollutants from the different industries of the country, their adverse effect, and different ways to improve and control pollution in order to keep environment pollution free and healthy for living.

INTRODUCTION

Environmental pollution is as old as the civilization itself. The protection of environment has become a major issue around the global for the well being of the people and economic development. From the industries solid, liquid and gaseous pollutants are released enormously and contaminate our environments. Industrial solid waste is an important part of the total waste problem. Water is a source of life and energy, rapid pace of industrialization, population expansion, and unplanned urbanization have largely contributed to the severe water pollution and surrounding soils. The main sources of freshwater pollution can be attributed to discharge of untreated sanitary and toxic industrial wastes, dumping of industrial effluent, and runoff from agricultural fields. It is well known that 70–80% of all illnesses in developing countries are related to water contamination, particularly susceptible for women and children [1]. Excessive release of heavy metals into the environment due to industrialization and urbanization has posed a great problem worldwide. Unlike organic pollutants, the majority of which are susceptible to biological degradation, heavy metal ions do not degrade into harmless end products [2]. The presence of heavy metal ions is of major concern due to their toxicity to many life forms. Heavy metal contamination exists in aqueous wastes of many industries, such as metal plating, mining operations, tanneries, radiator manufacturing, smelting, alloy industries and storage batteries industries [3]. Air pollution can be defined as any atmospheric condition in which substances

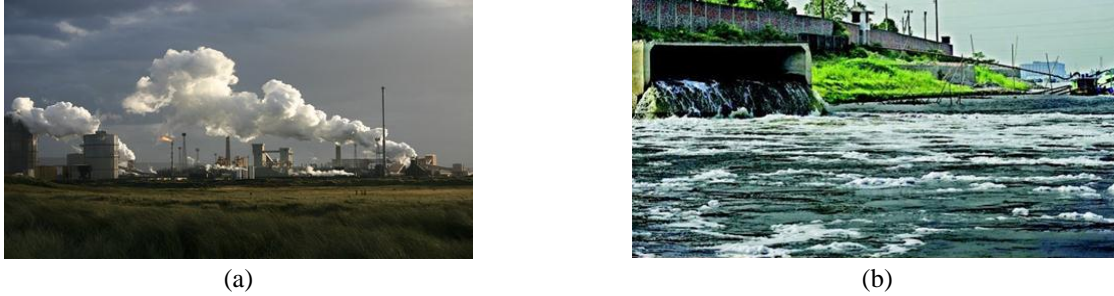


FIGURE 1. Various industrial pollution scenario

are present at concentrations high enough above their normal ambient level to produce a measurable effect on man, animals, vegetation, or materials. The most important pollutants are Carbon monoxide (CO), Sulfur dioxide (SO₂), Nitrogen oxides (NO_x), Ozone (O₃), Hydrocarbons (HC) and Suspended Particulate Matter (SPM). Dhaka is one of the mega cities of the world, witnessed a very fast growth of urban population in recent times. Air pollution in Dhaka city is reported to be serious and damaging to public health. A study of auto-impact of air quality of Dhaka city has been conducted in the year 2000, it is revealed that traffic congestion, fuel quality and brick field emission are the main reasons of air pollution in Dhaka city [4].

VARIOUS INDUSTRIAL POLLUTION SCENARIO IN BANGLADESH

Iron and steel industry

Iron and steel industry is rapidly increasing in Bangladesh. The country has somewhere between 250 and 300 rolling mills currently in operation. Bangladesh's domestic steel output is estimated at around 2.2 million tons a year, with sales valued at \$1.2 billion. Some 30 percent of this output is contributed by a few big firms. At the present time some 40 ship breaking and recycling yards are in operation in Bangladesh. Many ship breaking yards operate in developing nations with lax or no environmental law, enabling large quantities of highly toxic materials to escape into the general environment and causing serious health problems among ship breakers, the local population, and wildlife. In Bangladesh, for example, 40,000 mangrove trees were illegally chopped down in 2009. The World Bank has found that the country's beaching locations are now at risk from sea level rise [5].

Table 1. Heavy metal concentration in the sediments of ship breaking sites in Bangladesh

Sampling stations	Trace metal concentration (µg/g)							
	Fe	Cr	Ni	Zn	Pb	Cu	Cd	Hg
Salimpur	12	68	23	84	37	21	0.57	0.02
Bhatiari	35	87	35	102	122	40	0.83	0.02
Sonaichhari	41	78	49	143	148	31	0.94	0.12
Kumira	21	23	25	120	42	28	0.59	0.05
Sandwip	3	19	4	22	9	2	0.19	0.02

The steel industry also produces a number of wastes in large quantities such as blast furnace slag, dust and sludge, etc. There are a large number of outputs that are produced as a result of the manufacturing of iron and steel, the forming of metals into basic shapes and the cleaning and scaling of metal surfaces.

Leather industry

Leather making is several centuries old technology. However, the wastes generated from this industry make it fall in the "red" category. There are reportedly around 220 tanneries in Bangladesh but, in fact, only 113 tanneries are in effective operation, out of these 20 units are reported to be fairly large. 105 of the tanneries are positioned arbitrarily in the Hazaribagh area in Dhaka where 84 per cent of the total supply of hides and skins are processed in a highly congested area of only 29 hectares of land. The tanneries discharge nearly 22,000 m³ of untreated and highly toxic (contains chromium) into the water body every day.

Table 2. Combined wastewater characterization

Parameter	Unit	Range	Mean
Flow Rate	m ³ /d	584-1068	4048
TSS	mg/l	50-9100	2750
COD	mg/l	2250-8200	5300
BOD ₅	mg/l	1150-3480	1920
Sulfide	mg/l	20.9-186.3	66
Total Cr	.mg/l	22-320	140

Solid and liquid wastes emanating from the tanning industry are known to contain various toxic trace metals. According to our study, Cr is the most toxic element found from the waste of tannery and responsible for cancer.

Textile industry

Textile is the most important sector of Bangladesh's economy. The textile industry is considered as the most ecologically harmful industry in the world. The eco-problems in textile industry occur during some production processes. Textile industry uses large quantity of water in its production processes and highly polluted and toxic waste waters are discharged into sewers and drains without any kind of treatment. The textile dyeing industries of Gazipur and Narayanganj generate large amount of effluents, sewage sludge and solid waste materials everyday which are being directly discharged into the surrounding channel, agricultural fields, irrigation channels, surface water and these finally enter in to Turag and Shitalakkhya River. It is estimated that factories processing 5 tons of fabric produce 750-1,800 ton/day of effluent water.

Table 3. Concentration ranges of the physicochemical properties of the effluents of Textile industry [6]

Parameter	Concentration	DOE standards (for Inland Surface Water)
Temperature (°C)	50.22	40
TSS (mg/l)	1123.11	150
TDS (mg/l)	9123.78	2100
Turbidity (FTU)	130.37	10
DO (mg/l)	2.36	4.5-8
pH	9.88	6-9
EC (µs/cm)	14109.56	1200
BOD (mg/l)	573.89	50
COD (mg/l)	1233.33	200

More than 80% industries have no industrial large treatment plant for effluent discharge. Less than 2% are composite units (knitting, dyeing, finishing) which have proper treatment plants. In order to mitigate pollution treatment plant have to employ. Common Effluent Treatment Plant (CETP) is the concept of treating effluents by means of a collective effort mainly for a cluster of small scale industrial units. The main objective of CETP is to reduce the treatment cost for individual units while protecting the environment.

Pharmaceutical industry

The pharmaceutical industry in Bangladesh is one of the most developed sector. This sector provides 97% of the total medicinal requirement of the local market. During the past few decades, pharmaceutical industries have registered a quantum jump contributing to high economic growth, but simultaneously it has also given rise to severe environmental pollution in Bangladesh. Recently, in this country the pharmaceutical industries are making headways in responsible for the disposal of hazardous waste. Hazardous wastes can take the form of liquids, solids, contaminated gas or sludge. The liquid and gaseous parts are released in water and air respectively with or without any treatment. In Bangladesh, pharmaceutical industries are responsible for 15.9% water pollution and 12.6% toxic chemical emission to the environment among the other polluting industries in the country [7]. Wastes containing toxic elements like cyanide and heavy metals, if discharged without any treatment are harmful to the aquatic life in the stream.

Table 4. Physicochemical characteristics of treated effluent generated from the Pharmaceutical Industries

Parameters	Units	Measured value	Allowable range
Color	-	Ok	Light Brownish
pH	-	7.5~8.2	6-9
COD	mg/liter	245~378	<400
BOD5	mg/liter	72~81	<100
TDS	mg/liter	1320~1506	<2100

Generally three types of waste stream are generated from pharmaceutical industries: process waste water, utility waste water, and domestic waste water. The combine waste streams from different areas of the pharmaceutical industries were subjected to consecutive three stages of treatment- (a) physical treatment, (b) chemical treatment, and (c) biological treatment. Biological treatments again can be subdivided into two types: (i) anaerobic and (ii) aerobic biological treatment.

Fertilizer industry

The fertilizer industries are playing a crucial role in the production of food grain to meet the requirements of increasing population. Pollution due to fertilizer industry is found in varying degrees in air, water and soil. Virtually every fertilizer industry produces some gaseous effluents. Emissions to the atmosphere from ammonia plants include sulphur dioxide (SO₂), nitrogen oxides (NO_x), carbon monoxide (CO), carbon dioxide (CO₂), hydrogen sulphide (H₂S), volatile organic compounds (VOC_s), particulate matter, methane, hydrogen cyanide, and ammonia. In a urea plant, ammonia and particulate matter are the emissions of concern. Nitric acid plants emit nitric oxide, nitrogen dioxide and trace amounts of nitric acid mist. Depending on the process, emissions in the tail gases can range from 215 to 4,300 mg/m³ for nitrogen oxides.

Table 5. Recommended pollution prevention practices in the fertilizer plants

Process	Pollution prevention practice
Ammonia plant	1. Where possible, use natural gas as the feedstock for the ammonia plant to minimize air emissions. 2. Use hot process gas from the reformer to heat the primary reformer tubes.
Urea plant	1. Using total recycling processes in the synthesis process, as a result microprill formation will be reduced.
Ammonium nitrate plant	1. Microprill formation & carryover of fines through entrainment can be reduced by prill tower. 2. Use of granulators can reduce dust emissions from the disintegration of granules.

Brick Industry

Brick industry is one of the largest sources of greenhouse gas emissions in the country, estimated to be on the order of 6 million tonnes of CO₂ annually & is also a major source of land degradation and deforestation. Bangladesh has about 6,000 authorized brickfields and numerous illegal ones. They are located near towns or major construction sites; i.e., Gabtali, Savar, Ashuliya, Keraniganj, Narshingdi, Gazipur and Manikganj. In Dhaka, there are around 4,500 brick kilns in operation, producing about 9.0 billion bricks per year. If Bangladesh maintains its current economic growth rate, continued use of outdated brick-firing technology would raise the level of greenhouse gas emissions to 9 million tons by 2018 by using coal in the purpose.

Table 6. Emission rates of different criteria pollutant from different brick kilns

Brick kiln technology	Emission rates (gm/kg of fired brick)				
	SPM	PM _{2.5}	SO ₂	CO	CO ₂
FCK	0.86	0.18	0.66	2.25	115
Zigzag	0.26	0.13	0.32	1.47	103
VS BK	0.11	0.09	0.54	1.84	70

ADVERSE EFFECT OF INDUSTRIAL POLLUTION

Adverse effect of industrial pollution on human

Severe environmental pollution is threatening human health and economic growth of Bangladesh. Bangladesh could avoid 10,000 deaths and save between 200 and 500 million dollars a year if indoor air pollution in four major cities can be reduced to acceptable limits. Immediate effect of smoke inhalation causes headache, vertigo, burning sensation of the eyes, sneezing, nausea, tiredness, cough etc. Its long term effect may cause asthma and bronchitis. Carbon monoxide hampers the growth and mental development of an expected baby. If CO enters the bloodstream, it reduces oxygen delivery to the body's organs and tissues. Nitrogen oxides cause bronchitis and pneumonia. Industrial emissions cause different waterborne disease and damage to health. Nitrogen dioxide can irritate the lungs and lower resistance to respiratory infections such as influenza. Major concerns for human health from exposure to particulate matter are effects on breathing and respiratory systems, damage to lung tissue, cancer, and premature death. High concentrations of SO₂ include effects on breathing, respiratory illness. Heavy metals such as lead, cadmium, chromium, mercury etc. responsible for chronic poisoning, cancer, affect the kidneys, liver, nervous system, and other organs.

Adverse effect of industrial pollution on environment

It leads to the depletion of natural resources air pollution, water pollution and soil pollution the generation of hazardous waste whose safe disposal become a big problem and the degradation of land quality. It also causes global warming, climatic changes, major consequences of industrialization and acid rain. It may also cause metallic contaminant like Cd, Zn, Hg etc., destroy of bacteria and beneficial microorganisms in the soil, undesirable disease caused by radioactive industrial pollutant.

TREATMENT OF INDUSTRIAL WASTES

Treatment is any process that changes the physical, chemical, or biological character of a waste to make it less of an environmental threat. Treatment can neutralize the waste, recover energy from a waste, render the waste less hazardous, or make the waste safer to transport, store, or dispose of.

Treatment of solid waste

Solid waste treatment is most important for industrial pollution control. Solid waste can be treated in various ways. The most significant controlling methods are Incineration, Gasification, Biological treatment, Storage of solid waste, Deactivation, Micro-encapsulation and filling, Dumping and application, Reuse of solid waste.

Treatment of liquid wastes

Treatment of liquid wastes is also most important because it contaminates soil and water. For the treatment of liquid wastes, different treatment methods can be adopted. One of them is anaerobic technology which was used earlier for treating wastewaters of different industries such as paper and pulp, distilleries, tanneries, textile and food processing, ranging from high-strength waste to low-strength waste. Various reactor configurations such as anaerobic contact reactor (ACR), up flow anaerobic sludge blanket reactor (UASB), fluidized bed reactor (FBR) and anaerobic fixed film reactor (AFFR) have been developed to treat wastewaters from different industries treatment. The anaerobic biological treatment of pharmaceutical wastewater and achieved 60–70 % COD removal efficiency. Recently most popular treatment method is membrane bioreactor (MBR). The MBR has been used for the large-scale wastewater treatment of industrial wastewater, domestic wastewater and municipal wastewater. Activated carbon remains an expensive material for waste treatment. In recent years, the need for safe and economical methods for the elimination of heavy metals from contaminated waters has necessitated research of low cost agricultural waste by-products such as sugarcane bagasse, rice husk, sawdust, coconut husk, oil palm shell, neem bark etc., for the elimination of heavy metals from wastewater have been investigated by various researchers.

Treatment of gaseous wastes

Air pollution caused by the gaseous wastes from the industries can be mitigated by techniques without emission control devices and using emission control devices. Without emission control devices practice includes change in fuel, improve dispersion, good operating practices, plant shutdown/relocation etc. SO₂ emission from the industries can be controlled largely by the scrubbing or flue gas desulphurization (FGD) processes. One approach in reducing nitrogen oxide emission is to remove a large part of the nitrogen contained in the fuels. This system promises as high as 90% removal of nitrogen oxides from the flue gases. The combustion gases are moved across a bed of copper oxide, which reacts, with the sulfur oxide to form copper sulfate. The copper sulfate acts as a catalyst for reducing NO_x to ammonia. Approximately 90% of the NO_x and SO_x can be removed from the flue gases through this process.

RECOMMENDATIONS TO CONTROL INDUSTRIAL POLLUTION

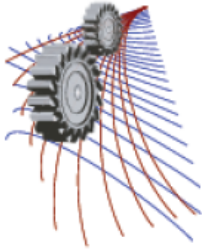
- The government should strictly impose rules and regulations to improve pollution scenario.
- Increased awareness among industrialists about the pollution problem and their legal and social responsibility to prevent it.
- It should be mandatory that industries construct and then regularly and efficiently operate their ETPs and monitor their effluents to keep them within the standards set by law.
- Voluntary or public provision of common ETPs may be a solution to serve adjacent small scale industries, operating on a cost sharing basis.
- National and community level bodies should be established and validated to monitor water quality of canals and rivers, and legal actions against offending industries should be taken.
- Environment pollution act should be up to dated.
- Environment technologies, methods should be introduced and a comprehensive environmental database may be developed.

CONCLUSION

The development of Bangladesh accelerated by the rapid establishment of industries. All the development of the country will go in vain if the wastes from the industries are not efficiently managed. With the development of industries, environmental issues have become a major concern due to impact on public health and progress of Bangladesh. So, the solid, liquid and gaseous wastes released from the industries should be treated properly according to government rules. By applying the introduced methods industrial wastes will be controlled at low cost and will keep the environment healthy for the inhabitants.

REFERENCES

1. WHO/UNICEF, Global Water Supply and Sanitation Assessment Report 2000,WHO, Geneva, 2000
2. V.K. Gupta, M. Gupta, S. Sharma, Process development for the removal of lead and chromium from aqueous solution using red mud – an aluminum industry waste, *Water Res.* 35 (5) (2001)1125–1134.
3. K. Kadirvelu, K. Thamaraiselvi, C. Namasivayam, Removal of heavy metal from industrial wastewaters by adsorption onto activated carbon prepared from an agricultural solid waste, *Bioresour. Technol.* 76 (2001) 63–65.
4. D. A. Begum, “Air pollution: A Case Study of Dhaka City”, presented at the conference “BAQ-2004”, Organized by Society of Indian Automobile Manufacturers, Agra, India, December, 2004.
5. Sarraf, Maria (Dec 2010). "SHIP BREAKING AND RECYCLING INDUSTRY IN BANGLADESH AND PAKISTAN" (PDF). siteresources.worldbank.org. International Bank for Reconstruction and Development/ The World Bank. Retrieved 3 Aug 2015.
6. M. S. Sultana, M. S. Islam, R. Sahaa and M.A. Al-Mansur, “Impact of the Effluents of Textile Dyeing Industries on the Surface Water Quality inside D.N.D Embankment, Narayanganj, Bangladesh”, *Journal of Scientific and Industrial Research*, 44(1), pp.66, 2009. Available online at www.banglajol.info.
7. Musson SE and Townsend TG. Pharmaceutical compound content of municipal solid waste. *Journal of Hazardous Materials* 2009;162(2-3): 730-735.



Reservoir quality assessment using wireline log data: a case study in Bengal Basin

Mohammad Islam Miah and Mafruha Akhter Ovi

¹*Department of Petroleum and Mining Engineering, Chittagong University of Engineering and Technology, Chittagong-4349, Bangladesh*

²*Department of Physics, University of Dhaka, Dhaka-1000, Bangladesh*

^aCorresponding author: islam_pme@yahoo.com

Abstract. The quality of a hydrocarbon reservoir is defined by its hydrocarbon storage capacity and deliverability. The hydrocarbon storage capacity is characterized by the effective porosity and the size of the reservoir, whereas the deliverability is a function of the permeability. Porosity and permeability are key parameters that are readily measured on rock samples, from well logs and well testing. This study shows the shaly sand reservoir assessment using wireline log data. Reservoir zone is detected by Resistivity and Porosity logs with helping by Lithology logs and Caliper log. Lithology identification and sand thickness is calculated from well logs. Effective porosity has been estimated from neutron-density combination formula. Water saturation is estimated from Archie's formula, Simandoux model and Indonesia Equation. The gross reservoir areas have been estimated at three different structure depth cases like Gas Down To (Lowest Known Gas), Spill point and common Gas Water Contact of this field. Reserve is estimated from volumetric method using aforementioned parameters then compared with material balance method.

INTRODUCTION

This field is the second largest gas producing field in the eastern part of Bangladesh. It lies in the south central part of the Bengal Basin and on the western margin of the Tripura high. The surface location of this field is E2857375 m and N697847 m. The reservoir sands in the field's area are composed of stacked sands which are divided into three groups A, B and C Sands. The major gas bearing sand of A-group is A₂ sand [1] which is shown in Figure 1. Porosity and permeability is the major key parameter for a reservoir. The effective porosity is the ratio of interconnected pore space volume to the total bulk volume of the rock. Porosity in sandstone varies primarily with grain size distribution and grain shapes, packing arrangement, cementation and clay volume [2]. Rock porosity can be obtained from the

porosity logs and core analysis. For all these devices, the tool response is affected by the formation porosity, fluid, and matrix, and experimental procedures. Hydrocarbon saturation is important reservoir rock property for estimating reserve. Permeability is the ability of fluid flow through the porous medium of a reservoir rock. In 1991, Geochem Group Ltd. studied about special core analysis based on core samples recovered from this field under over-balanced pressure with limited sand thickness [3]. Interkomp Kanata Management Limited (IKM) [4] studied about Geological, Geophysical and Petrophysical Analysis of the X Gas Field based on combined evidence of seismic data, well data and log data but in this report, shale volume is estimated from only Gamma Ray method using some constant value and estimated porosity is without clay correction for shaly sand hydrocarbon (gas) reservoir. On the other hand, water saturation is estimated by only one method and Reservoir Management Project studied about Petrophysical analysis of this field based on Petro-log software using some constant value [5]. The total hydrocarbon reserve of this field was previously estimated by different organizations such as Interkomp Kanata Management (IKM) 1991, National Committee for Gas Demand & Reserve, 2002 and Petrobangla, 2009. The accuracy of reserve estimation which depends on the availability of sufficient data to characterize the reservoir's areal extent, gas formation volume factor, reservoir quality (porosity and permeability), initial water saturation, and variations in net thickness. The main objective of this study is reservoir quality assessment including hydrocarbon reserve estimation using wireline log data.

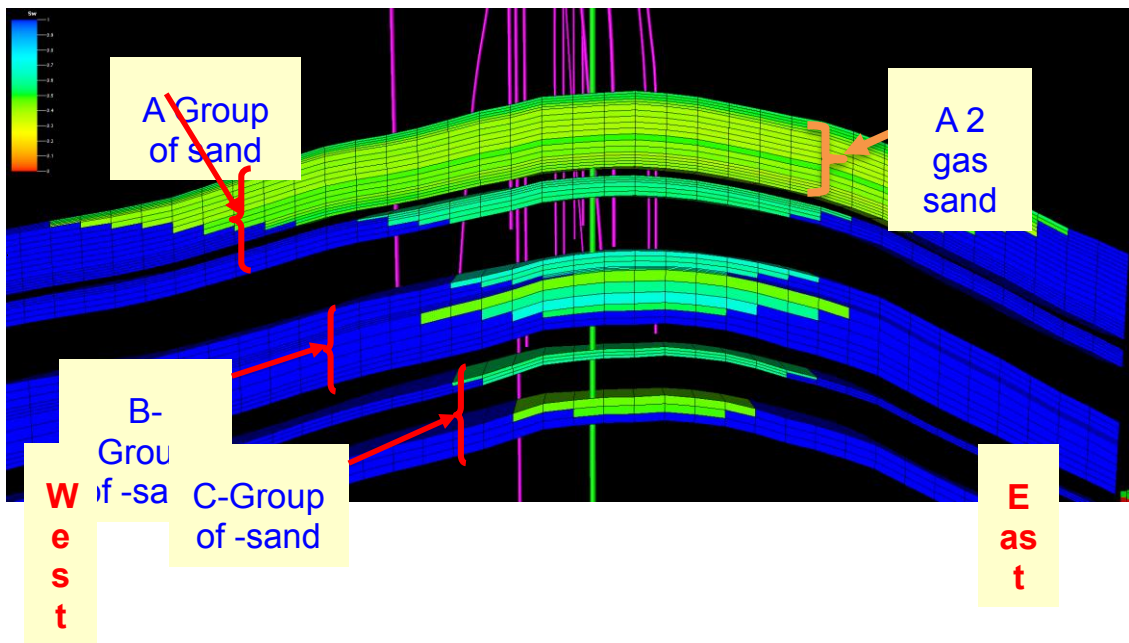


FIGURE 1. Structural Cross-Section of Anticline fold in this field [6]

METHODOLOGY

In this study the average reservoir porosity is estimated from density and neutron log. The effective porosity has been estimated from neutron-density combination formula [7]. Permeable zone is detected by Caliper log, comparing with Bit size of drill hole. Log derived permeability is found from Wyllie & Rose equation [8] where irreducible water saturation (S_{wirr}) of 20%, irreducible saturation exponent (E_{PERM}) of 4.6, permeability constant (C_{PERM}) of 6500 and porosity constant (D_{PERM}) of 6 have been assumed [5]. Formation water resistivity (R_w) is estimated from Inverse Archie's formula [9]. Water saturation (S_w) has been estimated from several models [10-14]. Area of gas sand reservoir is determined at three different depths such as Gas Down To (GDT) or Lowest Known Gas (LKG), Up to Spill Point and common Gas Water Contact (GWC) using seismic depth structure maps (Figure-2). A commercial

software package Petrel™ is used to synthesize the seismic and log data to construct the geological model of the A₂ sand. The bulk volume is determined by multiplying the calculated gross area with the thickness of the gas reservoir. The initial gas formation volume factor (B_g) has been estimated from gas composition [15]. The basic formula has been used for volumetric reserve estimation [16]. Reservoir volume estimation performed after finding area, gross and net sand thickness, petrophysical parameters such as porosity, water saturation and fluid properties such as gas compressibility factor (Z), initial gas formation volume factor, etc. Area is the main input parameter for volumetric reserve estimation. Net volume of reservoir rock containing the gas reserve is determined by geological information based on cores, electric or radioactive logs, drilling records and drill stem and production tests. Reservoir rock volume is usually obtained by planimetrying isopachous maps of productive reservoir rock or by the polygon method for computing volumes [16]. The accuracy of volumetric estimates depends on the availability of sufficient data to characterize the reservoir's areal extent, gas formation volume factor, effective porosity and initial water saturation, and variations in net thickness. The summarized methodology of this research has been shown in Figure-2 as the following flow chart:

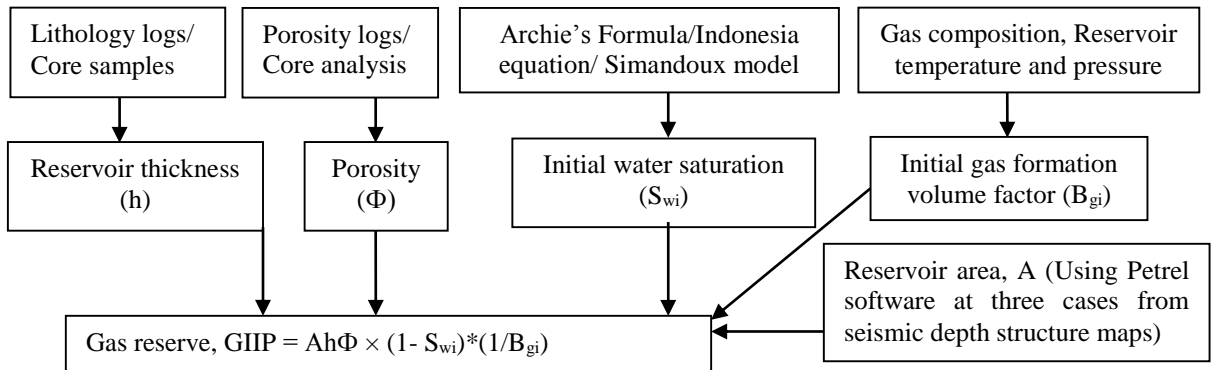


FIGURE 2. Flow chart for reservoir quality assessment.

RESULTS AND DISCUSSIONS

Reservoir Petrophysical Parameters and Quality

In porosity assessment, matrix density and fluid density have been used of 2.68 and 1.00 gram/cc, respectively. According to log data analysis, average bulk density and neutron porosity is 2.39 gram/cc and 19-22%. Average effective porosity found is 17% from the log data analysis using Neutron-Density combination formula with clay corrected. The average water saturation of 32% from Simandoux method of A₂ gas sand found from X field well no.1 has been used as initial water saturation (S_{wi}). Then gas saturation (S_g = 1-S_{wi}) has been determined as 68%. The gross average sand thickness of A₂ gas sand found from logs is 152 feet and net thickness of 131.46 feet. The Net to Gross sand ratio has been found as 0.87. The log derived permeability is about 230 mD.

Gas Formation Volume Factor

The gas formation volume factor is defined as the volume of gas at reservoir conditions required to produce one standard cubic foot of gas at the surface. The gas specific gravity has been estimated is 0.5844 from gas composition of A₂ gas sand. The gas compressibility factor (Z) is 0.952 using standing and Katz chart (1942) at initial reservoir pressure and temperature are 3992 psia and 647.8°R (IKM, 1991b), respectively. The initial gas formation volume factor is 0.004372 resft³/SCF.

Gross Reservoir Area

Reservoir area has been calculated at three different depths using Geological model. In this study, three possible cases are considered for fluid contact of A₂ gas sand to estimate reservoir area. The main problem lies here in reservoir volume estimation of A₂ sand is the areal extent with respect to Gas Water Contact. GWC for A₂ gas sand has not been found. Recent studies under Reservoir Management Project-2 in 2009 assumed a common GWC for A-Group sands at 2812m SS. The Lowest Known Gas (LKG) or Gas Down To (GDT) for A₂ gas sand has been found from logs of X field 14 well at depth 2883.26m MD (2729.4m SS) in this structure. This has been considered as “GDT Case” for volume estimation. The maximum closing contour of A₂ gas sand found from the depth map (Figure-2) is at 2800m SS which approach the Spill Point. “Most likely” or “Medium” case has been defined as taking the extension of A₂ gas sand up to this level (Spill point). “Maximum case” has been defined here by taking the common GWC for A₂, A₃ and A₄ gas sands of this structure at depth 2812m SS (Figure-3). In GDT case (2729.4m SS) and Most likely/Medium case (Spill point at 2800m SS), the resulting gross area are 16896.18 and 28164.26 acres, respectively. At Common GWC (2812m SS), the reservoir gross area is found to be 30291.29 acres.

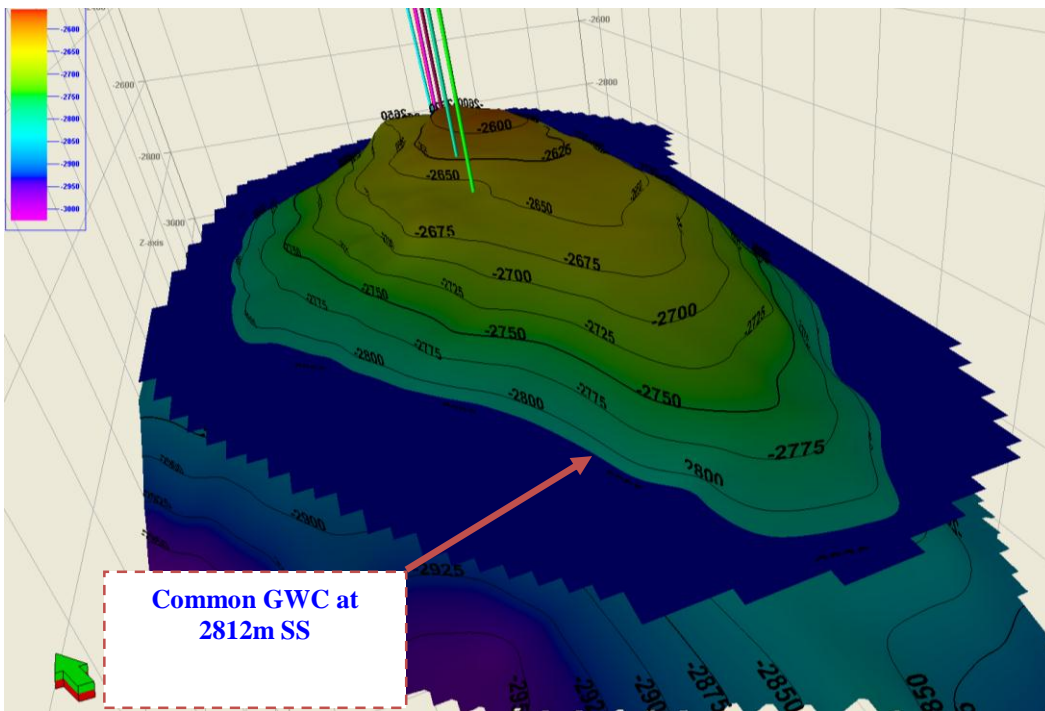


FIGURE 3. A₂ sand depth map showing common GWC at 2812m SS

Hydrocarbon Reserve

Summarized results of volumetric reserve estimation of A₂ gas sand has been shown in Table-1 using different parameters at three different cases.

TABLE 1. Estimated volumetric reserve for gas sand reservoir

Volumetric parameters	Case-1 (GDT/LKG)	Case-2 (Spill point)	Case-3 (Common GWC)
Reservoir area (acres)	16896.18	28164.26	30291.29
Gross thickness (feet)	151.78	151.78	151.78
Net thickness (feet)	131.46	131.46	131.46
Net-Gross ration (fraction)	0.87	0.87	0.87
Bulk rock volume (acre-feet)	2564502.72	4274771.38	4597612.00
Net rock volume (acre-feet)	2221172.27	3702473.62	3982092.98
Porosity (fraction)	0.17	0.17	0.17
Net pore volume(acre-feet)	377599.29	62940.52	676955.81
Gas saturation (fraction)	0.68	0.68	0.68
Hydrocarbon pore volume (acre-ft)	256767.50	428005.95	460329.95
Gas Initially In Place, GIIP (TCF)	2.56	4.26	4.59

The estimated GIIP (2-4.59 TCF) for volumetric reserve is pessimistic that the material balance of flowing wellhead pressure approach (7.92 TCF) [6].

UNCERTAINTY AND LIMITATION OF THE STUDY

Reservoir net thickness may be changing through the formation causes for reservoir geometrically shape and shalyness. Assumed homogeneous porosity and water saturation may be changed through the formation because these parameters vary with respect to depth of the wells. Log derived permeability may be changed within the reservoir.

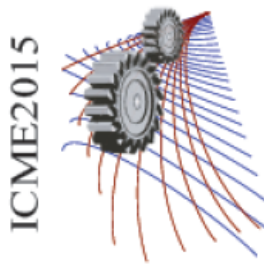
CONCLUSION

Reservoir is shaly sand where sand thickness is varies from well to well and A₂ gas sand is the main reservoir which net to gross thickness ratio is 0.87 from log data analysis. Reservoir porosity and saturation quality is good. The gross reservoir area ranges from 16,896.18 – 30,291.29 acres at different structure depth cases like Gas Down To, Spill point and common Gas Water Contact of A₂ gas sand reservoir using Petrel software, respectively. GIIP is about 2.56-4.59 TCF based on geological conditions.

REFERENCES

- [1] RPS, “X Field Geological Report”, Petrobangla, Dhaka, Bangladesh, 2009a, p. 36.
- [2] Akhanda, A. R. and Islam, M. Q., “Introduction to Petroleum Geology and Drilling”, Publication-cum-Information Office, Bangladesh, 1994, p. 78.
- [3] Geochem Group Ltd., “Special Core Analysis of X Gas Field-11 Report”, 1991.
- [4] IKM, “Geological, Geophysical and Petrophysical Report of X Gas Field”, Petrobangla, Bangladesh, 1991, p.88.
- [5] RPS, X Field Petrophysical Report, Petrobangla, Dhaka, Bangladesh, 2009a, p. 64.
- [6] Houqe, M. M., “Material Balance of a Gas Reservoir of Surma Basin by Flowing Wellhead Pressure Approach”

- [7] Miah, Mohammad Islam, "Porosity assessment of gas reservoir using wireline log data: a case study of bokabil formation, Bangladesh", Elsevier Journal of Procedia Engineering 90 (2014) 663-668, doi: 10.1016/j.proeng.2014.11.789, 28 December, 2014.
- [8] Crain E. R., "The Log Analysis Handbook, Volume-1, Quantitative Log Analysis Methods", PennWell Publishing Company, Tulsa, Oklahoma, USA, 1986, p. 328.
- [9] Miah, M. Islam and Howlader, M. F., "Prediction of Formation Water Resistivity from R_{wa} Analysis of Titas Gas Field Using Wireline Log Data", Journal of Petroleum and Gas Exploration Research (JPGER), ISSN 2276-6510, Vol. 2(4), 2012, p. 57-60.
- [10] Asquith, G. B. and Krygowski, D., "Basic well log analysis", AAPG, Tulsa, Oklahoma, 2004, p. 216.
- [11] Bassiouni, Z., "Theory, Measurement, and Interpretation of Well Logs", First Printing, Henry L. Doherty Memorial Fund of AIME, SPE (, Richardson, TX, 1994, p. 372.
- [12] Archie, G. E., "The electrical resistivity log as an aid in determining some reservoir characteristics", SPE-AIME Transactions, V. 146, 1942, p. 62-64.
- [13] Hamada, "An integrated Approach to determine shale volume and hydrocarbon potential in shaly sand", 1996 SCA Conference Paper Number 9641. pp. 1-16.
- [14] Simandoux, P., Mesures dielectrique en milieu poreux, application a mesure de saturation en eau, etude des massifs argileaux, Revue de l'ins. Francais du Petrole, Supplementary Issue, 1963, p. 193-215.
- [15] McCain, W. D. Jr., "The Properties of Petroleum Fluids, Second edition, Penn Well Publishing Co., Tulsa, Oklahoma", 1990, p. 548.
- [16] Lee, John et al., "Gas Reservoir Engineering", SPE Textbook Series, Volume 5, Richardson, TX, USA, 1996, p. 349.



Integration Of Solar Based Renewable Energy In National Grid To Decrease The Scarcity Of Electricity Of Bangladesh

Riyazul Kabir¹ and Capt Abdul Munyeem¹

¹*Department of Mechanical Engineering, Military Institute of Science & Technology, Dhaka-1215, Bangladesh*

Abstract. Taking Bangladesh as a case study, this paper describes the loss of solar energy in different home and offices. Likewise, it describes the way to incorporate them in the national grid. We focus in the area involved in collecting, converting and delivering sustainable energy, looking in a particular detail at the potential role of solar power. Now a day it is must to set a solar panel for high storied buildings. But in most of the cases the buildings do not get full benefits of it. This causes the loss of energy. As our country is having deficiency in electricity, we can use this renewable energy into national grid. Our project plays two important roles in reducing electricity crisis. First of all the produced electricity by solar energy can be delivered to the national grid. As a result of this operation the government may give a tariff as a feedback. It may be done either by reducing the user's electricity bill or it may be done by giving the money back. Secondly, by increasing the efficiency of the solar panel. So that it can detect sunlight accordingly and moves its panel towards the Sun. This project will definitely increase the efficiency of the solar panel and decreases the crisis of electricity in our country.

INTRODUCTION

Bangladesh is experiencing an acute shortage of electric power that is likely to be worsening day by day. The present crisis in power supply hints at the troublesome time to come ahead. In Bangladesh, almost 80% of the people live in the village. Around 55.2% of the population has access to electricity, and per capita commercial energy consumption is among the lowest in the world. ^[1] In light of the present demand for electricity; by 2020 the energy mix will be changed considerably from what it is today. Since Bangladesh is a country which is abundant in natural resources; the substantial availability of renewable energy sources in the form of solar, biomass, biogas, hydro power and wind energy can provide opportunities of sustainable energy based development. The long time average sunshine data indicates that the period of bright sunshine hours in the coastal region of Bangladesh varies from 3-11 hours daily ^[2]. The possibilities of using solar power are already being tested and will mostly increase. These data indicate that there are good prospect for solar thermal and photovoltaic application in Bangladesh. The country's electricity distribution board is failing to cope with the exponential growth in demand for power in the capital and all over the country. Therefore, the researchers intend to investigate whether there is any future prospect for solar energy in Bangladesh.

Solar photovoltaic (PV) systems are in use throughout the country with over 2.9 million household-level installations having a capacity of 122.2 MW (April 2014). Scaling-up of solar PV systems assisted by the development partners are being implemented through Infrastructure Development Company Limited (IDCOL), Rural Electrification Board (REB), Local Government Engineering Department (LGED), Bangladesh Power Development Board (BPDB), NGOs and Private Organizations implementing solar energy program. There is a strong potential for solar energy within the country. Dissemination of solar home systems (SHSs) is being promoted mainly by IDCOL, private sector companies and NGOs based on the direct-sale approach and provision of refinancing funds for micro-financing of SHSs to participating organizations (mostly NGOs) through IDCOL. ^[3]

The prime ambitions of this thesis work are concentrating on the use of both the solar power and the grid power at the same time. Initially all the Sun rays fall on the photovoltaic panels as a DC current. This is then converted to AC current by the inverter. Gained AC current we suggest to give in the national grid by a transformer. The whole procedure will be monitored very carefully. For this we have taken Mirpur DOHS (Defense officers housing society) as a case of study.

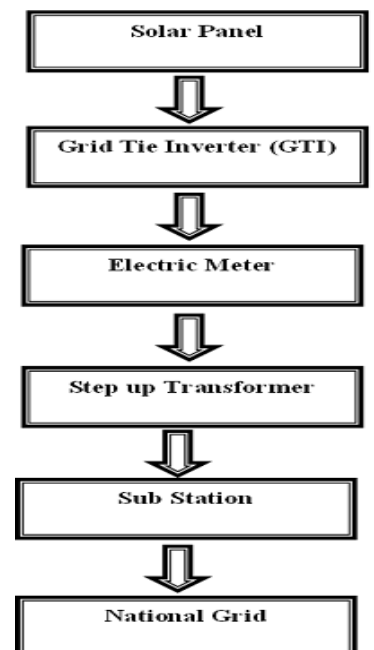
Scope

The Ministry of Power and Energy has been mobilizing Tk 40,000 crore (\$5.88 billion) to generate 5,000 MW of electricity to reduce load shedding into a tolerable level within next four and half years during the term of the present government. Under the plan, the Power Development Board (PDB) would produce 500 MW gas-fired electricity between July and December 2009 to overcome load shedding within December. The PDB would hire furnace-oil based 1,000MW of electricity from private sector from January to June 2010, the plan said. In 2011, the government would install furnace-oil based 800 MW capacity of power plant. The PDB officials would seek suitable place to establish the plant. Besides the government would also hire another diesel or furnace oil based power plant having capacity of 700 MW in 2012 to keep load shedding into mild level. However, the government also contemplates to establish four coal-fired based power plants with capacity of producing 500 MW of electricity each with public and private partnership (PPP) in Rajshahi and Chittagong region. The government has initially tried to create fund of Tk 6,000 crore (\$1 billion) to implement the plan. The power division has tried to utilize the government's budgetary allocation of Tk. 2000 crore for PPP in this regard. [4]

But still we need more replacement in electricity deficiency. Renewable energy can be used to replace it. Bangladesh is endowed with plentiful supply of renewable sources of energy. Solar Energy is inexhaustible and pollution free. It is available everywhere; but the greatest amount is available between two broad band's encircling the earth between 15° and 35° latitude north and south. Fortunately, Bangladesh is situated between 20°43' north and 26°38' north latitude and as such Bangladesh is in a very favorable position in respect of the utilization of solar energy. Annual amount of radiation varies from 1840 to 1575 kwh/m^2 which is 50-100% higher than in Europe. Taking an average solar radiation of 1900 kwh/m^2 , total annual solar radiation in Bangladesh is equivalent to 1010×10^{18} J. present total yearly consumption of energy is about 700×10^{18} J. this shows even if 0.07% of the incident radiation can be utilized, total requirement of energy in the country can be met. At present energy utilization in Bangladesh is about 0.15 watt/sq. meter land area, whereas the availability is above 208 watt/sq.

Procedure

To supply the electricity produced by the solar panel to the national grid there is an arrangement. At first the solar panel should be connected with a Grid tie inverter instead of battery. This type of inverter converts the DC current to AC current which can be taken to the national grid. The line from the inverter then connected to step up transformer to decrease the loss due to transmission. The line from the step up transformer then gathered together in the substation of an area. Form the substation the produced electricity is transmitted to the national grid. To keep the accountability of how much a user is contributing to the national grid, a meter is placed on the user end which gives the exact reading of the user generated electricity. The whole system can be represented by the flow chart.



There are few components associated with the system. These components are:

Solar panel: Photovoltaic (PV) cells are assembled together to create a solar module. It has anywhere from 2 to 200 cells assembled together, encased in tempered glass and aluminum to make them

weather resistant. Modules can be made in a many sizes and shapes to fit their application. Panels come in standard rectangular, triangular, foldable, and even thin-film rolls. This means they can be used in a wide variety of applications. Panels generate direct current (DC) electricity.

Grid tie inverter: Operating a renewable energy system in parallel with an electric grid requires special grid-interactive or grid tie inverters (GTI). The power processing circuits of a GTI are similar to that of a conventional portable DC-AC converter that operates as a stand-alone device. The main differences are in their control algorithm and safety features. A GTI basically takes a variable voltage from a DC source, such as solar panels array or a wind system, and inverts it to AC synchronized with the mains. It can provide power to your loads and feed an excess of the electricity into the grid. Depending on power and voltage levels, GTIs circuits normally have from one to three stages. In solar applications, to maximize the system efficiency, a GTI also has to meet certain requirements defined by the photovoltaic panels. Solar panels provide different power in different points of their volt-ampere (V-I) characteristic. The point in the V-I curve where output power is maximum is called maximum power point (MPP). The solar inverter must assure that the PV modules are operated near their MPP. This is accomplished with a special control circuit in the first conversion stage called MPP tracker (MPPT).

Electric Meter: Electric meters installed at customer’s premises to measure electric energy delivered for billing purposes. They are typically calibrated in billing units, the most common one being the kilowatt hour [kWh]. Watt-hour meter or is an electrical instrument that measures the amount of electrical given to the national grid by the consumers. They are usually read once each billing period.

Step-up transformer: A transformer is a device that changes (transforms) and alternating potential difference (voltage) from one value to another value be it smaller or greater using the principle of electromagnetic induction. On a step-up transformer there are more turns on the secondary coil than the primary coil. The induced voltage across the secondary coil is greater than the applied voltage across the primary coil or in other words the voltage has been “stepped-up”. There will be some transmission losses while supplying the produced electricity from house to the substation. As a result to minimize the losses we are using the step up transformer.

Illustration

Taking Mirpur DOHS as a Case Study

Mirpur DOHS is the largest among all other DOHS covering 138.81 Acre of land having 1,290 allotted plots for the defense officers. Inside the residential area, there is a playground, a central

jam-e-mosque, a large water body with many other proposed

modern facilities for the residents. Above 9,000 families are expected to live in this residential area within next 3 years or so. Adjacent to Defense Services Command & Staff College of the Mirpur Cantonment, Mirpur DOHS is located in Dhaka District, Mouza: Chalkdigoon, Baonia, Chakoli, Police Station: Pollabi, Ward no.: 02, Post Office: Mirpur-1216. [5]

Solar panel: Let, 2 kw solar panel be installed in the rooftop of every building. Unit price per watt solar panel= 70 taka [6]. So, total cost of the user for installing 2 kw solar panel = (2×1000×70) = 140,000 Tk

Inverter cost: Weather protected inverter = 80,000 Tk [6].

Effective hour of solar energy: Average hr of sunshine

$$= \frac{\sum 12 \text{ month sunshine}}{12} = \frac{49.6}{12} = 4.125 \text{ hr}$$

Total solar electricity produce in Mirpur DOHS,

$$= \text{total plot} \times \text{avg. sunshine} \times 2\text{Kw} = (1290 \times 4.125 \times 2)\text{kwh} = 10642.5 \text{ kwh}$$

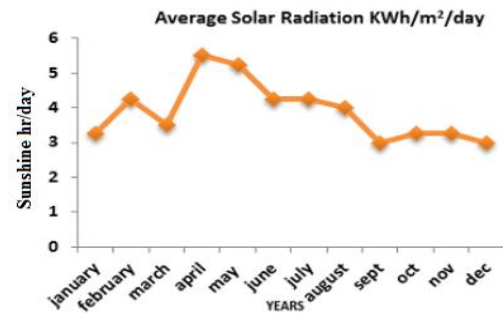


Fig. 1. Monthly average solar radiation in Bangladesh [5]

Wiring Cost

We have to require three types of wire. i) Solar panel to inverter. ii) Inverter to transformer. iii) Transformer to substation

i) Solar panel to inverter: Core flexible solar cable per unit coil = 12,500 taka [6]. In Mirpur DOHS, average height of an Apartment is 6th Floor and one coil is enough. This cost will bear by the consumer.

ii) Inverter to transformer: Total LT (low tension) cable requirement = 7000 m [9] Cable name: BYA1X35rm retail price 23,101 Tk per 100 meter. So, total cost = (total length of the cable × price per 100 meter)/(100 meter)
= (7000×23,101)/100=16,17,070 Tk

iii) Transformer to substation: Total HT (High tension) cable requirement = 2000m [9]. Cable name: NYSEYFGbY3×50rm retail price 2, 86,759Tk per 100 meter. So, total cost = (total length of the cable × price per 100 meter)/(100 meter) = (2000×2,86,759)/(100 m)=57,35,180 Tk.

Transformer Cost= 102,00,000 Tk [9]

Mirpur DOHS users will bear only the solar panel and inverter cost that is (1, 40,000 +80,000) or, 2,20,000 Tk and government will bear the step-up transformer cost, wiring cost.

Total cost of government = wiring cost +transformer cost =1,02,00,000 + 7352250 = 1,75,52,250 or, 1.76 core taka

Solar Energy in Dhaka City

Dhaka City Corporation is divided in to two parts as south and north respectively. Dhaka city corporation south is smaller than the Dhaka city corporation north. The entire area of the Dhaka city corporation are founded by the simply addition of this two areas. To calculate the area in where solar energy will generate effectively is calculated by subtracting the areas for the roads and highway and 10% of the total area which is not elective due to having ponds, canal etc. then comparing with the area of Mirpur DOHS we can easily find out the approximate solar energy production in Dhaka City Corporation. The calculation shows below:

Area of Dhaka city corporation south = 45 km^2 [8]. Area of Dhaka city corporation North = 82.7 km^2
(www.dncc.gov.bd) So, total area of Dhaka city corporation = DCCS + DCCN = 127.7 km^2

From the above table of Road Maintenance Management System (RMMS), we come to know that length of the total roads in Dhaka city is 1286.02 km and pavement area of the road 8.84 sq- km^2 . Again we get the road area of Dhaka City Corporation that is 12.09 sq- km^2 .

Now, area for road in Dhaka city = 12.09 km^2 and 10% of total area deducted = 12.77 km^2

Effective area of Dhaka city =total area of DCC – total road area – 10% of total area

$$= (127.7-12.09-12.77) km^2$$

$$= 102.84 km^2$$

In area of Mirpur DOHS is 0.562 km^2 and here generate 10.6425 MWh electricity. We can be calculated the total possible electricity of the whole Dhaka city corporation by simply comparing with the Mirpur DOHS areas electricity production. So, from Dhaka city corporation area total solar electricity may produce

$$= \frac{\text{effective area of Dhaka city corporation} \times \text{Mirpur DOHS electricity production}}{\text{area of Mirpur DOHS}}$$

$$= \frac{102.84 \times 10642.5}{0.562}$$

$$= 1947464 \text{ kWh} = 1947.5 \text{ MWh}$$

Again the cost of Dhaka city for the installation of the solar energy production is calculated by the same procedure follows for the calculation of electricity production in Dhaka City. In chapter-6 we got that cost requirement for the small area of 0.562 km^2 is 1,76,00,000

So, total cost in Dhaka city = $\frac{\text{effective area of Dhaka city corporation} \times \text{Mirpur DOHS electricity production cost}}{\text{area of Mirpur DOHS}}$

$$= \frac{102.84 \times 1,76,00,000}{0.562} = 322,06,12,099 \text{ taka or } 323 \text{ core taka (Approx.)}$$

From the above calculation, we can be decided that the solar energy generate in the whole Dhaka City Corporation is 1947.5 MWh and the cost requirement for the installation of the project is approximately 323 core TK.

Suggested payback

Here,

Total cost of Dhaka city: 323, 00, 00,000 TK

Total solar power generate: 1945.46 MWh

So, total electricity generate in a year = total solar energy in a day \times 365 days = $(1945.46 \times 365) = 710093 \text{ MWh}$

It will be beneficial both the user and the government. If the solar energy saves 5Tk/ kWh then the primary cost for the setup of the solar energy will collected from the calculation of following. Year requirement to return primary cost to the government,

$$= \frac{\text{Primary cost}}{\text{suggested per kWh cost} \times \text{yearly kWh electricity generation}} = \frac{323,00,00,000}{5 \times 71009300} = \mathbf{9.1 \text{ years}}$$

A system can be introduced that the government will reduce the billing double to supply by the consumer. For example, if a consumer is us supplying 15 kW form his solar panel to the national grid then the government will reduce 30 kW from his total consumption of the month.

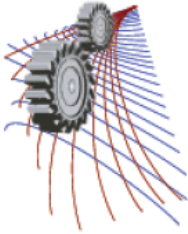
CONCLUSION

In concluding part of this paper it can be stated that, the result that is found is successful one to implement the project in real. The initial target of the project of creating a cost effective feasible system in the area of Mirpur DOHS can be fulfilled as well as Dhaka city and consequently in full area of Bangladesh. This work tried to make an overall assessment of all the parameters that can be retrieved from the system. Eventually we derived the amount of cost that can be saved due to the contribution of the solar panel per year.

The summary of this paper exhibits that, there is a considerable opportunity of Bangladesh to meet its future power demand and thus economic growth through renewable resources. Renewable energy Sources discussed above can help Bangladesh to produce more power in order to reduce Load shedding problem. Time has come to look forward and work with these renewable energy fields to produce electricity rather than depending wholly on conventional method. With the help of these resources Bangladesh can generate electricity & may able to meet the required demand in the future.

REFERENCE

- [1] Bangladesh alternative energy sources limited.
- [2] Bangladesh_Energy_Situation. (2014). Retrieved from energypedia:
https://energypedia.info/wiki/Bangladesh_Energy_Situation
- [3] Global Energy Network Institute. (2014). Retrieved from www.geni.org: <http://www.geni.org>
- [4] Akter, N. (2014). Alternative energy resources of Bangladesh.
- [5] According to Mirpur DOHS porishad
- [6] Easir Arafat, M. D. (2014). synergic BD ltd
- [7] Md. Meganur Rahaman, A. p. (2013 December 27-28). Solar Base Renewable Energy for the Sustainable Future of Bangladesh, BIAM foundation, Dhaka, Bangladesh. proceeding of 4th global engineering science & technology conference, ISBN: 978-1922069-43-6.
- [8] CTP Mr. Seraj, Dhaka City Corporation South, contact: 01715023000
- [9] R Kabir," Incorporation of Solar Based Electricity in National Grid to Improve The Power Production Capacity of Bangladesh" undergraduate thesis, December 2014,MIST.



Major Nuclear Accidents and its Implications on Reactor Design

M.I. Khan¹, M.S. Salek, R. Akter¹, S.S. Nusaka¹ and M.A.R. Sarkar¹

¹*Dept. of Mechanical Engineering, Bangladesh University of Engineering & Technology, Dhaka-1000, Bangladesh*

Abstract. This paper is based on three major nuclear reactor accidents and their consecutive implications on future nuclear industry. Nuclear disaster is an accident which deeply affects people physically, emotionally and genetically and also which affects a nuclear nation economically and morally. Some serious nuclear power plant accidents like Three Mile Island Accident, Chernobyl Disaster and Fukushima Accident strongly affected the development and evolution of nuclear technology. The first and till now the worst nuclear accident in USA occurred in the pressurized water reactor at the Three Mile Island, which was a major turning point in the global development of the nuclear power. Until then, in the period of 1963-1979, a large number of nuclear reactors were readily constructed. But following the accident, and later the catastrophically Chernobyl accident, the cessation of nuclear power industry came down both in USA and on a Global scale. After decades of slow development of nuclear power, recently the industry accelerated due to climate change concerns and power dependency. More safe and efficient nuclear reactors have been designed over the years taking lessons from the previous two accidents. Newer Nuclear reactors are inherently safer and more fuel efficient. But just when the nuclear industry was attempting recovery, the Fukushima accident occurred in a substantial scale. This caused the reassessment on the safety of nuclear reactors worldwide which is still underway.

INTRODUCTION

The Three Mile Island accident is regarded to be the first major nuclear accident in the history of commercial nuclear power generation. It had two pressurized water reactors (PWR), the second unit was readily destroyed in the accident. The TMI accident was a major cause of the decline in nuclear construction through the 1980s and 1990s. After this accident, the next major accident was the Chernobyl disaster, which is known to be the most severe accident that happened in the nuclear history. It had 4 water cooling graphite moderated nuclear reactor of RBMK 1000 design. Both fault in designs and erroneous decisions of the operators led to this disaster. On March 11, 2011 an earthquake of magnitude 9.0 followed by a 15 meter tsunami struck Fukushima Daiichi nuclear power plant and initiated a nuclear disaster. The Fukushima power plant consists of 6 light water type BWR. These three accidents with their course of action and implications on the Nuclear power industry have been discussed in details in this paper.

THREE MILE ISLAND ACCIDENT

Two Reactors were built in the 1970s in the Susquehanna River near Harrisburg, Pennsylvania. Both were Pressurized –water type, manufactured by Babcock and Wilcox. The main construction began on TMI-1 on 1968 and it had first received a license to operate in 1974. It has now operated for over 40 years. The second Reactor TMI-2 suffered an accident after one year of its operation. The accident to unit 2 happened on March 28th, 1979, at 4pm, when the reactor was operating 97% of its power.

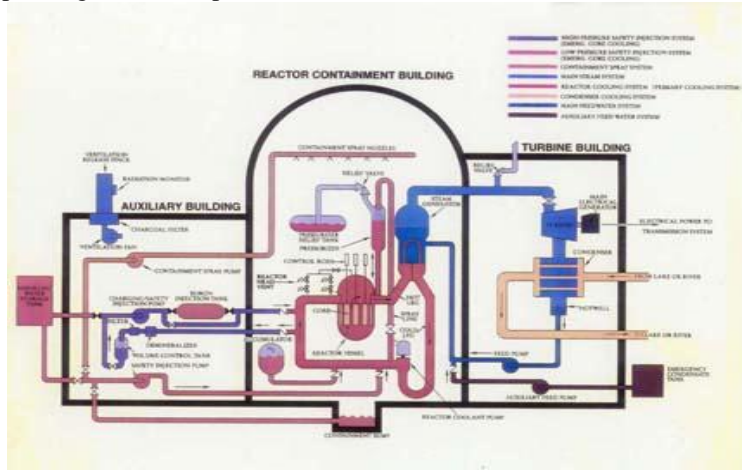


Fig. 1. Three Mile Island reactor 2.

Sequence of the accident

The sequence of the accident was dominated by two main causes, which are shown in two consecutive flow diagrams below:

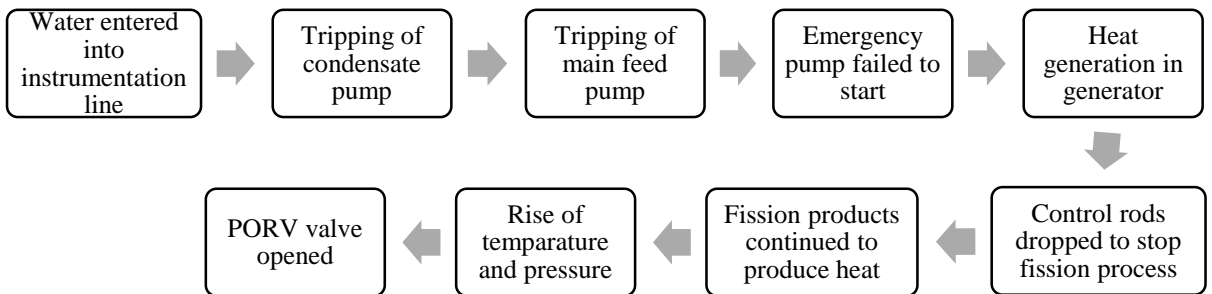


Fig. 2. First drawback: Water enters into service airline.

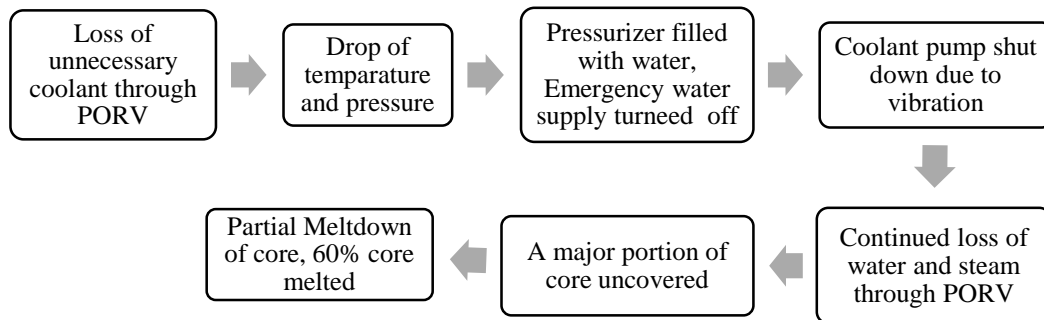


Fig. 3. Second drawback: PORV failed to close in time.

Core damage

The major consequence of the TMI accident was the core damage in TMI-2 reactor. This occurred in the following three time periods into the accident:

- 100 minutes into the accident:
 - ✓ 1.5 m of core was uncovered for 1 hour and at the core was covered for at least half an hour.
 - ✓ Major core damage with production of huge amount of hydrogen due to zirconium-steam reaction. A considerable amount of fission products from the fuel was released to the RCS.
- 7.5 hours into the accident:
 - ✓ 1.5 m of core was exposed in this period.
 - ✓ The fuel temperatures obtained were relatively lower than that for the first period.
- 11 hours into the accident:
 - ✓ Water level decreased to between 2.1 m to 2.3 m for a period of 1-3 hours.

The major consequences of the core damage are as follows:

- 30-40% of the total zirconium inventory was oxidized.
- 1500-2000 cubic meters of active liquid had to be disposed from the containment.
- The upper part of the core was seriously damaged (about one third of it) and the active core material had to be removed.
- Many radioactive gases were released within the containment from the fuel, which includes noble gases (30-40%⁰, Iodine (10-15%⁰, Strontium, Caesium, Xenon-133 (approx. 13 million curies) etc.
- Liquid by-products were also discharged, though the amount was insignificant; 0.24 curies of Iodine-131 and 12.4 curies of Tritium and mixed products.

Impact of the accident

The main impact of the accident was industrial, rather than radiological or health-related. The nuclear power industry came to an abrupt halt after the accident. Here are some of the major changes that have occurred since the accident:

- Plant design and equipment requirements were strengthened and upgraded. This includes fire protection, piping system, auxiliary feed water system, containment building isolation, reliability of individual components and the ability of plants to shut down automatically.
- The critical role of human performance in plant safety was finally identified, since the major cause of the accident were two operational glitches. This led to revamping operator training and staffing requirements,

followed by improved instrumentation and controls for operating the plant, and establishment of fitness-for-duty programs for plant workers to guard against alcohol and drug abuse.

- Emergency preparedness were enhanced, including requirements for plants to immediately notify NRC of significant events and an NRC Operation Center staffed 24 hours a day. Drills and response plans are now tested by licenses several times a year, and state and local agencies participate in drills with Federal Emergency Management Agency and NRC.
- Integrating NRC observations, finding and conclusion about license performance and management effectiveness into a periodic, public report.
- Senior NRC managers regularly analyze plant performance for those plants needing significant additional regulatory attention.
- NRC's resident inspector program was expanded– first authorized in 1977 – to have at least two inspectors live nearby and work exclusively at each plant in the U.S. to provide daily surveillance of license adherence to NRC regulatory attention.

Chernobyl disaster

Chernobyl Disaster is known to be the most severe accident in the history of commercial Nuclear Power. The accident took place in 1986 at the Chernobyl Nuclear Power Plant situated 130km north of Kiev, Ukraine, and about 20km south of the border with Belarus.

INES labelled this accident as a level 7 disaster alongside Fukushima Disaster. This is the only accident to cause fatalities from radiation.

At the time of the accident, 4 reactors of the Soviet RBMK-1000 design were operating. It was different from western reactor design as it was principally designed for Plutonium production and used for both plutonium and electrical power production. A rare combination of graphite moderator and water coolant was used in these reactors.

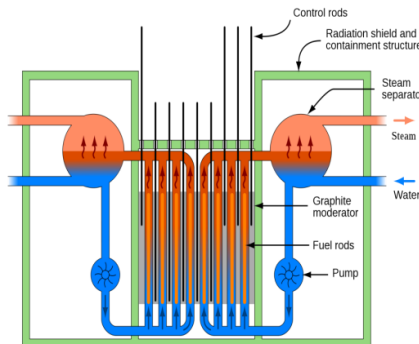


Fig. 4.Schematic of RBMK.Fig. 5.Chernobyl Disaster.

What happened at the plant?

The sequence of the accident along with the causes is described in a flow diagram below

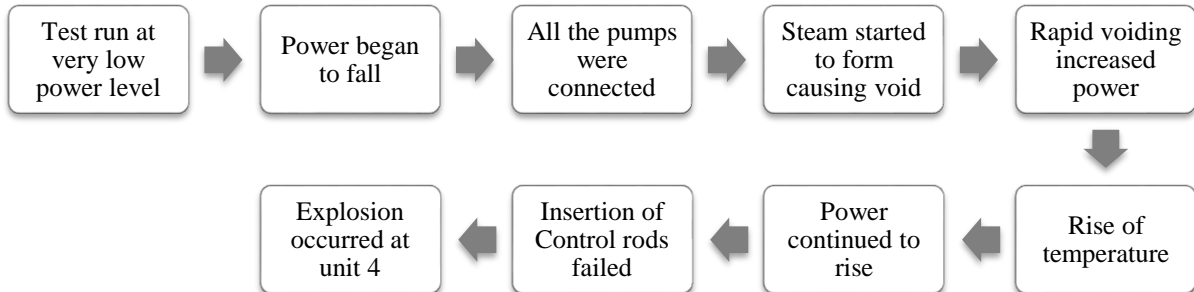


Fig. 6. Sequence of the accident.

Causes of accident

In the reports of Soviet Union after the accident, operator error came out to be the sole cause of the accident. Having said so, serious design faults in RBMK reactor worsened the scenario and made it very difficult for the operator to manage the power plant and prevent the explosion of unit 4[3]. The two main causes are explained in detail below:

Operator error

- To perform a test on turbine generator number 8, operators started to reduce power of the plant at a very low level violating the plant specification. The plant must not have run below 700MW for long in order to be stable.
- Auto shutdown signal was blocked and consequently power fell below 30MW.
- Emergency core cooling system was switched off.
- All the main circulation pumps and feed water pumps were connected to the core.
- Scram signal was delayed.

Design error

- Control rods insertion was slow, it would not insert fully before 20 seconds where it took 2 seconds to insert in western reactors.
- Control rods were made of boron carbide with graphite tip that increased reactivity.

- Very low Operating reactivity margin (equivalent control rods in the core) of 8 control rods was noted during the accident whereas it shouldn't have been below 15.
- There was no containment to prevent radiation.
- Flammable graphite moderator burst and vaporized radioisotopes in the atmosphere.

Changes in design of RBMK reactor

After the accident all Soviet-designed reactors were improved vastly to ensure safety. Modifications have been made to the RBMK reactor [4]. They are as follows:

- *Decrease in void coefficient of reactivity:* Void coefficient of reactivity was ensured to be negative by:
 - ✓ Installing 80-90 additional fixed neutron absorber in the core.
 - ✓ Increasing fuel enrichment from 1.8 to 2.4% U-235
 - ✓ Operating reactivity margin was increased from 26-30 to 43-48 equivalent control rods.
- *Increase in emergency safety system efficiency:*
 - ✓ Control rod design was changed.
 - ✓ Scram rod insertion time was reduced from 20 to 12 seconds.
 - ✓ Fast acting emergency protection system was installed.
- *Additional changes:*
 - ✓ Graphite displacers were added to the control rod.
 - ✓ A computer program was installed in the control room to indicate the ORM in the core.
 - ✓ Fuel channels at all unit and group distribution headers were replaced.
 - ✓ SKALA process computer was replaced.
- *System upgrade and other improvements:*
 - ✓ Emergency core cooling system and Reactor cavity over-pressure protection system was upgraded.
 - ✓ When the reactor is operating emergency safety system is prevented from bypassed.
 - ✓ Sufficient sub-cooling at the core inlet by avoiding operational modes that cause reduction in DNB ratio of the coolant at the inlet as ensured.

Fukushima Disaster:

Fukushima Daiichi Nuclear disaster is the worst nuclear disaster after Chernobyl. This major accident of INES level 7 was initiated by an earthquake of magnitude 9.0 and a resultant tsunami on Friday 11 March.2011 but in the report of Fukushima Nuclear Accident Independent Investigation Commission they found this to be 'manmade' as the plant severely lacked basic safety requirements in case of these natural disasters.

Fukushima Daiichi NPP is located on a 3.5 sq. km site in Futaba district of Fukushima, Japan. At the time of the accident 6 light water type BWR was operating at the plant. Unit 1 was capable of producing 460MW, Unit 2-5 produced 784MW and Unit 6 produced 1100MW electric power.

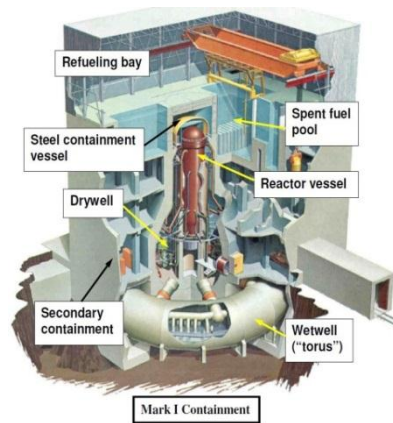


Fig. 7. Mark I Containment.

Causes of the Fukushima Disaster

For better understanding primary reasons of the accident may be divided into several categories.

Direct damage by Tsunami

Main reason of the Fukushima accident was the 9.0 magnitude earthquake followed by the 13 meter Tsunami. Tsunami initiated the disaster by disabling all the 13 generators of the plant and thereby caused complete station blackout. The main power supply system being gone at a time, it became impossible to maintain normal plant activities. Besides, cooling systems of 3 reactors were disabled. Tsunami destroyed roads leading to the plant and so access to the plant became difficult and primary damage control actions were hampered.

Station blackout

The plant lost its offsite power during the earthquake. Then the 13 meter high Tsunami disabled its onsite AC power generators all together. The DC batteries couldn't help much; they discharged rapidly. These resulted in complete station blackout which in turn caused fuel overheating.

Insufficient cooling of fuel

Fuel cooling systems of 3 reactors were damaged directly by the Tsunami. As the station went completely black sometime after the Tsunami cooling of fuel was severely interrupted. Overheating of fuel led to rapid oxidation and generation of excess Hydrogen. Accumulation of excess Hydrogen at the upper portions of the reactor buildings caused explosion at Unit 1 & 3.

Accumulation of Hydrogen & explosion

During the blackout cooling of fuel by the usual cooling system was not possible. So the operators vented the containment with an intention to keep the containment pressure under control. But this helped some gases to leak into the reactor building. Excess Hydrogen generated by fuel overheating leaked into the reactor building and started to accumulate. As a result explosion occurred at Unit 1 & 3.

Compact NPP layout

As discussed earlier the Fukushima Daiichi Nuclear power plant had a compact layout. This created some problems during the accident-

- Hydrogen explosion at Unit 3 damaged some fire pumps of unit 2.
- Fire at Unit 4 might have been initiated by the Hydrogen leakage from Unit 3.

Spent fuel pool affected by Hydrogen explosion

Spent fuel pools of the reactors were located at the upper portion of the reactor buildings. Thus they were exposed to the Hydrogen explosions at Unit 1 & 3. Also cooling system of the spent fuel pool failed resulting 1 week long manual cooling effort.

Suggested Possible Modifications

Since the Fukushima accident possible modifications in nuclear power plant to avoid such disasters are still of a great research interest for the scientists and nuclear engineers. Some possible modifications that have been discussed since then can be categorised as follows-

1.1.1. Power system modification

- Separated containment at higher altitude for diesel generators & switch gears has been designed.
- Portable emergency power supply systems (i.e. generators, turbines etc.) have been installed.
- Combined active & passive safety system to avoid complete station blackout have been installed.

1.1.2. Venting system modification

- Use of pipes with higher strength for pressure vessel venting.
- Direct venting of the containment to the stack in absence of cooling.
- Use of passive containment cooling to meet the need of venting (as a substitute).

1.1.3. Recombiners & igniters

- Installation of more Hydrogen recombiners&igniters to the upper portion of the building has been made.
- Reduction/replacement of Hydrogen generating elements with other elements have been made to prevent emission of hydrogen.

1.1.4. Diversification of plant layout

- Multi-unit sites & diversified plant layout have been designed.
- One or more generator rooms above & below the grade have been built.
- Considering administration buildings, emergency safety system equipped buildings, parking lots etc. for enhancement of physical separation from the plant.

1.1.5. Spent fuel assembly modification

- Dry casks with a 'top hat' chimney have been designed for enhancement of air cooling.
- Retrofitting with a passive cooling system has been designed.
- Individual containment structure for spent fuel pools has been formed to prevent escape of radiation from the plant.

CONCLUSION

Based on the knowledge and experience gained from the disasters, initiatives are being carried out currently at the nuclear power plants through Japan to raise their safety levels even further.

After TMI, the post-accident stage required about ten years, and substantial effort, cost, and the development of special decommissioning technologies. The hazards of core meltdown and subsequent decommissioning might further be minimized by some selected remedies. However, these remedies have been applied over the years, but these have not minimized the number of nuclear accidents; in fact two major accidents, Chernobyl and Fukushima disaster occurred after TMI accident, each causing more damage than the former one. All these accidents had one effect in common, that is the core meltdown, and this could not be minimized even after several safety steps undertaken since the TMI accident.

An autonomous external nuclear instrumentation that can independently measure reactor water level and fissile fuel distribution before, during, and after a reactor accident or routine shutdown has been proposed by one of the authors in our reference papers. Nuclear regulators and utilities can consider the adoption of autonomous water-level and fuel-concentration monitoring systems for both existing and planned reactors. This could be one of the several steps to prevent such nuclear catastrophes in the future.

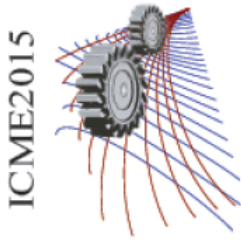
Fire protection, piping system, auxiliary feed water system, containment building isolation, reliability of individual components and the ability of plants to shut down automatically are included for upgrading and strengthening of plant design. Emergency preparedness has been enhanced by including requirements for plants to immediately notify NRC of significant events and an NRC Operation Centre staffed 24 hours a day. Drills and response plans are now tested by licenses several times a year, and state and local agencies participate in drills with Federal Emergency Management Agency and NRC. NRC's resident inspector program – first authorized in 1977 – has expanded to have at least two inspectors live nearby and work exclusively at each plant in the U.S. to provide daily surveillance of license adherence to NRC regulatory attention.

However evidence over six decades shows that nuclear power is a safe means of generating electricity. The risk of accidents in nuclear power plants is low and declining. With nuclear power, safety depends on much the same factors as in any comparable industry: intelligent planning, proper design with conservative margins and back-up systems, high-quality components and a well-developed safety culture in operations.

REFERENCES

1. Third Edition: John R. Lamarsh (author), Anthony J. Baratta (author), Introduction to Nuclear Engineering
2. John G. Collier and L. Myrddin Davis, Accident at Three Mile Island
3. The causes of the Chernobyl Event: Jacques Frot, ex-director at Mobil Oil Française and a member of SFEN - SocieteFrancaised'EnergieNucleaire.
4. RBMK Reactors: World Nuclear Association (updated June 2010).
5. Alexander De Volpi, Nuclear Reactor Safety: Lessons from Three Mile Island and Fukushima. Summer 2012 edition of the Federation of American Scientists Public Interest Report.
6. Denton, H.R. . The causes and consequences of the Chernobyl nuclear accident and implications for the regulation of U.S. nuclear power plants (1987)Annals of Nuclear Energy Volume 14, Issue 6, Pages 295-315.
7. INES The International Nuclear and Radiological Event Scale User's Manual 2008 Edition, International Atomic Energy AgencyVienna ,http://wwwpub.iaea.org/MTCD/publications/PDF/INES-2009_web.pdf. IAES(2008).
8. Fukushima Nuclear Accident Update Log Updates of 2 June 2011. IAEA (2011)
9. Malko, M. V. 'The Chernobyl Reactor: Design Features and Reasons for Accident' <http://www.rrl.kyoto-u.ac.jp/NSRG/reports/kr79/kr79pdf/Malko1.pdf>
10. Chernobyl Accident <http://www.world-nuclear.org/info/chernobyl/inf07.html>. World Nuclear Association (1986)
11. World Nuclear Association, "Nuclear Power in Russia" <http://www.worldnuclear.org/info/default.aspx?id=26576&terms=floating>.
12. World Nuclear Association "RBMK Reactors", <http://www.world-nuclear.org/info/inf31.html>
13. World Nuclear Association:Fukushima Accident 2011"http://www.worldnuclear.org/info/fukushima_accident_inf129.html
14. World Nuclear Society, Safety of Nuclear Power Reactors, (updated 24 June 2011) <http://www.world-nuclear.org/info/inf06.html>.

15. U.S. Nuclear Regulatory .Comission (1987). Report on the Accident at the Chernobyl Nuclear Power Station, NUREG-1250 Washington, DC.
16. Chernobyl Catastrophe; Reasons and Consequences (expert's conclusion). Part one. Direct Reasons of the Accident at the Chernobyl NPP. Dosimetrical Control. Protection Measures and their Efficiency. Edited by V.B.Nesterenko and D.S.Firsova. SENMUR. TEST. Minsk. 1993, pp.48-49 (in Russian).
17. Case Study in Engineering, Chernobyl by EFO Staff <http://engineeringfailures.org/?p=1>
18. IAEA (2011), Fukushima Nuclear Accident Update Log Updates of 2 June 2011.
19. MIT (2011). "Technical Lessons Learned from the Fukushima-Daichii Accident and Possible Corrective Actions for the Nuclear Industry: An Initial Evaluation". Center for advanced nuclear energy systems. MIT-NSP-TR-025 Rev. 1, 26 July 2011. http://mitnse.files.wordpress.com/2011/08/fukushima-lessons-learned-mit-nsp-025_rev1.pdf
20. World Nuclear Association,"Fukushima Accident 2011"http://www.worldnuclear.org/info/fukushima_accident_inf129.html
21. Report of the Japanese Government to the IAEA Ministerial Conference on Nuclear Safety (2011). "The Accident at TEPCO's Fukushima Nuclear Power Stations" ,<http://www.iaea.org/newscenter/focus/fukushima/japan-report/cover.pdf>.



Forced Convection Heat Transfer In A Microchannel With Nanofluid Incorporating Different Geometry

Saima Aktar Sumaiya, Maahi Muhiuddin Talukder, Dr. A. K. M. Monjur Morshed^{a,*}

^aBangladesh University of Engineering and Technology, Dhaka

Abstract. Microchannels are currently of great interest for use in compact heat exchangers and electronic circuits being extensively used where very high heat transfer performance is desired. In this present study, the effect of incorporating fins of different shape, circular and triangular, on fluid flow and heat transfer in microchannel heat sinks have been investigated comprehensively and the results were compared with that of microchannel without fin. Water and water based alumina ($H_2O + Al_2O_3$) nanofluid were used as the working fluid. Performance has been evaluated based on average Nusselt number and pressure drop characteristics. The study was performed numerically using commercially available CFD platform FLUENT. The microchannel with triangular fin was found to have the best thermal performance compared to the other two configurations.

Introduction

Thermal management is pivotal to effective functioning of devices comprising of electronic circuits. The placement of a large number of electronic circuits in a device platform leads to the generation of high heat fluxes. The failure to remove such high heat fluxes is likely to result in malfunction of circuits, which along with increased substrate temperature would eventually lead to the total failure of the device. The contradictory requirements of high heat dissipation and low temperature rise are commonly required for a wide range of applications. The microchannel heat sink can make those two contrasting features converge at one point which can be attributed to its unique construction enabling the designers to bring a heat source and a heat sink into close proximity, thus minimizing thermal resistance. Tuckerman and Pease[1] first performed experiments on silicon based microchannel heat sink. Peng and Peterson[2] presented an analytical and numerical study on the heat transfer characteristics of forced convection across a micro channel heat sink. Judy *et. al.* [3] did pressure drop experiments on both round and square microchannels. They tested distilled water, methanol and isopropanol over a Reynolds number range of 8 to 2300. Their results showed no distinguishable deviation from laminar flow theory for each case. Steinke *et. al.* [4] presented an analytical approach

for characterizing electronic packages, based on the steady-state solution of the Laplace equation for general rectangular geometries, where boundary conditions are uniformly specified over specific regions of the package. Qu and Mudawar [5] conducted a similar type investigation by developing a fully explicit two - dimensional incompressible laminar Navier-Stokes solver using a Cartesian grid. Developing flow heat transfer in micro-channel was investigated by Lee *et. al.* [6] and they proposed analytical correlation between Nusselt number and non-dimensional flow length for developing flow in microchannel. Heat transfer rate is very high in the developing zone compared to developed zone. The result of Al - Bakhit *et. al.* [7] found that entrance region the developing velocity profiles lead to higher values of overall heat transfer coefficient.

Gunnasegaran *et. al.* [8] studied the effects of geometrical parameters on heat transfer and fluid flow in microchannel heat sink. It is found that the temperature distribution is much uniform for the smallest hydraulic diameter of the micro-channel heat sinks, and pressure drop and friction factor are larger. Cho *et. al.* [9] investigated the cooling performance of microchannel heat sinks with different geometric structures under various heat flux conditions. Chai *et. al.* [10] studied and optimized the structural parameters of the microchannel with offset fan-shaped re-entrant cavities, triangular re-entrant cavities and aligned fan-shaped re-entrant cavities by numerical simulation of flow and heat transfer mechanism.

The first study on the possibility of increasing thermal conductivity of a solid-liquid mixture by adding more volume fraction of solid particles was done by Maxwell [11]. Several investigations revealed that the thermal conductivity of the nanoparticles suspension could be increased by more than 20% for the case of very low nanoparticles concentrations.

In this present study, a measure has been undertaken to examine the opportunities of enhancement of heat transfer by employing nanofluid as the working fluid and also by incorporating different roughness element in a simple straight rectangular microchannel. The numerical analysis has been performed using the commercial CFD package ANSYS FLUENT. The performance of the heat sink with different features has been compared on the basis of Nusselt number.

Model and Formulation

The microchannel we have used for our simulation purpose is 10 mm in length, 180 μm in height, and 57 μm in width. The substrate is 10mm in length, 900 μm in height, and 100 μm in width. The microchannel is not placed at the middle of the substrate , rather the centreline of the channel is offset from the centreline of the substrate by 90 μm . In the finned microchannel, the cylindrical fins are 30 μm in diameter and 50 μm in height. They are five such fins along the base of the channel and they are placed in such a way that the centre-to-centre distance between two adjacent fins is 1.5 mm. And in case of the triangular fin, the height of the triangular wedge is 50 μm , the base of the triangle is 30 μm , and the height of the triangle is 800 μm and there are three such fins placed along the base of the channel. Fig. 1 and 2 depict different aspects of our models.

Discretization of the computational domain has been done by GAMBIT by creating mesh. In case of simple channel the mesh created is structured in nature. But in case of the finned channels the mesh generated is unstructured and the elements were tetragonal or hybrid.

The channel inlet has been chosen to be pressure-inlet and the flow is assumed to be fully developed flow. The pressure at the inlet is varied at 10, 20, 30, 40, 50 KPa (gauge). The channel outlet has been chosen to be pressure-outlet. The pressure at outlet has been kept constant at atmospheric pressure or 0 pascal (gauge). At inner wall surfaces no slip condition prevails i.e. $u = v = 0$. For thermal boundary conditions, adiabatic boundary condition is applied to all the boundaries of the solid region except at the heater surface i.e. the bottom surface. Heat flux at the bottom surface has been varied as 50, 90 and 150 W/m^2 .

Governing equations take the following form:

Continuity equation:

$$\frac{\partial \rho}{\partial t} + \nabla \cdot (\rho \vec{V}) = 0 \quad (1)$$

Momentum equation:

$$\rho \frac{\partial \vec{V}}{\partial t} + \rho (\vec{V} \cdot \nabla) \vec{V} = -\nabla P + \rho \vec{g} + \nabla \cdot \tau_{ij} \quad (2)$$

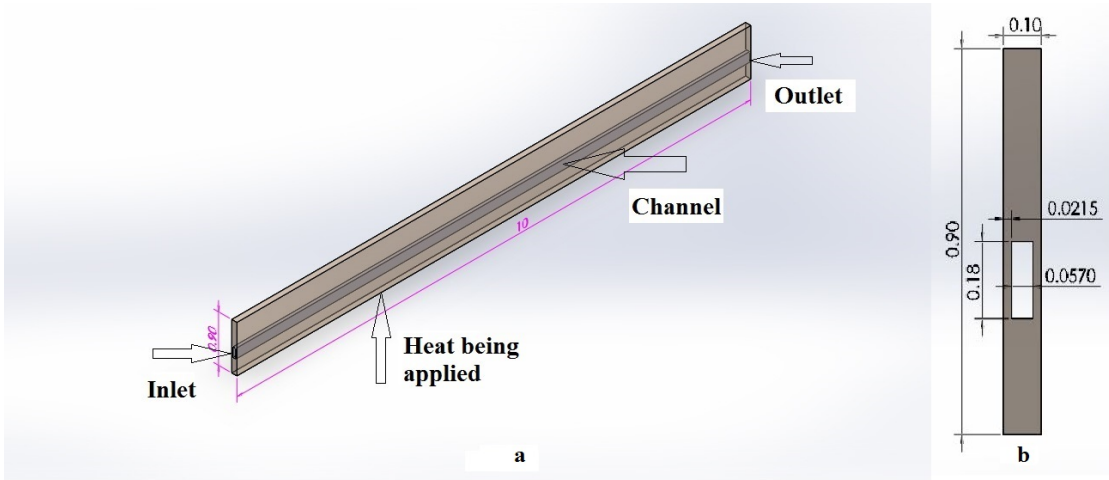


Fig. 1. (a) Simple Microchannel, (b) Front view of the model

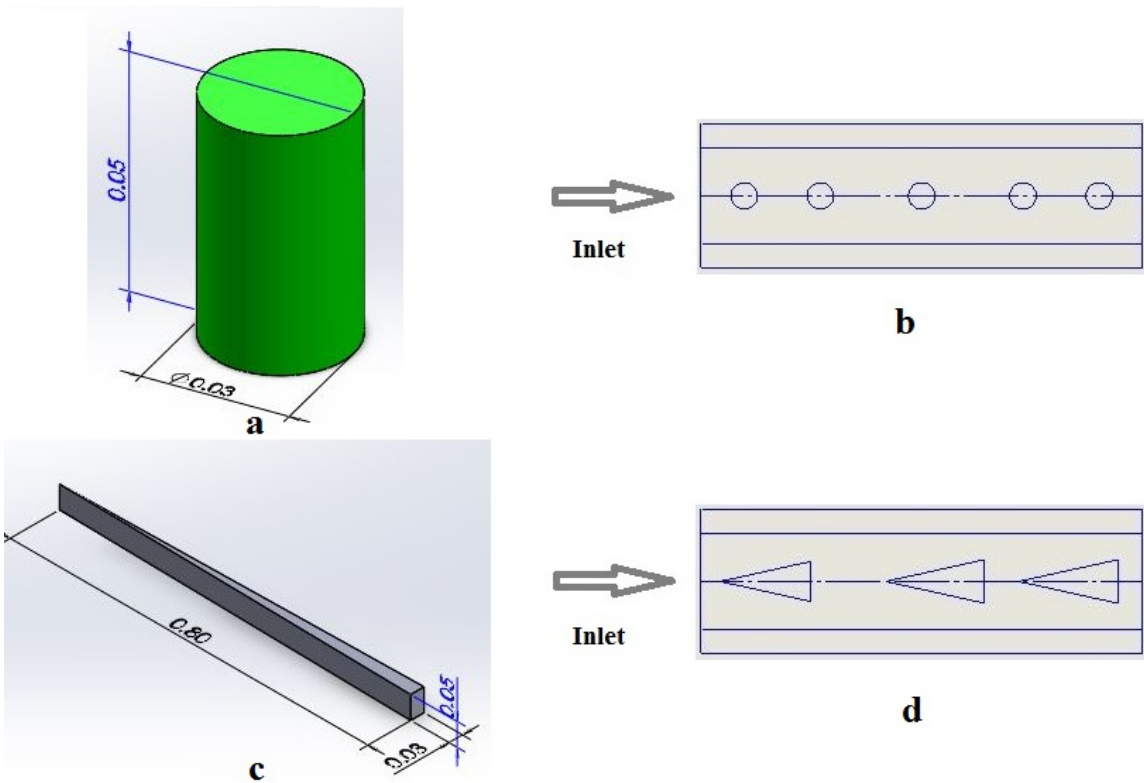


Fig. 2. (a) Cylindrical Fin, (b) Top view of the model with cylindrical fins, (c) Triangular ribs, (d) Top view of the model with triangular ribs

Energy equations:

$$k\nabla^2 T = 0 \quad (3)$$

$$Re = \frac{\rho V D_h}{\mu} \quad (4)$$

$$Nu = \frac{h D_h}{k_f} \quad (5)$$

$$h = \frac{q}{T_w - T_i} \quad (6)$$

For nanofluid:

$$\begin{aligned}
 \rho_{nf} &= (1 - \varphi)\rho_{bf} + \varphi\rho_p \\
 C_{P_{nf}} &= (1 - \varphi\rho_{bf}) + \varphi C_{P_p} \\
 \mu_{nf} &= 123\varphi^2 + 7.3\varphi + 1 \\
 k_{nf} &= 4.97\varphi^2 + 2.72\varphi + 1
 \end{aligned} \tag{7}$$

Numerical Simulation

In order to perform numerical analysis of the model considered in this study, commercial CFD package ANSYS FLUENT has been used. At first water with constant properties has been used as the heat transfer fluid and silicon as the heat sink material with properties as $k = 140 \text{ W/m-K}$, $C_p = 714 \text{ J/kg-K}$, $\rho = 2330 \text{ kg/m}^3$. Later in this study, nanofluid consisting of water with 4% volume fraction of Al_2O_3 has been used as the coolant with properties of the particle as $k_p = 36 \text{ W/m-k}$, $C_{p_p} = 773 \text{ J/kg-k}$ and $\rho_p = 3880 \text{ kg/m}^3$. Pressure based solver has been employed since incompressible fluid has been used. As the governing equations involved are nonlinear and contain many dependent variable, implicit formulation has been used. Maximum Reynolds number under consideration being 103.4, a laminar model has been used to solve the governing equations. SIMPLE scheme has been used for pressure velocity coupling. To discretize the governing equations second order upwind scheme has been employed. The convergence criteria have been set as 10^{-8} for energy and 10^{-4} for all other variables. A mesh independence test has been conducted to claim the

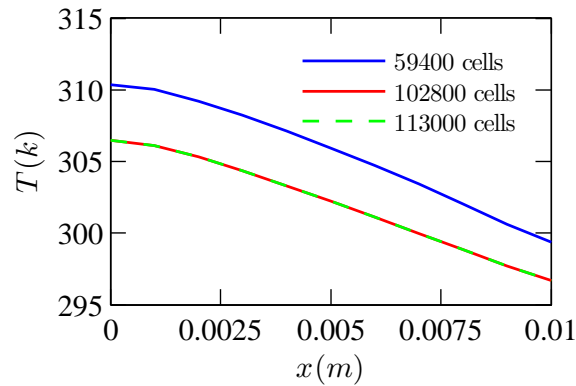


Fig. 3. Temperature Profile along the Channel for Different Mesh Size

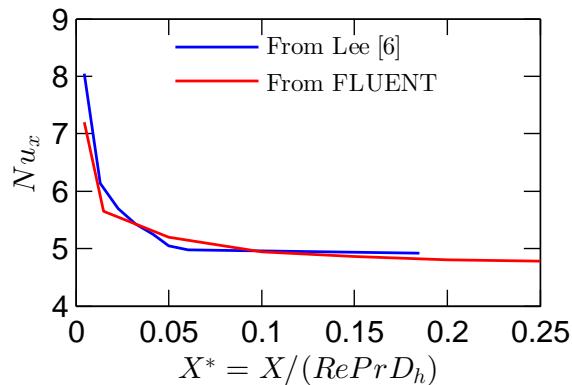


Fig. 4. Comparison of Numerical Results with Analytical Solution

reliability of the results obtained. Three different mesh of 59400, 102800 and 113000 cells have been created for the straight channel. For each of the three mesh temperature profile along the channel have been plotted. The mesh with 102800 cells has shown negligible difference of about 0.5% as compared to the mesh of 113000 cells as illustrated by Fig. 3. Hence, the mesh with 102800 cells has been adopted to generate the case study results hereafter. At the very beginning of the study Nu is calculated for the straight channel with water as working fluid from the numerical results obtained from FLUENT. This result is compared with that obtained from Nusselt number correlations proposed by Lee *et al.* [6]. Although the numerical results don't match exactly with the analytical results, they tend to follow the same pattern. The maximum discrepancy is about 7%. The reason behind this discrepancy lies with the quality of the mesh. Since the numerical results follow the same trend as that of the analytical one, we get inspiration to proceed for further investigation. The discrepancy between analytical and numerical result is illustrated in Fig. 4.

Results and Discussion

Heat transfer performance of microchannel heat sink with different geometry was investigated in this study. At first we studied the simple straight rectangular channel with water as the heat transfer fluid. We determined the temperature profile, heat transfer coefficient, Nu for this geometry. Then cylindrical fins were incorporated in the straight channel to take advantage of the increased surface area and similar investigation was performed. The numerical results obtained for this geometry were compared with those of straight rectangular channel. A higher heat transfer coefficient and higher Nu reveals improvement in heat transfer which validates that greater surface area results in better heat transfer rate. In order to take advantage of increased surface area along with the effect of boundary layer interruption, we incorporated triangular ribs in the straight rectangular channel. Similar investigations were performed as that of straight channel and straight channel with cylindrical fins to obtain the numerical results. The results were compared with the previous ones. Although the heat transfer coefficient and Nu are clearly higher than those of straight rectangular channel, they have only slightly been improved than those of cylindrical fins. The slightly better performance is possibly due to the effect of boundary layer interruption introduced by the ribs. Fig. 5 and 6 shows the improvement of incorporating cylindrical fins and triangular ribs. Whether water or nanofluid is used as working fluid, fins and ribs enhance cooling capacity of microchannel heat sink. The results indicate that Nu of microchannels with fins and ribs can 1.25 - 1.31 times of simple straight rectangular channel. These roughness elements disturb the flow and create recirculation flow and decrease the thermal boundary layer thickness, thus enhancing heat transfer rate and hence cooling capacity.

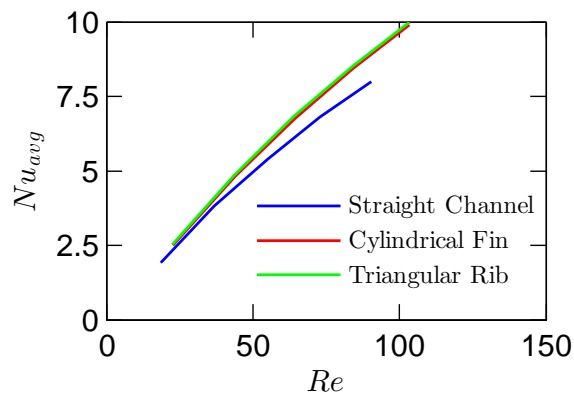


Fig. 5. Variation of Average Nusselt Number with Reynolds Number (Water)

Initially water was used as the working fluid in this study which provides quite good results. In quest of further improvement of heat transfer nanofluid was employed as the working fluid. Small solid particles suspended in a fluid are supposed to improve its thermal conductivity since the thermal conductivity of solid metals is higher than that of the fluids. To take advantage of this fact a single phase model of nanofluid with physical and thermal properties-all assumed to be constant with temperature was employed to study the heat transfer performance of the microchannel

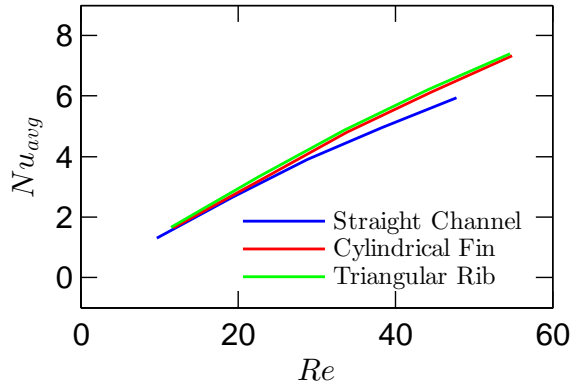


Fig. 6. Variation of Average Nusselt Number with Reynolds Number (Nanofluid)

heat sink. In the single phase model the fluid with the suspended nanoparticles is assumed to be continuous. The advantage of using single phase lies with its simplicity and less computational time required. In this study nanofluid composed of distilled water and Al_2O_3 nanoparticles with volume fraction of 4% was employed. The numerical results reveal higher heat transfer coefficient for nanofluid which in turn means higher Nu. It is due to the higher thermal conductivity of the nanoparticles than the base fluid (water) and also a better energy exchange process resulting from the chaotic movement of nanoparticles. Using nanoparticles has improved the thermal conductivity of the working fluid by 11.67% as compared to the base fluid. Nanoparticles have also improved the average Nu up to 1.35 times as compared to base fluid.

Although the nanofluid actually being a two phase fluid, the results show that it acts as a single phase fluid than a liquid-solid mixture. The results also represent that nanofluid enhances the effectiveness of the microchannel heat sink for all the geometries considered in this study. It is evident from Fig. 7, 8 and 9 that for the same value of Re, nanofluid provides better heat transfer performance. We can further conclude that nanofluid can significantly increase heat transfer rate even for relatively small volume fraction.

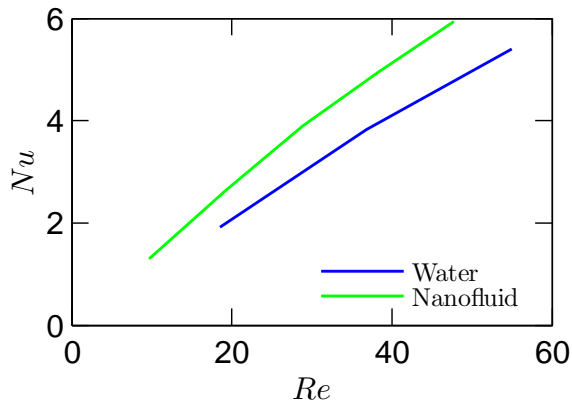


Fig. 7. Comparison of Nu between Water and Nanofluid for Straight Rectangular Channel

For each case considered in this study including geometry and coolant, three different value of heat flux have been used to heat the Silicon substrate. The values of heat flux were 50 W/cm^2 , 90 W/cm^2 and 150 W/cm^2 . The temperature profile of the heat sink along the length of the channel should be linear theoretically due to constant flux applied. We have also got almost linear profile of temperature in each case. The temperature increases towards outlet. The reason behind this is that at inlet the fluid is capable of extracting more heat. As a result it takes away more heat with it from the inlet region. As it approaches the outlet, its ability of removing heat from the solid decreases. That's

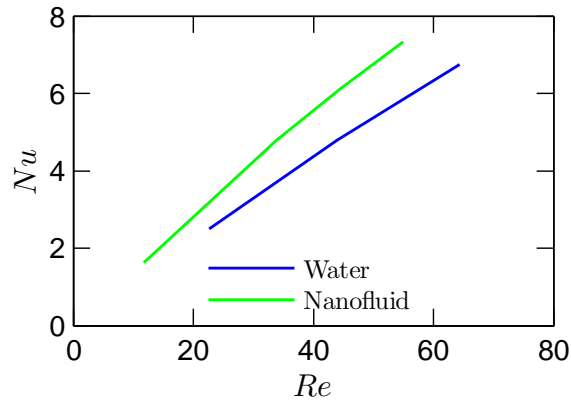


Fig. 8. Comparison of Nu between Water and Nanofluid for Rectangular Channel with Cylindrical Fin

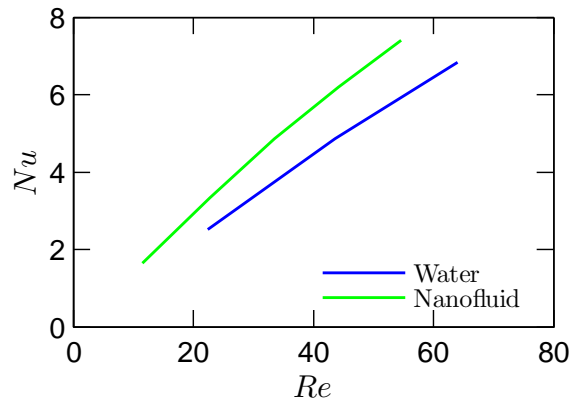


Fig. 9. Comparison of Nu between Water and Nanofluid for Rectangular Channel with Triangular Ribs

why, the temperature of the Silicon substrate is higher near the outlet region. Again due to increasing value of flux, the temperature of the solid at each section increases. However, heat flux has almost no effect on the local Nu.

Reynolds number (Re) has significant effect on convective heat transfer. To get a detailed scheme of the implication of Re on the performance of the microchannel heat sink, computations have been carried out by varying pressure difference between inlet and outlet of the fluid channel. In this current study pressure difference has been varied in the range of $P = 10 - 50$ KPa (g) with an increment of 10 KPa for all geometry and working fluid. With elevating pressure the velocity of the working fluid increases which in turn increases Re. Higher Re implies that forced convection is dominant over natural convection which means that forced convection governs the flow. When water is used as the working fluid, Re varies in the range of $Re = 18.55 - 103.4$ including the effect of different geometry. In case of nanofluid Re varies in the range of $Re = 9.67 - 54.57$ including the effect of different geometry. show that for the same value of Re, nanofluid provides better heat transfer performance.

Convective heat transfer phenomena are best described in terms of Nu. The higher the Nu, the higher is the convective heat transfer. In this current study, we have determined both Nu_x i.e. Nu along the channel and average Nu. The variation of Nu_x along the length of the channel has been determined for various pressure differences between the inlet and outlet. The profiles of local Nu for all the geometries and working fluids considered in this study have almost the same pattern. Nu_x is dependent on temperature gradient. Fig. 10 shows profile of Nu along the channel with triangular ribs with nanofluid as the coolant. As temperature gradient near the inlet zone is higher, Nu is higher in this area. This phenomenon also validates the fact that at the beginning of the channel, fluid is capable of transferring more heat from solid surface and so convective heat transfer is higher in this region. As the fluid proceeds through the

channel, its temperature increases and hence heat transfer rate decreases. Therefore, convective heat transfer decreases near the outlet zone.

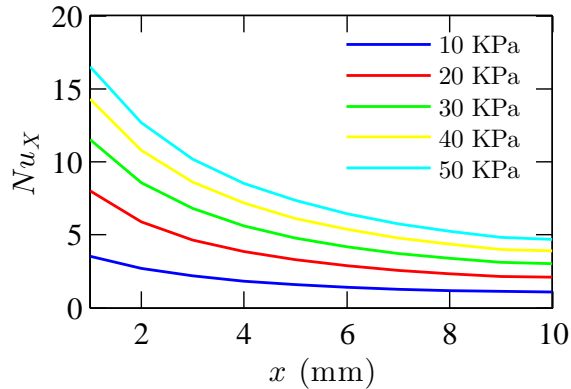


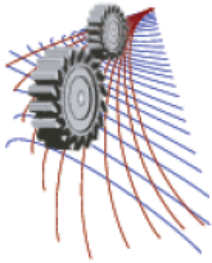
Fig. 10. Profile of Nusselt number along the channel in Rectangular Channel with Triangular Ribs with Nanofluid

Conclusions

The present study has dealt with conjugate heat transfer in microchannel heat sink including the effect of various geometry and working fluid by means of finite volume based simulations on fluid flow and thermal characteristics. The possibilities of enhancement of heat transfer have been investigated by incorporating cylindrical fins and triangular ribs in the simple straight rectangular channel. Nanofluid has been employed to explore the further improvement of heat transfer capabilities. Incorporating fins and ribs have clearly improved Nu and therefore heat transfer rate. Triangular ribs in the microchannel have slightly better impact than cylindrical fins. Cylindrical fins can improve the average Nu by 1.24 to 1.3 times compared to the straight rectangular channel while triangular ribs can improve up to 1.31 times. It is evident from numerical results that nanofluids can improve heat transfer performance by improving the thermal conductivity of the working fluid. Using nanofluid in the microchannel can improve the thermal conductivity by 11.67% and the average Nu by 1.35 times compared to the base fluid.

References

- [1] D. B. Tuckerman, R. Pease, High-performance heat sinking for vlsi, *Electron Device Letters*, IEEE 2 (1981) 126–129.
- [2] X. Peng, G. Peterson, The effect of thermo-fluid and geometrical parameters on convection of liquids through rectangular microchannels, *International Journal of Heat and Mass Transfer* 38 (1995) 755–758.
- [3] J. Judy, D. Maynes, B. Webb, Characterization of frictional pressure drop for liquid flows through microchannels, *International Journal of heat and mass transfer* 45 (2002) 3477–3489.
- [4] M. E. Steinke, S. G. Kandlikar, Single-phase liquid friction factors in microchannels, in: *ASME 3rd International Conference on Microchannels and Minichannels*, American Society of Mechanical Engineers, 2005, pp. 291–302.
- [5] W. Qu, I. Mudawar, Experimental and numerical study of pressure drop and heat transfer in a single-phase micro-channel heat sink, *International Journal of Heat and Mass Transfer* 45 (2002) 2549–2565.
- [6] P.-S. Lee, S. V. Garimella, D. Liu, Investigation of heat transfer in rectangular microchannels, *International Journal of Heat and Mass Transfer* 48 (2005) 1688–1704.
- [7] H. Al-Bakhit, A. Fakheri, A hybrid approach for full numerical simulation of heat exchangers, in: *ASME 2005 Summer Heat Transfer Conference collocated with the ASME 2005 Pacific Rim Technical Conference and Exhibition on Integration and Packaging of MEMS, NEMS, and Electronic Systems*, American Society of Mechanical Engineers, 2005, pp. 839–846.
- [8] P. Gunnasegaran, H. Mohammed, N. Shuaib, R. Saidur, The effect of geometrical parameters on heat transfer characteristics of microchannels heat sink with different shapes, *International Communications in Heat and Mass Transfer* 37 (2010) 1078–1086.
- [9] E. S. Cho, J. W. Choi, J. S. Yoon, M. S. Kim, Experimental study on microchannel heat sinks considering mass flow distribution with non-uniform heat flux conditions, *International Journal of Heat and Mass Transfer* 53 (2010) 2159–2168.
- [10] L. Chai, G. Xia, M. Zhou, J. Li, Numerical simulation of fluid flow and heat transfer in a microchannel heat sink with offset fan-shaped reentrant cavities in sidewall, *International Communications in Heat and Mass Transfer* 38 (2011) 577–584.
- [11] J. C. Maxwell, *A treatise on electricity and magnetism*, volume 1, Clarendon press, 1881.



Effect of Aspect Ratio on Convective Heat Transfer for Flat Cross Section Using Nanofluid

Syed Rafat Faysal, Ifat Rabbil Qudrat Ovi, A.K.M Sadrul Islam

Department of Mechanical & Chemical Engineering, Islamic University of Technology, Gazipur-1704, Bangladesh

^aCorresponding author: rafatmre@iut-dhaka.edu

ABSTRACT. For a typical cooling application, enhancement of convective heat transfer greatly depends on tube cross sections. This phenomenon was studied by performing numerical simulations on different cross sections for laminar flow with Nanofluids, containing different volume fractions (1%, 2% & 3%) of Aluminum oxide water. Constant axial heat flux with constant peripheral wall temperature i.e. H1 boundary condition was applied and results were validated with existing cross sections. After accomplishing CFD analysis on several cross sections, convective heat transfer coefficient was found highest in case of flat cross section and then the effect of aspect ratio on Nusselt number was investigated. Result shows that Nusselt number increases exponentially with aspect ratio and after reaching a certain aspect ratio, and beyond that Nusselt number becomes constant.

INTRODUCTION

Energy consumption of a heat exchange system can be reduced by enhancing the performance of heat exchanger. Heat exchanging is necessary in many applications of thermo fluid systems. There are many factors which affect the heat transfer performance of a heat exchanger. In this study we focus on geometry factor and the characteristics of fluid which act as a medium of heat transfer to enhance the heat transfer rate. To improve the thermal characteristics of fluid and to enhance the heat transfer rate this study has great importance.

For heat transfer usually various types of fluids are used. Such as refrigerants, water, engine oil, ethylene glycol etc. Actually they have poor heat transfer performance. So to get a desired heat transfer rate effectiveness of a heat exchanger should be very high. Many endeavors have been made to improve the heat transfer characteristics of fluid. Among them the most significant one is adding additives with liquid. For the sake of technology and advancement of fluid dynamics a new type of fluid has been emerged named as Nanofluid. It is a combination of base fluid and nanoparticles which are significantly smaller than 100 nm. Nanofluid shows better heat transfer characteristics than both conventional fluids and fluid containing micrometer sized particles. Several researcher confirmed that Nanofluid is the new window which can improve heat transfer performance.

Pak and Cho [1] experimented with Nanofluid (Al_2O_3 +water) for heat transfer with turbulent flow with (1%-3%) volume fraction. They achieved a phenomenal result, they found that, Nusselt number increases with the increase of volume concentration and Reynolds number.

Zeinali et al. [2] made several experimentations in circular tube for laminar flow condition with different concentration of particles. With the increase of volume concentration they got greater heat transfer coefficient.

Lai et al. [3] made an experiment in stainless steel test tube under constant heat flux boundary condition under low Reynolds number with Nanofluid (Al_2O_3 +water). They observed that there is 8% increase of Nusselt number for 1% volume concentration of Nano particle.

Ollivier et al. [4] numerically studied the possible application of nanofluids as a jacket water coolant in a gas spark ignition engine. For that purpose authors accomplished numerical simulations of unsteady heat transfer through the cylinder. Authors reported that because of higher thermal diffusivity of nanofluids, the thermal signal variations for knock detection increased by 15% over that forecast using water alone.

Mapaet el [5] found an imperative aspect about using Nano particles, they found that Nano particles reduce the thickness of thermal boundary layer.

Kang et al [6] investigated effectiveness and pressure drop in micro cross-flow heat exchanger, They found an interesting phenomena that heat transfer rate is strongly dependent on average temperature of fluid.

Farajollahi et al. [7] formed an experimental analysis to study heat transfer of Nanofluids in a shell and tube heat exchanger. The Nanofluids used were Al_2O_3 /water and TiO_2 /water under turbulent flow conditions. They found that Nano particle enhanced heat transfer performance significantly. A new study by Tasciuc[8] has shown that liquids embedded with nanoparticles show superior performance and stability when exposed to electric fields, which could lead to new types of miniature camera lenses, cell phone displays, and other microscale fluidic devices.

Those studies encourage us to work with Nanofluid (Al_2O_3 +water) and another thing is that Al_2O_3 is readily available and cheap in nature. Also, it has a good stabilizing effect with water which is the base fluid for our current study. At, the first stage of our study, we have selected four geometric cross sections. H1 boundary condition is applied for each of them with different volume concentrations of Nanofluid. Our investigation is confined within laminar flow only. Hussein and Sharma [9] did their experiment on turbulent flow region for selecting geometric cross section .They suggested to choose the flat geometry which is identical with our choice.

Shah and London [10] had done an extensive study to observe the effect of aspect ratio on Nusselt number for rectangular cross section. In this study, we investigate the effect of aspect ratio on Nusselt number for flat cross section.

In this study, the effect of heat transfer with the increment of Nano particle concentration is investigated for different geometry. Flat cross section is selected among them for extended study. Most importantly, a range of data is obtained by varying the geometric ratio of flat cross section, so that anyone can choose the optimum aspect ratio according to their application purpose.

PHYSICAL PROPERTIES OF NANOFLUID

Specific Heat and Density

Estimation of density of Nanofluid can be done based on mixture rule as given in literature [11] which is formulated as follows:

$$\rho_{nf} = (1 - \Phi)\rho_{bf} + \Phi\rho_p$$

On the other hand, energy balance gives Specific heat of Nanofluids:

$$(\rho C_p)_{nf} = (1 - \Phi)(\rho C_p)_{bf} + \Phi(\rho C_p)_p$$

Thermal conductivity and viscosity

For calculation of Thermal conductivity modified Maxwell's equation is used:

$$k = \left[\frac{k_p + 2k + 2(k_p - k)(1 + \beta)^3 \Phi}{k_p + 2k - 2(k_p - k)(1 + \beta)^3 \Phi} \right]$$

Here, β is the Nano layer thickness to the nanoparticle diameter ratio and is considered to be 0.1 in the present study particularly in equation (3). It is to be noted that average particle size has been taken as 15 nm. Another important property viscosity was estimated in the present study using Einstein (1956) equation as follows:

$$\mu_{nf} = (1 + 2.5 \Phi) \mu_{bf}$$

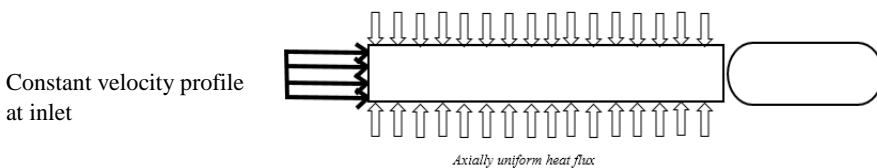


FIGURE 1: Schematic of problem

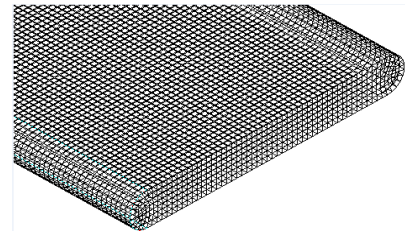


FIGURE 2: Meshing of the geometry

GOVERNING EQUATION

The basic equations to solve the fluid motion and the heat transfer are Continuity, momentum and energy Equation as given below [12]:

$$\nabla \cdot (\vec{v}) = 0 \quad (1)$$

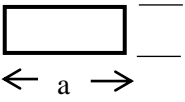
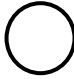

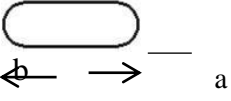
$$\nabla \cdot (\vec{v}\vec{v}) = -\nabla p + \nabla \cdot (\vec{\tau}) \quad (2)$$

$$\nabla \cdot (\vec{v}(\rho E + p)) = k\nabla \cdot \nabla T + \nabla \cdot (\vec{\tau} \cdot \vec{v}) \quad (3)$$

These equations do not have a direct analytical solution except for very simple cases, and hence have to be solved in the discretized form in a domain. In this study, they are solved using finite volume technique using commercial computational fluid dynamics (CFD) software FLUENT.

MODEL ANALYSIS

TABLE 1: Different cross sections

Shapes	Cross section
Rectangular	
Circular	
Elliptical	
Flat	

First of all, different types of cross sections (Figure 1) such as circular, rectangular, elliptical and flat with same hydraulic dia was numerically investigated. Meshing is done by ANSYS meshingSoftware in different cross sections water and then Nanofluid with different volume concentrations (1%, 2% & 3%) enters at an inlet temperature . constant velocity was given at inlet keeping Reynolds number 100 in all the cases. H1 boundary condition was applied assuming a heat flux and outlet is set to pressure outlet and water exits under atmospheric pressure. No slip at wall is assumed. Setting standard properties of water and nanofluid the simulation was performed. Then flat cross section was selected and the above process was repeated for aspect ratios like 1, 2.2, 2.4, 8, 10, 20, 30, 40, 60, 70, 80until Nusselt number become constant.

The numerical simulations were performed using CFD software package FLUENT. In order to introduce Pressure into the continuity equation the SIMPLE algorithm was used. The energy equation is activated during the analysis to predict heat transfer effect in the pipe. Steady state analysis was performed with pressure based solver. With the help of a second order upwind scheme the mass, momentum, and energy equations were solved. The simulations are performed for a convergence criterion 10^{-6} .

BOUNDARY CONDITION

Two types of constant heat flux boundary condition are possible, H1 and H2. H1 boundary condition requires that Heat flux remains constant in the axial direction and the temperature is held constant in the peripheral (angular) direction. In the present study, H1 boundary condition is applied in the wall.

GRID INDEPENDENCE TEST

Grid independence test was done for a flat cross section having ratio 2.2 and hydraulic dia 10.294 mm with water. Simulations have been performed with different number of mesh elements as shown in Figure: 3. with increasing the elements only computation time increases while results don't vary that much, so in every case number of elements were chosen in that way so that computation time required less while results remain more or less accurate.

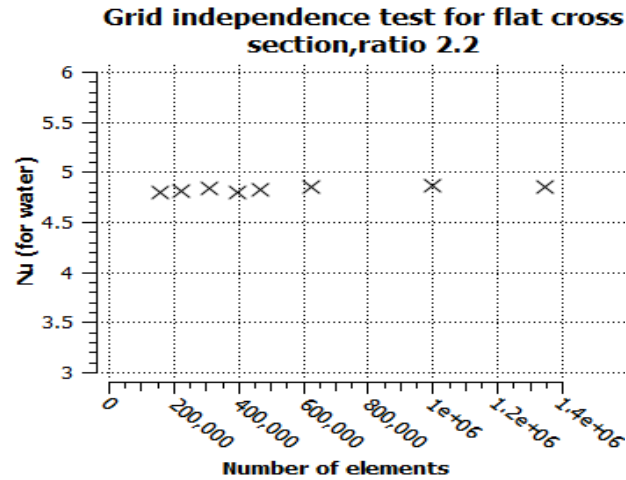


Figure 3: Grid Independence Test

MATHEMATICAL FORMULATION:

The steady state continuity and energy equation with associated HI boundary condition for all the simulations were solved using finite volume method maintaining the following assumptions:

1. Steady state laminar flow
2. Incompressible flow
3. Fluid properties were constant with respect to length and temperature.
4. Natural convection effect was neglected.

Bulk Temperature was calculated using following equation:

$$T_b = \frac{\int_A (V*T)dA}{\int_A V dA}$$

Convective heat transfer co-efficient was calculated using energy balance equation:

$$h = \frac{q''}{T_w - T_b}$$

Nusselt number was calculated as follows:

$$Nu = \frac{hD}{K}$$

RESULT AND DISCUSSION

In order to find out the optimum geometry several simulations have been done for Flat, Rectangular, Elliptical & circular cross sections. For every case, All the simulations have been done retaining the Hydraulic dia and (a/b) ratio identical with Reynolds number 100. Each geometry is simulated with water, 1%, 2% and 3% Nanofluid applying afore mentioned boundary condition. The following graphs are obtained after the completion of simulations.

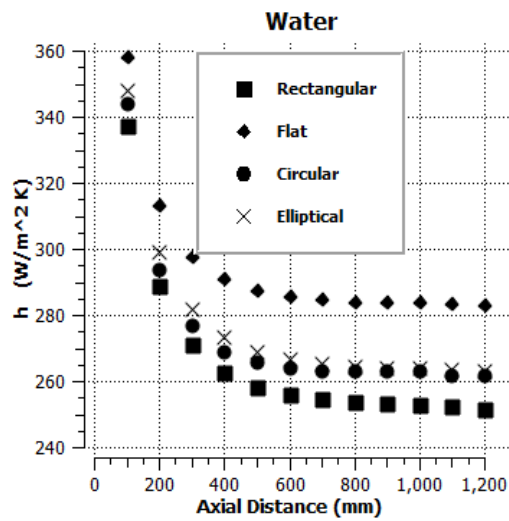


FIGURE 4: Graph of Convective heat transfer co-efficient h vs axial distance for different cross sections for water

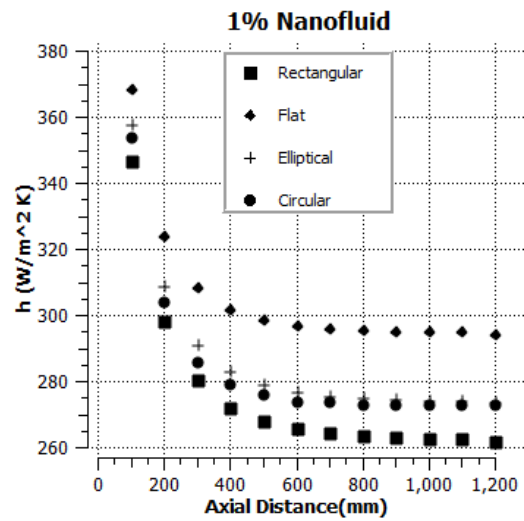


FIGURE 5: Graph of Convective heat transfer co-efficient h vs axial distance for different cross sections with 1% Nanofluid

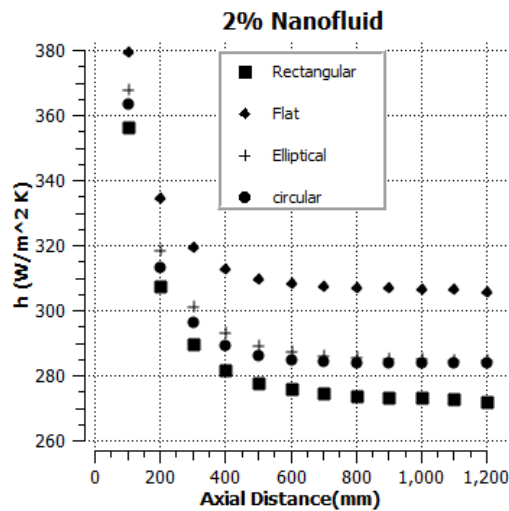


FIGURE 6: Graph of Convective heat transfer co-efficient h vs axial distance for different cross section for 2% nanofluid

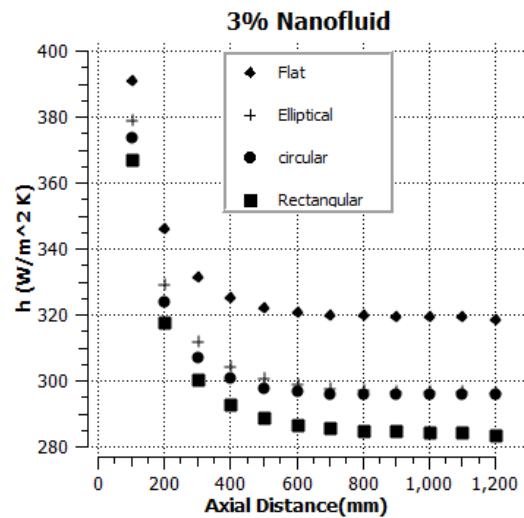


FIGURE 7: Graph of Convective heat transfer co-efficient h vs axial distance for different cross section for 3% nanofluid

Figure 4, 5, 6 & 7 distinctly illustrate that flat cross section surpasses the others by upholding superior convective heat transfer characteristics in all the circumstances. To study the effect of aspect ratio on Nusselt number, flat cross sections having a/b ratio 2.2, 2.4, 8, 10, 20, 30, 40, 60, 70, 80 were simulated with both water and Nanofluid according to data given in Table 2. And results are shown in the Figure 8.

Aspect ratio	a (mm)	b (mm)	Hydraulic dia, D_h (mm)
1	7.18	7.18	7.18
2.2	15.796	7.18	10.294
2.4	17.232	7.18	10.563
8	57.44	7.18	13.044
10	71.8	7.18	13.293
20	143.6	7.18	13.812
30	215.4	7.18	13.991
40	287.2	7.18	14.082
60	430.8	7.18	14.174
70	502.6	7.18	14.2
80	574.4	7.18	14.22

Cross sections	Ratio	Nu-from Simulation	Nu- from Literature[13]
Circular	-	4.34	4.36
Rectangular	1	3.63	3.61
Rectangular	2	4.16	4.12
Rectangular	3	4.77	4.79
Rectangular	4	5.37	5.33

TABLE 2: Dimensions of flat geometry for different aspect ratios

TABLE 3: Data validation

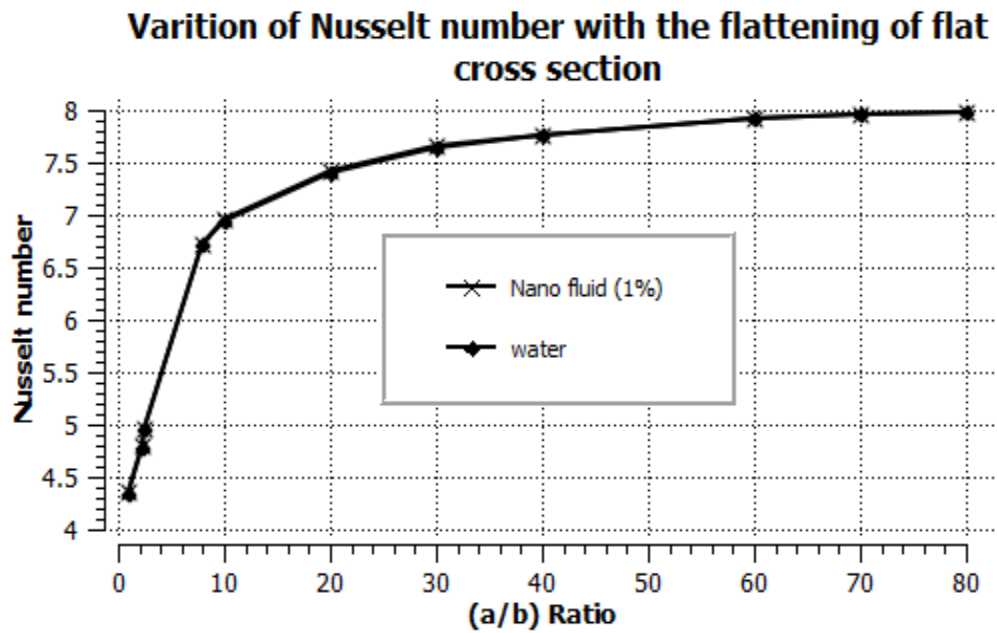


FIGURE 8: Variations of Nusselt number for different aspect ratios

From the figure it is obvious that, with the increase of a/b ratio Nusselt number increases and after Reaching a/b ratio 60 and beyond that Nusselt Number becomes more or less constant.

VALIDATION

Because of the inadequacy of data for flat Cross section under H1 boundary condition, results were validated with both rectangular cross sections of different a/b ratio and circular cross section and the results are given in the Table 3 below. H1 boundary condition requires that temperature should be constant at the peripheral direction, as the current results are validated with rectangular cross section, temperature profile for rectangular and flat cross section is given below

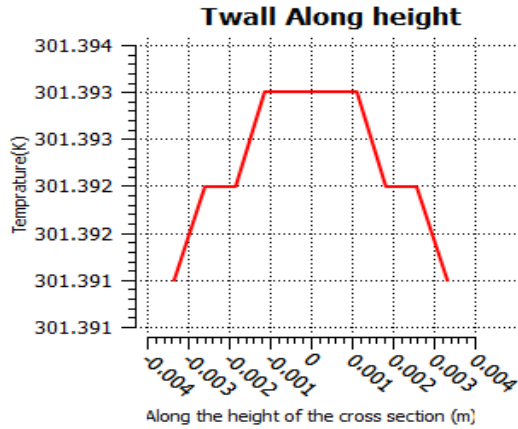


FIGURE 9: Temperature profile along height for Rectangular section

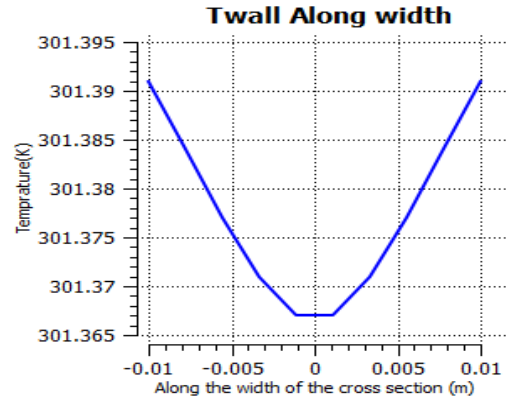


FIGURE 10 :Temperature profile along width for Rectangular section

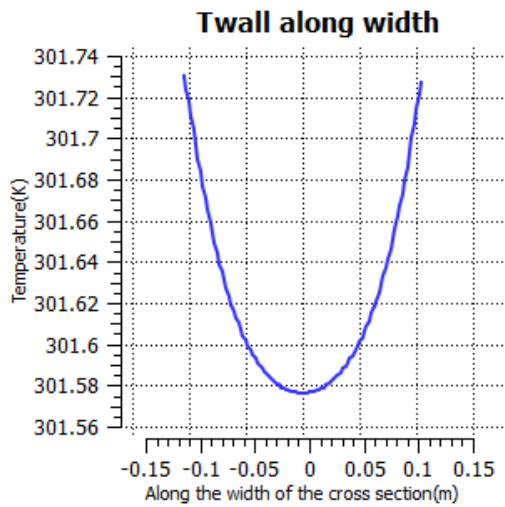


FIGURE 11:Temperature profile along height for flat section

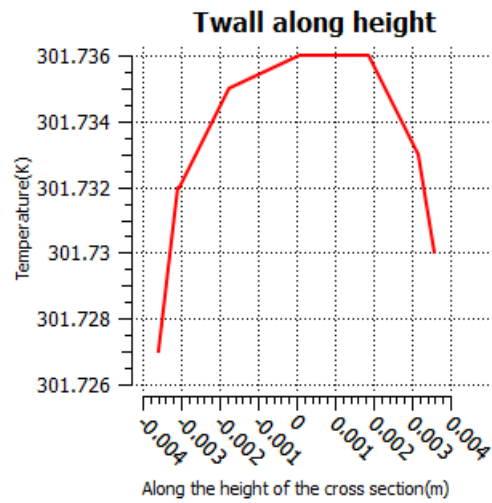


FIGURE 12:Temperature profile along height for flat section

From the Fig 9, 10, 11, 12 it has been observed that temperature remains almost constant along the height and width of the

NOMENCLATURE

C_p specific heat ($J\ kg^{-1}K^{-1}$)	q'' heat flux (Wm^{-2})
Nu Nusselt number (-)	\vec{v} velocity (ms^{-1})
h convective heat transfer coefficient ($Wm^{-2}k^{-1}$)	D hydraulic diameter (m)
k thermal conductivity ($Wm^{-1}k^{-1}$)	V velocity (ms^{-1})
T temperature (k)	Φ volume concentration (-)
μ viscosity (Nsm^{-2})	β ratio of nano layer
thickness to nano particle radius (-)	
ρ density (kgm^{-3})	

Subscripts

b	bulk
i	inlet
w	wall
bf	base Fluid
nf	nanofluid

wallboth for rectangular and flat section.so, we can say that H1 boundary condition is imposed correctly on all the cases.

CONCLUSION

The numerical simulations are carried out with uniform wall heat flux boundary condition for four different cross sections. The numerical model, for H1 boundary condition is validated with published data from literature [3] for rectangular cross sections. The addition of nano particles to the base fluid enhances the convective heat transfer co-efficient. However, further enhancement occurs with the increment of volume concentration of nanoparticle. The study concludes that flat geometry has the highest values of heat transfer co-efficient followed by elliptical, circular and rectangular geometry both for water and Nanofluid (1%, 2% and 3%). Large data sets are generated for wide range of aspect ratio varying from 1 to 80 for flat pipe with uniform wall heat flux configuration to observe it's effect on Nusselt number. It has been seen that Nusselt number increases exponentially with the aspect ratio and after reaching a certain aspect ratio, Nusselt number becomes constant. In a short, this study emphasizes on optimization of geometry as well as flowing fluid to improve heat transfer performance of radiator, electronic cooling system and other heat exchanging applications. On the basis of this study, a designer can choose desired aspect ratio of a heat exchanging device considering his design constraints and field of application.

REFERENCES

1. Hydrodynamic and heat transfer study of dispersed fluids with submicron metallic oxide particles, B.C. Pak, I.Y Cho, Experimental Heat Transfer 11 (1998) 151-170.
2. Experimental investigation of convective heat transfer of Al₂O₃/water nanofluid in circular tube S. ZeinaliHeris, M. Nasr Esfahan,,S.Gh. Etemad, International Journal of Heat and Fluid Flow 28(2007) 203-210
3. Convective Heat Transfer With Nanofluids in a Single 1.02-mm Tube, W. Y. Lai, B. Ducelescu, P. E. Phelan and R. S. Prasher, ASME 2006 International Mechanical Engineering Congress and Exposition.
4. Ollivier E, Bellettre J, Tazerout M, Roy GC. Detection of knock occurrence in a gas SI engine from a heat transfer analysis. Energy Convers Manage 2006; 47(7-8):879-93.
5. Mapa LB, Mazhar S. Heat transfer in mini heat exchanger using Nanofluids. Session B-T4-4, IL/IN sectional conference. Illinois: American Society for Engineering Education; 2005.
6. Kang SW, Tseng SC. Analysis of effectiveness and pressure drop in micro cross-flow heat exchanger. Appl Therm Eng 2007; 27:877-85
7. Farajollahi B, Etemad SG, Hojjat M. Heat transfer of nanofluids in a shell and tube heat exchanger. Int J Heat Mass Transfer 2010; 53:12-7.
8. Topnews. <http://www.topnews.in/nanofluids-be-used-make-new-types-camerasmicrodevices-and-displays-221378>; 2009 [07.11.09].
9. The effect of cross sectional area of tube on friction factor and heat transfer nanofluid turbulent flow, Adnan M. Husseina, K.V. Sharmac, R.A. Bakar, K. Kadirgama, International Communications in Heat and Mass Transfer Volume 47, October 2013, Pages 49-55.
10. Shah, R. K., and London, A. L., 1978, "Laminar Forced Convection in Ducts," Adv. Heat Transfer, Academic Press, New York, NY
11. A review on nanofluids-part I: theoretical and numerical investigations XQ Wang, AS Mujumdar - Brazilian Journal of Chemical Engineering, 2008.
12. Fluent 6.3 User'Guide, Fluent Inc., Lebanon, New Hampshire, 2006
13. Introduction to Heat Transfer, Sixth edition by Frank P. Incropera, David P. DeWitt, Theodore L. Bergman, Adrienne S. Lavine.